FAKULTÄT FÜR PHYSIK

DER TECHNISCHEN UNIVERSITÄT MÜNCHEN
FACHBEREICH: DENSE AND STRANGE HADRONIC MATTER (E12)

Measurable Consequences of an Attractive $\overline{K}N$ Interaction

Eliane Melanie Franziska Epple

FAKULTÄT FÜR PHYSIK

DER TECHNISCHEN UNIVERSITÄT MÜNCHEN
FACHBEREICH: DENSE AND STRANGE HADRONIC MATTER (E12)

Measurable Consequences of an Attractive $\overline{K}N$ Interaction

Eliane Melanie Franziska Epple

Vollständiger Abdruck der von der Fakultät für Physik der Technischen Universität München zur Erlangung des akademischen Grades eines

Doktors der Naturwissenschaften (Dr. rer. nat.)

genehmigten Dissertation.

Vorsitzender:		Univ.-Prof. Dr. Norbert Kaiser
Prüfer der Dissertation:	1.	Univ.-Prof. Dr. Laura Fabbietti
	2.	Univ.-Prof. Dr. Stephan Paul

Die Dissertation wurde am 13.6.2014 an der Technischen Universität München eingereicht und durch die Fakultät für Physik am 07.07.2014 angenommen.

Für Kirill

Abstract

In the field of low energy QCD the effective description of interactions between ground state hadrons plays a major role in nuclear physics. One of these interactions occurs between anti-kaons and nucleons, and is a topic of a long standing interest. A specific attention is lately drawn to the possible existence of bound states between $\overline{K}$s and nucleons. This old concept is based on the idea that the attractive interaction between anti-kaons and nucleons, that already manifests itself as the $\overline{K}N$-pole of the $\Lambda(1405)$-resonance, is strong enough to bind further nucleons by the help of a $\overline{K}$. The simplest form of these clusters is the $\overline{K}NN$ which consists of a $\overline{K}$ bound to two nucleons. This state might decay into $p\Lambda$ and is, thus, accessible via open strangeness production in p+p collisions.

This work continues the investigations in this field, as a rather puzzling impression is left behind from previous experiments, and further conclusions are needed. The work contains two major data analyses.

The first one is dedicated to the $\overline{K}N$ bound state, and selects the semi-exclusive reaction $p + p \rightarrow p + K^+ + \Lambda + X$. This was done to investigate the strange resonances $\Lambda(1405)$ and $\Sigma(1385)^0$ in their neutral decay channels $\Sigma^0\pi^0$ and $\Lambda\pi^0$, respectively. Besides resonance production, several other states contribute to this final state. Their relative strengths have been determined and the obtained production cross sections were in agreement with the results from an independent analysis of the $\Lambda(1405)$ decay into $\Sigma^\pm\pi^\mp$, done in a parallel work.

To set reasonable constraints for coupled channels calculations in the $\overline{K}N$ sector, a high-precision $\Lambda(1405)$-mass spectrum is needed. The obtained yield and uncertainty of the $\Lambda(1405)$ contribution to the final spectra, however, showed that the required precision is not given in the neutral decay channel. Nonetheless, the extracted production cross section of the $\Sigma(1385)^0$-resonance provided a crucial constraint for the analysis of the $\Lambda(1405)$ in its charged decay channels $\Sigma^\pm\pi^\mp$, since the latter analysis requires this external constraint.

The second analysis is dedicated to the $\overline{K}NN$ state in which the semi-exclusive statistic $p+p \rightarrow p+K^{+}+\Lambda+X$ was narrowed to the exclusive reaction $p+p \rightarrow p+K^{+}+\Lambda$ by exploiting the specific event kinematic. In total ≈ 20,000 events with a background contamination of ≈ 10% were selected. The aim of this analysis was to search for a possible contribution of the $\overline{K}NN$ to the $p\Lambda$ final state.

The data from the exclusive event selection were analyzed with help of a partial wave analysis (PWA) from the Bonn-Gatchina group. In this way, a good description of the full event kinematic was obtained with waves that include the production of $N^{*+}p$ and non-resonant $pK^{+}\Lambda$ intermediate states, which can interfere. The $p\Lambda$ invariant mass spectrum, which could contain the decay products of the $\overline{K}NN$, can be described well without a contribution of the latter.

A statistical analysis was performed to quantify this observation and determine an upper limit on the production cross section for the $\overline{K}NN$ in p+p reactions at 3.5 GeV. The investigation of the local p_0-value revealed an overall good agreement between model and data within 3σ. In a next step, the production of a $\overline{K}NN$ was included consistently into the PWA solution and the agreement with the data was tested for several possible quantum numbers, masses and widths of the latter. The upper limit was determined for a CL_s value of 95% and reads ≈ 2–7% (Γ = 30 MeV/c^2), 3–10% (Γ = 50 MeV/c^2) and 3–12% (Γ = 70 MeV/c^2) of the total $pK^{+}\Lambda$ production cross section with $M_{\overline{K}NN}$ = 2220 - 2370 MeV/c^2.

The quantitative result of this thesis draws the conclusion that if a $\overline{K}NN$ exists, its branching into $p\Lambda$ is either small, or it is produced with a low cross section in p+p reactions or it is so broad that a differentiation from background becomes difficult. The possibility remains, however, that it has larger coupling strengths to other final states which might still allow an experimental verification.

Zusammenfassung

Im Bereich der nieder-energetischen QCD spielt die effektive Beschreibung von Wechselwirkungen zwischen Hadronen-Grundzuständen eine wichtige Rolle in der Kernphysik. Eine dieser Wechselwirkungen tritt zwischen Anti-Kaonen und Nukleonen auf und ist ein Thema von lang anhaltendem Interesse. Besonders im Fokus stand in letzter Zeit die mögliche Existenz von Bindungszuständen zwischen Anti-Kaonen und Nukleonen. Dieses alte Konzept basiert auf der Idee, dass eine anziehende Wechselwirkung zwischen Anti-Kaonen und Nukleonen, die sich bereits im $\overline{K}N$-Pol der $\Lambda(1405)$-Resonanz offenbart, so stark sein könnte, dass weitere Nukleonen mit Hilfe von Anti-Kaonen verbunden werden könnten. Die einfachste Form eines solchen Clusters stellt das $\overline{K}NN$ dar, das aus einem $\overline{K}$ und zwei Nukleonen besteht. Dieser Zustand könnte in ein $p\Lambda$ Paar zerfallen und ist daher in expliziter Seltsamkeitsproduktion in p+p Kollisionen messbar.

Diese Arbeit setzt die Untersuchungen in diesem Feld fort, da ein recht widersprüchliches Bild von vorherigen Experimenten hinterlassen wurde und deswegen weitere Befunde notwendig sind. Die Arbeit teilt sich in zwei größere Datenanalysen.

Die erste Analyse ist dem $\overline{K}N$-Bindungszustand gewidmet und selektiert die halbexklusive Reaktion $p+p \to p+K^{+}+\Lambda+X$. Dies wurde gemacht, um die seltsamen Resonanzen $\Lambda(1405)$ und $\Sigma(1385)^{0}$ in ihren neutralen Zerfallskanälen $\Sigma^{0}\pi^{0}$ bzw. $\Lambda\pi^{0}$ zu untersuchen. Neben diesen Resonanzen tragen noch weitere Zustände zu diesem Endzustand bei. Deren individuelle Beitragsstärken wurden bestimmt und die ermittelten Produktionswirkungsquerschnitte waren vereinbar mit den Ergebnissen einer unabhängigen Analyse des $\Lambda(1405)$ Zerfalls in $\Sigma^{\pm}\pi^{\mp}$, die in einer parallelen Arbeit angefertigt wurden.

Um verwertbare Beschränkungen für coupled-channels Rechnungen im $\overline{K}N$-Fachgebiet zu erzeugen, benötigt man ein sehr präzises $\Lambda(1405)$ Massenspektrum. Der erhaltene Beitrag des $\Lambda(1405)$ im Endspektrum und seine Unsicherheit zeigte jedoch, dass die erforderliche Präzision in dem neutralen Zerfall-

skanal nicht zu erreichen ist. Nichtsdestotrotz lieferte der gewonnene $\Sigma(1385)^0$ Produktionswirkungsquerschnitt einen wichtigen Beitrag zur $\Lambda(1405)$ Analyse in den geladenen Zerfallskanälen $\Sigma^{\pm}\pi^{\mp}$, da diese Analyse eine externe Beschränkung für den $\Sigma(1385)^0$ Beitrag benötigt.

Der zweite Teil der Analyse widmete sich dem $\overline{K}NN$-Zustand, wobei die halbexklusive Statistik $p + p \rightarrow p + K^+ + \Lambda + X$ in die exklusive Reaktion $p + p \rightarrow p + K^+ + \Lambda$ verringert wurde, unter Ausnutzung der speziellen Kinematik der Ereignisse. Insgesamt wurden etwa 20,000 Ereignisse mit einer Untergrund Kontamination von $\approx$ 10% selektiert. Das Ziel dieser Analyse war die Suche nach einem möglichen Beitrag des $\overline{K}NN$'s zum $p\Lambda$ Endzustand.

Die Daten der exklusiven Ereignisselektion wurden mit Hilfe einer Partial Wellen Analyse der Bonn-Gatchina Gruppe analysiert. Dadurch wurde eine gute Beschreibung der gesamten Ereignis-Kinematik erreicht, mittels Wellen, die die Produktion von $N^{*+}p$- und nicht-resonanten $pK^+\Lambda$ Zwischenzuständen, welche interferieren, beinhalten. Das $p\Lambda$ invariante Massenspektrum, das die Zerfallsprodukte der $\overline{K}NN$ beinhalten könnte, kann gut ohne den Beitrag desselben beschrieben werden.

Eine statistische Analyse wurde durchgeführt, um diese Beobachtung zu quantifizieren und eine Obergrenze für den Produktionswirkungsquerschnitt des $\overline{K}NN$ in p+p Reaktionen bei 3.5 GeV zu bestimmen. Die Untersuchung des lokalen p_0-Werts zeigte eine umfassend gute Übereinstimmung zwischen Modell und Daten innerhalb von 3σ. In einem nächsten Schritt wurde die Produktion eines $\overline{K}NN$'s konsistent in die PWA Lösung eingefügt und die Übereinstimmung mit den Daten wurde für etliche mögliche Quantenzahlen, Massen und Breiten des Letzteren geprüft. Die Obergrenze des Produktionswirkungsquerschnitts wurde für einen CL_s-Wert von 95% bestimmt und ergibt sich zu $\approx$ 2–7% (Γ = 30 MeV/c^2), 3–10% (Γ = 50 MeV/c^2) und 3–12% (Γ = 70 MeV/c^2) des totalen $pK^+\Lambda$ Produktionswirkungsquerschnitts mit $M_{\overline{K}NN}$ = 2220 - 2370 MeV/c^2.

Das quantitative Ergebnis dieser Arbeit zieht die Schlussfolgerung, dass falls das $\overline{K}NN$ existieren sollte es entweder eine kleine Kopplung zu Λp besitzt, oder mit einem niedrigen Wirkungsquerschnitt produziert wird, oder so breit ist, dass eine Unterscheidung vom Untergrund schwierig wird. Darüber hinaus besteht jedoch weiterhin die Möglichkeit, dass das $\overline{K}NN$ eine stärkere Kopplung zu anderen Endzuständen besitzt, was eine experimentelle Bestätigung ermöglichen würde.

Contents

Part I

Introduction and Theory

1 | Introduction

1.1 Fundamental Forces and Elementary Particles

The beginning of modern particle physics is marked by the early 1960s. Back then the situation seemed much like a gold rush, as more and more particles were discovered. Although exciting, the situation turned out to be rather unsatisfying for the physicists as they were faced with a constantly increasing number of "elementary" particles. Aiming at a comprehensive and compact understanding of the building blocks of matter hundredths of fundamental components seemed to be a rather odd and puzzling thought.

A lot of effort was put into the simplification of this situation where the progress in theoretical particle physics at that time was dominated by the works of Murray Gell-Mann. He and George Zweig independently introduced a new classification scheme for these recently discovered particles, now known as hadrons, that involved new elementary particles: the quarks [2, 3]. In this view, the hadrons were build up by a group of two or three quarks, respectively.

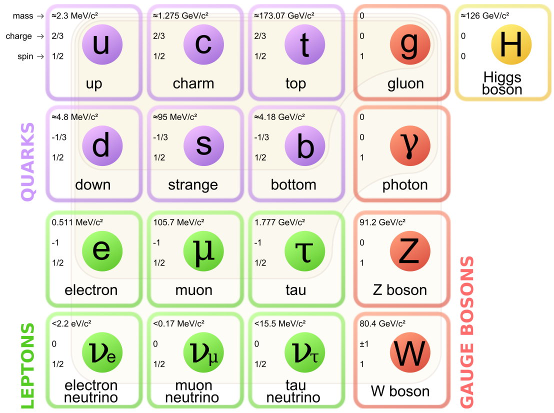

Figure 1.1: Known particles and exchange bosons of the standard model of particle physics [1].

Today, the known components of matter and their interaction are well described by the Standard Model (SM) of particle physics, see Figure 1.1. In this picture, matter is made out of quarks and leptons which both come in three generations. The fundamental interactions (strong, weak, and electromagnetic) are incorporated by the exchange of gauge bosons, shown in Figure 1.1. Although, many believe in the existence of a more fundamental theory that will be able to supersede the latter, the SM has only recently again proven its success by the discovery of its last missing piece - the Higgs boson [4, 5].

1.2 Strong Interaction and QCD

The strong interaction in the Standard Model is described by the theory of quantum chromodynamics (QCD). Within this field theory the interaction of the strongly interacting fermions (quarks) is mediated by the exchange of bosons (gluons) of which both carry a new quantum number: the color charge. Owed to the fact that gluons also carry color charge, they are self-interacting. This leads to a wealth of new phenomena such as asymptotic freedom and confinement.

Asymptotic freedom is marked by the weak strength of the strong force at small distances and large energies. This is described by the "running" coupling constant α_s that models the changing strength of the strong interaction, shown in Figure 1.2. At these large energy scales QCD can be treated preturbativley and this approach has proven its power by an accurate description of many observables.

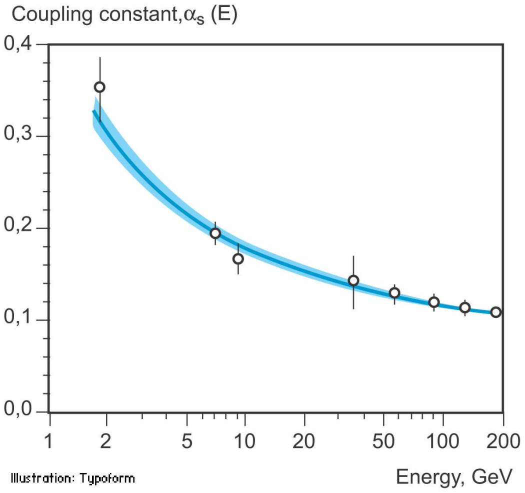

Figure 1.2: The "running" coupling constant α_s of the strong interaction [6]. The prediction of QCD (blue band) agrees well with the measured values.

At low energies, where the strong interaction is dominated by confinement, one needs to apply different methods in order to describe the measurements. In this regime, quarks and gluons are no longer treated as individual objects but are confined within groups, known as hadrons. The world we live in is dominated by this low energy regime and the observation of confined quarks in form of $q\bar{q}$ (Mesons) and qqq (Baryons) systems.

1.3 Ground State Hadrons and Effective Field Theories

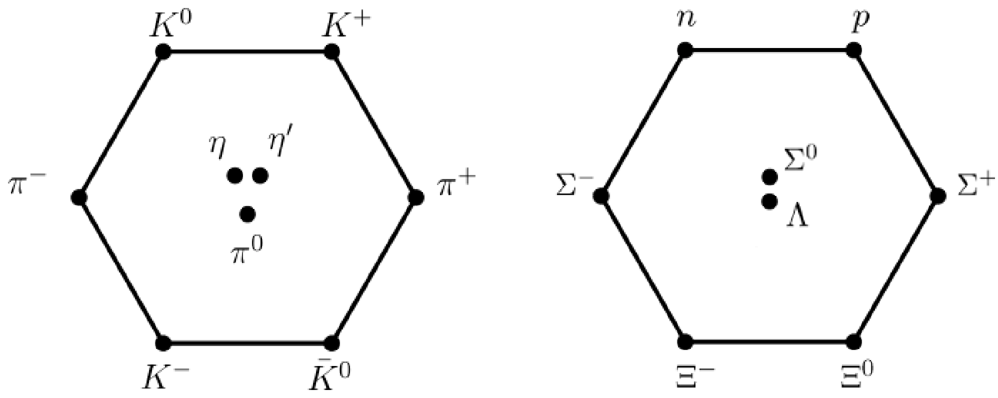

Figure 1.3: The ground state octets and singlets of hadrons. Left: Pseudo-scalar mesons ($J^{PC}=0^{-+}$), right: ground state baryon octet and singlet states ($J^P=\frac{1}{2}^+$).

Low-energy QCD with $N_f = 3$ quark flavors can be described within the concept of an effective field theory. This theory is called chiral perturbation theory (ChPT) and treats the confined hadrons as the relevant degrees of freedom. It incorporates all important symmetries of its underlying fundamental theory, QCD [7]. An important symmetry of this Lagrangian is the chiral symmetry[1]. This $SU(3)_L \text{x} SU(3)_R$ symmetry is broken twice: once spontaneously, which causes the appearance of eight Goldstone bosons with degenerate masses, that can be identified with the mesons shown in Figure 1.3 on the left, and a second time explicitly, which explains the experimentally observed mass difference [8] among these bosons due to the finite quark masses [7].

The chiral Lagrangian couples the ground state baryons to the ground state mesons and is, thus, used to explain basic hadronic interactions. The experimental and theoretical determination of Baryon-Baryon (BB) and Meson-Baryon (MB) interactions is, in this view, a test of QCD at low energy scales. Such programs have been carried out for NN [9], ΛN [10, 11], ηN [12, 13, 14] and $\overline{K}N$ [15, 16, 17, 18] interactions, for example. The latter of these forces was found to be strongly attractive in its isospin I=0 component. This gives rise to a lot of measurable consequences that are discussed in the following.

---

[1] The interaction is equivalent for left and right handed quarks as well as for different flavours.

1.4 Low Energy $\overline{K}N$ Interaction

As discussed, ChPT is a useful theory for the description of the low energy sector of QCD. In contrast to other Meson-Baryon channels like πN or K^+N this approach fails, however, when applied to the $\overline{K}N$ interaction [19]. This has three reasons [20]:
1) The $\overline{K}N$ interaction is strongly attractive in the I=0 channel and hence develops a bound state just below the threshold.
2) The $\Sigma\pi$ interaction, also attractive, develops a broad (I=0) resonance at about the energy of the $\overline{K}N$ bound state. These effects alone would lead to two separate objects observed in experiments.
There is, however, 3) a strong coupling between the $\Sigma\pi$ and the $\overline{K}N$ channel which leads to an interference of the bound state and the resonance in the I=0 channel, known experimentally as the $\Lambda(1405)$.

This picture is obtained by a non-perturbative chiral SU(3) coupled channels approach [19, 21, 22], in which the $\Lambda(1405)$ is generated dynamically from the Meson-Baryon interaction.

Coupled channels framework

To treat the $\overline{K}N$ interaction in a coupled channels framework all channels with S=-1 and Q=0 must be taken into account. These are the ten following channels: K^-p, $\overline{K}^0n$, $\pi^0\Lambda$, $\pi^0\Sigma^0$, $\pi^+\Sigma^-$, $\pi^-\Sigma^+$, $\eta\Lambda$, $\eta\Sigma^0$, $K^+\Xi^-$ and $K^0\Xi^0$. The relativistic unitary T-Matrix T_{ij} of the ten coupled channels can be described by a self-consistent Bethe-Salpeter equation [15]:

$$T_{ij} = V_{ij} + V_{il}G_lT_{lj}. \tag{1.1}$$

To constrain this phenomenological approach by chiral dynamics the MB interaction, derived from the next-to-leading order MB chiral Lagrangian, is used to construct the interaction kernel V_{ij} in this equation. The diagonal matrix G_l is given by [15]:

$$G_l(Q) = \int \frac{d^4k}{(2\pi)^4} \frac{\mathrm{i}}{[(Q-k)^2 - M_l^2 + \mathrm{i}\epsilon](k^2 - m_l^2 + \mathrm{i}\epsilon)} \quad , \tag{1.2}$$

with M_l and m_l being the mass of the baryon and the meson in channel l. This equation (1.1) is an integral equation which sums up a series of diagrams to an infinite sum, illustrated in Figure 1.4. If the T-Matrix is calculated the scattering

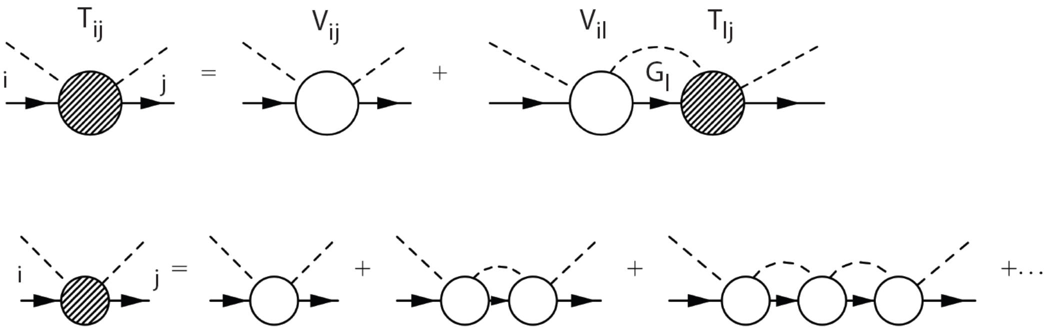

Figure 1.4: The infinite sum of diagrams (lower part) calculated within the Bethe-Salpeter equation (upper part) [23].

amplitude f_{ij} can be derived according to [15]:

$$f_{ij}(\sqrt{s}) = \frac{1}{8\pi\sqrt{s}} T_{ij}(\sqrt{s}) \quad . \tag{1.3}$$

This connects the theoretical framework to experimental observables, discussed in the following.

1.4.1 Experimental Constraints

The low energy $\overline{K}N$ interaction can be divided into three major regions on the energy axis: the resonance region, the threshold region, and the scattering region. In each part the complex scattering amplitude has distinct features which can be compared to different experiments. In order to allow solid predictions for yet unresolved phenomena in the S=-1 sector, the free parameters in the coupled channels approach need to be constrained by a fit to the measured data. In most attempts the scattering and threshold region is used to make predictions of the resonance region, namely the positions of the two Λ(1405) poles. In Ref. [24] the measured Λ(1405) mass distributions from photo-production are used to make predictions on the scattering region, for example. Either way can be used to test the solidity of the model parameters and make predictions for observables.

The Scattering Region

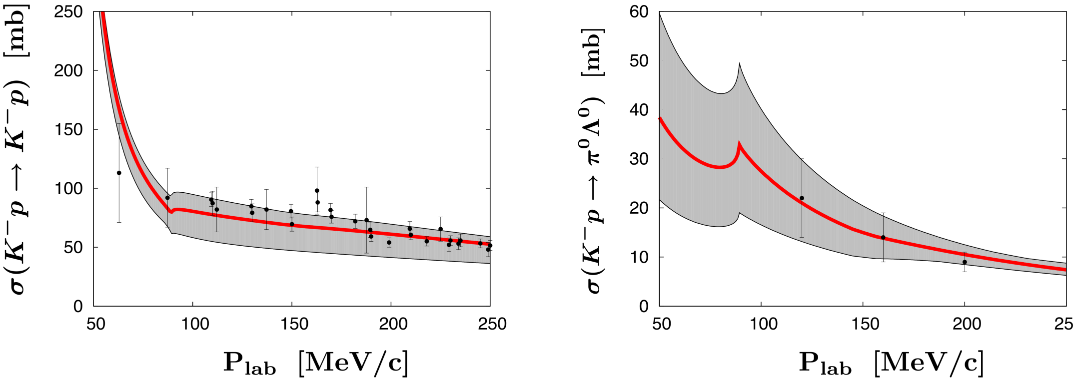

Figure 1.5: Two out of six K^-p scattering channels fitted by the model of [15].

Equation 1.3 shows the connection of the calculated scattering matrix to an experimental cross section via the square of the scattering amplitude. With this connection the model parameters can be constrained by experimental data. Figure 1.5 shows two measured scattering cross sections as a function of the beam momentum compared to model fits of Ref. [15].

The available database includes the following reactions: $K^-p \rightarrow K^-p, \bar{K}^0n, \pi^+\Sigma^-$, $\pi^-\Sigma^+$, $\pi^0\Sigma^0$, $\pi^0\Lambda$, $\eta\Lambda$, $\pi^0\pi^0\Sigma^0$, the $\pi^-\Sigma^+$ event distribution from $K^-p \rightarrow \Sigma^+(1660)\pi^-$ and the $\pi^0\Sigma^0$ event distribution from $K^-p \rightarrow \pi^0\pi^0\Sigma^0$ with $p_K = 0.687$ GeV/c, respectively (see e.g. Ref. [18] and references therein for the experimental data)

The Threshold Region

The threshold region describes the $\overline{K}N$ interaction at rest. As it is experimentally extremely challenging to measure the scattering process at zero and near zero momentum, no scattering data at threshold are available. There is, however, access to this region via the measurements of kaonic atoms.

Firstly, the threshold branching ratios γ, R_c and R_n have been determined by the measurement of stopped K^- on hydrogen [25, 26]:

$$R_c = \frac{\sigma(K^-p \to \text{charged particles})}{\sigma(K^-p \to \text{all})}, \quad \gamma = \frac{\sigma(K^-p \to \pi^+\Sigma^-)}{\sigma(K^-p \to \pi^-\Sigma^+)} \tag{1.4}$$

$$R_n = \frac{\sigma(K^-p \to \pi^0\Lambda)}{\sigma(K^-p \to \text{all neutral states})}.$$

Secondly, from the measured energy shift, compared to the pure electromagnetic value, (ΔE) and the width (Γ) of the 1s state in kaonic hydrogen (where the effect of the strong potential is large) the complex scattering length a(K^-p) can be determined. The scattering length expresses the value of the scattering amplitude at threshold a(K^-p) = $f_{K^-p\to K^-p}(\sqrt{s} = m_{K^-} + M_p)$ and can be deduced from the values ΔE and Γ [15]. Figure 1.6 summarizes the three recent experimental values for ΔE and Γ and the fitted values from different chiral models.

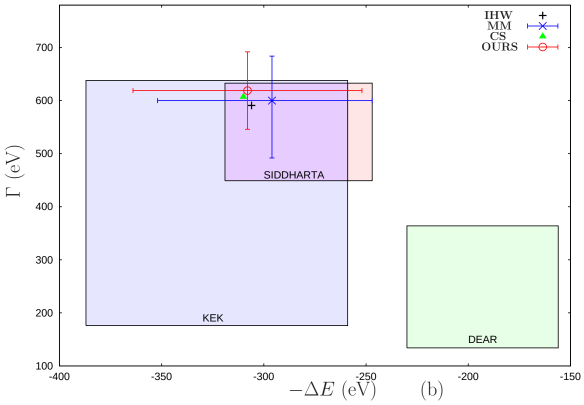

Figure 1.6: Experimental data of 1s state of kaonic hydrogen ($-\Delta E$ and Γ) [27] (KEK), [28] (DEAR) and [29] (SIDDHARTA). The theoretical predictions stem from [15] (IHW in black plus symbol), [16] (CS in green triangle) and Ref. [17] (MM in blue cross), the work quoted as OURS coincides with the source of the figure in Ref. [18].

The Resonance Region

The resonance region describes the sub-threshold $\overline{K}N$ interaction. This part of the $\overline{K}N$ scattering amplitude becomes important when the behavior of antikaons in medium or kaonic nuclear bound states (Section 1.6) are studied. Due

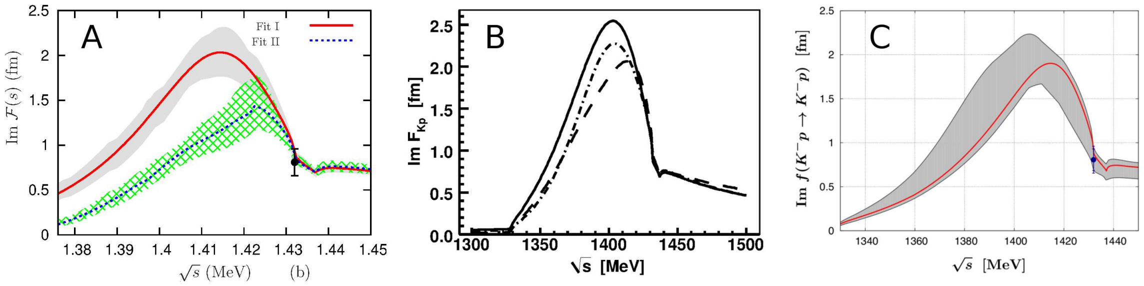

Figure 1.7: Theoretical predictions for the subthreshold K^-p scattering amplitude. A is from Ref. [18], B from Ref. [16] and C from Ref. [15].

to the attractive $\overline{K}N$ interaction, a low-energy kaon in the vicinity of nucleons is described by the sub-threshold regime. This important region is, however, not directly accessible by experimental observations. The reason for this is the strong coupling of the $\overline{K}N$ and the $\Sigma\pi$ channel. Both channels bear an attractive interaction that creates a bound state ($\overline{K}N$) and a resonance ($\Sigma\pi$) which interfere and produce a mass distribution, known as the Λ(1405).

The fact that the observable in this energy region is an interfered sum of two scattering amplitudes hinders a direct extraction of information. The sub-threshold $\overline{K}N$ amplitude is, thus, predicted with help of the coupled channels approach constrained to the scattering-, and threshold region. Even though, there are a lot and precise measurements available, the sub-threshold extrapolations show larger differences between the models, as indicated in Figure 1.7. It displays the imaginary part of the K^-p scattering amplitude, predicted by different groups. The predictions differ significantly in the point where the strongest absorption of the K^-p channel appears.

This sub-threshold amplitude is a basic ingredient for the prediction of the Λ(1405) mass distribution. To obtain this distribution also the $\Sigma\pi$ amplitude for the I=0 channel has to be evaluated. The I=0 $\overline{K}N$ amplitude is obtained from the K^-p and K^-n scattering amplitude of which the latter is not as well constrained as the first. An interference pattern of both channels ($\overline{K}N - \Sigma\pi$), of which the relative weight might differ depending on the reaction channel in which the Λ(1405) is produced, gives the prediction for the Λ(1405) lineshape.

1.5 $\overline{K}$ Potentials at ρ_0

The $\overline{K}N$ interaction, discussed so far, is calculated in the vacuum $\rho = 0$. Besides the uncertainties on the pure amplitude the extrapolation into the medium adds additional uncertainty.

The advertised potentials can be divided into two classes. The "shallow" ones giving usually values of $-V_{\bar{K}} \approx$50–60 MeV [30, 31, 32, 33, 34] at $\rho = \rho_0$, and the $\overline{K}N$ threshold and the "deep" ones usually with potential depths in the order of $-V_{\bar{K}} \approx$150–200 MeV [35, 36, 37, 38, 39, 40] at $\rho = \rho_0$. The latter one is obtained by a global fit to all kaonic atom data throughout the periodic table. A major difference among these two classes is based on the chiral or phenomenological treatment of the $\overline{K}N$ interaction, whereby the chiral potentials are in most cases "shallow". The work of [16, 40] tries to resolve this discrepancy by stating that the fits to the atomic spectrum probe mainly sub-threshold $\overline{K}N$ energies where the interaction is stronger and, thus, the optical potential with this amplitude delivers deeper potential values than the ones constructed at threshold.

The discussion of the strength of the potential and the sub-threshold extrapolation of the $\overline{K}N$ scattering amplitude becomes important in view of possible bound states of anti-kaons with nucleons. These bound states are a natural extension of the picture that treats the $\Lambda(1405)$ as being partially a $\overline{K}N$ bound state. In case of a sufficiently deep potential also larger bound states like $\overline{K}NN$ or $\overline{K}NNN$ could exist, named kaonic cluster, and discussed in the following section.

1.6 Anti-Kaon Nuclear Bound States

The idea of bound states between kaons and nucleons is as old as the discovery of these strange particles itself. Even before the exact nature and amount of kaon states were known, "*At the time of writing it is far from clear how many distinct K-particles (of given charge, say) there are.*" [41], speculations about bound states between these new particles and normal nuclear matter began [41, 42, 43]. While the early speculations involved kaons (K^+, K^0), it was soon clear that the fundamental component for a bound state, the attractive interaction, was missing [44]. On the contrary, the interaction of anti-kaons and nucleons was found to be attractive. This discovery, as interesting as it was, did not simplify the picture. In contrast to kaons, anti-kaons can be absorbed by matter[2], which reduces drastically the lifetime of possible anti-kaon nuclear clusters, making them *quasi*-bound states. Despite this drawback, the scientific interest in these theoretical objects began.

In the literature many names for bound states of anti-kaons and nucleons appear. Some of them are used in the following: (anti-)kaonic nuclear cluster, (anti-)kaonic nuclear bound state, (kaonic) quasibound state, Λ^*-hypernuclei, strange dibaryon, deeply bound kaonic cluster (DBKC), kaonic dibaryon, nuclear kaonic hydrogen molecule.

1.6.1 The First Generation - Evolution of anti-Kaonic Nuclear Bound States

The pioneers in this exciting field were approaching the idea of bound states between anti-kaons and nucleons from many perspectives. The very first work on this field stems from Y. Nogami in 1963 [45]. This work is motivated by the interpretation of the $\Lambda(1405)$ as a $\overline{K}N$ bound state by R. H. Dalitz and S. F. Tuan [46, 47, 48]. Nogami discusses the three isospin configurations of the $\overline{K}NN$ system and predicts a small binding energy for the most stable configuration of ≈10 MeV. The properties of the smallest kaonic cluster are discussed in Section 1.6.4.

In the early eighties, three works by Russian authors appeared which discussed the possibility of bound states of a K^- with a ^{4}He nucleus [49, 50, 51]. Their work was primarily motivated by the measurements of anomalously large 2p-level shifts of kaonic He [52, 53][3]. The authors found out that the K^--^{4}He system contains a nuclear level with l=1 and a binding energy and width both of ≈0.5 MeV [50]. Their findings are, however, at question given the fact that these early measurements were wrong (Footnote 3).

The data from heavier kaonic atoms have been more reliable and have also provided motivation for a large number of works discussed in the following. In order to extract an effective $\overline{K}N$ scattering length, multiple attempts have been carried out to fit all available data of kaonic atoms (except K^-H and K^--^{4}He) with help of theoretical models. These fits revealed that the atomic levels have negative energy shifts[4], with respect to the pure Coulomb level, although

---

[2] This is the reason why kaons were initially preferred as bound state partners.

[3] Re-measurements of this system 30 years later solved a long standing puzzle by reporting a significantly smaller value for the 2p-level shift [54, 55].

[4] less binding.

the real part of the optical potential is attractive. This net repulsion is related to the strong absorptive part of the optical potential which acts effectively as a "repulsive" hard core [56, 57, 58]. Due to this strong absorptive part, an unexpected phenomenon, the so-called Krell oscillations[5] [59], occurs in kaonic atoms. This phenomenon is well described in Refs. [60, 61] and is caused by an interplay of the strong absorptive part of the optical potential (which acts effectively repulsive) and the attractive real part. What connects this oscillating behavior with the discussion of kaonic nuclear bound states is the fact that this phenomenon goes hand in hand with the appearance of so-called "inner" and "outer" states of the kaonic atom. The "outer" or also named *atomic* states refer to the usual case where a kaon is located in an atomic orbit. The "inner" states, which are also named *nuclear* states, describe a kaon inside of the nucleus which is therefore considered as a kaonic nuclear bound state. This appearance of kaons in the nucleus has been of continuous interest during the years [31, 56, 57, 58, 59, 60, 61, 62, 63, 64]. While on the one hand the great interest in these states is stressed many authors are on the other hand quite reserved whether one could ever observe these states directly, as they are expected to be very broad due to the strong absorptive nature of the interaction.

Quantitative predictions about the properties of these nuclear states have been put forward in Ref. [56] claiming that a $\mathrm{K}^{-\,32}$S bound state could only exist for Re$V_{\bar{K}N}$ ≈ 0– -100 MeV and Im$V_{\bar{K}N}$ <15 MeV. In Refs. [57, 63] it is stressed that kaonic nuclear states in heavier nuclei would have large widths of $\Gamma = 50$ MeV up to over 100 MeV. The authors of Ref. [31] give very detailed predictions for the nuclear levels in C, Ca and Pb. They find binding energies of 4–40 MeV and widths of Γ = 40–200 MeV, which can cause a substantial overlap between the different levels of excited states.

The work of Ref. [65], in contrast to the previously mentioned reports, constructs the elementary $\overline{K}N$-potential not by a fit to the kaonic atom spectrum but by solving the coupled Lippmann-Schwinger equations for five isospin channels $\overline{K}N$, $\Sigma\pi$, $\Lambda\pi$. The free parameters of the model were constrained by a fit to the scattering and reaction data above threshold. This elementary model was then used to calculate the behavior of a kaon inside a nucleus with the help of an optical potential. Despite the different approach, they found bound states of $\bar{K}$ and ^{12}C with a moderate binding of ≈60 MeV and widths of 20-100 MeV.

In harsh contradiction to these discussions stand two works by S. Wycech, one coauthored by R. Staronski [53, 66]. They discuss the possibility of deeply

---

[5] This is an oscillating behavior of the calculated energy shift and width of the kaonic atom state dependent on the strength of the nuclear interaction.

bound kaonic states (DBKS) in a helium nucleus. Their work has also been motivated by the first generation measurements of kaonic helium, which according to them, hint to a $\bar{K}\alpha$ bound state. They estimated a binding of a kaon to the nucleus as strong as 100–150 MeV. As a result of this strong binding a significant amount of phase space for the decay of such systems would be closed, see Section 1.6.5. This reduced phase space causes the states to be as narrow as ≈20 MeV.

At that time, the topic was not intensively discussed among the different groups and a real change was only put forward several years later, discussed in the following.

1.6.2 The Second Generation - A Boost to the Field

A renewed interest was initiated by the works of T. Kishimoto [67] in (1999) and Y. Akaishi and T. Yamazaki [68, 69] in (2001). T. Kishimoto was predicting large cross sections of the (K^-,N) transfer reaction for the creation of a kaonic nuclear bound state with help of K^--beams impinged on nuclear targets. In his calculation he assumed a binding of BE = 100–150 MeV and obtained cross sections for the cluster production in ^{12}C as large as $d\sigma/d\Omega$ = 100–400 $\mu b/sr$. This amazing result triggered some response by other theoreticians doubting the correctness of the large cross section and the narrow width of the nuclear states [30, 70]. Further interest was triggered by Kishimotos first connection of the $\overline{K}N$ potential depth to a possible condensation of anti-kaons in the core of neutron stars [67].

Y. Akaishi and T. Yamazaki on their behalf argued that a $\overline{K}NNN$ state, namely K^- ^{3}He+$\bar{K}^0$ ^{3}H, would be bound by 108 MeV with a width of 20 MeV. These characteristics have peculiar origins. According to the authors the binding is so strong due to the shrinkage of the whole nucleus which substantially lowers the bound state energy. Due to this lower energy, however, the $\Sigma\pi$ decay channel is closed (Section 1.6.5). Further, the $\overline{K}NNN$ was constructed such that it incorporates mainly the I=0 component of the $\overline{K}N$ interaction (3:1). In this isospin channel the decay into $\Lambda\pi$ is forbidden due to isopin conservation, so that this state can only majorly decay by its small I=1 component. This specific construction of the $\overline{K}NNN$ state is the reason for its small width [68, 69], which was also confirmed by other authors [30].

Back-to-back with these new theoretical predictions a first experimental proposal was put forward to cross check them [71]. Soon this experiment was conducted and the first results that reported signal candidates did induce a large controversy, see Section 1.6.6. An overview of this era is given in Ref. [72].

1.6.3 State of the Art

Meanwhile, the field has reached a level of vivid discussion and proposals for cluster candidates. In this line, a kaon is added to various other hadrons. Figure 1.8 shows the most commonly discussed two- and three-body systems [73]. Larger clusters, like the $\overline{K}NNN$ the $\overline{K}\,\overline{K}NN$ or states with two different mesons, like $\pi\overline{K}N$ are also found in the present literature [74, 75]. This subsection will give a brief overview on the current predictions for the simplest cluster $\overline{K}NN$ which are mainly obtained in two ways: Faddeev-, and variational calculations.

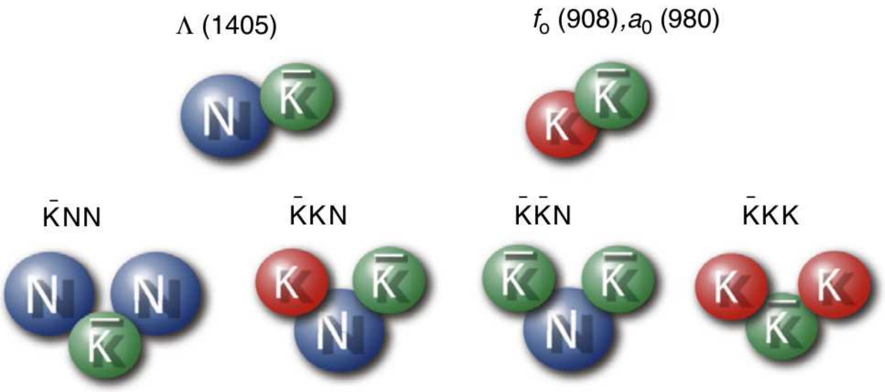

Figure 1.8: Family of few-body kaonic nuclear clusters [73].

Faddeev Calculations

In a Faddeev approach the three-body T-matrix is approximated by a sum of matrices T^i ($T = T^1 + T^2 + T^3$) that describe the reaction:

$$j + (ki) \to i + (jk), \tag{1.5}$$

which accounts for elastic and rearrangement processes of the three particles (i,j=1,2,3) [76]. In this way the three-body problem can be split into two-body interactions while the third particle is treated as a spectator. Thus, the two-body T-matrices can be used to build up T^i [75]. The full mathematical concept of this approach is explained for example in Refs. [76, 75].

The $\overline{K}NN$ has been calculated within a coupled channel Faddeev approach in [75, 76, 77, 78, 79, 80, 81, 82, 83]. This coupled channel approach has the advantage that the conversion ($\Sigma\pi N - \overline{K}NN$) is taken into account and such the binding energy and mesonic decay widths are calculated within the same framework. The results of these calculations are summarized in Table 1.1.

Variational Calculations

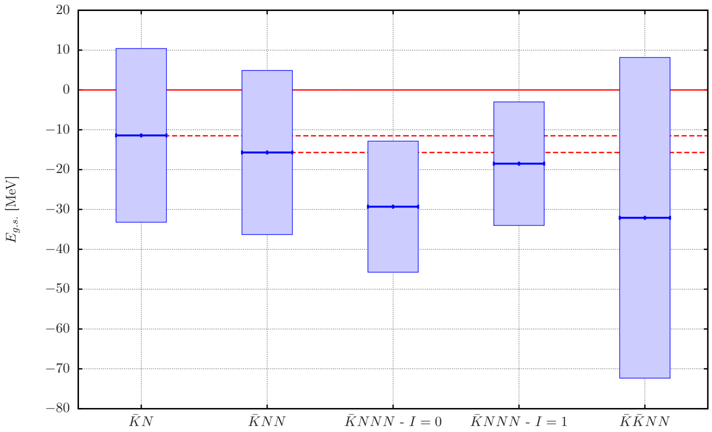

Figure 1.9: The results of the calculated ground state (g.s.) properties of kaonic nuclear clusters, binding energy and width, from Refs. [74, 84].

In a variational approach the energy of the three-body system is minimized iteratively. For that a trial wave function $\Psi(\overline{K}, N, N)$ is constructed that describes the configuration among the three particles. By evaluating the expectation value of the three-body Hamiltonian $\hat{H}(T, V_{NN}, V_{\bar{K}N})$ with the trial wave function the energy of the system is obtained. The total energy of the system is then minimized with respect to the parameters λ_i of the wave function $\frac{\partial E}{\partial \lambda} = 0$. The minimum energy of the system corresponds to the binding energy of the cluster. If the input values of the parameters that were used to construct the wave function coincide within a certain accuracy with the values that minimize the energy, the procedure converges and delivers appropriate results. Several works have used a variational approach to determine the properties of the $\overline{K}NN$ state [69, 74, 85, 86, 87, 88, 89, 90, 91]. The results are summarized in Table 1.1. Figure 1.9 shows a graphical representation of the width and binding energy of different kaonic nuclear bound states calculated in Ref. [74].

One disadvantage of variational calculations is that the imaginary part of the

$\overline{K}N$ interaction has to be treated perturbatively and, thus, the width of the $\overline{K}NN$ state needs to be calculated separately [85]. An advantage compared to the Faddeev approach is that one obtains the wave function of the kaonic cluster and with this its spacial distribution.

An evaluation of the distances between the three particles, obtained from the wave function, states that the $\overline{K}NN$ is essentially a bound state of Λ(1405)-p [85, 87]. In this sense the term Λ*-Hypernuclei, that has been used as early as in 1990 [65] for the kaonic nuclear bound states, is justified and consequently, the $\overline{K}NN$ system has also been calculated in a variational approach as a Λ*-N bound state [88, 92].

Comparison

No matter which of the two methods is used to calculate the $\overline{K}NN$ three-body system, one needs, in both cases, realistic NN and $\overline{K}N$ potentials as input. The $\overline{K}N$ interaction can be taken from different models, chiral or phenomenological ones. Depending on the model the $\overline{K}N$ interaction is then treated energy-dependent or static. Further, the two body binding energy between $\overline{K}N$ can be either treated as 12 MeV or 27 MeV deep, depending on the theoretical position of the Λ(1405) mass. The NN potential inside the $\overline{K}NN$ system is usually taken from external works dealing with nucleon nucleon interaction[6].

The results of the different calculations are summarized in Table 1.1. Here, the predictions for the binding energy BE, the mesonic decay width Γ_m, and the non-mesonic decay width Γ_{nm} are summarized. The two nucleon absorption process present in the decay of the $\overline{K}NN$ system (Section 1.6.5) and accounted for by Γ_{nm}, is only taken into account by some of the calculations. It is in most cases only an estimate. To stress the discrepancy between the calculations, they are sorted according to their treatment of the $\overline{K}N$ interaction. The differences between the predictions are discussed in Refs. [82] and [83], and two effects were named responsible. First, as suggested in Table 1.1, the energy-independent $\overline{K}N$ interaction that has been used within phenomenological potentials causes a systematic deeper binding than the use of energy dependent chiral potentials. Second, the use of coupled ($\overline{K}N - \Sigma\pi$) or single channels ($\overline{K}N - \overline{K}N$) can alter the results in view of the expected binding strength [76, 82].

---

[6] Argonne18 [85, 86], Argonne AV4‘ [74], Tamagaki potential G3RS [87], Bonn potential and Nijmegen soft-core potential [88].

Table 1.1: Overview of different predictions for the binding energy BE, mesonic- Γ_m and non-mesonic Γ_{nm} decay widths of the $\overline{K}NN$ (in MeV), inspired from Refs. [84, 93]. The symbols ($^{\clubsuit}$,$^{\heartsuit}$) mark different works by the same authors.

	Chiral, energy dependent				
	var. [74]	var. [85, 86]	Fad.$^{\clubsuit}$ [81]	Fad. [82, 77]	Fad.$^{\heartsuit}$ [83]
BE	16	17–23	9–16	26–35	32
Γ_m	41	40–70	34–46	50	49
Γ_{nm}		4–12		30	
	Non-chiral, static calculations				
	var. [90, 69]	Fad.$^{\heartsuit}$ [78, 76]	Fad.$^{\clubsuit}$ [79, 80]	var. [89]	var. [91]
BE	48	50–70	60–95	40–80	40
Γ_m	61	90–110	45–80	40–85	64–86
Γ_{nm}	12			∼20	∼21

In most of the calculations the width of the $\overline{K}NN$ system is considerably larger than the binding energy which leads many authors to the conclusion that it will be problematic to measure this state.

1.6.4 The $\overline{K}$NN State, the Simplest Kaonic Cluster

If one considers a kaonic cluster in its simplest form, consisting of two nucleons and one anti-kaon, its properties differ depending on the spin-isospin structure of the three-body system. Here, all possible nucleon anti-kaon combinations are introduced.

The most popular ansatz is to use a configuration were the two nucleons are in an isospin 1 state and the total $\overline{K}NN$ isospin combines to 1/2. This configuration of the NN isospin triplet state can be written as, see [89]:

$$\Psi_A = ((NN)_1 K)_{1/2}. \tag{1.6}$$

The spin between the two nucleons is then S_{NN}=0. This $\overline{K}NN$ state can appear in two possible charge combinations. For the Q=+1 case this is a linear combination of a ppK^- and a $pn\bar{K}^0$. In case the cluster has zero charge Q=0 its particles combinations are pnK^- and $nn\bar{K}^0$. If one re-couples the isospins in a longer calculation [94] so that the basis is the $\overline{K}N$ system, one can write the wave function as [89]:

$$\Psi_A = \frac{\sqrt{3}}{2}((NK)_0 N)_{1/2} + \frac{1}{2}((NK)_1 N)_{1/2}. \tag{1.7}$$

In this basis, one clearly sees that this state is in favor (3:1) of the stronger $\overline{K}N$ attraction with I=0. This strength of the isospin 0 component makes Ψ_A the best candidate for a bound $\overline{K}NN$ system.

If the anti-symmetric pn combination (I_{NN}=0, S_{NN}=1) is considered, the wave function looks like follows [89]:

$$\Psi_B = ((NN)_0 K)_{1/2}. \tag{1.8}$$

In this configuration, each charge state is built by only one particle combination. In case of Q=0 it purely consists of pnK^- and in case of Q=+1 it is a state of $pn\bar{K}^0$. The re-coupling of the isospins to the $\overline{K}N$ base yields the following form [89]:

$$\Psi_B = -\frac{1}{2}((NK)_0 N)_{1/2} + \frac{\sqrt{3}}{2}((NK)_1 N)_{1/2} \tag{1.9}$$

In this arrangement the $\overline{K}N$ isopin=0 component is only minor (1:3) and, hence, the Ψ_B state is less bound than the Ψ_A combination.

The third three-body configuration is build with a total isospin of 3/2:

$$\Psi_C = ((NN)_1 K)_{3/2}\,. \tag{1.10}$$

This is the only particle combination that comes with a negative charge or with positive charge +2. The particle combinations are the following: either nnK^- for Q=-1 or $pp\bar{K}^0$ for Q=+2. Here, the nn and pp pairs are in an $I_{NN} = 1$ and $S_{NN} = 0$ state. If one re-couples the isospins, this state appears to be purely in the $\overline{K}N$ isospin=1 configuration and is, thus, expected to be, if at all, less bound than the others:

$$\Psi_C = ((NK)_1 N)_{3/2}. \tag{1.11}$$

The properties of all three $\overline{K}NN$ states are summarized in Tables 1.2 and 1.3. As the decay products of the three clusters are the same, only Ψ_C can be distinguished from Ψ_A and Ψ_B by the charge of the products while the latter two would simultaneously appear in an invariant mass spectrum if both states exist [74].

Although most of the works in this field focus on the description of the bound state in the formation Ψ_A, some have also mentioned and calculated the properties of the other two configurations Ψ_B and Ψ_C. Case Ψ_B is mentioned in

Table 1.2: Different Properties of the $\overline{K}NN$ configuration.

Wave	I_{NN}	S_{NN}	I_{tot}	J^P	Q	Term
Ψ_A	1	0	1/2	0^-	0, +1	"ppK^-", ${}^2_{\bar{K}}H$
Ψ_B	0	1	1/2	1^+	0, +1	"dK^-"
Ψ_C	1	0	3/2	0^-	-1, +2	-

Table 1.3: The resulting wave function Ψ_i for the different particle combinations of the two nucleons and one anti-kaon.

	$I_{NN} = 1$			$I_{NN} = 0$
Anti-Kaon	nn	pp	pn	pn
K^-	Ψ_C	Ψ_A	Ψ_A	Ψ_B
$\bar{K}^0$	Ψ_A	Ψ_C	Ψ_A	Ψ_B

Refs. [45, 87, 89] and calculated in Refs. [74, 75, 95]. In these recent works it was concluded that the state Ψ_A overlaps with Ψ_B as they have binding energies of 16 and 8-9 MeV, respectively, but large widths of 40 and 30 MeV, which will make a distinction in a mass spectrum impossible [74]. In Ref. [95] the existence of this state is put at doubt, however, as it appears only as bound for one of their tested $\overline{K}N$ interaction potentials which, at the same time, reproduces the measured scattering data only roughly.

While the properties of Ψ_A and Ψ_B are calculated, the configuration with total isospin 3/2 (Ψ_C) is only mentioned in Refs. [45, 87, 89].

1.6.5 Decay Modes and Width

The idea behind the existence of measurable anti-kaonic nuclear clusters is that with a deep binding energy some of the possible decay channels may be closed completely or have such a reduced phase space that the quasi-bound states could be considerably narrow. Such a possibility of deeply bound kaonic clusters was first mentioned in Refs. [53, 66], with a discussion of its decay patterns. The possible decay modes of the three-body systems $\overline{K}NN$ (Ψ_A, Ψ_B,

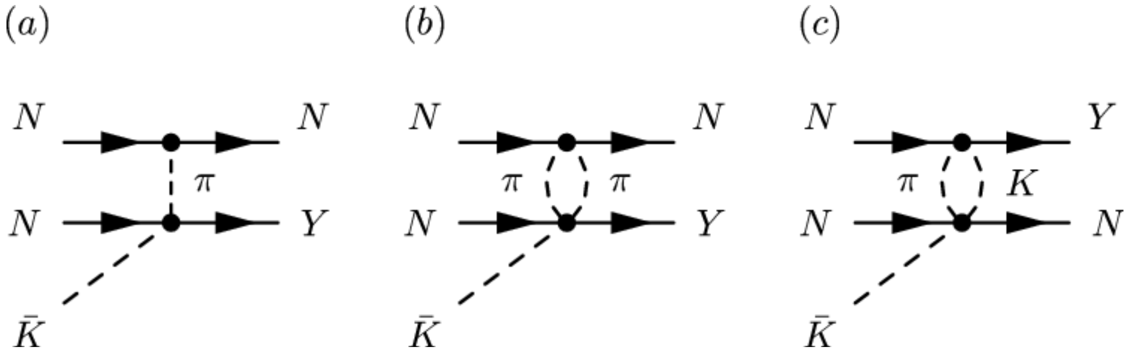

Figure 1.10: Feynman diagrams of the $\overline{K}NN$ decay via two-nucleon absorption. The first diagram is forbidden in case of $S_{NN} = 0$ (Ψ_A and Ψ_C) [85].

and Ψ_C) are the following:

$$\overline{K}NN$$

$$\longrightarrow \Sigma + N + \pi \tag{1.12}$$

$$\longrightarrow \Lambda + N + \pi \tag{1.13}$$

$$\longrightarrow \Sigma + N \tag{1.14}$$

$$\longrightarrow \Lambda + N \tag{1.15}$$

The decay of the nuclear bound state proceeds via internal capture or scattering processes. One decay mode proceeds via one- or two-nucleon absorption of the kaon which is discussed, for example, in Ref. [85]. One-nucleon absorption leads to the final states in Equations (1.12) and (1.13) via two-nucleon absorption results in a pion-less final state in Equations (1.14) and (1.15). Possible diagrams of the two-nucleon absorption processes are shown in Figure 1.10.

A second decay mechanism can occur via the internal formation of a $\Lambda(1405)$-resonance, as discussed for example in Ref. [96]. The decay via this doorway is only possible for $\overline{K}N$-pairs in an isospin 0 state (not apparent in Ψ_C). Figure 1.11 shows possible decay diagrams with the internal formation of the Λ^* and the final states in Equations (1.14) and (1.15). It was found that the ratio of decay widths in this decay scenario is relatively independent on the nuclear density and approaches $\Gamma_{\Lambda N}/\Gamma_{\Sigma N} \approx 1.2$ [96], resulting in a total non-mesonic decay width of 22 MeV at normal nuclear density.

Due to the large absorption cross section for the anti-kaon, the width of the possible bound states is often predicted as rather large, see Table 1.1. In case of a strong binding mechanism, the energy of the bound system could be lowered so much that some of the possible decay channels would be closed and, thus,

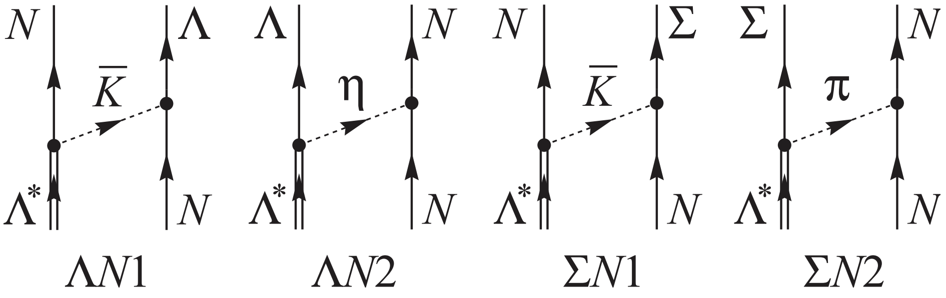

Figure 1.11: Feynman diagrams of the $\bar{K}NN$ decay via the Λ^*-doorway [96].

the width of the kaonic cluster substantially narrows. Figure 1.12 illustrates the decay threshold of the $\bar{K}NN$ system with respect to its unbound mass. In case of a binding energy of ≈100 MeV, for example, the decay into $\Sigma N\pi$ is blocked. An observation of the $\bar{K}NN$ system is thus crucially connected with its binding energy as broad states are generally hard to measure.

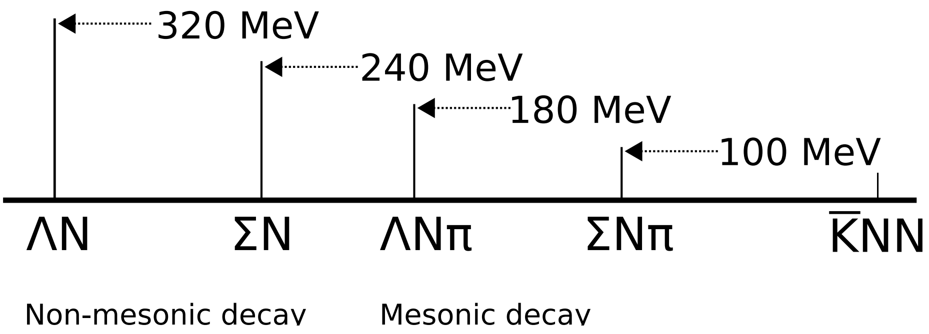

Figure 1.12: The decay channels that are closed at a certain binding energy of the kaonic cluster.

The exact branching of the decay channels in Eqs. (1.12)–(1.15) is not known as there are no experimental observations. Theoretically, the values have been predicted by different groups, see Table 1.1. In Ref. [97] the ratio of the two absorption modes is given as Equations (1.12)+(1.13)≈80% and Equations (1.14)+(1.15)≈20%. The predicted values for Γ_m and Γ_{nm} in Table 1.1 also suggest branchings in the range of (1.12)+(1.13)≈62-95% and (1.14)+(1.15)≈5-28%. The ratio of the two non-mesonic decay modes is only discussed in Ref. [96] and quoted in the previous paragraph. The ratio of the two mesonic decay modes was quoted in another work as $\Gamma_{\Lambda N\pi} < 15\%$ and $\Gamma_{\Sigma N\pi} > 85\%$ [98]. The dominance of the mesonic decay modes is striking, given that experimental searches have been done only for the decay channel in Eq. (1.15), so far.

A signature of kaons bound to larger systems may only be visible, if the width of the state does not exceed the level spacing between the different excited states. In a recent study of larger kaonic nuclear systems within a chirally motivated coupled-channel model [99] it was stated that the level spacing of larger nuclear clusters (all but H, He and Li) is in fact of the same size as the width of the bound states itself which would make a direct observation impossible.

1.6.6 Experiments to Search for Anti-Kaonic Nuclear Clusters

This section is well described by a statement of S. Wycech:
"*The search for nuclear states of anti-kaons is a fascinating story of successes and failures*" [100]. Many attempts have been conducted to observe these predicted states. Many of them have seen a signal and many of these were later withdrawn. This is an overview of these attempts.

Experiments at KEK — PS

In 2004 the results from the E471-experiment at KEK were published [101, 102, 103]. These experiments have investigated the reaction:

$$K^- + {}^4\mathrm{He} \rightarrow N + X, \tag{1.16}$$

with stopped K^-. The nucleon (N), produced together with the X, was selected to be either a proton or a neutron, respectively. In this experiment X was tested for the $\overline{K}NNN$ hypothesis. While the detection of the proton selects X with an isospin of I=1 and charge Q=0, the detection of a neutron selects both isospin states of X (I=0 or 1) and a positive charge Q=+1 [103]. The experimental data showed a strong signal for $\overline{K}NNN$ (I=1, Q=0) of M=3118 MeV/c^2 and a width of Γ < 22 MeV/c^2 and a non-significant signal for the $\overline{K}NNN$ (I=1/0, Q=+1) with M=3141 MeV/c^2 and a width of Γ < 23 MeV/c^2. According to the theoretical argumentation in Refs. [68, 69], however, the isospin I=0 state was expected to be deeply bound and narrow, (Section 1.6.2) and not vice versa. The experimental findings shown in Figure 1.13 were, in this respect, quite surprising.

Although these findings triggered some excited interpretations, a re-measurement (experiment KEK-PS E549) with a higher statistic and an improved time resolution showed a structureless spectrum of the observables in Figure 1.13 [104, 105]. The previously reported signals were attributed to effects of detector mis-calibration and an upper limit (95% CL) of the kaonic cluster production rate per stopped kaons was established. These upper limits for the two charge states are displayed in Figure 1.14. The reported upper limit for a state $S^0(3115)$ is 0.2% per stopped kaon and excludes the previously reported production rate of ≈1% [105].

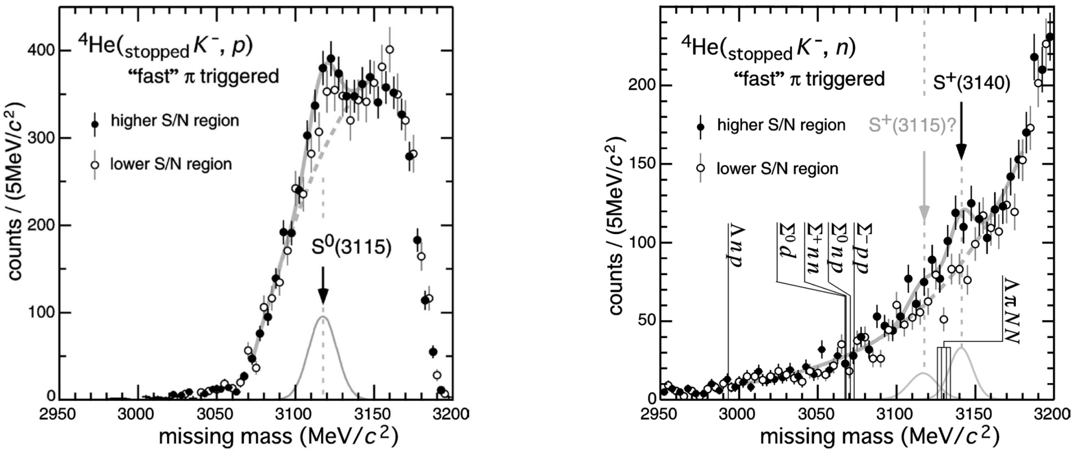

Figure 1.13: Missing mass spectrum of the nucleon in Equation (1.16). Left panel with N being a proton, right panel N being a neutron, taken from Ref. [103].

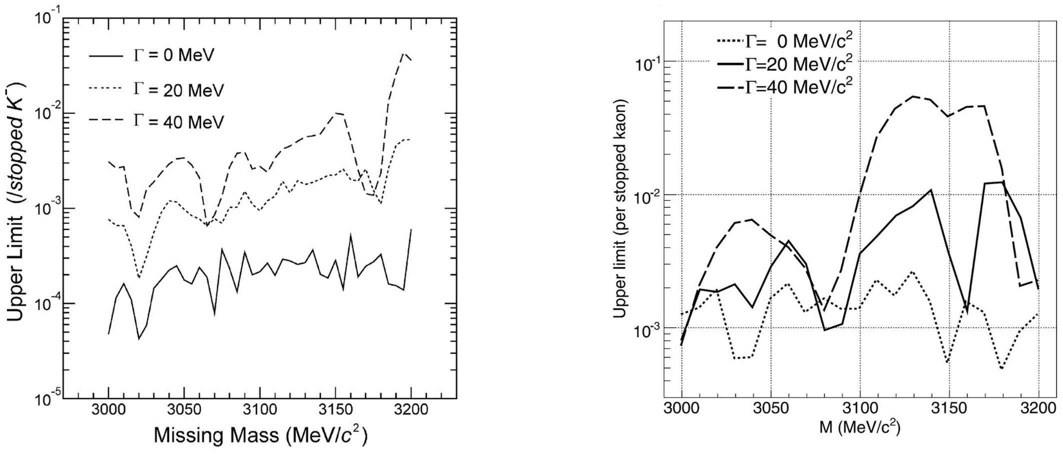

Figure 1.14: Extracted upper limit (95% CL) of a $\overline{K}NNN$ kaonic cluster production via Reaction (1.16). Left panel with N being a proton, right panel N being a neutron, taken from Ref. [104, 105].

Experiments at BNL — AGS

The proposed transfer reaction from Ref. [67] was carried out at the BNL facility (Experiment E930) with K^- of 0.93 GeV/c by the following reaction [106]:

$$K^- + {}^{16}\mathrm{O} \rightarrow n + X, \tag{1.17}$$

where X may stand for the possible production of a kaonic nuclear bound state.

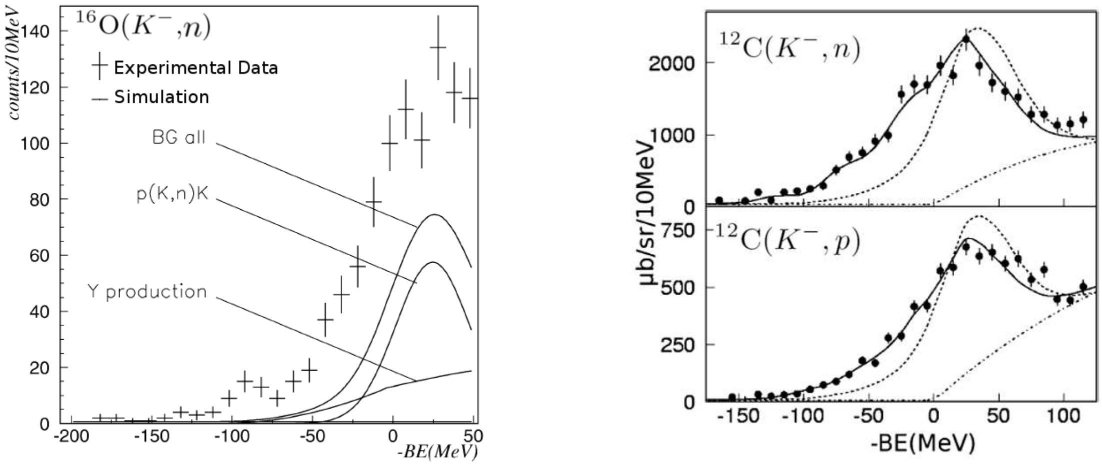

Figure 1.15: Left panel: missing mass spectrum to the neutron of Reaction (1.17) [106]. Right panel: missing mass spectra of Reaction (1.18) [107, 108].

The left panel of Figure 1.15 shows the missing mass spectrum of the detected neutron. The large amount of statistic in the bound region (-200–0) MeV was addressed to the strong attractive $\bar{K}N$ interaction. The small structure at -90 MeV was reported as an evidence for the formation of a kaonic nuclei in a p-shell. The smaller structure at 130 MeV was interpreted as a kaon in an s-shell. These results were stated as the first observation of kaonic nuclei.

A similar experiment, carried out at the KEK-PS facility (Experiment KEK-PS E548) reported no such structures [107, 108]. The reaction was induced by 1 GeV/c kaons:

$$K^- + {}^{12}\mathrm{C} \rightarrow N + X, \tag{1.18}$$

$$K^- + {}^{16}\mathrm{O} \rightarrow N + X, \tag{1.19}$$

where N is either a proton or a neutron. The published spectra (right panel in Fig. 1.15) revealed no distinct peak structures in the bound region (-150–0) MeV.

The absence of peak structures was explained by the fact that these states are probably smeared out bumps in the spectrum.

Experiments at CERN — LEAR

A substantially different experiment was carried out with the magnetic spectrometer OBELIX [109, 110]. There, different from all previous experiments, the signals of $\overline{K}NN$ and $\overline{K}NNN$ were searched for in $\bar{p}$+^{4}He annihilations at rest:

$$\begin{aligned} &\bar{p} + {}^4\text{He} \rightarrow p + \pi^- + p + \pi^+ + \pi^- + R, \qquad (1.20)\\ &R = n,\\ &R = n + K^0. \end{aligned}$$

Here, R stands for a missing rest. During the analysis it was observed that the later discovered state only appears in events where R=$n + K^0$. Why this is the case could not be explained. When combining the p and π^- from these 5-prong events, the resulting spectrum showed some indication for Λ-hyperons, however, with a large background underneath the signal (left panel of Figure 1.16). As no mass resolution of the Λs was extracted, the hyperons were selected

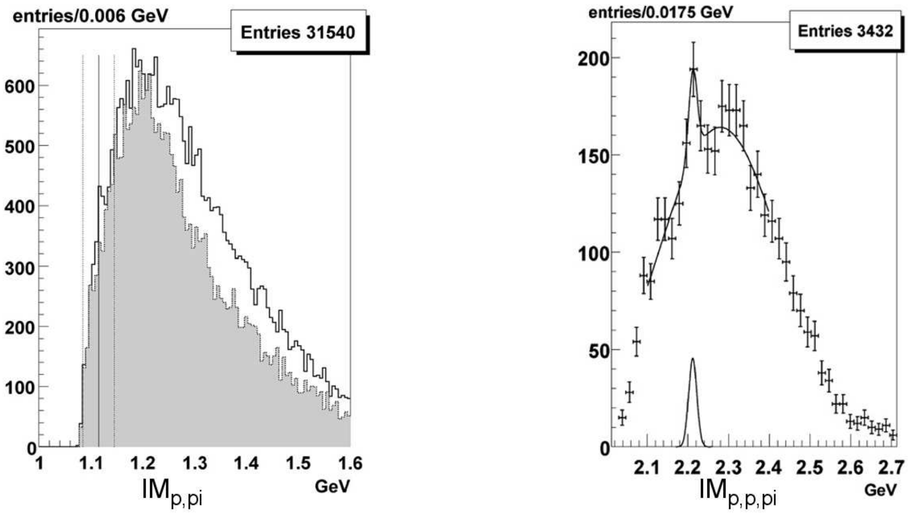

Figure 1.16: Figures from [109]. Left panel: Invariant mass of proton and pion with an enhancement around the Λ mass of ≈ 1116 MeV/c^2 . The dashed lines indicate the selected range of statistic that was combined with a second proton and plotted in the right panel. The right panel shows the fitted distribution with a signal assumption.

in a mass window of ±30 MeV/c^2 around the nominal Λ mass and then combined with the second proton, delivering eventually a signal for a new state X. The result is shown in the right panel of Figure 1.16. The spectrum shows an enhancement at 2212.2±4.9 MeV/c^2 with a width of $\Gamma < 24.4\pm8$ MeV/c^2. The comparison of the yield in the Λ peak and the 67±22 events associated to a new state X shows that a large fraction of Λ's stem from the X system which is quite astonishing. The overall frequency of X production in ($\bar{p}$+^{4}He) was estimated to be 0.015%. The results were presented as indications for the production of a $\overline{K}NN$ bound state [109, 110], whereas in Refs. [111, 112, 113] the results were interpreted as a signature of a cusp effect due to the coupling to the $\Lambda p\pi$-channel, similar to those observed in Refs. [114, 115]. Either way, a re-measurement of this reaction system would be needed to cross check these experimental findings with an independent analysis (see J-PARC proposal [116]).

Further, an analysis searching also for $\overline{K}NNN$ bound states by the decay into Λd was put forward in the reactions:

$$\begin{aligned} &\bar{p} + {}^4\mathrm{He} \rightarrow p + \pi^- + d + \pi^+ + \pi^- + R, \\ &R = n, \\ &R = n + K^0. \end{aligned} \tag{1.21}$$

Analogue to the analysis in the $\overline{K}NN$ case, the d was combined to p-π^- pairs with a mass consistent with a Λ mass ±30 MeV/c^2. The resulting spectra of the p, π^- and p, π^-, d pairs are shown in Figure 1.17. It was stated that, if the peak is due to a deeply bound kaonic cluster, the binding energy is 121 MeV.

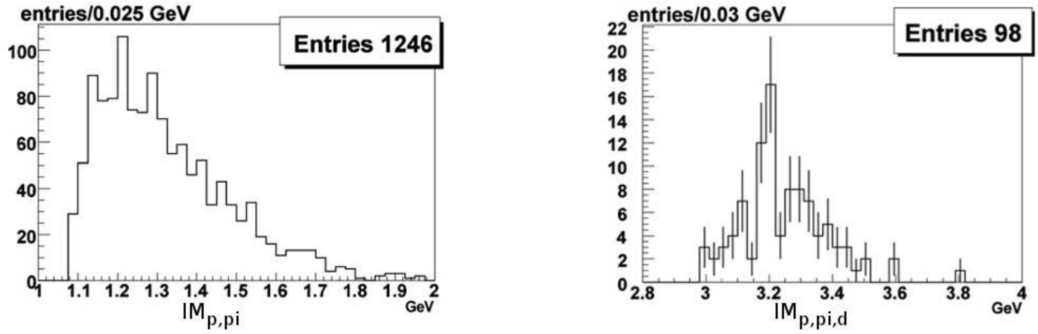

Figure 1.17: Figures from [109]. Left panel: Invariant mass of proton and pion with a slight enhancement around the Λ mass of ≈ 1116 MeV. The right panel shows the invariant mass of proton pion and d for p, π^- pairs close to the nominal Λ mass.

Experiments at LNFN — DAϕNE

The FINUDA collaboration [117] reported a signal which they measured by stopped K^- on thin nuclear targets via the following reaction:

$$K^- + {}^6\text{Li},\, {}^7\text{Li},\, {}^{12}\text{C} \rightarrow p + \Lambda + A', \tag{1.22}$$

where A’ accounts for the rest nucleus. The analysis filtered out p-Λ pairs from Reaction (1.22) that were emitted back-to-back ($cos(\theta)^{LAB}_{\Lambda}$ < -0.8) in order to guarantee the stopped kinematics of the K^-. The $p\Lambda$ invariant mass spectrum under this condition is shown in the left panel of Figure 1.18. The spectrum was announced as an evidence for the production of a $\overline{K}NN$ bound state with positive charge, M = 2255±6 MeV/c^2 and a width of Γ = 67±14 MeV/c^2 [117]. This is equivalent to a binding energy of BE = 115 MeV for the system. The estimated production rate for this state was in the order of 0.1% per stopped kaon.

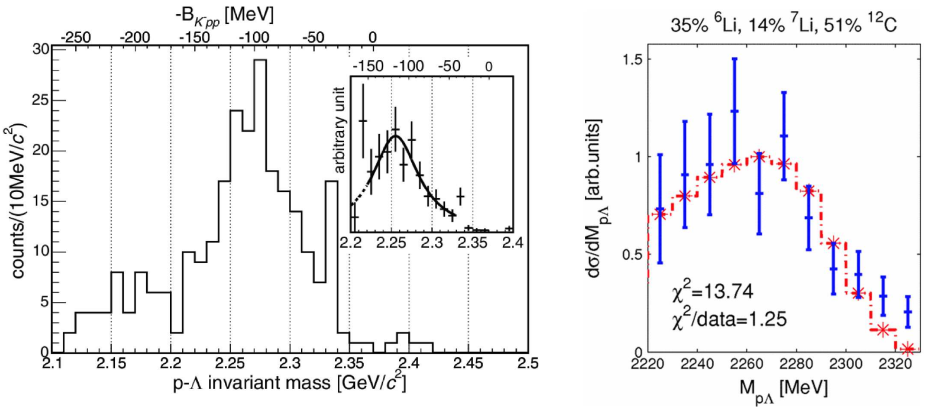

Figure 1.18: Left panel: Measured $p\Lambda$ invariant mass for large opening angles, inlet shows the acceptance corrected distribution [117]. Right panel: Data in comparison to simulations not invoking the production of a kaonic nuclear bound state but final state interaction [118].

Many points from this interpretation were criticized [118, 119, 120]. While Ref. [118] suggested two nucleon absorption of the kaon with subsequent final state interaction (FSI) of the p and the Λ, Ref. [120] described the measured spectrum by single-nucleon knock-out reactions with FSI of the two outgoing particles. In Ref. [119] the claim of the creation of a self-bound three-body system inside a larger nucleus rather than a kaon bound to all nucleons was criticized and the data could be explained as well with FSI effects, combined with the Fermi motion of the nucleon pair on which the kaon gets absorbed.

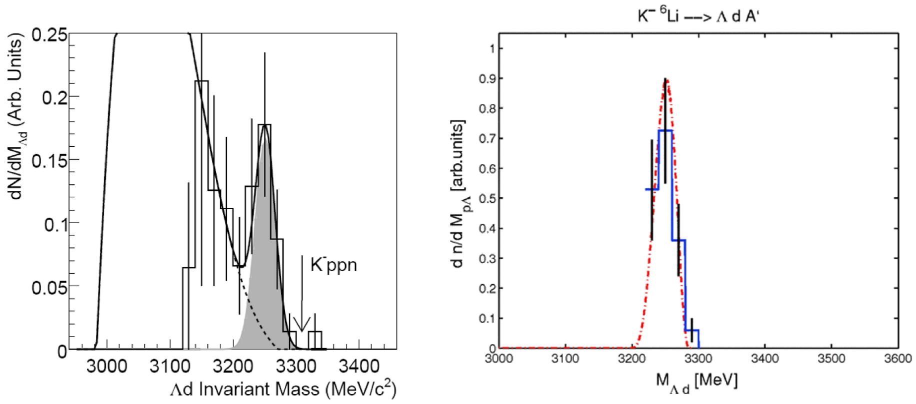

Figure 1.19: Left panel: Measured Λd invariant mass. Data are fitted with background distribution and an additional signal strength indicated by the gray area [122]. Right panel: Data in comparison to simulations not invoking the production of a kaonic nuclear bound [123].

Further attempts have been undertaken by the FINUDA collaboration to find hints of heavier nuclear clusters like $\overline{K}NNN$ [121, 122]. The left panel of Figure 1.19 shows the invariant mass of Λd which are the decay products of the $\overline{K}NNN$. The spectrum was described by background and a new signal indicated in gray. The signal was assigned with a mass M = (3251±6) MeV/c^2 and a width $\Gamma_{\Lambda d}$ = (36.6±14.1) MeV/c^2 and a production rate of (4.4±1.4)$10^{-3}/K^-_{stop}$. The structure was interpreted as due to the absorption of a K^- on an α-cluster inside Li with the production of a kaonic nuclear bound state $\overline{K}NNN$ [121].

The work was again criticized for their interpretation of the data and it was shown that the distribution could as well be explained by the absorption of a K^- by three nucleons, see right panel of Figure 1.19 [123]. Further doubts were raised by the fact that in the KEK-PS E549 experiment the observed Λd spectrum from K^-+^4He reactions showed also a structure at 3250 MeV/c^2 that was, however, interpreted without the involvement of a kaonic cluster, but by three nucleon absorption [124].

Experiments at CEA-Saclay — SATURNE

In 2010, a work with re-analyzed data from the DISTO collaboration was published which announced an indication for the formation of a deeply bound $\overline{K}NN$ state [125, 126]. The investigated reaction was, as presented in this thesis, a p+p collision:

$$p + p \rightarrow K^+ + X \rightarrow p + K^+ + \Lambda, \tag{1.23}$$

with a proton beam of $E_{kin} = 2.85$ GeV. The data were measured inside the DISTO spectrometer and such the observables are distorted by acceptance effects. In opposition to an acceptance correction the data were compared to phases space distributions inside the detector acceptance in order to reveal physical signals. The method is quoted as "Deviation spectrum" method (DEV):

$$DEV = \frac{Measured}{PS\ Acc}, \tag{1.24}$$

where Measured and PS Acc denote an event distribution of an observable from data and phase space simulation, respectively. This method is a division of the observables from measured data by the spectra obtained from phase space simulations. It is only equivalent to a correction of the data (CORR) with a phase-space-model for the Dalitz plot distribution:

$$CORR = \frac{Measured}{AccCorr} = Measured \cdot \frac{PS\ 4\pi}{PS\ Acc}, \tag{1.25}$$

as in this specific case the phase space distribution in 4π (PS 4π) is uniform and can be substituted by 1. According to the argumentation in Refs. [125, 126], a DEV spectrum shows a non-flat behavior in case of a deviation of the production process from uniform phase space.

This approach has been previously applied on a set of data from $p+p \rightarrow K^+X$ reactions at three different beam energies [127]. The authors have divided their inclusive $p\Lambda$ spectra by phase space and found deviations. They attempted to describe the data by including a $p\Lambda$ resonance with mass 2.38 GeV, which, however, did not fit well to the measured momentum distributions of the kaons. Interesting in the context to DISTO is the fact that the authors stress the presence of N* resonances in the data, and state that the observed deviations can also originate from these resonances.

The analysis performed had the aim to carve out structures in the observables that can be associated with an excess compared to the phase space model. Figure 1.20 displays the angular distribution of the proton and kaon against its momentum in the center-of-mass system. The figure exhibits two deviations from phase space: one for protons with a momentum of 0.7 GeV/c, and one for kaons with a momentum of 0.4 GeV/c. The enhancement in the kaon momentum was interpreted as a two-body production as shown in Equation (1.23).

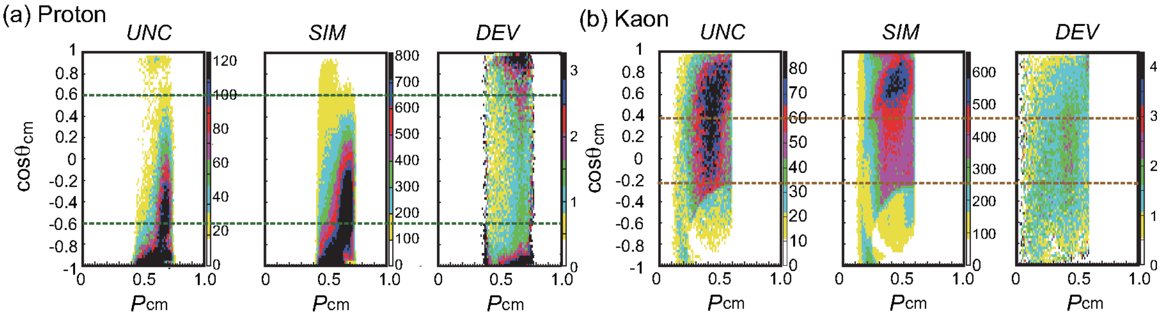

Figure 1.20: Measured-, model- and DEV event distributions of the proton (left) and the kaon (right) of Reaction (1.23). Figure taken from [125].

The enhancement is pronounced for large production angles of the kaon and the proton ($cos(\theta)_{p}^{CM} < 0.6$ and $-0.2 < cos(\theta)_{K^+}^{CM} < 0.4$), as indicated by the green and red lines in Figure 1.20. The event selection for proton angles was motivated by a selection of events with large momentum transfer which could enhance the relative amount of produced $\overline{K}NN$ states [126]. As mentioned in Ref. [126] a selection of emission angles of either the proton or the kaon is fundamental for the appearance of a structure in the $p\Lambda$ invariant mass spectrum as emphasized by Figure 1.21 for the selection on proton angles. Here, a bell shaped deviation from phase space distribution is observed with a fitted mass of M = 2267±3(stat)±5(syst) MeV/c^2 and Γ = 118±8(stat)±10(syst) MeV/c^2. This is equal to a binding energy of BE = 103 MeV for the three-body system [125]. This deviation can be emphasized by a combination of both selections on the kaon and the proton angle, which is shown in Figure 1.22. The extracted signal is quoted with a significance of 26σ and a production cross section of the order of the Λ(1405) which is about 20% of the total Λ production rate at this

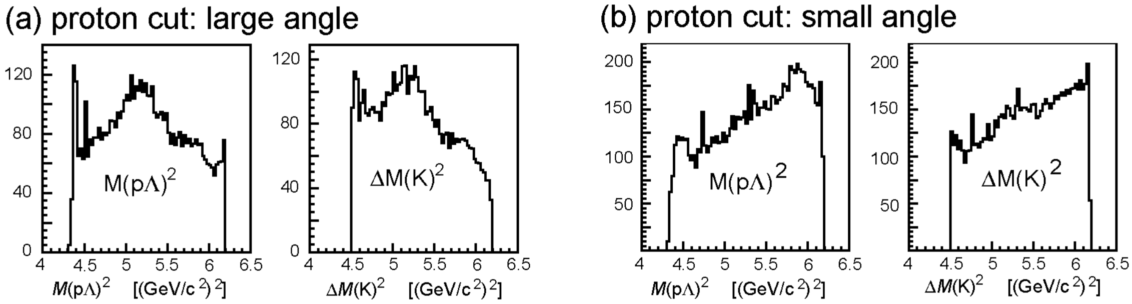

Figure 1.21: DEV event distributions for events with large (left) and small (right) proton angle in the CMS system. Figure taken from [125].

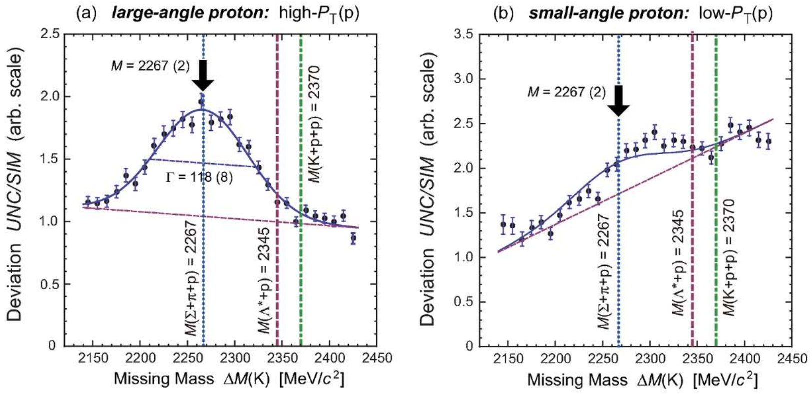

Figure 1.22: DEV event distributions for events with large (left) and small (right) proton angle in the CMS system both for large kaon angles. Figure taken from [125].

energy [125] or 14% of the total $pK^+\Lambda$ final state as quoted in [128].

In a second re-analysis Reaction (1.23) was also investigated at a lower beam kinetic energy of E_{kin} = 2.5 GeV [128]. The analysis was performed as discussed for the case at the higher beam energy. A deviation from the phase space model, that could be addressed to a new state, was not observed. Thus, the production cross section of the X(2265) at the low beam energy was reported as 0.2% of the $pK^+\Lambda$ production cross section [128].

In conclusion, the structure in the DEV spectrum observed by the DISTO collaboration was only present at 2.85 GeV, absent in 2.5 GeV and needed major kinematic cuts in order to appear in the spectrum. The importance of these cuts is precarious, as a deviation of the measured spectrum from phase space distributions is clearly visible under no cut conditions in the momentum distributions of the particles. Furthermore, a comparison to a phase space model is generally questionable due to the long history of reported special production kinematics involved in the $pK^+\Lambda$ final state. A deviation from phase space, thus, simply indicates the large limitations of this model for the data description. A critical review on this analysis, in light of the results reported by this and other works, can be found in Chapter 7.

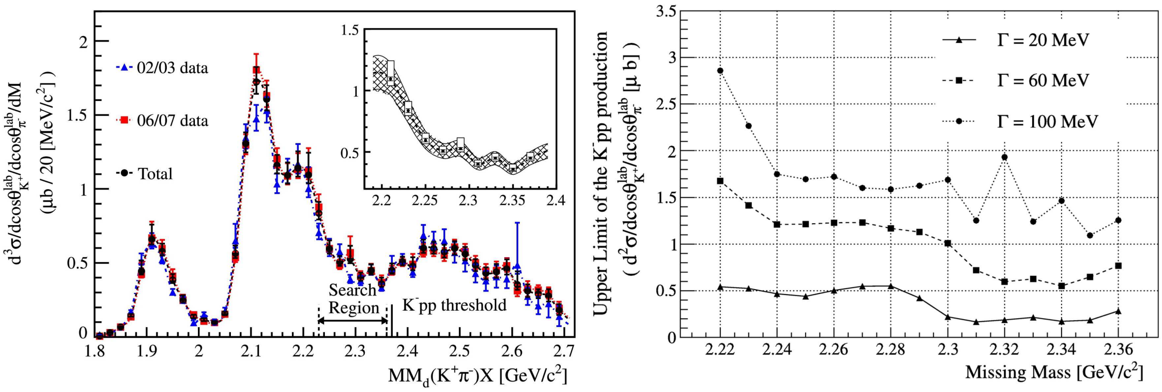

Figure 1.23: Left panel shows the $MM_{K^{+},\pi^{-}}$ spectrum of Reaction (1.26), right panel shows the extracted upper limit for the production of a $\overline{K}NN$ in the investigated reaction.Figure taken from [129].

Experiments at SPring-8

The LEPS collaboration at the SPring-8 facility searched for a $\overline{K}NN$ of positive charge in the following reaction [129]:

$$\gamma + d \rightarrow K^{+} + \pi^{-} + X, \tag{1.26}$$

with E_{γ}=1.5-2.4 GeV. They argued that this reaction can be seen as a virtual strangeness induced reaction d(K^{-},π^{-})X or d(K^{*-},π^{-})X, which has never been measured before. To recover eventual properties of the $\overline{K}NN$, they investigated the inclusive missing mass spectrum $MM_{K^{+},\pi^{-}}$ without a selection on possible decay channels. The measured spectrum is shown in the left panel of Figure 1.23. The data could be described well by a cocktail of ordinary reaction channels. Therefore, an upper limit of the production cross section for the nuclear bound state X was performed. The upper limit at a 95% CL as a function of a hypothetical mass and width of the state X is given in the right panel of Figure 1.23. These values correspond to about 1.5-5% (Γ = 20 MeV/c^{2}), 5-15% (Γ = 60 MeV/c^{2}) and 9.9-26% (Γ = 100 MeV/c^{2}) of a typical cross section for hyperon production such as $\gamma + d \rightarrow K^{+} + \pi^{-} + \Lambda + (p_{s})$ [129].

Upcoming Results

As no real convergence between the different exclusions and signal claims is visible, the need for new experimental data is essential. Several results are on the way: A search for kaonic nuclear bound states with the KLOE drift chamber by the AMADEUS collaboration [130, 131]; A search for the $\overline{K}NN$ in strong decays of the $\Upsilon(1S)$ at B-factories [132, 133] like BaBar and BELLE; A search for a $\overline{K}NN$ of negative and zero charge in the reaction d(γ,$K^+\pi^+$)X and d(γ,K^+)X, respectively, by the LEPS collaboration [134]; A search for a $\overline{K}NN$ of positive charge in the reaction ^{3}He(*inflight*-K^-,n)X [135] and via d(π^+,K^+)X at p_{K^+} = 1.7 GeV/c (Experiment E27) [136] both at J-Parc.

1.6.7 Concluding Remarks

In the theory community the argue whether one deals with a shallow or deep potential continues [107, 39]. Depending on the potential and models the predicted properties of the kaonic nuclear bound states are significantly different. There is a general agreement that these states should exist. The question if their properties are so opportune that one could see their footprint in an experiment, is far from being answered.

Most signals, reported by experimental groups, did not withstand re-measurements or were interpreted elsewise (KEK, BNL, OBELIX, FINUDA). On the other

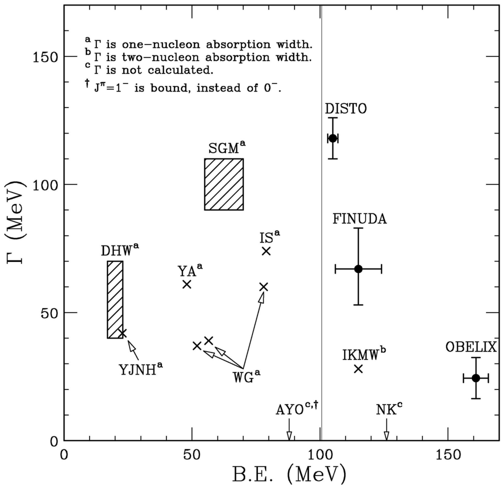

Figure 1.24: Overview showing the large spread of theoretical predictions and experimental announcements concerning the properties of the $\overline{K}NN$ system [137]. References are as follows: Yamazaki and Akaishi **YA** [90, 69], Shevchenko, Gal and Mares **SGM** [78, 76], Ikeda and Sato **IS** [79], Dote, Hyodo, and Weise **DHW** [85, 86], Ivanov et al. **IKMW** [138], Nishikawa and Kondo **NK** [139], Yamagata et al. **YJNH** [140], Wycech and Green **WG** [89], and Arai, Yasui and Oka **AYO** [88].

hand there have been experiments which did not observe any noteworthy structure in their measured spectra and reported upper limits for the according production of anti-kaonic nuclear bound states. A figurative impression of the current confusion in this field [137] is shown in Figure 1.24. Here, several properties as predicted and experimentally claimed for the $\overline{K}NN$ system are summarized and show no consistent picture. The question remains if there is any experimental access to the properties of these nuclear clusters. This work is a continuation of the previous efforts. The later reported analysis will show whether HADES sees a signal of the positively charged $\overline{K}NN$ in p+p collisions or not.

2 | Experiment and Methods

2.1 The HADES Setup

The analyzed data were recorded with the **h**igh-**a**cceptance **d**i**e**lectron **s**pectrometer – **HADES**. The design of the spectrometer is presented in Figure 2.1. The left panel shows an expanded view of the spectrometer where the sixfold geometry is nicely visible. The right panel shows a cross section through the spectrometer in its compact configuration. The system consists of six identical

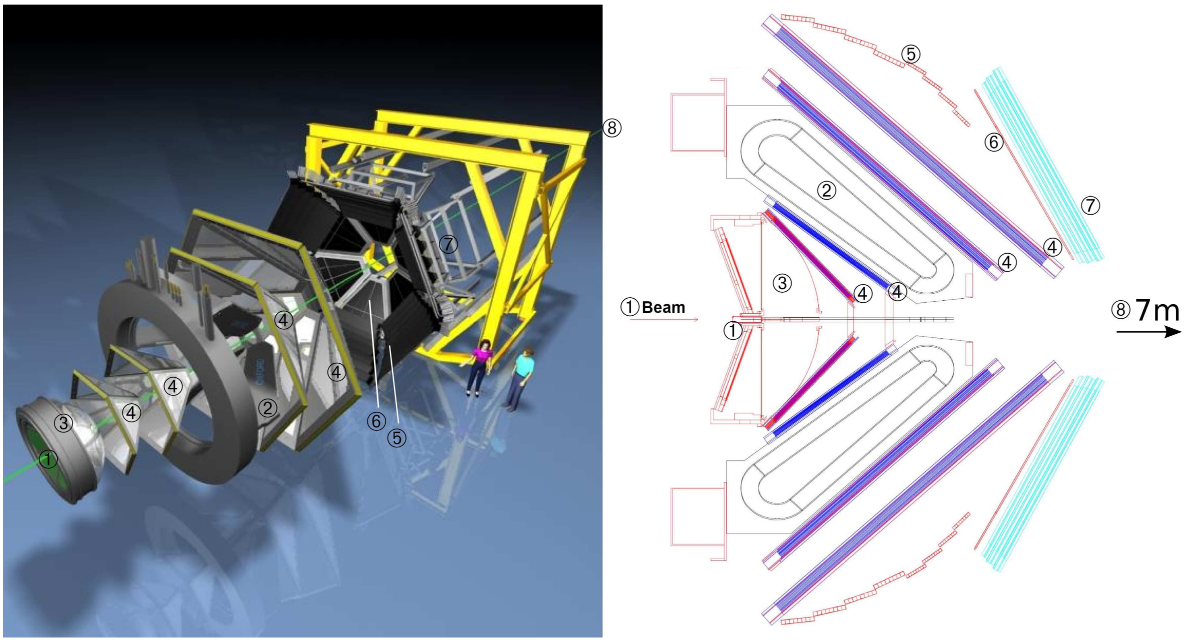

Figure 2.1: The HADES Detector. Left: Expanded view of the different layers, right: cross section of the compact position [141, 142]. The different detector parts are marked with numbers and discussed in the text.

sectors arranged around the beam axis. It has a polar acceptance from 15° to 85° and a nearly full azimuthal coverage (85%). The momentum resolution of the detector is $\Delta p/p \approx 3\%$. The subsystems are marked with numbers and are discussed in the following; a detailed report of the technical design is published in Ref. [142].

① – Beam and Target

The beam of the analyzed experiment was consisting of protons with a kinetic energy of 3.5 GeV ($\hat{=}$ $p(proton)$=4.34 GeV/c, $E_{tot}(proton)$=4.44 GeV, $\sqrt{s_{pp}}$=3.18 GeV) and an intensity of $\sim 10^7$ particles/s [143].

The beam protons were incident on a fixed liquid hydrogen target (LH_2). It was cooled down to 20 K at atmospheric pressure causing a density of 0.35 g/cm^2, and a total interaction probability of ∼0.7%. The target had a length of 4.4 cm and a diameter of 2.5 cm.

The data were recorded after a first-level trigger decision (LVL1) which required at least three hits in the META system (M3), see Point ⑤ and ⑥. In total $1.17 \cdot 10^9$ p+p events were written to tape and can be analyzed.

② – The Magnet ILSE

The inhomogeneous toroidal magnetic field between MDC layer II and III is created by the Magnetic spectrometer ILSE (**I**ron**l**ess **s**uperconducting **E**lectromagnet). It causes charged particles to bend their flight direction in the polar angle which is used to determine their momentum via the bending radius. The magnet is constructed such to guarantee a nearly field free region around the target and MDC layers I and IV. In this way, the particles have almost straight tracks while crossing the MDC chambers and are bent only between MDC layer II and III. The magnet has a six-fold geometry arranged around the beam axis and creates a magnetic field of about B_{max}=0.9 T in the center of the sector.

③ – The RICH Detector

The first particle detector upstream the beam is the **r**ing-**i**maging **ch**erenkov detector (RICH), which consists of two separated, gas-filled chambers. This detector is used for real time e^+-e^- identification. It is constructed such, that it is blind for traversing hadrons; only leptons and fast mouns will create Cherenkov light in the second half of the detector that is filled with a radiator gas. The photons from the Cherenkov light are reflected by a mirror back into the first half of the detector, which is separated from the radiator part by a CF_2 window. This first half is filled with CH_4 and equipped with CsI photo cathodes to detect the photons via the photo-effect. The emitted electrons from the CsI layer are collected on the wires of a **m**ulti-**w**ire **p**roportional **c**hambers (MWPC), so that a signal can be processed.

④ – The MDC Detectors

The **m**ini **d**rift **c**hambers (MDC) are arranged in four modules and six sectors around the beam axis. Two of the sectors (MDC I and II) are placed before and two (MDC III and IV) are placed behind the magnet. This detector system is used to measure the hit positions of a traversing particle which later allows to determine its path-length and momentum via a Runge-Kutta track fitting algorithm. The good spatial resolution of the detectors (∼100 μm) is a result of the six wire planes in each module, that are oriented with a 20° offset in stereo angle with respect to each other. In this way a precise intersection point of all fired wires is obtained. The chambers are filled with a helium based counting gas (He:i-Buthane=60:40) that gets ionized by a traversing particle. The produced secondary electrons create particle avalanches close to the wire which induce a signal. The energy-loss of the particles is proportional to the deposited charge on the wire and, thus, also a dE/dx information can be retrieved from this detector.

⑤ – The TOF Detectors

The large polar angles (44° to 88°) of the time-of-flight detector system are covered by the TOF detectors. They consist of 64 rods combined to 8 modules. The rods have cross-sections of 20x20 mm (inner) and 30x30 mm (outer). The scintillator rods are read out from both sides by photo multipliers. This allows a spatial hit resolution of 25-27 mm and a time resolution of ∼150 ps. The stop-time information, as well as the deposited energy dE/dx, is used for particle identification.

⑥ – The TOFino Detectors

These detectors are similar to the TOF detectors and cover small polar angles (15° to 44°). Each sector is covered by four paddles with a cross section of 10x10 mm. The paddles are read out at one side only, which results in a time resolution of 420 ps. The hit position can not be determined with this detector alone but with the help of the pre-shower system. This time-of-flight detector delivers the stop-time of a particle, as well as the deposited energy dE/dx, which are used for particle identification.

⑦ – The Pre-Shower Detectors

The single-sided readout of the TOFino detectors combined with the larger granularity hinders a determination of the hit position. Thus, the TOFino system is equipped with a pre-shower detector. This detector has alternating layers of gas filled wire-chambers and lead-converters for a shower creation. The particle induced showers are registered in the wire-chambers. The wire-chambers determine the hit position of the traversing particle while the shower geometry in the alternating layers delivers information whether the particle was a hadron or a lepton (if p>400 MeV).

The three detectors TOF, TOFino and pre-shower build the META sytem (**m**ultiplicity **e**lectron **t**rigger **a**rray). This interconnection of the three systems is used for the LVL1 trigger decision, which needs the hit multiplicity information.

⑧ – The Forward Wall

This detector was used for the first time in the analyzed p+p beam-time. It is a scintillating hodoscope with three different module sizes: 1.5x1.5 cm (5-rows), 4x4 cm (2-rows), and 8x8 cm (3-rows) from inner to outer which deliver the hit position of a particle. The scintillators deliver a time-of-flight information of ∼700 ps. It was placed 7m downstream the target, covers an acceptance of 0.33° to 7.17° in polar angle and a full azimuthal coverage. It was originally installed for the spectator tagging in the d+p (1.25 GeV) experiment and the event plane reconstruction in Au+Au, but in the presented analysis the FW is also used to reconstruct the proton four-vector from exclusive event selections.

2.2 Particle Identification – PID

The particle identification in HADES is different for leptons and hadrons. The whole design of the spectrometer is optimized for lepton identification which is done with help of a measured Chrerenkov ring in the RICH detector and the shower geometry in the pre-shower detector. These two information are matched with a reconstructed track in the MDC drift chambers and so the lepton candidates are identified.

Charged hadrons, on the other hand, can be identified only via their energy-loss or the time-of-flight. With these two methods the particle identity can be determined so that the mass of the particle can be set to a nominal value taken from literature [8].

PID with dE/dx

The theoretical energy-loss of a particle traversing matter can be described by the Bethe-Bloch equation [144]:

$$\frac{dE}{dx} = \frac{4\pi n z^2}{m_e c^2 \beta^2} \cdot \left(\frac{e^2}{4\pi\epsilon_0}\right)^2 \cdot \left[\ln\left(\frac{2 m_e c^2 \beta^2}{I \cdot (1-\beta^2)}\right) - \beta^2\right] \tag{2.1}$$

with β=v/c, v the velocity of the particle, E the energy of the particle, x the distance traveled by the particle, c speed of light, z$\cdot$ e the particle charge, e the charge of the electron, m_e the rest mass of the electron, n the electron density of the traversed material and I the mean excitation potential of the material.
This equation describes the kinetic energy-loss per traversed distance of a particle via its interaction with the shell atoms in the material. Equation 2.1 shows that the energy-loss is only dependent on the velocity β and the charge $z \cdot e$ of the particle. The energy-loss at a certain velocity is, thus, one unique value for all particles. When the energy-loss is plotted against the momentum, however, the different particles show a splitting of their energy-loss curves due to their different masses.

The energy-loss information dE/dx can be retrieved from the MDC, TOF and TOFino detectors. Figure 2.2 shows the energy loss of particles in the MDC drift chamber from the p+p (3.5 GeV) experiment. Here, particles with a momentum lower than 1 GeV can be distinguished from another with help of a graphical cut in the dE/dx vs. momentum plane.

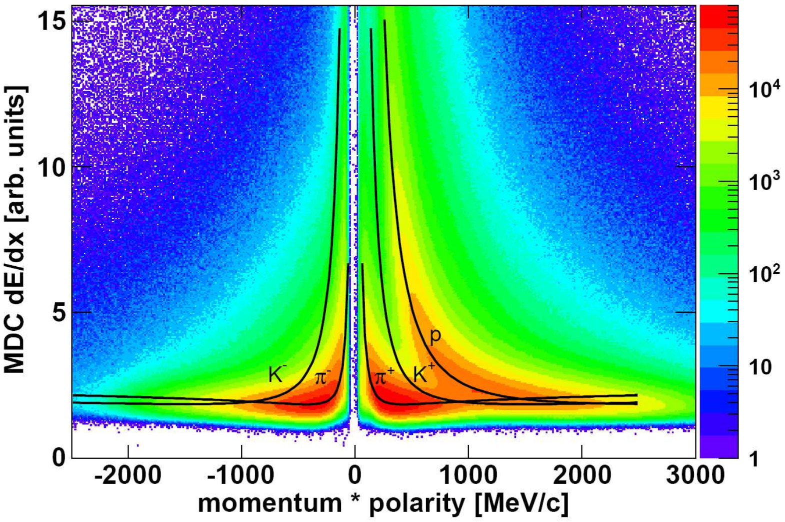

Figure 2.2: Energy-loss dE/dx in the MDC drift chambers. The theoretical lines are shown by the black Bethe-Bloch curves [23].

PID with TOF

A second, independent option to determine the PID of a particle proceeds via the measured time-of-flight. The momentum of a particle is only dependent on the relativistic velocity β and the mass:

$$p = m \cdot c \cdot \frac{\beta}{\sqrt{(1-\beta^2)}}, \tag{2.2}$$

with

$$\beta = \frac{v}{c} = \frac{track\text{-}length}{tof \cdot c}. \tag{2.3}$$

This provides the possibility to determine the PID of a particle via its time-of-flight and the measured momentum. The momentum and track-length of a particle are determined from a Runge-Kutta fit algorithm that uses the hit information from the MDC chambers to reconstruct the complete particle path through the spectrometer. The time-of-flight is measured via the time difference between the event-start-time of the start-detector and the hit time in the META system.

Unfortunately, the start-detector was not active in the p+p experiment so that a-priori no start-time information is available. This hinders a direct access to the time-of-flight, yet this quantity can be reconstructed, see Ref. [145]. The main points of the reconstruction procedure are the following: first a PID hypothesis of a track is build, an according mass is assigned to that track; based on Equation 2.2 its flight velocity is reconstructed; together with the velocity, the measured track length, and the stop-time, the start-time of the track can finally be restored. This is done for all tracks in the event. Then, a truncated average from all the track-start-times in one event is build and taken as a general event-start-time. This reconstructed start-time is afterwards used together with the stop-signal from the track of interest to build the actual time-of-flight of the particle and with this, finally, reconstruct its mass.

The particular reconstruction can be done in various ways, and several methods were tested in parallel. The ways differ under which circumstances a certain particle is included in the algorithm or not. If the information of the different detectors are included with a different weight and whether some particles are, later, thrown out from the algorithm. Appendix B shows a specific example from the time-of-flight reconstruction procedure where the different options were quantitatively compared with respect to the kaon purity in exclusive $pK^+\Lambda$ production, see also Chapter 4.

2.3 Simulation Process

To cross check and verify the correctness of the developed data analysis, process simulations are very helpful. In such simulations, events are generated with a Monte Carlo simulation tool and then the particles in these events are tracked through the full detector, whereby the single interactions of the particle with the detector material are modeled in detail. Then the same event selection, as applied for the experimental data, is performed for the simulated events.

The comparison of simulated and measured spectra allows to distinguish known from unknown sources and offers the possibility to extract detailed information from the measured data. The simulation steps are described in the following.

2.3.1 The PLUTO Event Generator

Events can be simulated with the PLUTO Event generator (v4.11) developed for HADES [146, 147]. For heavy-ion collisions at intermediate energies particles can be produced according to a thermal energy spectrum. For elementary reactions, like p+p collisions, the particles are produced according to a uniform distribution in the phase space volume, while guaranteeing energy and momentum conservation. If needed, angular distributions between the produced particles or mass distributions of broad resonances can be implemented.

In case several channels are simulated simultaneously, their respective production yield follows the implemented cross sections. The output cocktail is an incoherent sum of all possible final states.

2.3.2 The Detector Geometry in GEANT

The events from the PLUTO simulation are further processed through a GEANT simulation [148] of the HADES detector. In this simulation, the interaction of particles with the detector material is modeled. Thereby, the particle is deflected in the magnetic field, scatters off material, creates avalanches in gas filled areas, knocks out secondary particles from the detector material, and in this way loses its energy. The interaction points with the detector material are the output information of this simulation tool.

2.3.3 The Detector Response

To model a realistic detector response, the GEANT signals from the interaction points are processed through a DST (data summary tape) simulation. Here, the analog detector readout is modeled and the signals are further digitized. In this way, detector noise, inefficiency, and finite resolution effects are modeled. Then the particle tracks are reconstructed from the hit points in the same way as in the real experiment, resulting in a momentum resolution of $\Delta p/p \approx 3\%$. The trigger settings are also applied to the simulated events so that in the final result the events have the same form as the experimental data.

2.4 Final State Selection

This thesis contains two major data analyses. The one regarding the production of the $\Lambda(1405)$-resonance is introduced in Chapter 3. The one which discussed the $pK^+\Lambda$ final state is introduced in Chapter 4.

As the underlying event kinematic in case of $pK^+\Lambda$ production is rather complex, this section will discuss the major physics aspects that are connected to this final state.

2.4.1 The pK$^+\Lambda$ Final State

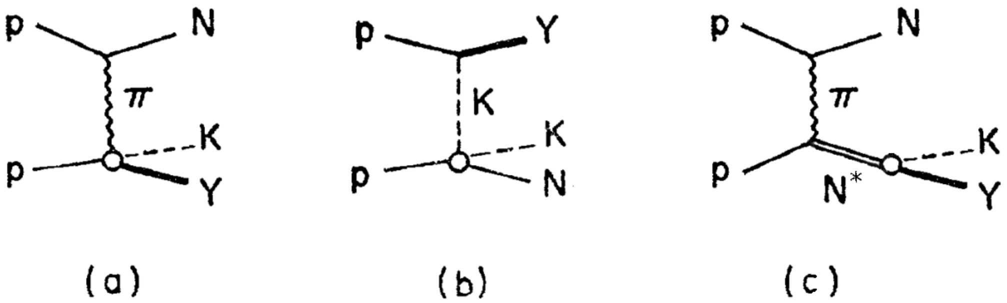

Figure 2.3: Possible production mechanisms leading to a $pK^+\Lambda$ final state [149].

The reaction:

$$p + p \rightarrow p + K^+ + \Lambda \tag{2.4}$$

is the simplest way to produce open strangeness in p+p collisions and is investigated since the pioneering work of Ref. [150] in the 60s. While experiments with bubble chamber detectors collected only few statistics [127, 151, 152], modern experiments are ideal to investigate Reaction (2.4) to great detail. An example therefore is the DISTO detector at SATURNE [153, 154], and the COSY-TOF [155, 156, 157] and ANKE [158] collaborations at COSY. The main purpose of the experimental programs carried out by these groups is the investigation of: the production mechanisms behind Reaction (2.4), the $p\Lambda$ final state interaction, the creation of intermediate N^{*+}-resonances in the production process, the ΣN cusp effect, and the possible existence of di-baryons or pentaquarks. Figure 2.3 shows the standard mechanisms for the production of the $pK^+\Lambda$ final state. These processes involve pion-exchange (a), kaon exchange (b) and contains for reactions with pion exchange also the possibility to create intermediate N^{*+}-resonances (c).

Intermediate N*-Resonances

While the very early works in this field neglected process (c) [159], it was soon accepted that intermediate N^{*+}-resonances contribute strongly to the $pK^+\Lambda$ final state via their decay into $K^+\Lambda$. Nowadays, the production of intermediate resonances is a well established concept [155, 156, 157, 160, 161, 162].

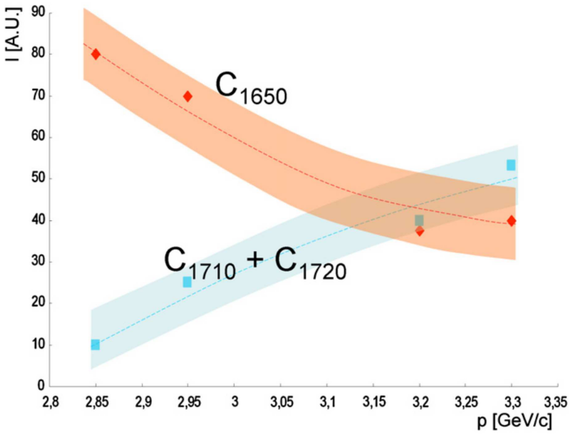

Figure 2.4: Contribution of N(1650) compared to the sum of N(1710) + N(1720) as a function of the beam momentum [157].

Their production strengths were investigated quantitatively for energies of E_{Kin} =2.16, 2.4 and 2.45 GeV [157]. In this work, the relative contribution of several N^{*+}-resonances and non-resonant $pK^+\Lambda$ production was determined. It was found that resonance production is by far the dominant process at these energies. Figure 2.4 illustrates the result of their analysis where the relative contribution of the resonances $N^{*+}(1650)$ and $N^{*+}(1720)+N^{*+}(1720)$ is presented.

These findings have major implication in the description of the production process. The following reaction summarizes possible $pK^+\Lambda$ production processes via intermediate states:

$$p + p \rightarrow p + K^+ + \Lambda \tag{2.5}$$

$$\rightarrow N^{*+} + p \tag{2.6}$$

$$\llcorner\!\!\rightarrow \Lambda + K^+$$

$$\rightarrow \Theta^{++} + \Lambda \tag{2.7}$$

$$\llcorner\!\!\rightarrow p + K^+$$

$$\rightarrow X^+ + K^+ \tag{2.8}$$

$$\llcorner\!\!\rightarrow p + \Lambda$$

While Process (2.5) illustrates the non-resonant production of the three final state particles, the Processes (2.6) - (2.8) contain intermediate states as sources for the final state particles. Process (2.6) contains an intermediate N^{*+}-resonance, Process (2.7) contains an intermediate pentaquark with charge +2 which

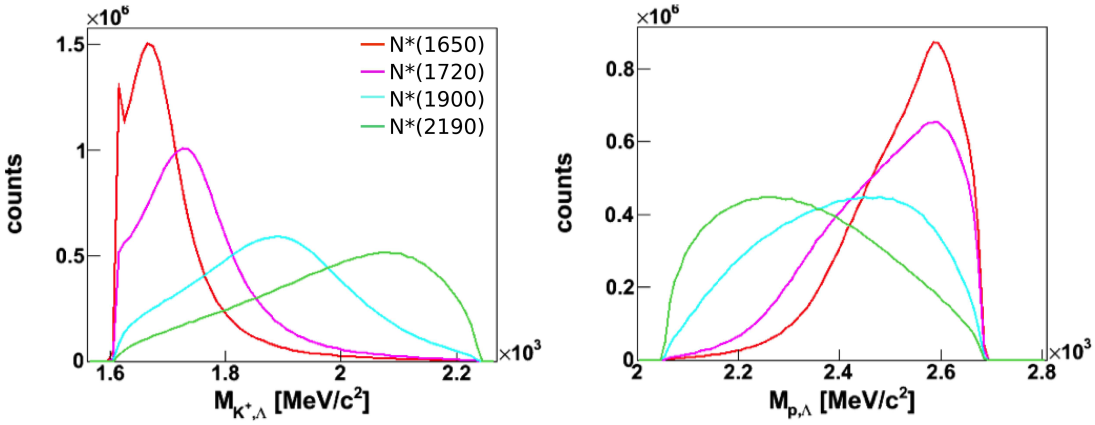

Figure 2.5: Simulated invariant mass distribution in 4π for the production of the $pK^+\Lambda$ final state via Reaction (2.6) with different intermediate N*-resonances.

was investigated in Ref. [163], and Process (2.8) contains the production of a strange di-baryon, which is discussed in a following section.

Altogether, these processes are subsequent two-body reactions and hence the particle kinematics are strongly correlated. Thus, every process with intermediate states contains kinematic reflections also in observables not directly related to the N*-resonance. Especially two-body invariant masses are affected by this phenomenon. For $pK^+\Lambda$ production at E_{Kin} = 3.5 GeV this effect was explained and intensively studied in Ref. [164]. This finding means that if intermediate states are present in the production, their kinematic has to be modeled with care to understand the complete event kinematic. Figure 2.5 shows PLUTO simulations of production process No. (2.6) in which N*-resonances with different masses were simulated and the effect of kinematic reflections in the $p\Lambda$ invariant mass spectrum was studied. The distributions show that the $p\Lambda$ invariant mass is very sensitive to the production of N^{*+}-resonances.

Final State Interaction

A topic of great interest is the final state interaction that occurs between hadrons. Via the production of $pK^+\Lambda$, the final state interaction between Λ and proton is intensively studied [156, 157, 165, 166]. Since the interaction between protons and Λ's is known to be attractive, this should also have consequences for measured cross sections and mass distributions. Especially the invariant mass distribution of $p\Lambda$ is sensitive to this effect. As determined experimentally the mass distribution should show an enhancement at lower mass values, as presented for example in Figure 7.2 of Chapter 7. The $pK^+\Lambda$ reaction with polarized beams was further exploited to retrieve quantitative information on the $p\Lambda$ interaction in its triplet and singlet spin configuration [166]. Also the total cross section of $pK^+\Lambda$ production close to threshold is enhanced due to this effect which results in an increased ratio of $pK^+\Lambda$ to $pK^+\Sigma^0$ cross sections at low excess energies [167, 168]. As this effect is concentrated at small opening angles between the particles that are associated to small $p\Lambda$ invariant masses, larger invariant masses (and with this the $\overline{K}NN$ signal region) are not affected by this interaction.

Di-Baryons

Reaction Nr. (2.8) contains the production of a strange di-baryon with a subsequent decay into $p\Lambda$. It is a topic of long interest to find such states [159], which have various properties. One example are the strange di-baryons D_s and D_t which are expected close to the $p\Lambda$ threshold. They were investigated by the HIRES collaboration [169], after some signals have been found in earlier experiments [170, 171]. The work of the former experiment did, however, not confirm these findings and determined an upper limit for the production strength of the di-baryon (see also Ref. [93] for a discussion on di-baryons).

In the view of the $\overline{K}N$ interaction and its measurable consequences the production of a strange di-baryon might also be associated with a $\overline{K}NN$. Thus, Process (2.8) is of special interest and could look as follows:

$$
\begin{array}{l}
p + p \xrightarrow{3.5GeV} \overline{K}NN + K^+ \\
\qquad\qquad\quad \llcorner\!\!\rightarrow \Lambda + p \\
\qquad\qquad\qquad\quad \llcorner\!\!\rightarrow \pi^- + p.
\end{array}
\tag{2.9}
$$

Since the $pK^+\Lambda$ final state might indeed be sensitive to the production of a $\overline{K}NN$, the $p\Lambda$ invariant mass distribution is of great interest.

Models for the Production Process

As discussed, this $p\Lambda$ invariant mass observable could be distorted by $p\Lambda$ final state interaction for very low masses and kinematic reflections of the production of N^{*+}-resonances. In order to take these effects into account, detailed

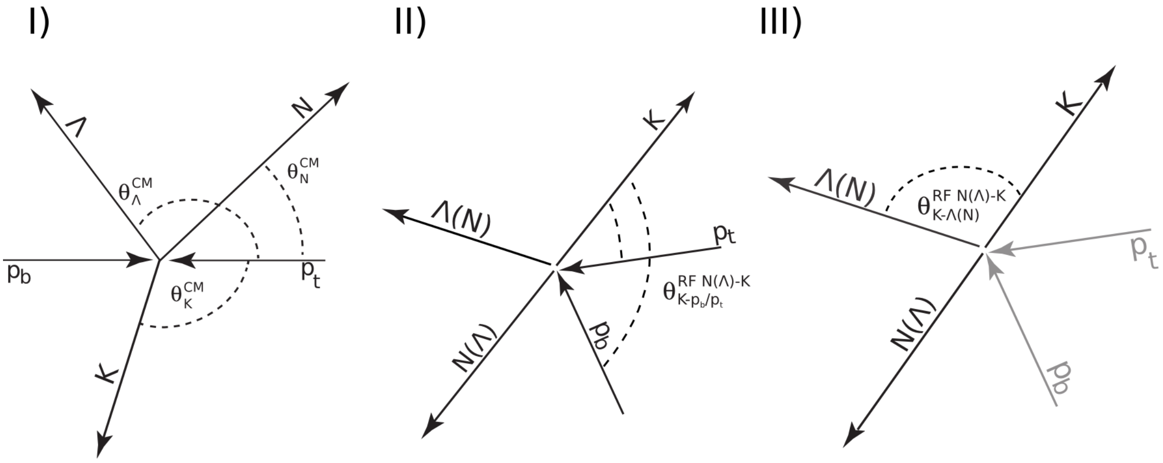

Figure 2.6: The Angles between the particles in different reference frames. I) shows the center of mass angles, II) shows the Gottfired-Jackson angles and III) shows the helicity angles [23].

models have to be employed that contain the standard production mechanisms of Figure 2.3. An extensive overview of established models for the production of $pK^+\Lambda$ is given in the doctoral thesis of W. Schröder [172]. Most common models describe the reaction by the exchange of a meson as illustrated in process (a) and (b) of Figure 2.3. In this way, production cross sections at single energies can be reproduced by adapting the free parameters in the respective models, but the description of the complete event kinematics, in form of differential observables, often fails [172].

To cross check the validity of models the comparison of the latter to many differential observables is needed. The observables used in this thesis for that purpose are discussed the following. The inclusion of intermediate resonances can be displayed by invariant masses of two particles such as $M_{p\Lambda}$, $M_{K^+\Lambda}$ and M_{pK^+}. More detailed event kinematics can be displayed by angular distributions in several reference frames [155]. Figure 2.6 illustrates how the angles are defined. A detailed description of the properties of the different angles is given in Ref. [23] and Chapter 6. The angles are denoted such, that the upper index indicates the rest frame in which the angles are investigated and the lower index indicates the angle in this frame or the opening angles between two particles, respectively.

Part II

Data Analysis and Results

3 | The Neutral Strange Resonances Σ^* and Λ^*

This chapter presents the data analysis of two neutral strange resonances: the $\Sigma(1385)^0$ with a mass of M=1384 MeV/c^2 and a width of Γ=36 MeV/c^2, and the $\Lambda(1405)$ with a mass of M=1406 MeV/c^2 and a width of Γ=50 MeV/c^2 [8]. These two resonances are produced in p+p collisions together with a proton and a K^+ in the final state via: $p+p \rightarrow Y^0+K^+ +p$; where Y^0 might as well be a ground state hyperon, namely Λ or Σ^0. An exclusive reconstruction of these strange particles requires also the identification of their decay products, as a missing mass spectrum to the p and K^+ would display an overlap of these nearby resonances.

Equations (3.1) and (3.5) show the decay branches of the two resonances. The only decay that differs among the two is their decay into neutral hyperons, since the decay of the $\Sigma(1385)^0$ into $\Sigma^0\pi^0$ is forbidden due to isospin conservation.

$$p+p \xrightarrow{3.5GeV} \Lambda(1405)+K^{+}+p \tag{3.1}$$

$$\rightarrow \Sigma^{-}+\pi^{+}$$

$$\rightarrow n+\pi^{-} \qquad 33.33\% \tag{3.2}$$

$$\rightarrow \Sigma^{+}+\pi^{-}$$

$$\rightarrow p+\pi^{0}$$

$$\rightarrow n+\pi^{+} \qquad 16.11\% \tag{3.3}$$

$$\rightarrow \Sigma^{0}+\pi^{0}$$

$$\rightarrow \Lambda+\gamma$$

$$\rightarrow p+\pi^{-} \qquad 21.35\% \tag{3.4}$$

$$\rightarrow n+\pi^{0}$$

$$\begin{array}{llll}
p+p \xrightarrow{3.5GeV} \Sigma(1385)^0+K^++p & & & (3.5)\\
\quad \longrightarrow \Sigma^-+\pi^+ & & & \\
\qquad \longrightarrow n+\pi^- & & 5.85\% & (3.6)\\
\quad \longrightarrow \Sigma^++\pi^- & & & \\
\qquad \longrightarrow p+\pi^0 & & & \\
\qquad \longrightarrow n+\pi^+ & & 2.83\% & (3.7)\\
\quad \longrightarrow \Lambda+\pi^0 & & & \\
\qquad \longrightarrow p+\pi^- & & 55.68\% & (3.8)\\
\qquad \longrightarrow n+\pi^0 & & &
\end{array}$$

This difference makes a distinction of the Σ^* and Λ^* feasible. An unambiguous separation is possible if one reconstructs the particles directly from the invariant mass of their decay products in the neutral channels (3.4) and (3.8). This is not achieved in this analysis, as the HADES spectrometer is not capable of identifying long-lived, neutral particles, such as neutrons, π^0, and γ.

Nevertheless, the mass spectra of the particles can be disentangled by examining the missing mass to the primary p and K^+ (MM_{pK^+}) under different event selections. To do so, an observable that is sensitive to the additionally produced γ in the decay of the $\Lambda(1405)$ (Eq. (3.4)) must be carefully evaluated. This observable is the missing mass to all charged particles in the event ($MM_{pK^+p\pi^-}$), which is different for the two cases (3.4) and (3.8).

The here presented data analysis exploits this fact in order to reconstruct the $\Lambda(1405)$-mass spectrum from its decay into $\Sigma^0\pi^0$, and to evaluate the production cross section of the $\Sigma(1385)^0$ in the p+p reaction.

The $\Lambda(1405)$ was also investigated by the reconstruction of its charged decay products, $\Sigma^\pm\pi^\mp$, despite the drawback from the inseparable $\Sigma(1385)^0$ contamination in the mass spectrum [23, 173]. This is reasonable, as the branching ratio of the $\Sigma(1385)^0$ into this decay is low, so that only a small number of events might contaminate this spectrum. To constrain the yield of the $\Sigma(1385)^0$ however, an external reference for its production cross section is needed. This input will be delivered from the analysis, explained in this chapter.

3.1 Event Selection

The final state of the resonance production and decay contains the primary produced proton and the K^+, as well as the neutral decay products from the resonance decays. In this analysis a Λ-hyperon from the decay is reconstructed via its daughter particles p and π^-. The event selection is two-fold: in one case, events where required to have four registered tracks in the main HADES detector, three with positive-, and one with negative charge; in the other case, events were accepted if there were three registered tracks in the HADES detector and one hit in the Forward Wall hodoscope. In the latter case the registered tracks in the main spectrometer contain two of positive and one of negative charge. These two different data sets are referred to as HADES data-set and WALL data-set in the following description. A sketch which illustrates the differences between these data-samples is shown in Figure 4.1 of Chapter 4.

3.1.1 Particle Identification

In both data-sets the charged tracks, detected in the main HADES spectrometer, were assigned with a particle ID via their energy loss in the MDC drift chambers, as described in Section 2.2 and shown in Figure 3.1. This selection is

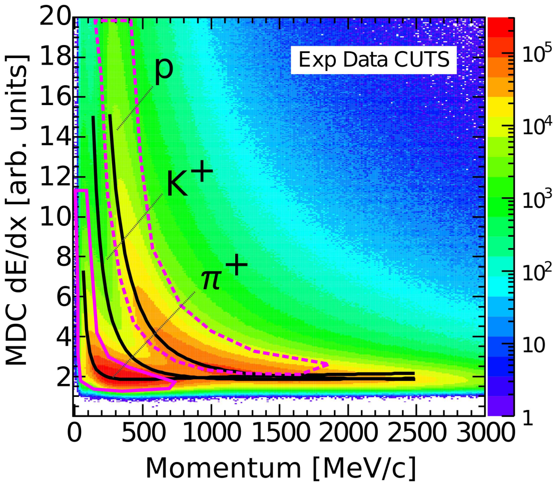

Figure 3.1: The energy loss per distance in the MDC drift chambers as a function of the particle momentum. The black lines represent the theoretical energy loss for pions, kaons and protons. The pink shapes define an area which determines the PID association of pions and protons.

applied to protons and pions whereas the additional positively charged particle was first only assumed to be a kaon. The particles are selected with help of two-dimensional cuts which define a region of high probability for the dE/dx vs. mom value to belong to a certain particle species. These cuts are shown in Figure 3.1 together with the nominal energy loss of the particles, according to the theoretical Bethe-Bloch curve. After this particle identification, the analysis of the two data-sets proceeds separately.

3.1.2 Reconstruction of the $\Lambda(1116)$-Hyperon

After the selection of the four particles, the Λ-hyperon is reconstructed from the invariant mass of its decay products: the proton and the π^-. Figure 3.2 shows the signals of the reconstructed Λ's for the HADES and WALL data sets under further cut conditions, explained in the following. The mass-resolution of the HADES signal is better than the signal from the WALL data-set, since in the latter case the proton which is used to reconstruct the Λ was detected in the FW hodoscope. Therefore, the momentum resolution for this proton is worse than for the other particles. Still, a clear signal of the Λ-hyperon is visible in the right panel of Figure 3.2 which shows the great capabilities of this detector.

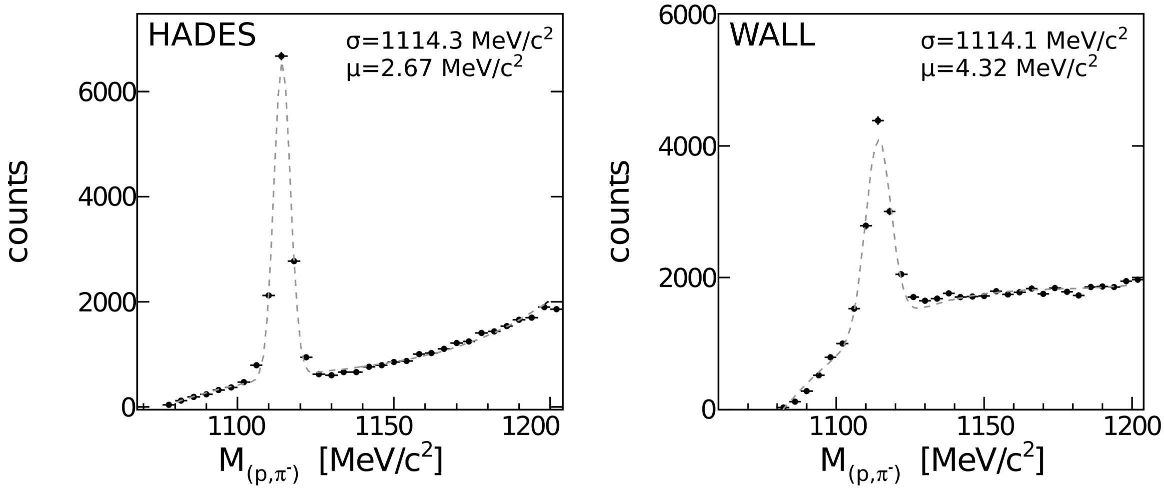

Figure 3.2: The invariant mass of p–π^- pairs for pre-selected exclusive events that could contain strangeness.The left panel shows the signal reconstructed from the HADES data-set and the right panel shows the signal reconstructed with help of the proton detected in the FW.

HADES Data-Set

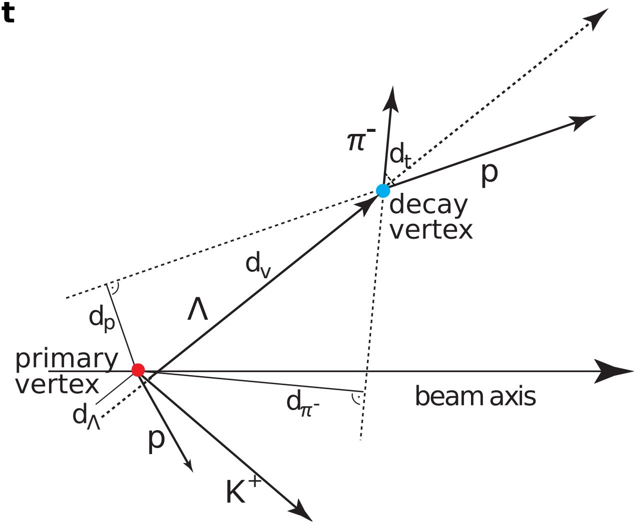

Figure 3.3: Schematic view of the Λ-hyperon decay into proton and π^-. The different distances between particle tracks and intersection points can be used to suppress combinatorial background [23, 141].

The combinatorial background, underneath the signal, can be effectively suppressed by considering the Λ-decay topology, as illustrated in Figure 3.3. d_Λ, d_p and d_{π^-} display the distance of closest approach between the respective particle track and the primary vertex. d_v is the distance between the primary-, and the secondary vertex, and d_t is the track distance between the two decay particles p and π^-. The detailed influence of the track cuts on the Λ-signal were tested in Ref. [145]. For the purpose of a good signal, the following cut values were selected: distance between the proton and pion track ($d_t < 18$ mm), distance of closest approach of the Λ to the primary vertex ($d_\Lambda < 23$ mm), and a constraint that the distance of closest approach has to be bigger for the π^- than for the proton ($d_{\pi^-} > d_p$). These cuts increase the signal-to-background ratio of the Λ-signal [145]. The left panel of Figure 3.2 illustrates the signal after the cuts have been applied. In order to obtain a realistic impression how large the background in the selected events might be, the event kinematics were constrained to an area relevant for semi-inclusive Λ-hyperon production. This is: MM_{pK^+}>1000 MeV/c^2, as real strangeness signals start with the appearance of the exclusive pK$^+$Λ production at MM_{pK^+}=1116 MeV/c^2, and likewise: $MM_{pK^+\Lambda}$>-70 MeV/c^2, as below that mass range pure combinatorial background is located. With these cuts, the Λ-signal in Figure 3.2 reveals a good estimation for the background in the mass spectra, underneath the events with strangeness production. Finally, p-π^- pairs were selected as Λ-candidates, if their invariant mass was within 1106-1122 MeV/c^2.

WALL Data-Set

In this case, the track topology can not be used for the background suppression, as no track information from the proton is known. The proton was reconstructed via a straight line from the primary vertex to the hit point in the FW. This is justified, as the magnetic field strength should be negligible at these low polar angles. For the momentum resolution itself, the true off-set of the proton track from the primary vertex (d_p) does not play a large role as an error source, since the distance of the FW to the primary vertex is 7 m. The only track observable that is available from the Λ-decay, shown in Figure 3.3, is d_{π^-}. It was, however, found that cuts on this observable have no large influence on the signal quality of the Λ.

As in the case of the HADES data, the Λ-signal in Figure 3.2 is shown in a kinematic range where strangeness can be produced (MM_{pK^+}>1000 MeV/c^2 and $MM_{pK^+\Lambda}$>-126 MeV/c^2). The Λ-hyperon was finally identified by p-π^- pairs with an invariant mass of 1101–1129 MeV/c^2.

3.1.3 Kaon Signal and Mis-Identification Background

A last observable that is used to filter out exclusive strangeness production in the p+p statistic, is the reconstructed mass of the K^+ candidates. Until this point in the analysis, the kaon was not specifically assigned with a PID. It was only assumed that the third positively charged track in the event corresponds to the kaon. Figure 3.4 shows the reconstructed kaon mass, according to the method discussed in Section 2.2, and after the Λ selection. In the left panel, kaon candidates of the HADES data-set are shown, and the right panel shows kaon candidates of the WALL data-set. Although no further PID selection was performed on these particles, a clear signal of the kaon is visible in both cases. This is mainly due to the fact that strangeness (S=-1) was explicitly selected in these events by the Λ reconstruction and, thus, strangeness conservation requires a S=+1 particle in the event, demonstrated by the kaon signal in Figure 3.4.

As noticeable from the Figure, the kaon candidates are in some cases truly protons or pions. For this reason, only events with a kaon candidate mass of 270–700 MeV/c^2 for the HADES statistic, and a mass of 340–750 MeV/c^2 for the WALL statistic were accepted for the final analysis.

Despite this selection, both statistics will suffer from a small contribution of

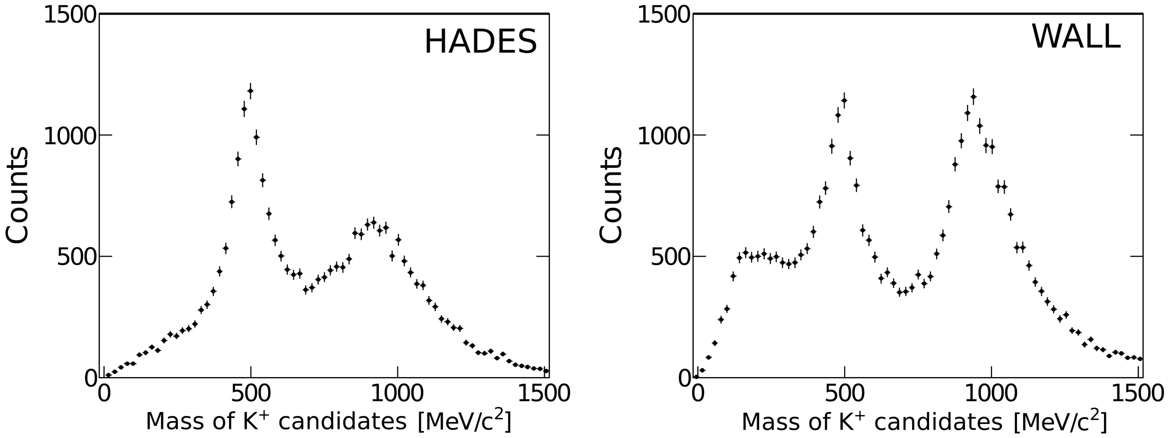

Figure 3.4: The reconstructed particle mass of the kaon candidates for the HADES (left) and WALL (right) data-sets.

events in which a proton or a π^+ is falsely mis-identified as a K^+, yet this mis-identification background can be modeled with help of an adapted side-band analysis, described also in Appendix A.2 of Ref. [23].

The Side-Band Background

To model this source of background in the selected statistic, two additional data-samples are created in which explicitly pions and protons (fake kaons) are selected from the kaon mass spectrum for the further analysis. This is done by a mass cut of -1000–0 MeV/c^2 for the pion sample and 1100–2000 MeV/c^2 for the proton sample[1]. In order to describe the measured data, two properties have to be adapted: first, the kaon kinematic in the data-sample has to be reproduced by the side-band data samples; and second, the relative contribution of proton and π^+ mis-identification in the selected kaon mass range has to be determined.

To adapt the kinematic of the side-band samples to the kaon kinematic, the kaon momentum is exploited. The sum of the side-band momentum distributions should match with the kaon momentum spectrum. This is achieved by

---

[1] Both sets were obtained prior to the Λ selection but in the same kinematic range as the kaon sample: M_{all}>70 and MM_{pK}>0.

scaling the two side-bands to the data bin-by-bin in momentum [23]:

$$SF(p) = \frac{Y_{K^+}(p)}{\alpha \cdot Y_{\pi^+}(p) + Y_p(p)}. \tag{3.9}$$

Here, SF(p) is the momentum dependent scaling factor, and Y_x name the yields of the three different data-samples per momentum bin. The scaling factor of Equation (3.9) has one degree of freedom (α), which is the relative contribution of protons and π^+ to the selected strangeness data sample. To fix this ratio to an optimal value, different versions of the side-band sample (different α) have to be compared to experimental observables.

The panels in the upper row of Figure 3.5 demonstrate the results of the momentum scaling procedure. As forced by Equation (3.9), the sum of both contributions models the kaon momentum perfectly. The observables that help to determine the correct scaling factor α are the following four observables: the invariant mass of p–π^- in three ranges (if MM_{p,K^+}>0 MeV/c^2, >1000 MeV/c^2 and >1300 MeV/c^2, respectively), and the left tail of the missing mass to the proton and K^+ (MM_{p,K^+} 0–1000 MeV/c^2), where only the contribution of mis-identification background is present. Two of these observables are presented in Figure 3.5 for the HADES data-set in the middle and lower row. The figure also shows an example of the background modeling for three different scaling factors α. One with too much relative proton content (left column) and one with too much pion content (right column). The middle column shows an example that belongs to one of the best descriptions. The best scaling factor should describe all four tested observables well and is extracted for HADES and WALL data separately. The scaled side-band samples describe these observables very well. The only important element to consider is, in fact, the correct background yield underneath the Λ signal. That beyond that the overall shape of the data is described so well shows the accuracy of this method.

With help of the scaling factor α and the momentum dependent scale-factor SF(p) the side-band events can be weighted such that any desired observable can be displayed with an reliable description of the contained background. Appendix A contains figures where the mis-identification background is shown for the observable MM_{p,K^+} in both data-sets.

The observables in Figure 3.5 reveal a small physical signal in the SB sample. This is due to the fact that the kaon mass distribution has a large width so that even the selection of fake kaons far left and right in the mass spectrum will contain a small amount of real kaons. This contribution can be well estimated with help of simulations. The latter are fed into the side-band analysis and such

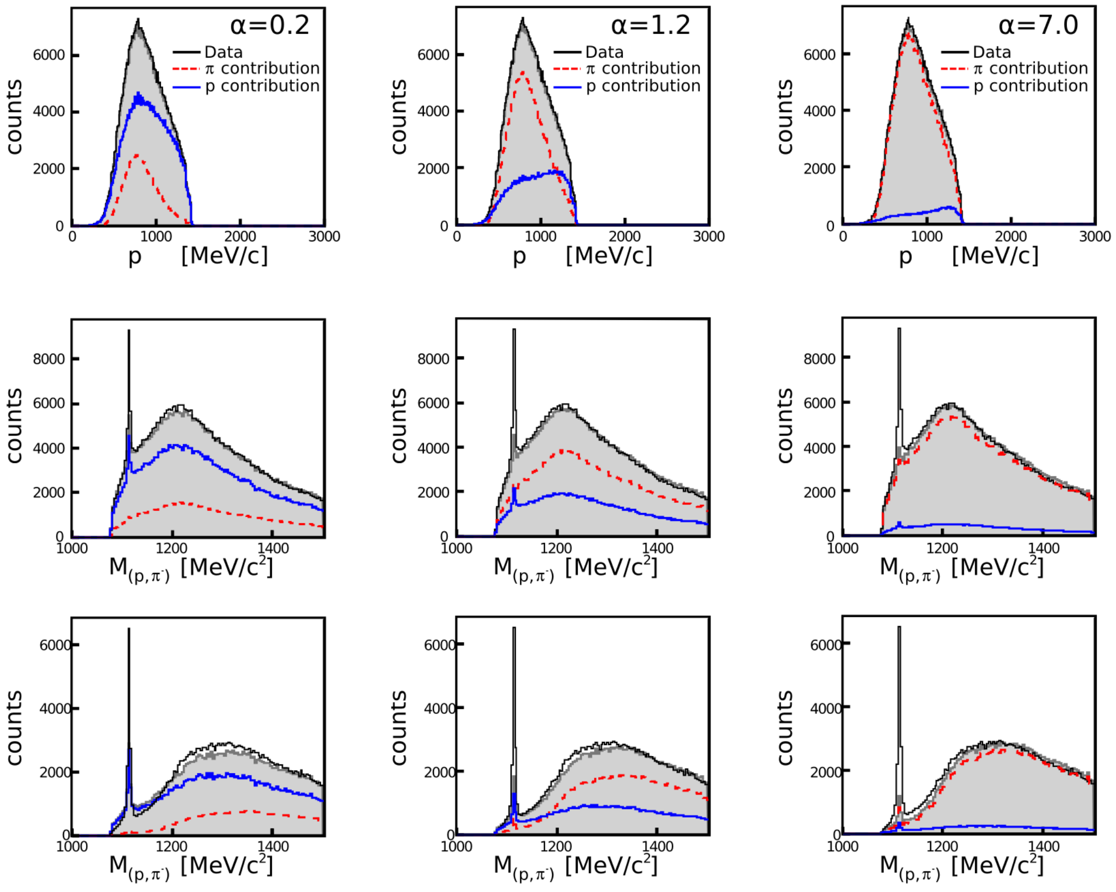

Figure 3.5: An example of the mis-identification background adaptation in the HADES data-sample. The upper row shows the momentum distribution in the kaon data-sample that is described by the scaled sum of the proton and pion side-band samples. The middle and lower rows shows the Λ signal in a mass range MM_{p,K^+}>0 MeV/c^2 and >1000 MeV/c^2. The three columns show the result for three different scaling ratios α of Eq. (3.9). While the left SB-background overestimates the combinatorial yield under the Λ, the right column is an example for an underestimated yield.

the signal strength in the real data sample relative the the strength in the side-band sample can be evaluated and eventually subtracted from the background.

3.2 Simulation Model for the Measured Data

To describe and understand the measured event distributions, simulations are needed. The simulations developed for that purpose contain several channels of strangeness production with the four charged particles: p, K^+, p, and π^- in the final state. The individual contribution of each channel can be estimated with help of measured cross sections at other beam energies. These different measurements can be fitted with a function that is proportional to the available phase space for the particle production. Then the cross section at 3.5 GeV beam kinetic energy can be deduced from the fit. This procedure was adapted and explained in the preceding work of this analysis [145]. The result of this procedure should be seen as a provisional result. Figure 3.6 shows the event distribution of the missing mass to the primary p and K^+ in the HADES acceptance for the simulation cocktail.

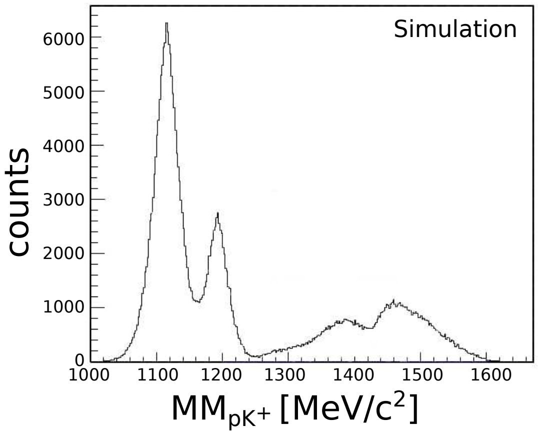

Figure 3.6: Simulated distribution of MM_{pK^+}, where many channels contribute to the total sum. The cross sections of the individual channels where extracted from a phase space fit, see Ref. [145].

The comparison of this spectrum to the measured event distribution, shown in the left panel of Figure 3.7, reveals striking differences. The mis-identification background which comes from non-strange events is certainly absent in the simulations, the yield of Σ^0-production (∼1200 MeV/c^2) is slightly too low, and the yield of the resonance production at higher energies is overestimated. Especially the statistic at 1500 MeV/c^2 is not visible in experimental data.

This mismatch is due to a limited validity of the phase-space interpolation of measured cross sections. The drawback of this approach was also shown for associate K^0 production in the same set of measured data [174]. The analysis of several exclusive production channels involving a K^0 showed large differences between the input cross sections from phase space fits and the output cross sections of the analysis. Table 3.1 shows these differences, obtained from the analysis. The range of the cross sections stems from the modeling of the simulation which can be included either with a flat or an-isotropic angular distribution in the CMS system. Still, the differences between input and output are large.

Table 3.1: Cross section from the analysis of associate K^0 production from the same experiment [174]. Compared are the input cross section from an external fit and the cross sections extracted from the analysis.

Channel	$\sigma_{PS\ fit}$ – input [μb]	$\sigma_{Multi\ \ fit}$ – output [μb]
$\rightarrow pK^0\Sigma^+$	20.43	24.25–26.27
$\rightarrow pK^0\Sigma(1385)^+$	5 .31	13.15–14.35
$\rightarrow pK^0\Lambda\pi^+$	18.40	2.37–2.57

The same effect is present for associate K^+ production, as visible in Figure 3.6. To deduce the right channels that contribute to the measured spectra and their according strength, the individual components have to be adapted to the experimental data, since an external reference was shown to be insufficient. This adaption is done in form of a fit algorithm which is described in the next section.

3.2.1 The Fitting Procedure

In the following approach, each simulated reaction channel was scaled such to the data that the incoherent sum of the different simulations describes the measured event distributions well. The fitting process uses several input channels, fit observables, and fit constraints in order to deliver the best result possible. The different aspects of the fit are explained in the following.

Input For The Fit

The possible contributions to the observed final yield that are included into the fit are the reaction channels listed in Table 3.2. The contribution of channels in which two pions were directly produced was found to be insignificant. The simulations of channel No. 4 have been modified to include an angular distribution of the Λ in the CMS system. This distribution is necessary in order to describe both data-sets equally well. The distribution of the Λs follows a sum of Legendre polynomials as shown by Eq. 6.1 in Chapter 6. The coefficients for the modification were extracted at E_{Kin} = 2.5 GeV and taken from Ref. [155].

Table 3.2: The implemented channels for the multi-fit and their according color code in the figures.

Number	Channel	Color
1	$\rightarrow pK^+\Lambda(1405)$	violet
2	$\rightarrow pK^+\Sigma(1385)^0$	light-green
3	$\rightarrow pK^+\Lambda\pi^0$ (non res.)	red
4	$\rightarrow pK^+\Lambda$	dark-blue
5	$\rightarrow pK^+\Sigma^0$	cyan
6	$\rightarrow pK^+\Sigma^0\pi^0$ (non res.)	pink
7	$\rightarrow pK^+\Lambda(1520)$	dark-green
9	$\rightarrow pK^+\Sigma^+\pi^-$ (non res.)	beige
0 and 12	mis-identification background	gray
-	incoherent sum of the fit	plum

Observables for the Fit

Each reaction channel has a slightly different event distribution in kinematic observables of the three measured particles p, K^+ and Λ. The best observable to distinguish the channel contributions from another is the missing mass to all the particles ($MM_{pK^+\Lambda}$). In order to maximize the stability of the procedure, this observable was fitted differentially in different bins of MM_{pK^+}. The ranges in MM_{pK^+} are as follows:
1) 0–800 MeV/c^2, 2) 980–1150 MeV/c^2, 3) 1160–1225 MeV/c^2, 4) 1250–1310 MeV/c^2, 5) 1330–1430 MeV/c^2 and 6) >1440 MeV/c^2. Figure 3.7 highlights the different ranges in MM_{pK^+} of the fitting procedure, whereas Figures 3.8 and 3.9 show the event distribution of $MM_{pK^+\Lambda}$ in these six bins for the HADES and WALL

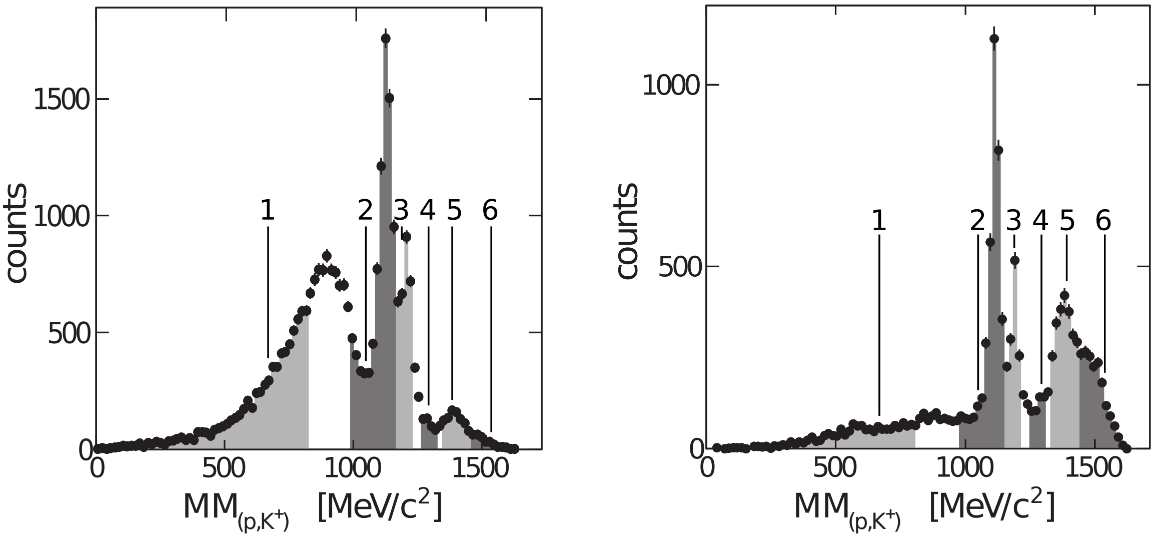

Figure 3.7: Missing mass to the proton and K^+ for HADES (left) and WALL (right). The numbers 1-6 correspond to the different ranges in which the observable $MM_{pK^+\Lambda}$ was fitted.

data set, respectively. To constrain the yield of the Λ(1520) better, the MM_{pK^+} was fitted directly in the mass range 1450-1620 MeV/c^2. Low masses of MM_{pK^+} can not be included into the fit as they are directly sensitive to the Λ(1405) mass distribution, which is not known exactly. The Figures 3.8 and 3.9 illustrate one example of a successful fit, where the sum of the nine contributions can describe all 12 histograms well, when fitted simultaneously.

Constraints for the Fit

To increase the stability of the fit, three constraints have been included. Channel No. 3 and No. 6 were constrained to have a lower contribution than Channel No. 4 (see Table 3.2).

Channel No. 9 was constrained to have a lower contribution than one third of the sum of Channel No. 1 and No. 2. The last constraint was implemented according to the results obtained from Ref. [23, 173]. It is an upper limit, as the results from Ref. [23, 173] obtained a cross section ratio of Channel No. 9 to the sum of No. 1 and 2 of R=(No. 9/(No. 1+No. 2))=0.37.

The mis-identification background that was already well constrained by the data is free to vary within ±5% of its initial strength.

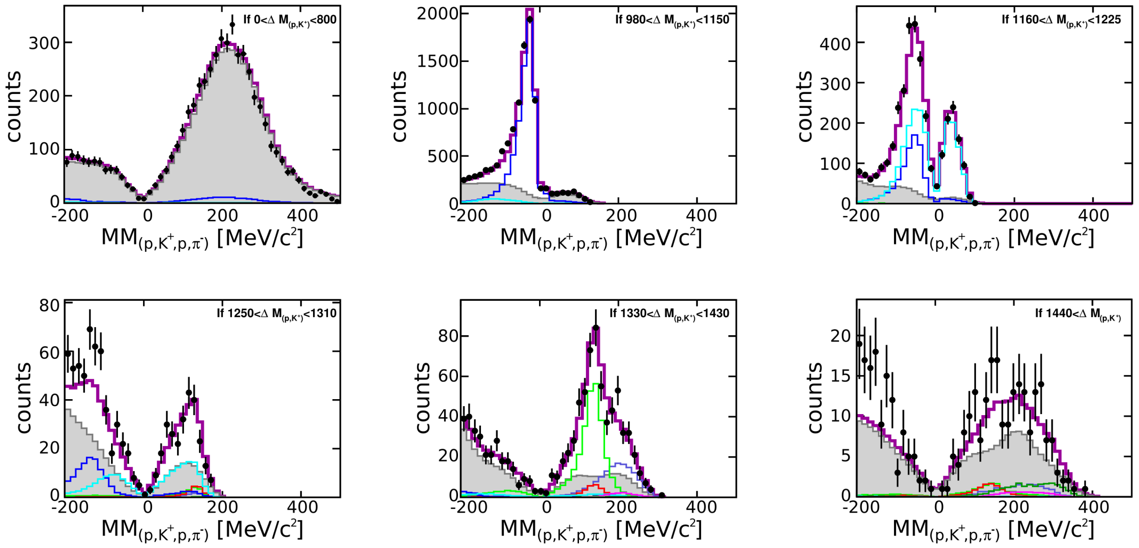

Figure 3.8: The event distribution of $MM_{pK^+\Lambda}$ in six different mass bins of MM_{pK^+}. The different panels show experimental data from the HADES statistic (black dots) together with the single channels (see Table 3.2 for the color description) and their sum (violet).

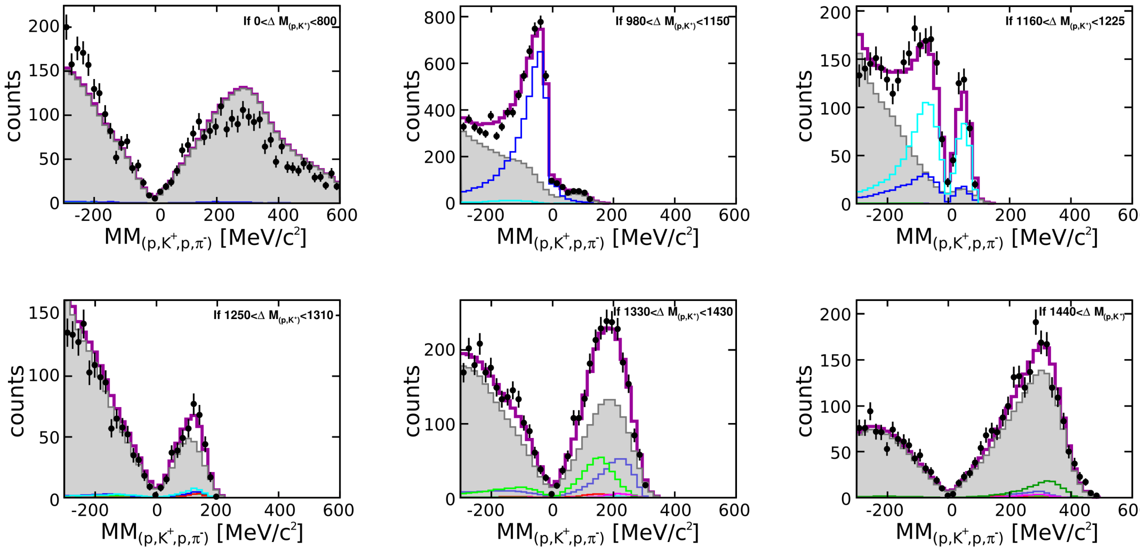

Figure 3.9: The event distribution of $MM_{pK^+\Lambda}$ in six different mass bins of MM_{pK^+}. The different panels show experimental data from the WALL statistic (black dots) together with the single channels (see Table 3.2 for the color description) and their sum (violet).

3.2.2 The Nominal Result

Figures 3.8 and 3.9 present the result of this fitting procedure, where the incoherent sum is compared to the fitted observables. The overall event distributions in the different bins are modeled well by the simulations (plum-colored histogram).

Having fixed the relative yield among the different contributions, all observables of interest can be described by the sum of the adapted cocktail. To do so, each histogram of a production channel has to be scaled according to its scale-factor that was used by the fit. Table 3.3 shows the scaling-factors which have to be multiplied to the histogram of the according channel. Also shown is the ratio of the $\Sigma(1385)^0$ to $\Lambda(1405)$ production which can be used as an input for the $\Lambda(1405)$ analysis from the charged decay channels $\Sigma^{\pm}\pi^{\mp}$ [23]. As the same amount of events was used in each channel simulation, the output scale-factors can be directly related to the ratio of the production yield and thus also to the cross section. For example, does this fit result predict a larger production cross section of the $\Lambda(1405)$ than the $\Sigma(1385)^0$.

Table 3.3: The result of the fit are the scaling factors for each simulated channel. The events have to be multiplied with this number to obtain the correct final yield that describes the experimental data.

Channel	Scaling Factor from the Fit
$\rightarrow pK^+\Lambda(1405)$	0.008692
$\rightarrow pK^+\Sigma(1385)^0$	0.004592
$\rightarrow pK^+\Lambda(1520)$	0.008409
$\rightarrow pK^+\Lambda$	0.032727
$\rightarrow pK^+\Lambda\pi^0$	0.001027
$\rightarrow pK^+\Sigma^0$	0.011388
$\rightarrow pK^+\Sigma^0\pi^0$	0.000744
$\rightarrow pK^+\Sigma^+\pi^-$	0.000276
Ratio $\Sigma(1385)^0/\Lambda(1405)$	0.528288
SB-background (Hades)	1.04982
SB-background (WALL)	0.95000
χ^2	2.12283

The relevant observable for this analysis is the missing mass to the p and K^+ four-vector (MM_{pK^+}), as it contains information about the $\Lambda(1405)$ mass distribution. Figures 3.10 and 3.11 show this observable for the HADES and WALL data-set, respectively. The mass distribution is displayed after the subtraction of the mis-identification background. The figures which include this background contribution are shown in Appendix A. Like the fit observables, these mass distributions can be described well by the incoherent sum of the cocktail. The contributions of the three resonances $\Lambda(1405)$, $\Sigma(1385)^0$ and also the $\Lambda(1520)$, are clearly visible. The yield of the $\Lambda(1405)$ and the $\Sigma(1385)^0$ can not be di-

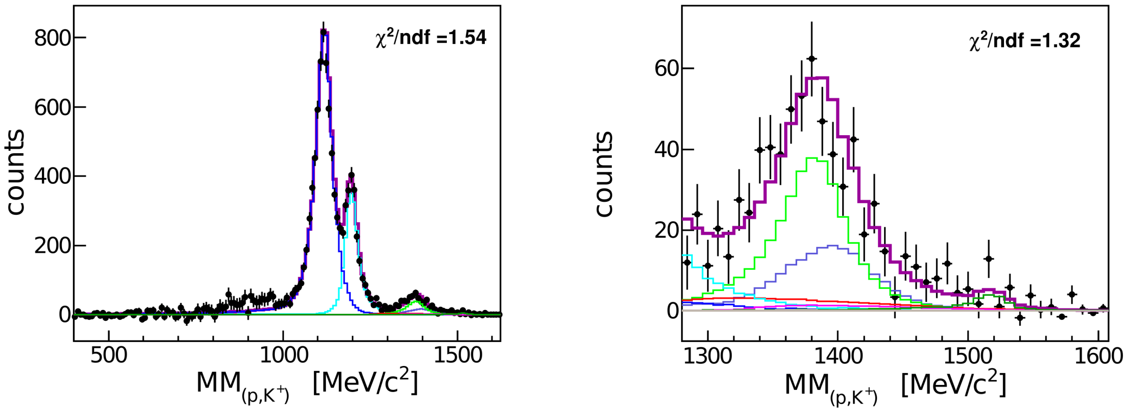

Figure 3.10: Missing mass to the proton and the K^+ for the HADES data set. Left panel shows the statistic for all channels, right panel shows an enlargement of the resonance region.

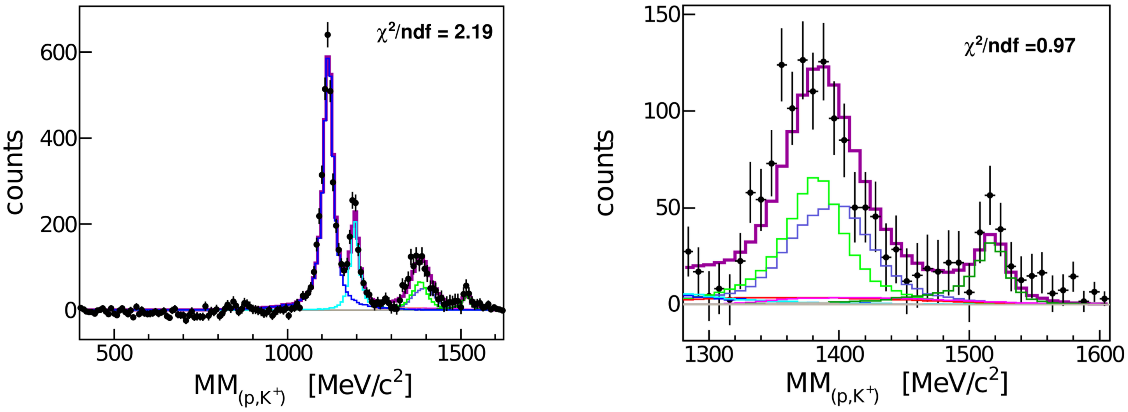

Figure 3.11: Missing mass to the proton and the K^+ for the WALL data set. Left panel shows the statistic for all channels, right panel shows an enlargement of the resonance region.

stinguished without the result of the multi-fit as they overlap. As visible in the Figures, the yield of the $\Lambda(1405)$ is not two times the yield of the $\Sigma(1385)^0$, as the scaling-factors in Table 3.3 might suggest. This is attributed to the different decay-branching ratios of the resonances (87% Σ^* and 33% Λ^*) into a final state with a Λ-hyperon, see Equations (3.1) and (3.5).

The simulated sum of all contributions, shown by the plum-colored histogram, is shifted slightly towards higher masses in respect to the experimental data. This effect is visible for the HADES and the WALL data-set. It can be explained with help of the results from Ref. [23, 173]. In this work, the lineshape from the $\Lambda(1405)$-resonance produced in p+p collisions was determined with a maximum in the mass distribution located at around 1385 MeV/c^2. The same impression is delivered by these figures. The effect is, however, not so strong due to the large contribution from the $\Sigma(1385)^0$ and the fact that these observables are not corrected for acceptance and efficiency.

3.2.3 Disentangling the Resonances

As discussed, the only observable that helps to discriminate $\Sigma(1385)^0$ from $\Lambda(1405)$ production is the missing mass to all measured particles. This observable is presented in Figure 3.12 for both data-sets in linear and logarithmic scale. The simulations of the $\Sigma(1385)^0$ production (see channel No. 2 in Table 3.2) shows a nice signal of the π^0 in both data-sets. Due to the poor momentum resolution of the forward wall the mass spectrum of the WALL data-set is significantly broader as compared to the HADES set. This broadening results in a different π^0 mass resolution. The two π^0 signals from the $\Sigma(1385)^0$ simulation have been fitted with a Normal distribution to extract the mass resolution. The values are μ= 134.7 MeV/c^2 and σ= 28.6 MeV/c^2 for the HADES data and μ= 147.0 MeV/c^2 and σ= 56.3 MeV/c^2 for the WALL data. The shifted value of the π^0 in respect to the nominal value of 135 MeV/c^2 [8] for the WALL data set might hint to a slight mis-calibration of this detector. This calibration error will only be visible in observables that use the secondary proton for a mass distribution. For the line-shapes of the resonances this is not relevant as they are displayed by the missing mass to the primary proton and K^+.

To disentangle the $\Lambda(1405)$ from the $\Sigma(1385)^0$ the data are selected according to their missing mass MM_{p,K^+,p,π^-}. Figure 3.12 shows that the channel with $\Lambda(1405)$ production (violet) has a slightly shifted mass distribution towards higher missing masses as compared to the $\Sigma(1385)^0$ (light-green), however,

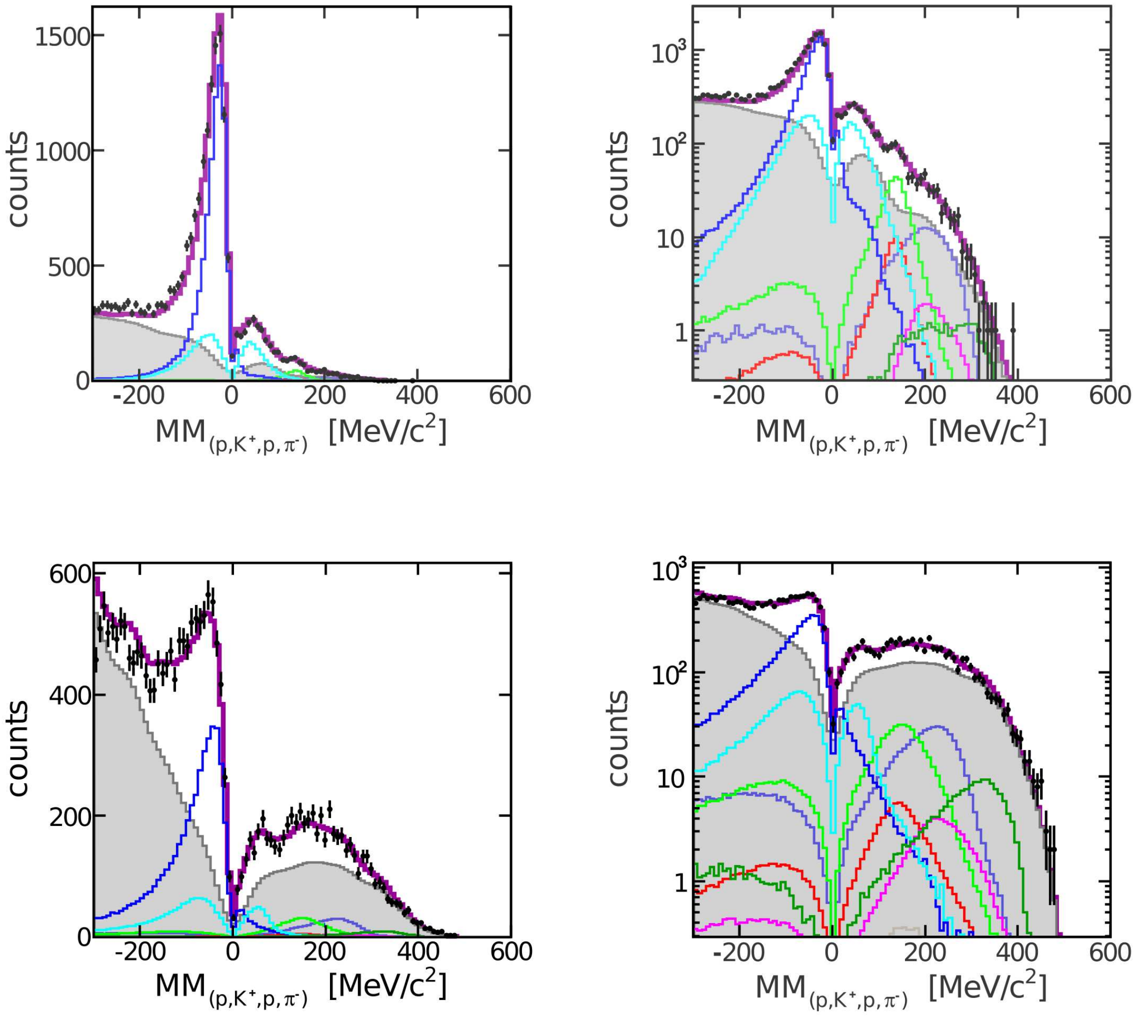

Figure 3.12: Measured mass distribution of MM_{p,K^+,p,π^-} for the HADES data-set (upper panels) and the WALL dataset (lower panels) shown by the black points. Compared to them are the incoherent cocktails of all simulated channels (plum-colored line). The histograms from the channel No. 2 and No. 3 (see Table 3.2) show a signal of the π^0.

these two mass distributions are also overlapping, making a complete disentanglement impossible.

The $\Sigma(1385)^0$-signal from its $\Lambda\pi^0$ decay

To enrich the data with signal from the $\Sigma(1385)^0$-reonance production, events with a missing π^0 have to be selected. Therefore a cut of $70 < MM_{p,K^+,p,\pi^-} < 175$ MeV/c^2 for the HADES events and $65 < MM_{p,K^+,p,\pi^-} < 230$ MeV/c^2 for the WALL events was applied. Figure 3.13 shows the mass distributions of MM_{pK^+} for events that are enriched with $\Sigma(1385)^0$ signal by the previous cuts, for both data-sets. The distributions clearly peak at around 1380 MeV/c^2.

The results are presented for two cases: one, where the missing mass to the proton and the K^+ is calculated from the measured four-vectors of the two particles; and one, where the missing mass is calculated from refitted four-vectors, so that the complete event kinematics of all particles fulfills the constraint that the missing mass to all charged particles is the mass of the π^0; while the invariant mass of the secondary proton and π^- is equal to the mass of the Λ-hyperon. As visible in the figures, this refit has no major effect on the mass resolution of the $\Sigma(1385)^0$.

With help of the simulation cocktail the different contributions to the spectra can be displayed. While the peak of the HADES data-set according to the fit result consists mainly of the contribution from $\Sigma(1385)^0$, the mass spectrum from the WALL data is contaminated by a large amount of signal from the $\Lambda(1405)$.

The reason seems two-fold:
First of all, the acceptance for the events in which a $\Lambda(1405)$-resonance is produced is higher for the WALL data visible by comparing Figure 3.10 with 3.11. This is explained by the fact that heavy resonances leave less production energy to their partners p and K^+ which are thus less likely to fly into the acceptance hole of the spectrometer at $\theta < 15°$ and can be detected. Second, is the MM_{p,K^+,p,π^-} resolution worse in the WALL data-set than in the HADES data set, as previously explained, which causes a generally larger admixture of $\Lambda(1405)$ in the $\Sigma(1385)^0$ mass spectrum for the WALL data.

A quantitative summary of different resonance yields in the mass spectrum and the contamination from the $\Lambda(1405)$-resonance is given in Table 3.4. Although the WALL data-set presents ~400 $\Sigma(1385)^0$ events, their contamination by the $\Lambda(1405)$ is high. As, however, the exact line-shape from the $\Lambda(1405)$ in this decay is not known, this contribution is critical as it can not be subtracted easily.

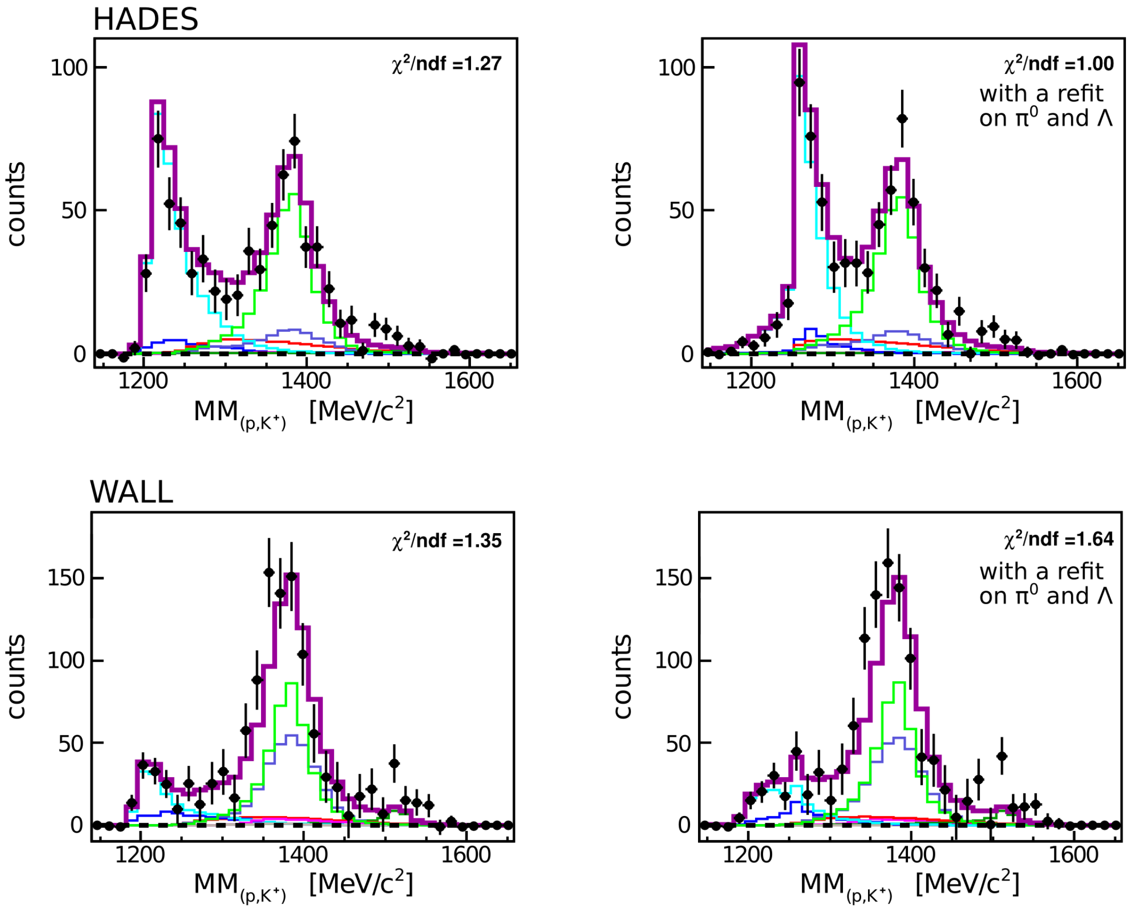

Figure 3.13: The missing mass to the proton and the K^+ (MM_{pK^+}) for refitted and un-refitted events, both selected for a missing π^0 in the eventf. Shown for both data-sets HADES upper panels and WALL lower panels. The sum of all channels (plum-colored) is compared to the experimental data (black dots). The single channels correspond to the colored histograms and are described in Table 3.2.

Table 3.4: Final yield of the $\Sigma(1385)^0$ analysis for both data-sets that is extracted with help of simulations.

Contribution	WALL	HADES
Total yield	1170	720
$\Lambda(1405)$ yield	320	62
$\Sigma(1385)^0$ yield	390	285
R (Λ^*/Σ^*) [%]	82	22

Thus, quantitative information of the $\Sigma(1385)^0$, like mass and width, are difficult to extract. In case of the HADES data-set the contribution of the $\Lambda(1405)$ is lower with 22% but also the statistic of $\Sigma(1385)^0$ with ~300 events.

In the literature, only two reports about $\Sigma(1385)^0$ production in p+p collisions are published: one from Klein et. al [175], and one from the ANKE collaboration [176]. While the signal in Ref. [175] is reconstructed by the invariant mass of its decay products $\Lambda\pi^0$ and is, thus, essentially free from $\Lambda(1405)$ contamination, the signal from Ref. [176] is reconstructed also via the missing mass to the proton and K^+, and faces, therefore, also the same problems as the here presented analysis. The exact strength of cross contamination is, unfortunately, not discussed quantitatively by the authors of [176], so that no comparison of the signal purity can be made. The reported signal strength is 170±26 counts.

The $\Lambda(1405)^0$-signal from its $\Sigma^0\pi^0$ decay

To enrich the events with the $\Lambda(1405)$ resonance signal, two cuts were tested: $MM_{p,K^+,p,\pi^-} > 170$ MeV/c^2 (A) and $MM_{p,K^+,p,\pi^-} > 195$ MeV/c^2 (B). These cuts should select events in which more than a π^0 is missing in the reaction, see Equation 3.1. The resulting mass distributions, after the selection, for both data-sets are presented in Figure 3.14. The large contamination by $\Sigma(1385)^0$ is obvious. Only the HADES data set under cut condition B shows a suppressed contribution of the $\Sigma(1385)^0$. Table 3.5 summarizes quantitative information about the signal contamination and the extracted $\Lambda(1405)$ yield. The relative contamination of $\Sigma(1385)^0$, expressed by the ratio R is high between 11-28%. The only case with a lower contamination of 11% has, at the same time, the lowest reconstructed yield of 90 $\Lambda(1405)$ events.

In order to deliver a good constraint for theoretical calculations of the $\overline{K}N$ interaction sub-threshold, a high statistic $\Lambda(1405)$ mass spectrum is needed which

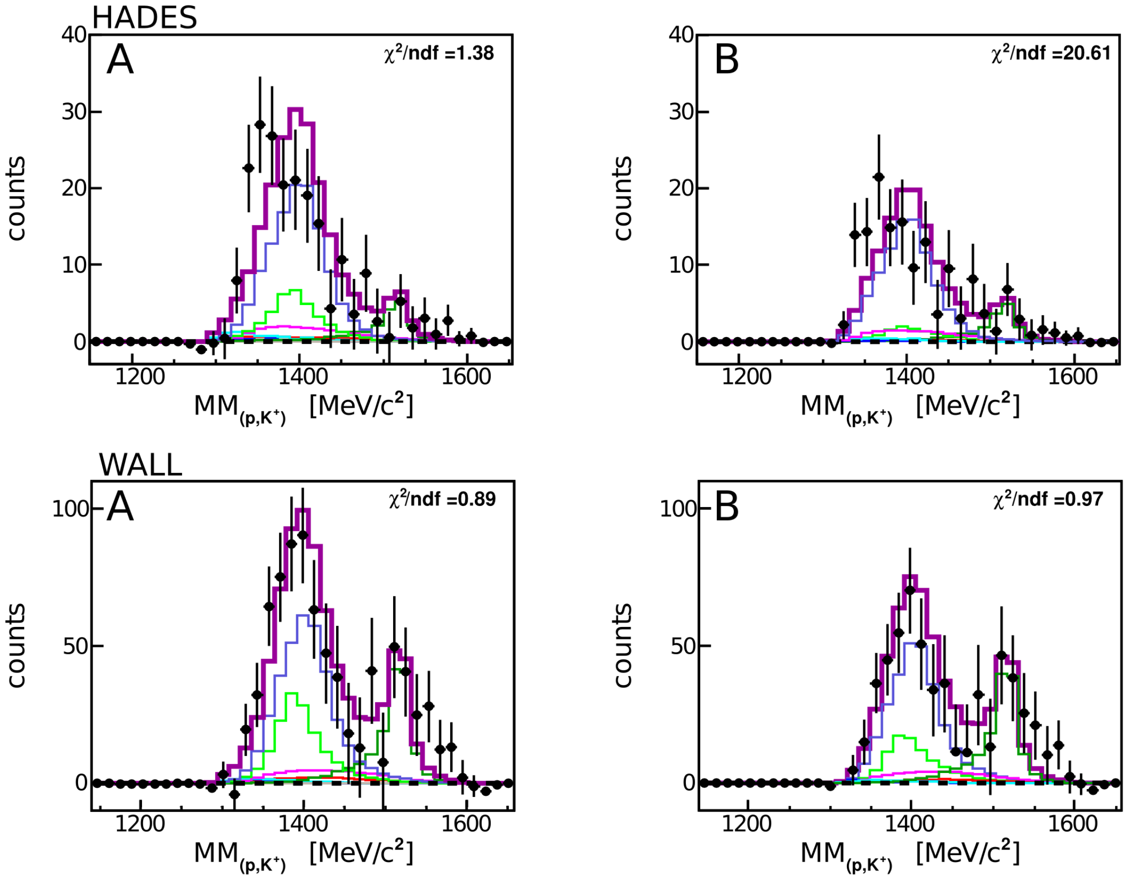

Figure 3.14: The missing mass to the proton and the K^+ (MM_{pK^+}) for the cut conditions A and B, to suppress contamination from the $\Sigma(1385)^0$. In both data-sets HADES upper panels and WALL lower panels. The sum of all channels (plum-colored) is compared to the experimental data (black dots). The single channels correspond to the colored histograms and are described in Table 3.2.

Table 3.5: Final yield of the Λ(1405) analysis for both data-sets that is extracted with help of simulations.

	WALL		HADES	
Contribution	Cut > 170	Cut>195	Cut > 170	Cut>195
Total yield	765	567	205	148
Λ(1405) yield	352	284	121	90
$\Sigma(1385)^0$ yield	155	88	34	10
R (Σ*/Λ*) [%]	44	31	28	11

has, at the same time, a low probability of ambiguous interpretations (eg. pure $\Sigma(1385)^0$ yield). This is not fulfilled by the present analysis. The statistic remains low, if the cut on the missing mass to all charged particles is strict. In case the cut is released, however, the contamination from $\Sigma(1385)^0$ becomes critical.

The only measurement of the Λ(1405)-signal from its decay into $\Sigma^0\pi^0$, so far, stems from the ANKE collaboration [176] and is not corrected for the losses caused by limited acceptance and efficiency. They reported a Λ(1405)-signal with a statistic of 156±23 reconstructed events. This statistic is in the same order as extracted by the here presented analysis, however, the ANKE-signal is quoted to be free from $\Sigma(1385)^0$ contamination due to the good separation quality. The ANKE collaboration showed with simulation [176] that essentially no events of the $\Sigma(1385)^0$ production contaminate the mass area of $MM_{p,K^+,p,\pi^-} > m_{\pi^0}$+55MeV/c^2. This must originate from a π^0-signal with a resolution of $\sigma \sim 18$ MeV/c^2 in their spectrometer. This exceeds the precision obtained with the HADES detector (28.6 MeV/c^2 and 56.3 MeV/c^2).

3.2.4 The Systematic Uncertainty

To test the influence of different event selections on the fit result, the fit has been repeated under different cut selections, fit constraints, and simulation properties. In order to test different selection cuts, the following track and mass cuts have been varied by ±10% and ±20%, respectively: distance between the decay proton and pion from the Λ (d_t), distance of closest approach between the Λ-track and the primary vertex (d_Λ) and the mass window of the Λ mass cut ($\mathrm{IM}_{p\pi^-}$). These are the cuts applied to the HADES data-sample. Further, the mass window of the Λ mass cut in the WALL data selection was varied. In this procedure, the cuts have been varied for simulated and measured data simultaneously. The changes of the different cuts were permuted either among the ±10% or the ±20% group, including in both cases also the nominal cut values, which resulted in 161 different event selections.

To test different fit constraints, the range in which the yield of the mis-identification background could be varied was changed. The nominal contribution of the mis-identification background to the experimental data is already well constrained by the procedure that models the mis-identification background (Section 3.1.3). Still, the yield was given a tolerance of ±5% so that the final strength of this contribution to the total experimental yield was determined by the fit. In two variations the mis-identification yield was constrained either to a tolerance of ±4% or ±6%, respectively. Each of the three tolerances was combined with the 161 different statistics from the cut variations.

To test different simulation properties, two of the eight simulated channels have been modified. In Ref. [23, 177] an angular distribution for the production $p+p \rightarrow n+K^{+}+\Sigma(1385)^{+}$ was extracted from the data. In view of this result also the channel $p+p \rightarrow p+K^{+}+\Sigma(1385)^{0}$ might contain a non-isotropic angular distribution of the $\Sigma(1385)^{0}$ in the p+p CMS system. Thus, the whole fitting procedure was repeated for two versions in the simulation: once with a flat differential cross section for the $\Sigma(1385)^{0}$ production and once with the same distribution, as measured for the $\Sigma(1385)^{+}$. In Ref. [23, 173] the mass peak of the $\Lambda(1405)$-resonance was determined to be rather low at 1385MeV/c^2 instead of 1405 MeV/c^2. To test the influence of this result on the fit procedure the simulations of the reaction $p+p \rightarrow p+K^{+}+\Lambda(1405)$ were included once with a $\Lambda(1405)$-mass of 1405 MeV/c^2 and once with a mass of 1385 MeV/c^2. All four variations were combined with the previously discussed selections, and fit constrains, resulting in 1932 different versions of the fitting procedure.

The different variations are summarized in Table 3.6. This variation in the fit results in diverging scaling-factors for the different contributing channels, which are illustrated in Figures 3.15 - 3.18. As a direct connection between the scaling-factors from the fit and the production cross section exists (Eq. 3.11) the scatter of the scaling-factors gives an estimate of the systematic uncertainty of the production cross section for the included channels.

The figures show that while the channels of direct Λ- and Σ^0-hyperon production are well determined by the fit (Figure 3.15), the other channels suffer from a large systematic uncertainty. This is obvious as the former channels are well separated from the others in the MM_{pK^+} spectra. The production of the $\Sigma(1385)^{0}$-resonance is better constrained than the production of the $\Lambda(1405)$-resonance and the $\Lambda(1520)$-resonance, which both have no lower limits of their

Table 3.6: The variation of different cuts and fit constraints to evaluate the systematic uncertainty of the multi-fit procedure.

Constraint	Nominal	Variation A	Variation B
d_Λ (HADES)	<23	±10%	±20%
d_t (HADES)	<18	±10%	±20%
$M_{p\pi^-}$ (HADES)	1106–1122	±10%	±20%
$M_{p\pi^-}$ (WALL)	1001–1129	±10%	±20%
	↑ Total: 161 cut variations ↑		
$M(\Lambda(1405))$	1405 MeV/c^2		1385 MeV/c^2
$d\sigma/dcos(\theta)_{\Sigma^*}$	Flat		$\hat{=}$ $\Sigma(1385)^+$ [177]
Mis-ident. background	tolerance ±5%	tolerance ±6%	tolerance ±4%

contribution. The channels: $pK^+\Sigma^0\pi^0$ and $pK^+\Sigma^+\pi^-$ are also not well constrained by the fit as they have a broad mass distribution in the missing mass to all particles and the missing mass to the proton and the K^+. The production of $pK^+\Lambda\pi^0$ is better constrained. It is the non-resonant component of the $\Sigma(1385)^0$ production and, as the cross section of the latter is rather well constrained, the variation for this channel is also limited. The mean value and the range of outcome values of the fit are summarized in Table 3.7 and create the range for the systematic uncertainty of the fit result.

Table 3.7: Result of the systematic error evaluation. Each channel has a spread of output cross sections that is represented by a mean and a range of observed values.

Channel $p + p \rightarrow$	Mean [μb]	Range [μb]
$pK^+\Lambda$	36.25	35.6–36.8
$pK^+\Sigma^0$	12.66	12.3–12.9
$pK^+\Lambda(1405)$	7.01	0–14
$pK^+\Sigma(1385)^0$	5.9	4.4-7.8
$pK^+\Lambda(1520)$	4.65	0–11
$pK^+\Sigma^+\pi^-$ (non-res.)	2.64	0–10
$pK^+\Lambda\pi^0$ (non-res.)	1.42	0–3.5
$pK^+\Sigma^0\pi^0$ (non-res.)	3.59	0–7.8

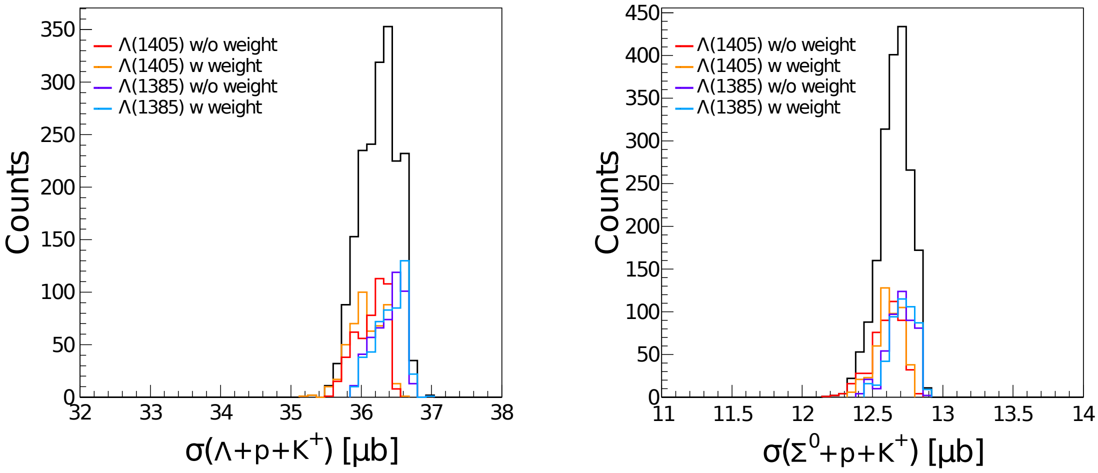

Figure 3.15: Extracted cross sections of 1932 different fit trials. Left: Cross section for $pK^+\Lambda$ production and right: for $pK^+\Sigma^0$ production.

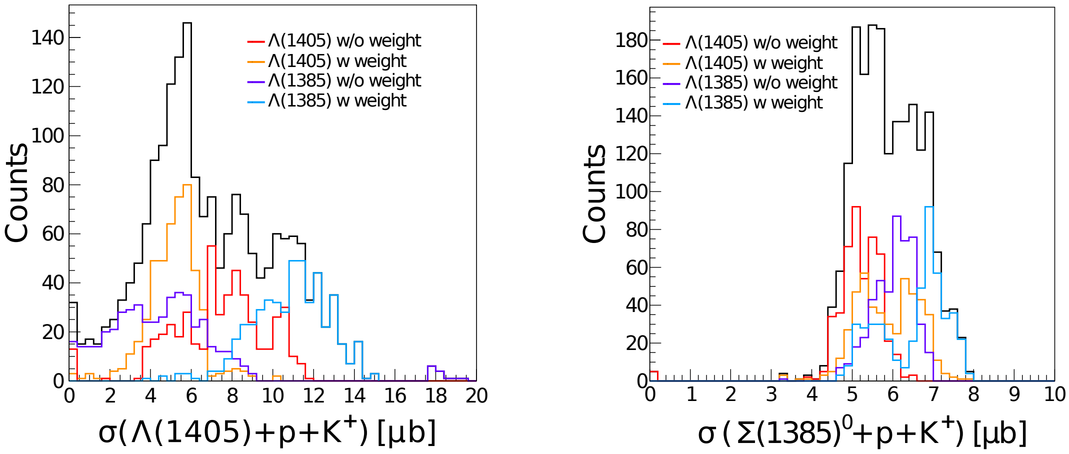

Figure 3.16: Extracted cross sections of 1932 different fit trials. Left: Cross section for $pK^+\Lambda(1405)$ production and right: for $pK^+\Sigma(1385)^0$ production.

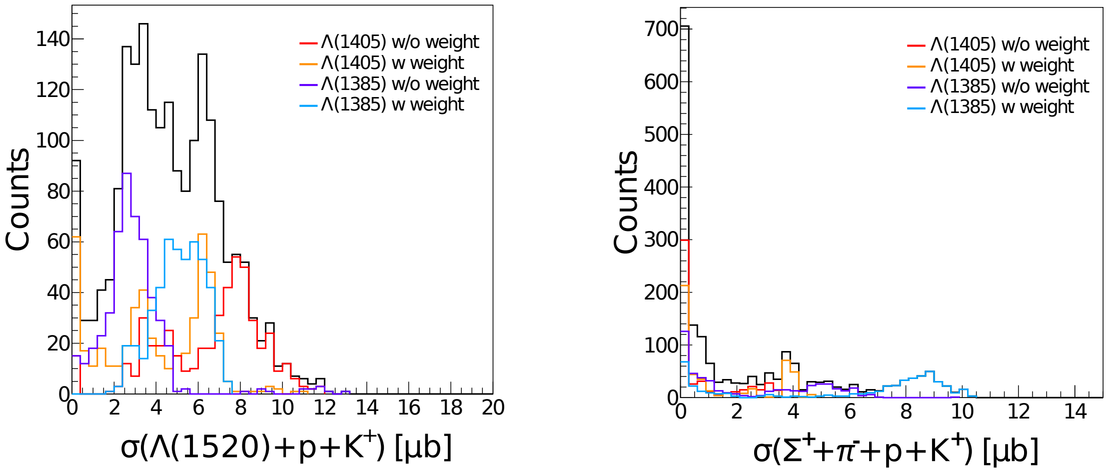

Figure 3.17: Extracted cross sections of 1932 different fit trials. Left: Cross section for $pK^+\Lambda(1520)$ production and right: for $pK^+\Sigma^+\pi^-$ production.

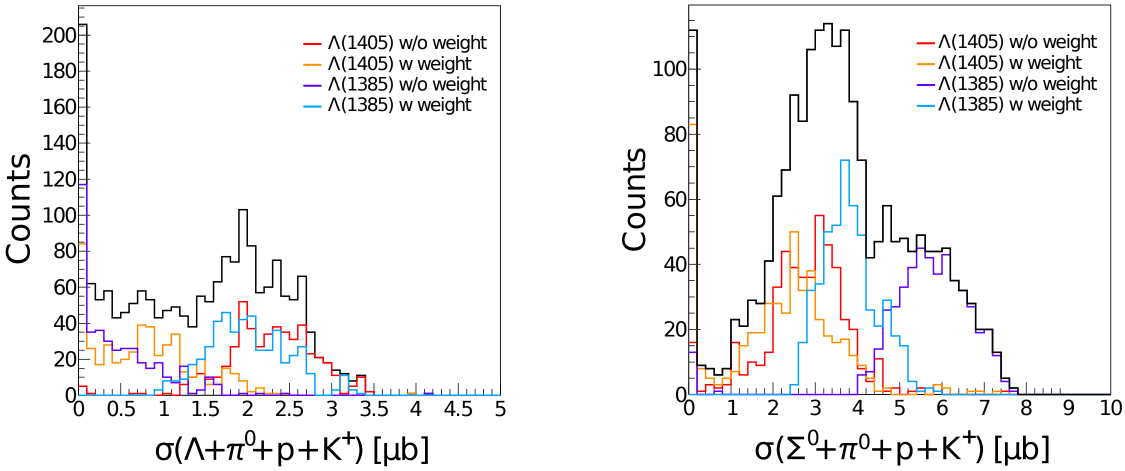

Figure 3.18: Extracted cross sections of 1932 different fit trials. Left: Cross section for $pK^+\Lambda\pi^0$ production and right: for $pK^+\Sigma^0\pi0$ production.

3.3 Production Cross Sections

The scaling factors from the fit-procedure are directly linked to the production cross section, which has already been exploited to create the Figures 3.15–3.18 and also the values in Table 3.7. This connection is derived as follows. The yield of a measured contribution from a certain channel can be modeled with simulation. To do so, the yield of the simulated channel (after the full scale simulation process) is scaled with the scaling-factor from the fit to match the measured distribution:

$$Y_{Exp,acc} = Y_{Sim,acc} \cdot SF, \tag{3.10}$$

with $Y_{Exp,acc}$ the experimental yield in the detector acceptance that is attributed to a certain channel, $Y_{Sim,acc}$ the simulated yield from the event generator in the detector acceptance, and SF the scaling factor that is applied to the simulated yield to reproduce the experimental data. To obtain an experimental yield in 4π and an according production cross section, the reconstructed event yield for each channel needs to be corrected for losses due to incomplete acceptance and efficiency. The correction is estimated with help of simulations. Therefore, the ratio of events in 4π and in the detector acceptance is build.

$$Y_{Exp,4\pi} = Y_{Exp,acc} \cdot \frac{Y_{Sim,4\pi}}{Y_{Sim,acc}} = Y_{Sim,acc} \cdot SF \cdot \frac{Y_{Sim,4\pi}}{Y_{Sim,acc}} = Y_{Sim,4\pi} \cdot SF. \tag{3.11}$$

$Y_{Sim,4\pi}$ is the number of initially simulated events per channel, which is $1{\cdot}10^8$ events for all of them. This relation is elegant as it connects the scaling-factor directly to the production yield of the respective channel.

Finally, the production yield is related to a cross section by a normalization of the measured p+p elastic scattering yield to the elastic cross section in the detector acceptance, described more exhaustive in Section 6.2.1. In short summary of this procedure: the measured events are normalized to a production cross section by scaling them by NF=$1.11{\cdot}10^{-8}$ mb:

$$\sigma_{Exp,4\pi} = Y_{Sim,4\pi} \cdot SF \cdot NF \; mb. \tag{3.12}$$

The statistical error of the experimental cross section in one channel can be written as:

$$\Delta\sigma_{Exp,4\pi} = \frac{Y_{Sim,4\pi} \cdot SF \cdot NF}{\sqrt{Y_{Sim,acc}}} \; mb \tag{3.13}$$

If the different yields are evaluated from their contributions in Figures 3.10 and 3.11 the statistical errors are the ones summarized in Table 3.8. The error

Table 3.8: Example of cross section for different conditions in the fitting procedure with their according statistical. (A) M_{Λ^*} = 1405, no Σ^* angular distr; (B) $M_{\Lambda^*} = 1405$, Σ^* angular distr; (C) $M_{\Lambda^*} = 1385$, no Σ^* angular distr; (D) $M_{\Lambda^*} = 1385$, Σ^* angular distr.

Channel $p+p\rightarrow$	σ_A [μb]	σ_B [μb]	σ_C [μb]	σ_D [μb]
$pK^+\Lambda(1405)$	9.65±0.55	6.13±0.44	5.75±0.69	11.54±0.85
$pK^+\Sigma(1385)^0$	5.10±0.24	6.34±0.33	6.14±0.27	6.81±0.46
$pK^+\Lambda(1520)$	9.33±1.26	6.64±1.07	4.40±0.87	6.62±1.52
$pK^+\Lambda$	36.33±0.51	36.30±0.51	36.59±0.51	36.60±0.42
$pK^+\Lambda\pi^0$	1.14±0.13	2.26±0.18	0.25±0.06	1.80±0.17
$pK^+\Sigma^0$	12.64±0.32	12.66±0.32	12.74±0.32	12.75±0.26
$pK^+\Sigma^0\pi^0$	0.83±0.13	2.36±0.13	5.62±0.35	3.66±0.35
$pK^+\Sigma^+\pi^-$	0.31±0.17	0.017±0.105	5.29±0.67	8.96±1.14
χ^2	2.12	2.23	2.33	2.27

is an average of the error obtained from the two figures. For each channel four examples out of the ~2000 variations are shown in the table. σ_A and σ_B show results obtained while fitting simulations with a Λ(1405) mass of M=1405 MeV/c^2 and σ_C and σ_D contain a Λ(1405) signal of M=1385 MeV/c^2. Further do σ_B and σ_D contain the modification of the differential cross section of the $\Sigma(1385)^0$ production in the center of mass frame. As expected, the relative error is increasing with a decreasing amount of yield (cross section) to evaluate the contribution.

The results from the here presented analysis can be compared to an independent analysis of the Λ(1405) production in the same recorded statistic but analyzed through its decay into the charged final stated $\Sigma^\pm\pi^\mp$. This analysis is independent as it is only connected to this analysis via the inclusion of the $\Sigma(1385)^0$ production cross section which is an external constraint. Due to the fact that the branching ratio of the $\Sigma(1385)^0$ into the analyzed final state $\Sigma^\pm\pi^\mp$ is low (8.6%) as compared to the Λ(1405) (49.4%), a large systematic uncertainty has, fortunately, no major effects on the yield of the $\Sigma(1385)^0$ under the Λ(1405) signal, so that this outcome is solid.

Table 3.9 compares the results of this analysis with the independent analysis from Ref. [23]. The values are shown with their statistical-, and systematic error. All cross sections have the same common error of 7% from the cross section normalization procedure. The results of this analysis are presented for σ_A and σ_D, see Table 3.8 for properties. While the fit giving the results σ_A is

Table 3.9: Comparison of the extracted cross sections of this analysis with the cross sections of the analysis from the charged decay channels of the $\Lambda(1405)$. $^\heartsuit$ shows results from this work. The values are quoted with their statistical-, and systematic error and contain the same common error of 7% from the cross section normalization procedure, not explicitly quoted.

Channel $p+p\rightarrow$	σ [μb] [23, 173]	σ_A [μb]$^\heartsuit$	σ_D [μb]$^\heartsuit$
$pK^+\Lambda(1405)$	$9.2\pm0.9^{+3.3}_{-1.0}$	$9.65\pm0.55^{+4.35}_{-9.65}$	$11.54\pm0.85^{+2.46}_{-11.54}$
$pK^+\Sigma(1385)^0$	-	$5.10\pm0.24^{+2.7}_{-0.7}$	$6.81\pm0.46^{+0.99}_{-2.41}$
$pK^+\Lambda(1520)$	$5.6\pm1.1^{+1.1}_{-1.6}$	$9.33\pm1.26^{+1.67}_{-9.33}$	$6.62\pm1.52^{+4.38}_{-6.62}$
$pK^+\Sigma^+\pi^-$ (non res.)	$5.4\pm0.5^{+1.0}_{-2.1}$	$0.31\pm0.17^{+9.69}_{-0.31}$	$8.96\pm1.14^{+1.04}_{-8.96}$
$K^+\Sigma^-\Delta(1232)^{++}$	$7.7\pm0.9^{+0.3}_{-0.9}$	-	-
$pK^+\Lambda$	-	$36.33\pm0.51^{+0.47}_{-0.73}$	$36.60\pm0.42^{+0.2}_{-1}$
$pK^+\Lambda\pi^0$ (non res.)	-	$1.14\pm0.13^{+2.36}_{-1.14}$	$1.80\pm0.17^{+1.7}_{-1.80}$
$pK^+\Sigma^0$	-	$12.64\pm0.32^{+0.26}_{-0.34}$	$12.75\pm0.26^{+0.15}_{-0.45}$
$pK^+\Sigma^0\pi^0$ (non res.)	-	$0.83\pm0.13^{+6.97}_{-0.83}$	$3.66\pm0.35^{+4.14}_{-3.66}$

completely independent of the work presented in Refs. [23, 173, 177], the fit resulting in σ_D includes their result, such as the shifted $\Lambda(1405)$ mass and the non-isotropic differential cross section for the $\Sigma(1385)^0$ production in the CMS system. The results are in agreement with each other except the value for the $pK^+\Sigma^+\pi^-$ (non res.) production, which seems way too low for σ_A. Due to the large systematic uncertainty this value is still compatible with the result from Ref. [23, 173].

A second iteration of the multi-fit with the external cross section constraints from Ref. [23, 173] might stabilize the fit and decrease the systematic uncertainty. However is no further use expected of this procedure as no independent result will be obtained from it and the $\Lambda(1405)$-resonance mass spectra are too low in statistic so that even a good handle on the $\Lambda(1405)$ production cross section is of no further use for the $\Sigma^0\pi^0$ decay channel investigation.

4 | Exclusive Event Selection and Model Description

In this chapter, the analysis of the reaction:

$$p + p \rightarrow p + K^{+} + \Lambda, \quad \Lambda \rightarrow p + \pi^{-}, \tag{4.1}$$

is discussed with the motivation to study the possible existence of the smallest of the anti-kaonic nuclear bound states, the $\overline{K}NN$. While the data selection is discussed in this chapter, their interpretation will be presented in Chapter 5 with the aim to extract tighter constraints for the expected cross section of the kaonic cluster production in p+p collisions.

4.1 Selection of the p+K^{+}+Λ Sample

A data sample containing $1.2 \cdot 10^{9}$ events of the type p+p → X, that had been measured by the HADES apparatus [142], was analyzed to find events with the exclusive production of the three particles $X = p + K^{+} + \Lambda$. This reaction is of particular interest as it must contain information about an intermediate $\overline{K}NN$ of positive charge (see Section 2.4), should the latter exist. Its production would look like follows: p+p $\rightarrow \overline{K}NN + K^{+} \rightarrow p + \Lambda + K^{+}$. Here, the kaonic bound state ($\overline{K}NN$) is produced together with a K^{+}. When only the K^{+} is measured, one can obtain all necessary information about the bound state by employing the missing mass technique. Hereby, one relies on the knowledge of the four-momenta of the two initial protons and performs the following calculation:

$$P_{\bar{K}NN} = P_{Beam-p} + P_{Target-p} - P_{K^{+}}, \tag{4.2}$$

where P_{x} are the four-momenta of the initial and final particles. The absolute value of the four-vector $|P_{\bar{K}NN}|$ corresponds to the mass of the kaonic cluster

$M_{\overline{K}NN}$. In this way, one could obtain the mass distribution of the kaonic bound state. Although an inclusive measurement of the K^+ is sufficient to reconstruct the properties of the kaonic bound state, it is not sufficient to select the Reaction (2.9) exclusively. Using this approach, one would get the sum of several reactions containing a K^+ [145], e.g $p\pi^0\Lambda K^+$.

Keeping in mind the expected minor contribution of Reaction (2.9) to the total production cross section of K^+ ($\hat{=}$ 0.1 mb, see Fig. 6.16 of Chapter 6), it is essential to select also the decay products of the $\overline{K}NN$, in order to suppress possible sources of background. Therefore, the decay of the $\overline{K}NN$ into $p+\Lambda$ is tagged as well in this analysis, in order to select Reaction (4.1) exclusively.

A novelty in the p+p campaign in April 2007 was the installation of a new detector, the so called Forward Wall hodoscope (FW or WALL). From this detector a time of flight information of the particles, flying into the very forward direction (0.33° to 7.17°), can be retrieved. As the data analysis showed that a large fraction of decay protons from the Λ were emitted in the forward acceptance hole of the HADES spectrometer [145], it was decided to use also the data taken by the Forward Wall for a further analysis. The information from this detector is, however, not sufficient to determine the particles PID so that an event hypothesis has to be applied to reconstruct the complete four-vector of the particle. Previously, it was checked with simulations that the cases in which the detected particle in the WALL is a proton amounts to roughly 89% [145]. Figure 4.1 summarizes the differences between the two data sets.

4.1.1 Event Selection

HADES Data-set

At first, those data were selected in which four tracks are reconstructed inside of the HADES detector (three of positive and one of negative charge). The track-bending of the particles inside of the magnetic field of the detector determines the momentum components of the four-vectors. To obtain the full four-vector of the particle, their masses have to be determined as well. The two protons and the pion were selected, as described for the $\Lambda(1405)$ and $\Sigma(1385)^0$ analysis in Chapter 3, according to their energy loss in the MDC chambers. The fourth particle, which should be the kaon, was preliminary taken as a third positive particle with no further constraints on its energy loss. By this approach a mass was assigned to each track.

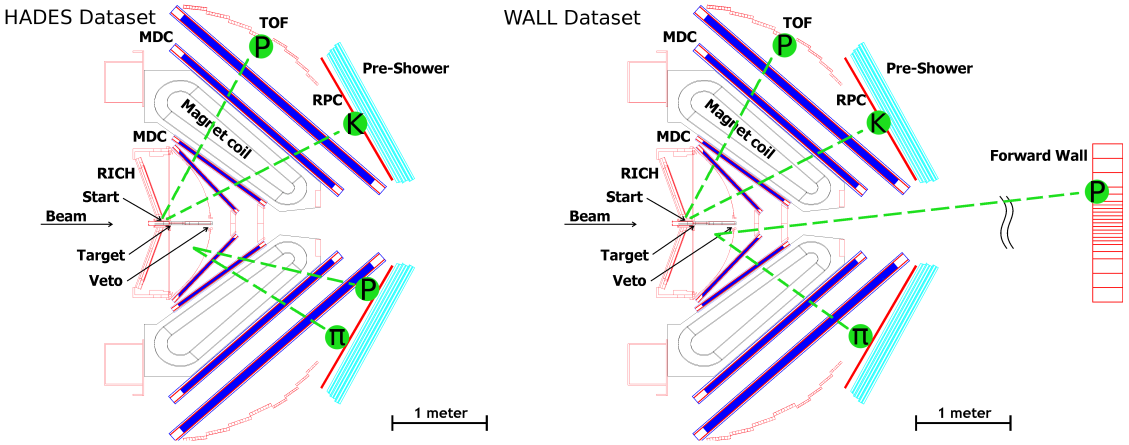

Figure 4.1: The two pictures show the differences between the two data-sets. The four tracks of each event have been registered in different detector parts.

WALL Data-set

The selection in the WALL data-set is similar to the HADES selection. As one particle was "missing" in the HADES detector the events were selected for three detected particles inside HADES and one additional hit in the forward wall, illustrated in Figure 4.1 on the right. While the hit in the FW was assumed to be a proton the other three particles in HADES were still identified via PID cuts. The four-vector of the proton in the forward wall was determined by the assumption of a straight track from the primary vertex to the hit position in the WALL. The absolute momentum was determined from the measured time-of-flight of the particle and the track length.

4.1.2 Constraints for the Data Selection

To select those data out of the statistic with four pre-selected particles, which contain exclusively reaction (4.1), one can use very basic physical constraints like momentum and energy conservation:

$$p_{p_1,x} + p_{p_2,x} + p_{\pi^-,x} + p_{K^+,x} = 0, \tag{4.3}$$

$$p_{p_1,y} + p_{p_2,y} + p_{\pi^-,y} + p_{K^+,y} = 0, \tag{4.4}$$

$$p_{p_1,z} + p_{p_2,z} + p_{\pi^-,z} + p_{K^+,z} = p_{z,Beam-p}, \tag{4.5}$$

$$E_{p_1} + E_{p_2} + E_{\pi^-} + E_{K^+} = E_{CM}. \tag{4.6}$$

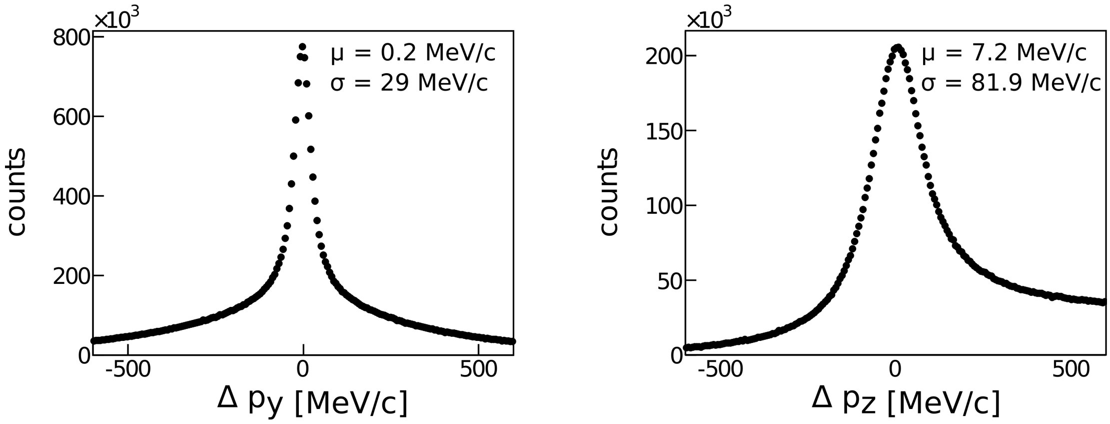

Figure 4.2: Δp_y and Δp_z for events that contain the four required particles in the HADES data-set, where $\Delta p_i = p_{fin} - p_{in}$.

Moreover, one of the protons and the π^- should stem from the decay of the Λ-hyperon. Thus, their four-momenta should be correlated, and the mass of the summed four-vectors is, in this case, distributed around the mass of the Λ-hyperon (1115.683 MeV/c^2). The resolution of the reconstructed Λ's is illustrated in Figure 3.2 of Chapter 3. As this is an exclusive event selection, the missing mass of the other proton and the K^+ should also correspond to the mass of the Λ-hyperon. This can be expressed as follows:

$$(P_{\pi^-} + P_{p_2})^2 = (M_\Lambda)^2, \tag{4.7}$$

$$(P_{Beam-p} + P_{Target-p} - P_{K^+} - P_{p_1})^2 = (M_\Lambda)^2. \tag{4.8}$$

These six observables (Eqs.(4.3)-(4.8)) can be displayed for the complete number of events containing the pre-selected particles. An example of the event distribution is illustrated in Figure 4.2, where Δp_y and Δp_z are shown for the HADES data-set[1]. One sees the enhanced yield around $\Delta p = 0$ MeV/c on the top of a broad background.

4.1.3 A Kinematic Fit as Filter for p+K$^+$+Λ Events

The, in the following, discussed selection concerns the HADES data-set. In case the analysis differs between the two sets discrepancies will be pointed out.

With the mentioned constraints of Eqs. (4.3)-(4.8), there are two options for data selection. One is to use hard cuts. Accordingly one takes only those

---

[1] The observables are constructed from the difference of initial and final vectors.

events for a further analysis that lie in a predefined window. For example, Figure 4.2 suggests to include only events where the missing momentum in $|p_y|$ is <90 MeV/c into the further analysis. This can be successively done for all observables that are sensitive to distinguish reaction (4.1) from background. This method is simple and straightforward. Yet, one does not take into account the correlation of observables among each other and so the cuts may not be optimally tuned. In order to do so one would have to define cuts on one observable as a function of some others. An example is the momentum dependent resolution. Higher momenta are measured with a higher absolute error. Many kinematic observables are dependent on the measured momenta. Therefore, the definition of hard cuts on a narrow kinematic-derived distribution like in Figure 4.2 would imply, that events containing larger momenta are systematically sorted out due to them being further smeared out in the distribution. Another disadvantage is that the background contribution in such analyses would be larger than necessary.

An alternative option for particle selection, in this specific case, is the kinematic fit [178, 179]. This fit uses the physical constraints of Eqs. (4.3) - (4.7) in spherical coordinates together with the known errors of the measurement in 1/p, θ, and φ, caused by the detector. The fit tests for each event how much the reconstructed four-momenta of the four particles have to be varied, based on their error, to fulfill the required physical constrains. The further the initial values have to be shifted in order to fulfill the constraints, the more unlikely it is that the event naturally fulfills these constraints. This is, for example, the case for events where originally more than four particles are produced or events which do not contain an intermediate Λ-hyperon (see Table 3.2 in Chapter 3 for possible sources of background).

A quantification of how well the data fit to the hypothesis of Reaction (4.1) is the p-value[2]. This is an output of the kinematic fit algorithm and is defined as:

$$p-value = \int_{\chi^2_{event}}^{\infty} P(\chi^2, Ndf) d\chi^2. \tag{4.9}$$

χ^2_{event} is the χ^2-value of the fitted event and $P(\chi^2, Ndf)$ the χ^2 probability density function for the given number of degrees of freedom (Ndf) of the fit. The p-value is a good variable to separate signal from background events and takes values between zero and one. While signal events show a flat p-value distribution between 0 and 1, background events have a prominent yield of p-values close to 0 and a sharply falling distribution for higher p-values. Figure 4.3 shows

---

[2] An exhaustive description of this observable is given in Chapter 5.

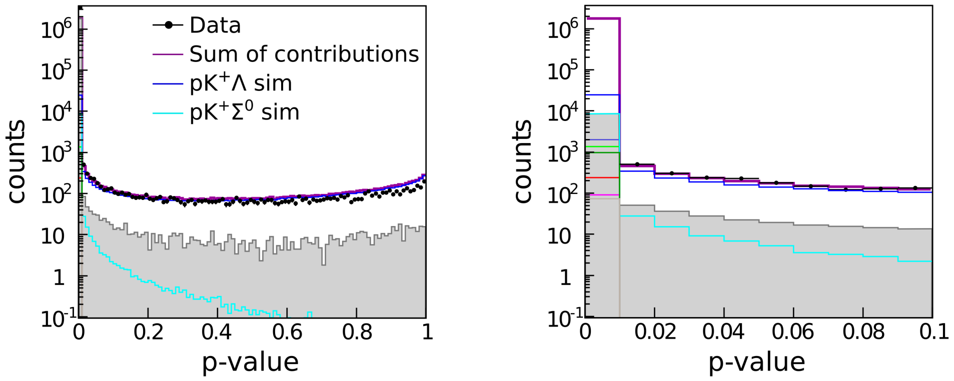

Figure 4.3: p-value distribution of a kinematic fit to the pre-selected data. A kinematic according to Equations (4.3) - (4.8) was required. The right panel presents a zoom into small p-values. Here all channels besides (4.1) and (4.10) are only located in the first bin of the histogram (for channel description see Table 3.2 in Chapter 3).

the p-value distribution for events that contain the four pre-selected particles. In the logarithmic representation the data show a relatively flat distribution with a eminent peak at very low p-values. The sum of simulated channels and the mis-identification background describes the measured data well[3]. These contributions are the same as for the $\Lambda(1405)$ and $\Sigma(1385)^0$ analysis as introduced in Chapter 3.

The right panel of Figure 4.3 displays a zoom into the low p-value region. Here, it is evident that all channels with more than four particles have a p-value within the first bin of the histogram. Only the simulations of reaction:

$$p + p \rightarrow p + K^+ + \Sigma^0, \tag{4.10}$$

have larger p-values, outside the first bin. This is attributed to the very similar kinematics in both reactions of (4.1) and (4.10) as the latter contains only one additional, γ-particle (from the Σ-decay) as compared to the former. This makes these two reactions hard to distinguish. The ratio between channel (4.10) and (4.1) is, fortunately, decreasing rapidly for increasing p-values. The other main background, stemming from the mis-identification of kaons, is also centered at low p-values.

---

[3] The scaling factors for the different simulations are taken from Table 3.3 in Chapter 3.

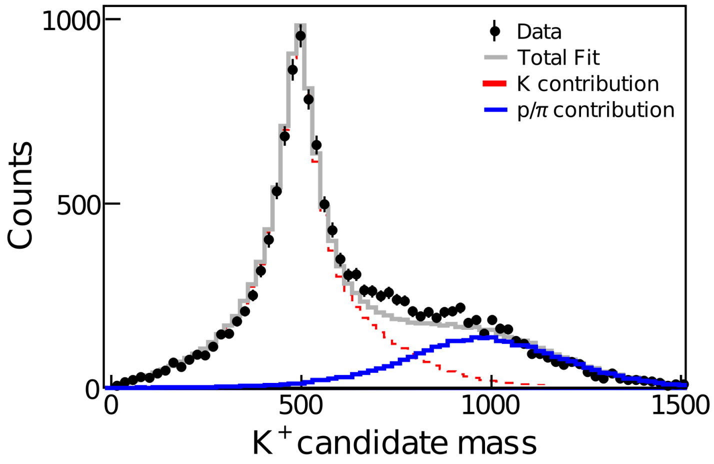

Figure 4.4: Mass distribution of the kaon candidate in the selected HADES statistic. Data points are black. Simulations of events that contain real kaons (red) are shown together with events where the kaon was in fact a pion or proton (blue). The sum of the scaled simulations is shown in gray.

To obtain a good compromise between efficiency (keeping many events) and purity (rejecting background events), the data selection was constrained to events with p-values>0.01. After this selection the contamination from events of type (4.10) in the $pK^+\Lambda$ data sample was estimated to about 1% in the HADES data-set, using the simulations illustrated in Figure 4.3. For the WALL the contamination of the previous reaction amounts to roughly 3%.

The second large background arises from the mis-identification of pions and protons as kaons. This property should be visible in the reconstructed mass distribution of the kaon candidates. The mass distribution is calculated with help of the measured time-of-flight. This quantity was, however, not directly accessible in the experiment and had to be reconstructed afterwards. Appendix B contains a detailed description of the possibilities for a time-of-flight reconstruction procedure.

Figure 4.4 shows the reconstructed mass distribution of the kaon candidates. The mass was reconstructed using method No. 1, described in Appendix B. Together with the measured data, simulations are shown in which the events were separated according to the real PID of the kaon candidate. The red histogram displays events where the kaon candidate was indeed a kaon and the blue histogram reveals events where the kaon was in fact a proton. This is visible by the enhanced yield in the mass spectrum around $m_p \approx 938\ MeV/c^2$. Events in which a pion was mis-identified as kaon are possible but apparently suppressed by the data selection, as no enhancement of yield is observed at the nominal pion mass of $m_{\pi^+} \approx 140\ MeV/c^2$. The yield that is attributed to the mis-identification of kaons as pions and protons is denoted as mis-identification background. The measured mass distribution, displayed in Figure 4.4, was fitted with the sum of the individual contributions from simulations. The sum of these contributions, displayed in gray, describes the measured data well. The total signal-to-background ratio (S/B) in the full range amounts to ≈ 2.9. This value can be improved by the selection of a mass region with an increased S/B ratio. Based on the scaled simulations this range was determined to $0 < m_{K^+-candidate} < 680\ MeV/c^2$ (230-640 MeV/c^2 for the WALL data-set). By restricting the data to this mass range, events with a mis-identified proton can be suppressed effectively. The S/B ratio in this mass region is 19.4. Additionally to those events where the time-of-flight could be reconstructed, there is a fraction of events where the kaon candidate had no hit in the detector system that measured the stop signal for the time-of-flight. Thus, the mass of the particle could not be reconstructed. In these cases there is no further criteria to separate good from bad events. With help of the simulations, the S/B ratio for these events can be estimated to 6.2. Although this value is worse than the S/B ratio in the selected mass range, this sample is kept since the data themselves amount to roughly 20% of the statistic inside the mass window. This inclusion decreased the total S/B value to 15.3 (for a detailed report about the WALL statistic see Appendix B).

The final result of these event selections is described in the next paragraphs.

Summary of HADES Analysis

A $pK^+\Lambda$ data sample of 13,155 events could be extracted from the complete p+p→ X statistic. The contamination of Reaction (4.10) is 1%, and the contamination from mis-identification background is 6.5%.

Summary of the WALL Analysis

From the WALL statistic 9,000 $pK^+\Lambda$ events could be retrieved from the complete p+p→ X statistic. The contamination of reaction (4.10) is 3%, while the contamination from mis-identification background is 11.7% and with this double as high as in the HADES statistic.

4.2 Characteristics of p+K$^+$+Λ Production

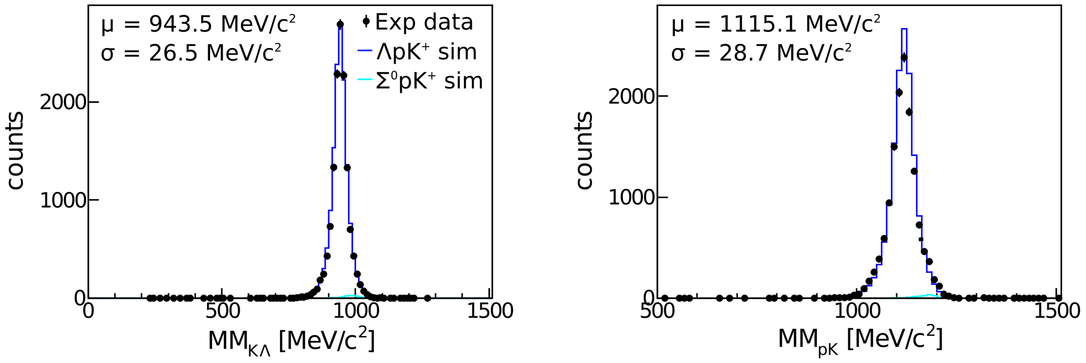

Figure 4.5: Left panel: Missing mass distribution to the K^+ and Λ exhibiting a proton signal. Right panel: Missing mass distribution to the proton and the kaon showing a Λ signal.

In the next step, the properties of the selected events were investigated in detail. The left panel of Figure 4.5 shows the missing mass distribution to the Λ and kaon four-vector ($MM_{K^+,\Lambda}$), in which a proton signal is visible, while the right panel presents the missing mass to the proton and kaon (MM_{p,K^+}) where a Λ signal is visible. These two figures serve as an example to demonstrate the resolution of the measured kinematics and are analogous to the momentum distributions in Figure 4.2. The proton, for example, has no intrinsic width, and the Λ width is negligible. The observed widths are, thus, a pure effect of the finite detector resolution. The kinematic fit treats the illustrated detector resolution properly, due to the inclusion of the parameter errors into the fitting procedure. One output that the fit provides (p-value) has already been used to constrain the data selection. Another output of the kinematic fit are new four-vectors that are close to the measured ones but are shifted such that they fulfill the physical constraints mentioned in Sec. 4.1.2. The advantage of these new, shifted four-vectors is an improvement in the resolution of all observables that are constructed out of these four-vectors. The missing mass distribution MM_{Λ,K^+} of the refitted vectors, for example, is a delta-function peaked at the mass of the proton[4]. These refitted kinematics are especially useful for observables like invariant masses of two particles as they are not a direct constraint of the kinematic fit. Figure 4.6 presents in the left panel the missing mass

---

[4] This follows as this observable is tightly constrained by selection criteria 4.8.

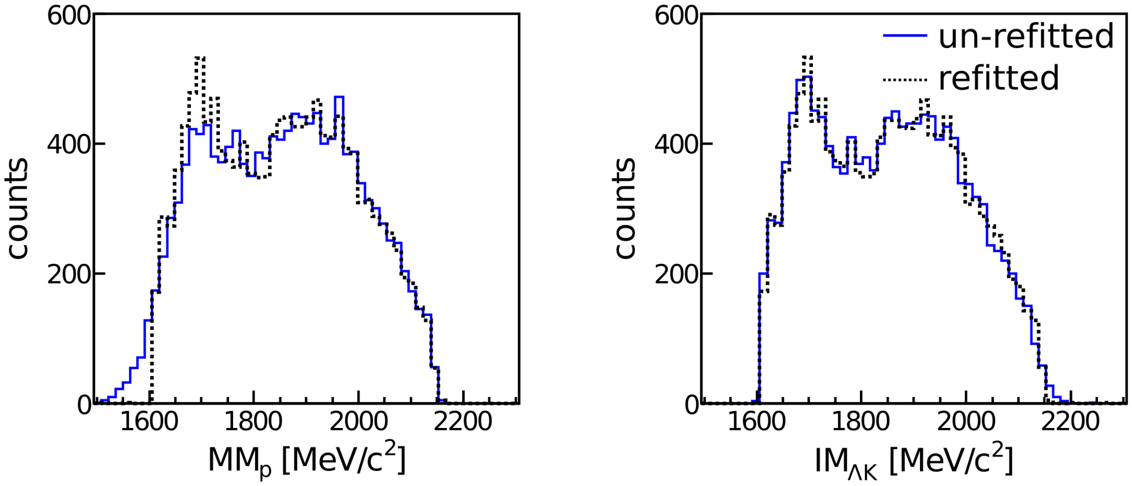

Figure 4.6: Left Panel: Missing mass to the proton. Right panel: Invariant mass distribution of K^+ and Λ. Both observables are shown for the measured four-vectors (blue dots) and the refitted ones (black line) for the HADES data-set.

to the proton (MM_p) and in the right panel the invariant mass of kaon and Λ (M_{Λ,K^+}). By kinematic constraints, these two observables should exhibit exactly the same distribution; due to the finite resolution of the spectrometer they do not (visible by the blue dots). The mass distributions of the refitted four-vectors (black line) inhibit a better mass resolution as these vectors fulfill energy and momentum conservation and are, thus, not so much distorted by effects due to the detector resolution. The refitted vectors show the same mass distribution for both observables. One can also observe that the refit did influence the proton properties more than the Λ and kaon properties as the mass distribution in the first histogram shows a stronger modification. The observables presented further in this thesis are all obtained from the refitted four-vectors.

4.2.1 Single Particle Kinematics

To understand the underlying dynamics in the production of the three particles $pK^+\Lambda$, the kinematics of each particle are useful observables to study. A sub-objective of this work is to understand the kinematics behind the production of the three particles $pK^+\Lambda$ and accordingly reproduce their behavior with a model. As discussed in Section 2.4, the simplest approach for the description

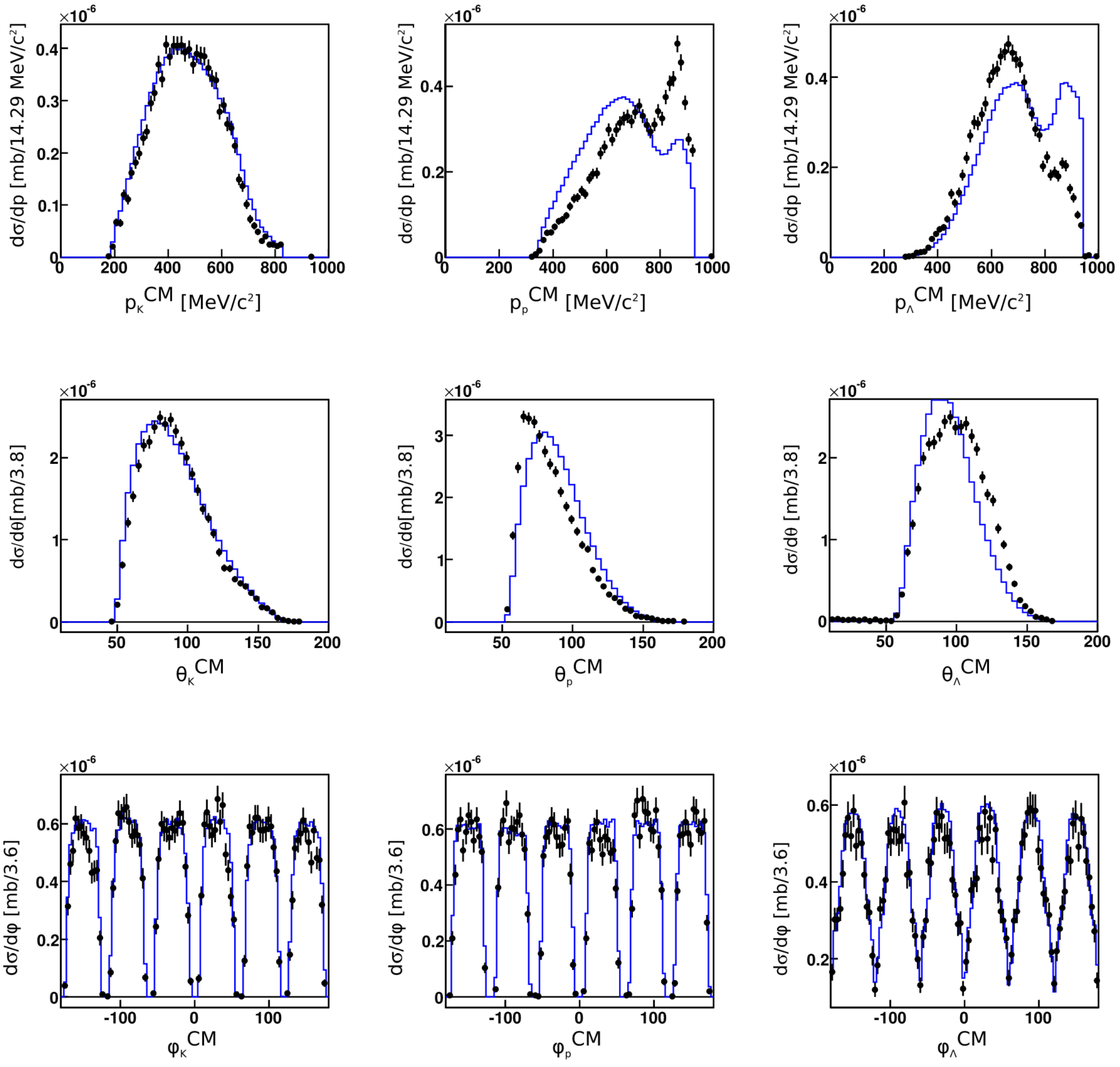

Figure 4.7: Components of the four-vector of the three particles in the CMS for the **HADES data set** (black points) shown with **phase space simulations of $pK^+\Lambda$** (blue dots).

of the kinematics is the assumption that the particles are produced via phase space without dynamics. This would result in a uniform event distribution in the Dalitz-Plot, which is a two-dimensional representation of the event kinematics.

The observables that are presented in the following are, however, not a direct measure of the real production properties. Their spectra are strongly affected by the acceptance of the HADES spectrometer. Thus, in order to judge whether the model describes the production kinematics correctly, it should only be compared to the data inside the acceptance of the spectrometer. If the kinematics in the acceptance differs between the model and the experimental data, they will also differ in the full phase space and in this way the model can be identified as wrong. Only if the model describes all independent observables well, it is probable that it reproduces the kinematics correctly. Figure 4.7 shows the momentum, theta and phi distributions in the center of mass system (CMS) each for p,K^+ and Λ, respectively. Simulations of Reaction (4.1), in which the particles are produced via phase space, are compared to the data. The agreement between the model and the measured data is rather poor. The kaon is the only particle that is described by the phase space simulations. Still, this does not mean that there are no complex kinematics involved in the production of the kaon. It means that the kaon is more independent from the underlying production mechanism than the proton or the Λ. The reason for this might be due to their two-step production via an intermediate N* that decays into a $K^+\Lambda$-pair. In this case the kinematics of the N* is mainly carried by the Λ as a result of the large mass difference to the kaon.

4.2.2 Multi-Particle Kinematics

It is obvious that if the simple kinematic of each particle is not described by a phase space production of $pK^+\Lambda$, more sophisticated observables that combine the kinematics of many particles, will also not be consistent with this hypothesis. In Figure 4.9 the experimental invariant mass distributions of two particles are compared to the resulting distributions of the phase space simulations. The differences between the two histograms in the $K^+\Lambda$ ($\hat{=}MM_p$) invariant mass distribution are striking. This observable will differ from a pure phase space distribution if intermediate N*-resonances are contributing to the production process. In this case, the kinematics of the K^+ and the Λ would be correlated and especially their invariant mass would not be distributed equally along the Dalitz-Plot but the statistic would be enhanced in the region corresponding to the N^* masses (see e.g. the Dalitz-plot in Figure 6.12 of Chapter 6).

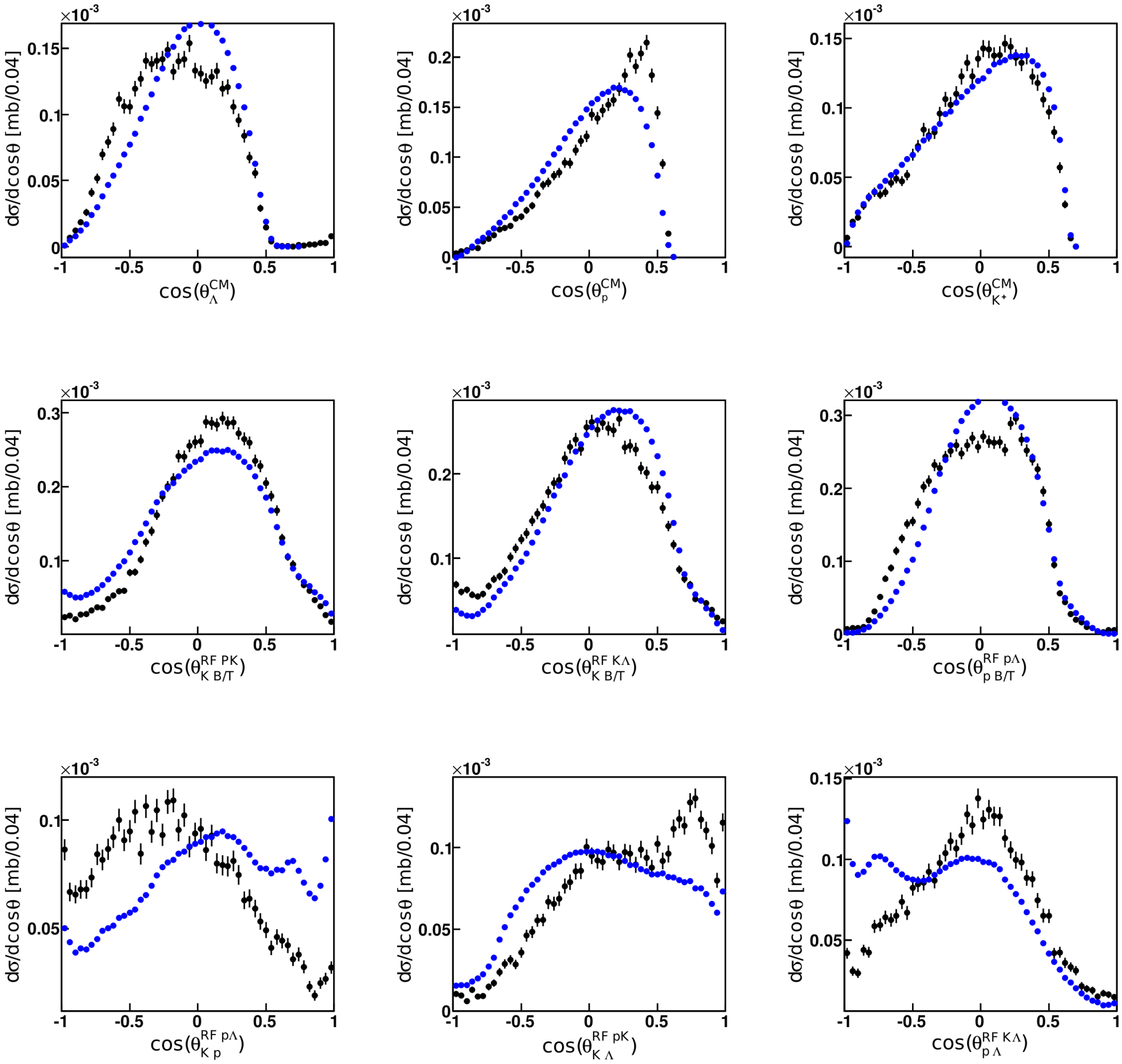

Figure 4.8: Angular correlations of the three particles for the **HADES data set** (black points) shown with **phase space simulations of $pK^{+}\Lambda$** (blue dots). The upper index at the angle indicates the rest frame (RF) in which the angle is investigated. The lower index names the two particles between which the angle is evaluated. CM stands for the center of mass system. B and T denotes the beam and target vector, respectively. See Figure 2.6 for further explanations.

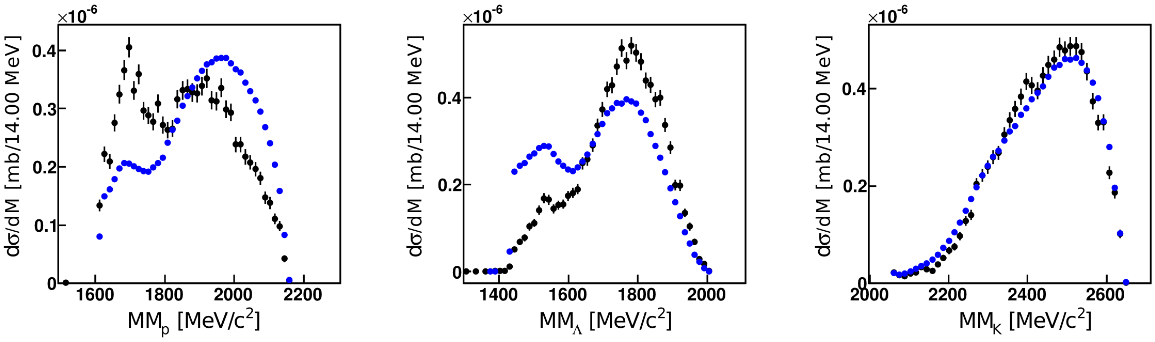

Figure 4.9: Invariant masses of two particles for the **HADES data set** (black points) shown with **phase space simulations of $pK^+\Lambda$** (blue dots).

The invariant mass of $p\Lambda$ which corresponds to the missing mass to the kaon is again described well by the phase space as already the kinematics of the kaon could be modeled with these simulations. Still, that matching does not mean that phase space is an appropriate model as it does not catch the complete kinematics which is visible in the angular distributions (Figure 4.8). Here, the spatial correlation of the produced particles can be demonstrated. The only observable which is described well by phase space $pK^+\Lambda$ production is the kaon angle in the CM system. This means that the kaon is not exhibiting a strong angular anisotropy in the CM system. The other eight angles do show that the complete event kinematics is missed by the model.

This result, combined with the reports from earlier measurements [155, 156, 157, 160, 161, 162], confirms that the production of $pK^+\Lambda$ cannot be understood as a simple phase space process. Motivated by the aim to model the production process exactly, and also in order to see if a kaonic cluster participated in the reaction, it was decided to use a partial wave analysis tool.

4.3 A Partial Wave Analysis for p+K$^+$+Λ Production

A partial wave analysis in general tries to decompose the scattering process into separate sub-processes according to the quantum numbers of the initial and final state. The differential cross section of the reaction (in this case a three particle production out of the collision of two particles) can be written as [180]:

$$d\sigma = \frac{(2\pi)^4|A|^2}{4|\mathbf{k}|\sqrt{s}} d\Phi_3(P, q_1, q_2, q_3), \tag{4.11}$$

$$P = k_1 + k_2. \tag{4.12}$$

Where $d\Phi_3$ is the phase space element of the three final state particles with the four-momenta q_i; k_i are the four momenta of the two initial state protons; $|\mathbf{k}|$ is the absolute value of the momentum of the beam proton calculated in the CMS; $\sqrt{s}$ is the center of mass energy of the colliding system; A is the transition amplitude from the initial to the final state. This transition amplitude can be decomposed into partial waves as follows [180]:

$$A = \sum_{\alpha} A^{\alpha}_{tr}(s) Q^{in}_{\mu_1 \ldots \mu_J}(S, L, J) A_{2b}(S_2, L_2, J_2)(s_i) Q^{fin}_{\mu_1 \ldots \mu_J}(i, S_2, L_2, J_2, S', L', J). \tag{4.13}$$

The initial $p+p$ system is characterized by their quantum numbers S, L, J, which denote their combined spin, orbital momentum and total angular momentum. Instead of treating the thee particles in the final state independently it is useful to select a two-particle subsystem and treat the third particle with respect to this system. Consequently S_2, L_2, J_2 denote the combined spin, orbital momentum and total angular momentum of the two particle subsystem. The total final state is then described by S', L' and J, where S' denotes the spin of the system when the two-particle state and the third particle are combined, and L' denotes the orbital momentum between the third particle and the subsystem. If q_i is the four-momentum of the third particle, the invariant mass of the subsystem can be written as:

$$s_i = (P - q_i)^2. \tag{4.14}$$

$A^{\alpha}_{tr}(s)$ is the transition amplitude from the initial to the final state where the multiindex α accounts for all combinations of $S, J, L, S_2, L_2, J_2, S', L', i$ and q_i and is associated with certain waves.
$A_{2b}(S_2, L_2, J_2)(s_i)$ contains the re-scattering process in the two-particle final channel;
$Q^{in}_{\mu_1 \ldots \mu_J}(S, L, J)$ are the spin-momentum operators of the initial state and describe the production process;
$Q^{fin}_{\mu_1 \ldots \mu_J}(i, S_2, L_2, J_2, S', L', J)$ is the spin-momentum operator of the final state and describes the decay processes.
The exact form of the operators can be taken from [181, 182]. The transition amplitude is parametrized as follows [183]:

$$A^{\alpha}_{tr}(s) = (a^{\alpha}_1 + a^{\alpha}_3 \sqrt{s}) e^{i a^{\alpha}_2}. \tag{4.15}$$

As the center of mass energy of this experiment was constant the third parameter a_3^α which is responsible for the energy dependence of each partial wave is not used. This means that each transition (α) from initial to final state is described by a strength and a phase.

The part of the amplitude that describes the energy dependence of the the scattering process with an intermediate state including a resonance is parametrized as a relativistic Breit-Wigner in the following form [182]:

$$A_{2b}^{\beta}(s_{K^+\Lambda}) = \frac{M\Gamma_{tot}}{M^2 - s_{K^+\Lambda} - iM\Gamma_{tot}}\,, \tag{4.16}$$

with M and Γ_{tot} expressing the mass and width of the intermediate resonance. In case that particles do not come from a resonance but interact via a rescattering in the final state, $A_{2b}^{\beta}(s_i)$ looks as follows:

$$A_{2b}^{\beta}(s_{p\Lambda}) = \frac{a_{\gamma\gamma'}^{\beta}\sqrt{s_{p\Lambda}}}{1 - \frac{1}{2}r_{\gamma\gamma'}^{\beta}q^2 a_{\gamma\gamma'}^{\beta} + iqa_{\gamma\gamma'}^{\beta}q^{2L_2}/F(q, r_{\gamma\gamma'}^{\beta}, L_2)}. \tag{4.17}$$

$a_{\gamma\gamma'}^{\beta}$ describes the scattering length of two particles γ and γ', $r_{\gamma\gamma'}^{\beta}$ describes the effective range of the two particle system and q denotes the relative momentum between p and Λ. While $\gamma\gamma' = pp$ or $p\Lambda$ is included in the formalism in general, for this special case, in which only $pK^+\Lambda$ events are investigated, $\gamma\gamma'$ stands for $p\Lambda$. The $F(q, r, L)$ is the Blatt-Weisskopf form factor. As in these cases only a two particle subsystem is considered the quantum number of the third particle is irrelevant. This is expressed by the multiindex β which runs over all combinations of the two particle system (S_2, L_2 and J_2) and is a sub-set of α.

The so far illustrated parts of the amplitude (4.16) and (4.17) describe the scattering process as a function of the energy. The angular dependence of the scattering amplitude, that is characteristic for a partial wave decomposition, is contained in the momentum part of the spin-momentum operators [184]. It is parametrized by Legendre polynomials that depend on the cosine of the scattering angle between initial and final state particles in the CMS, see Appendix A in Ref. [184] for details.

In this experiment, the initial state consists of two colliding protons, and the final state is composed of the three particles $pK^+\Lambda$, see Reaction (4.1). In Appendix C, all possible quantum numbers of the initial two-proton system are listed. For this experiment, the possibilities were limited to states with J<3. This leaves six combinations as possible initial states: $^1S_0$, $^3P_0$, $^3P_1$, $^3P_2$, $^1D_2$

and $^3F_2$. The states are characterized by the spectroscopic notation [185]:

$$^{2S+1}L_J, \tag{4.18}$$

where S is the total spin of the $p+p$ system, L is the orbital momentum between the two protons and J is the total angular momentum.

The final state interaction is manifold. As explained in Section 2.4, the final $pK^+\Lambda$ state may contain several intermediate particles. The most prominent ones are N^{*+} resonances that subsequently decay into K^+ and Λ, see Reaction (2.6). The Bonn-Gatchina framework performs a global fit of the data. This means, that specific waves contain already a certain mass distribution according to an implemented resonance parametrization. Mass and width parameters of the resonances are not determined by the fit but are used as external constraints. These constraints are provided by the PDG [8] which contains a list of N*-resonances. Not not all of them are, however, well established. Within this thesis no conclusion can be drawn about the precise contribution of the different N^{*+}-resonances to the investigated final state and hence no cross section of the latter will be extracted. Thus, all N*-resonances below the mass of 2100 MeV/c^2 that have a measured $K^+\Lambda$ branching above 1% were considered as possible contribution to the $K^+\Lambda$ yield. Table 4.1 lists the selected N*-resonances, their quantum numbers, masses, widths and branching ratios into $K^+\Lambda$. Especially the branching in $K^+\Lambda$ is not well known in most of the cases.

Using this table, one can construct several allowed transitions from a $p+p$ initial to a $N^{*+}+p$ final state. One transition will be discussed here as an example. A proton has the following quantum numbers $J^P = 1/2^+$, where J is the total spin of the particle and P is its parity. A system of two protons can, therefore, have

Table 4.1: Selected N*-resonances with their properties [8].

Notation in PDG	Old notation	Mass [GeV/c^2]	Width [GeV/c^2]	$\Gamma_{\Lambda K}/\Gamma_{All}$ %
N(1650) $\frac{1}{2}^-$	N(1650)S_{11}	1.655	0.150	3-11
N(1710) $\frac{1}{2}^+$	N(1710)P_{11}	1.710	0.200	5-25
N(1720) $\frac{3}{2}^+$	N(1720)D_{13}	1.720	0.250	1-15
N(1875) $\frac{3}{2}^-$	N(1875)D_{13}	1.875	0.220	4±2
N(1880) $\frac{1}{2}^+$	N(1880)P_{11}	1.870	0.235	2±1
N(1895) $\frac{1}{2}^-$	N(1895)S_{11}	1.895	0.090	18±5
N(1900) $\frac{3}{2}^+$	N(1900)P_{13}	1.900	0.250	0-10

Table 4.2: J^P realizations of a combined system of a $\frac{1}{2}^-$ and a $\frac{1}{2}^+$ particle.

L \ S_{tot}	0	1
0	0^-	1^-
1	1^+	$\mathbf{0}^+, 1^+, 2^+$
2	2^-	$1^-, 2^-, 3^-$
3	3^+	$2^+, 3^+, 4^+$

a total spin $S = 0$ or $S = 1$. If one considers the $S = 0$ combination and assumes no orbital momentum between the two particles ($L = 0$), the quantum numbers of the system are $J^P = 0^+$. This state can also be characterized in the spectroscopic notation (Equation (4.18)). Then, in this example, the $p + p$ combination is in the state $^1S_0$.

If one considers, further, a final state of an $N^*(1650)$ with the quantum numbers $J^P = 1/2^-$ produced together with a proton, one has to build all possible combinations of a $1/2^-$ and a $1/2^+$ state. These combinations are listed in Table 4.2.

In each transition from initial to final state, the total spin J and the parity P have to be conserved. If one searches for a transition from the $^1S_0$ initial state, one has to find a final state, which has also $J^P = 0^+$. As seen from Table 4.2, these quantum numbers are present for the configurations in which the spins of $N^*(1650)^+$ and a p add up to $S = 1$ and the orbital momentum between them is $L = 1$. This state is marked bold. In the spectroscopic notation this final state can be written as $^3P_0$.

To constrain the orbital momenta of the initial and final states, that may possibly be populated, one can orientate oneself at the available energy of the reaction. In the case presented here, the p beam had a kinetic energy of 3.5 GeV. This is equivalent to a center of mass energy of $\sqrt{s} = 3.176\ GeV$. Appendix C contains a detailed description of all the selected waves of the p+p initial as well as the $pK^+\Lambda$ final system.

4.3.1 Data Fitting Procedure

The parameters α_1 and α_2 (from Equation 4.15) of each transition wave are determined from the PWA by an unbinned fit (event-by-event wise) of the PWA-amplitude to the experimental data. As an input for the fitting procedure, experimental data are needed together with phase space simulations, that were filtered through the detector acceptance and treated in the same way by the analysis as the experimental data. Both data sets are provided in form of a list containing all components of the four-vectors of proton, kaon and Λ. All these components were fitted simultaneously in each single event. Important is that the events fulfill constraints like momentum and energy conservation which is a further argument to use vectors with refitted kinematics in the analysis, see Sec. 4.2. In addition, the PWA code needs a list of possible transition waves that can contribute to the investigated final state. The list with the transition amplitudes used in this analysis is shown in Tables 6.2-6.5 of Chapter 6. Appendix C describes how they were selected. In case the final state contains a resonance, its mass and width values have to be provided in an extra input list. Their exact properties can, in principle, be used as a free fit parameter. To decrease the number of degrees of freedom in the fit, however, the mass and width properties of the N*-resonances were fixed to the PDG values [8].

The PWA fits the sum of all transition amplitudes on an event-by-event base to the provided list of experimental data. The fit is based on a log-likelihood minimization. It repeats this fitting procedure for many iterations. The number of iteration steps is fixed by the user. In this work, a default number of 100 iteration steps is used. Unless no improvement of the log-likelihood value is observed the full iteration is performed; in case the fit arrives to a minimum earlier, the iteration is terminated and the final result is reported.

As an output, the fit delivers a value for α_1 and α_2 for all included waves. The overall quality of the fit is presented by the maximum likelihood value. In order to make a statement about the quality of the fit, based on this discrepancy variable, its probability density function (PDF) needs to be evaluated[5]. The PDF for this discrepancy variable (maximum log likelihood) was not determined. Still, this variable is a useful quantity on a relative scale. By comparing the log likelihood value of many fits the best fit can be determined through the largest negative value. To represent and cross check the fit result in a graphical way, each simulated event that was used as an input for the fitting procedure is assigned a weight to model the shape of the PWA solution. When filling these events with their according weights in a histogram the PWA solution can be compared to the measured data inside the acceptance of the spectrometer.

---

[5] See Chapter 5 for a detailed discussion about statistics.

4.3.2 Fit Cross Checks

In a first iteration, only the events of the HADES data set were fitted by the Bonn-Gatchina-PWA code. The best solution that has been obtained is presented in Figure 4.10 and 4.12. Here, five N*-resonances (N(1650), N(1710), N(1720), N(1875) and N(1895)) and four non-resonant waves were used in the fit. This corresponds to the N* fit version No. 9 in Table 4.3 and the non-resonant wave fit version No. 4 in Table 4.4. This solution yields a very good description of the measured data, as visible in Figures 4.10 and 4.12. As a cross check,

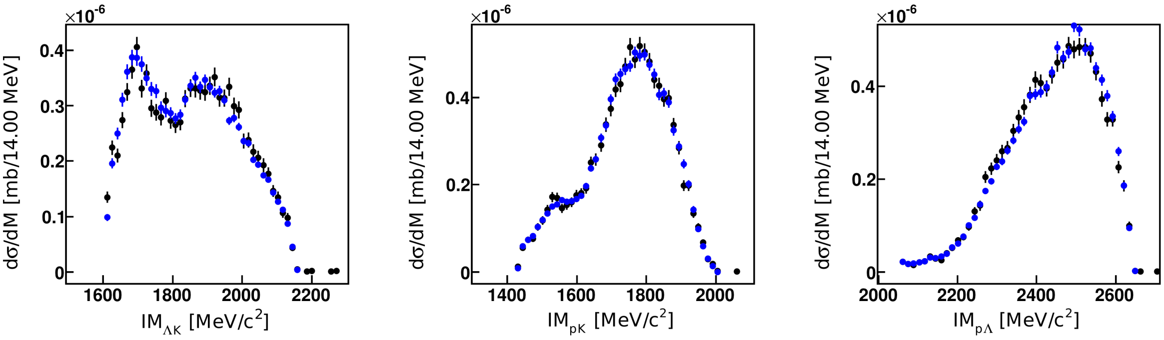

Figure 4.10: Invariant masses of two particles for the **HADES data set** (black points) shown with the **best PWA solution** (blue dots) fitted to these data.

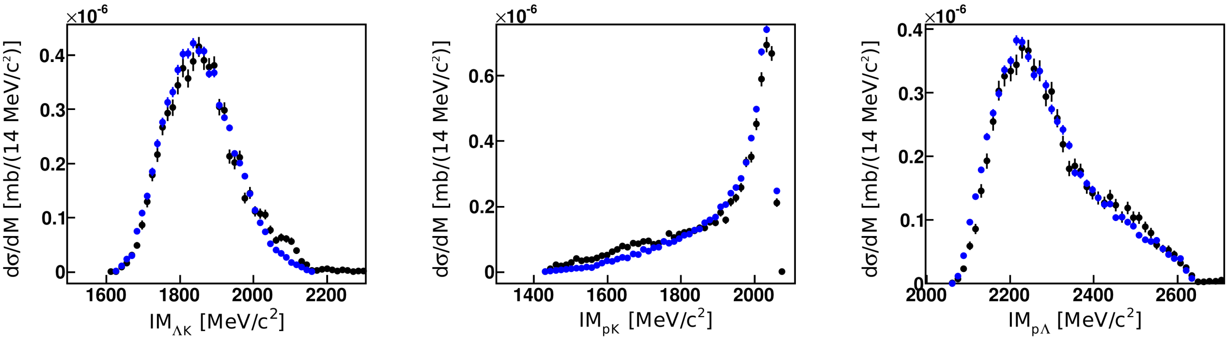

Figure 4.11: Invariant masses of two particles for the **WALL data set** (black points) shown with the **best PWA solution** (blue dots), obtained by a fit to the HADES data only.

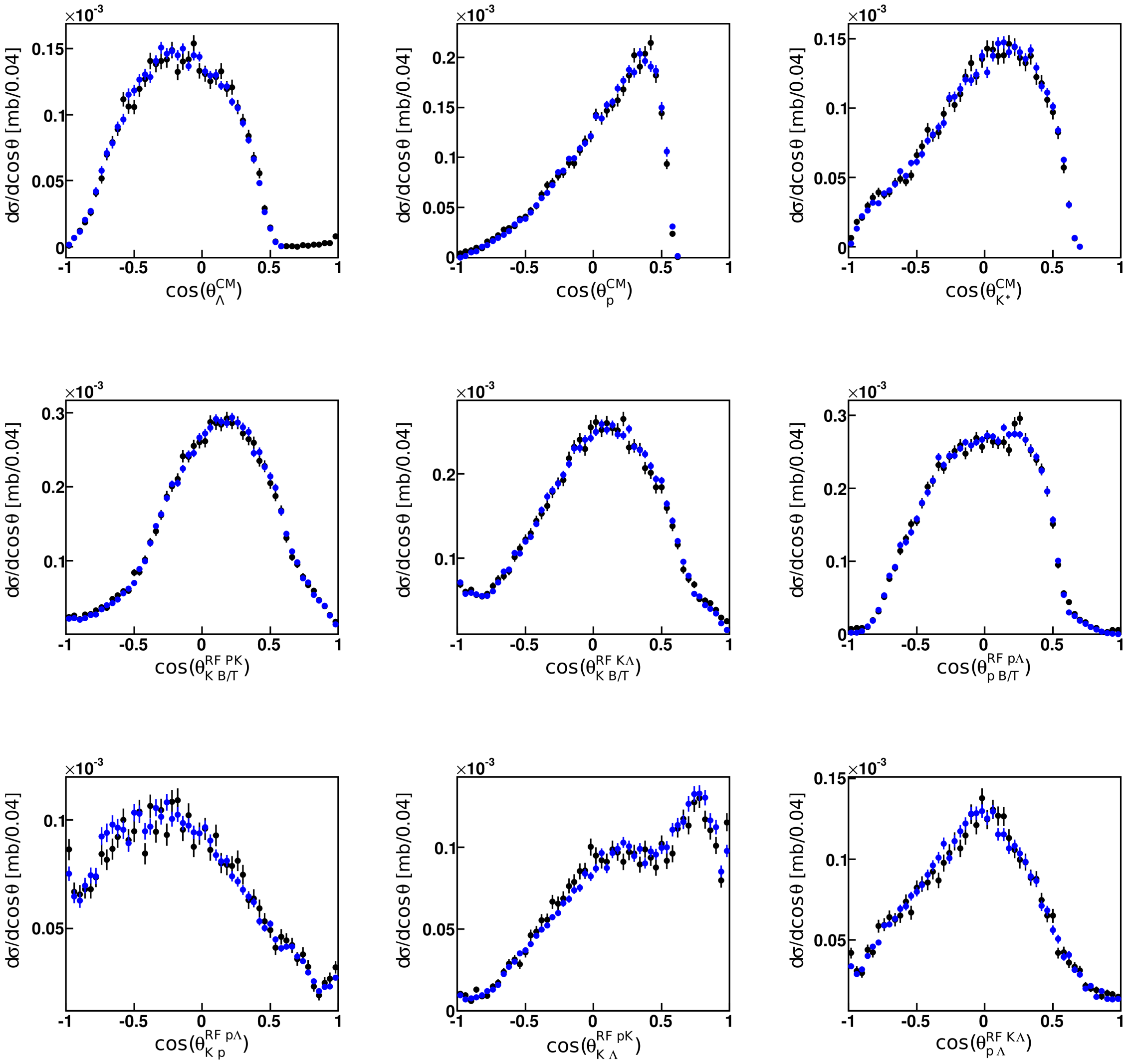

Figure 4.12: Angular correlations of the three particles for the **HADES data set** (black points) shown with the **best PWA solution** (blue dots) fitted to these data. See Figue 2.6 for further details about the observables.

the PWA solution, obtained only from the HADES events, was compared to the events in the WALL data sample. Figures 4.11 and 4.13 point out that the experimental data inside of the WALL acceptance (black data) can be described to a large extent by the PWA solution (blue points). Because the solution is not

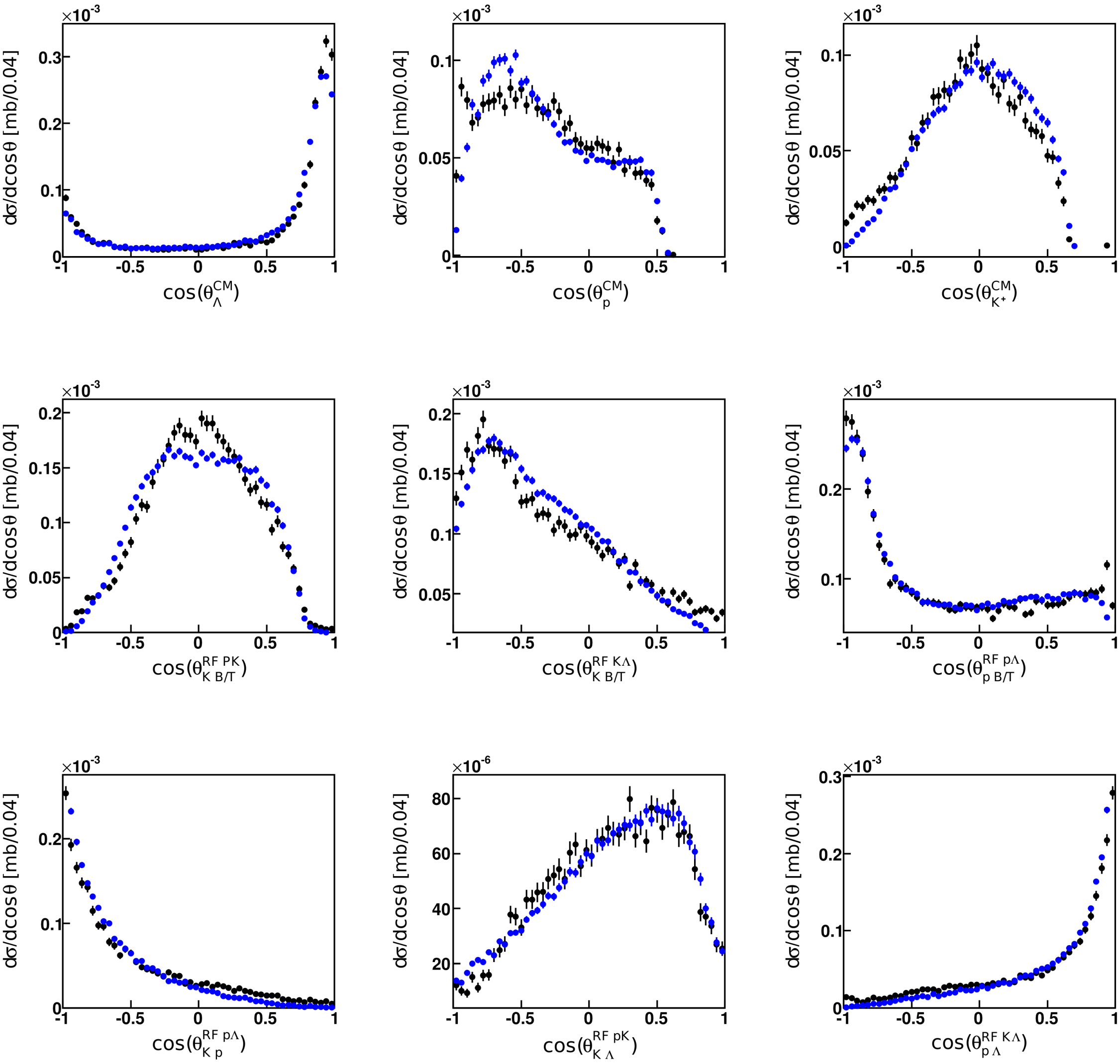

Figure 4.13: Angular correlations of the three particles for the **WALL data set** (black points) shown with the **best PWA solution** (blue dots), obtained by a fit to the HADES data only. See Figue 2.6 for further details about the observables.

biased by the WALL data-set, this is a proof of a certain predictive power of the solution for detector-blind regions. Since the HADES data-set contains no particles emitted in the very forward direction (0.33° to 7.17°), and the WALL does, these two data-set can not be seen as sub-sets of one-another but are

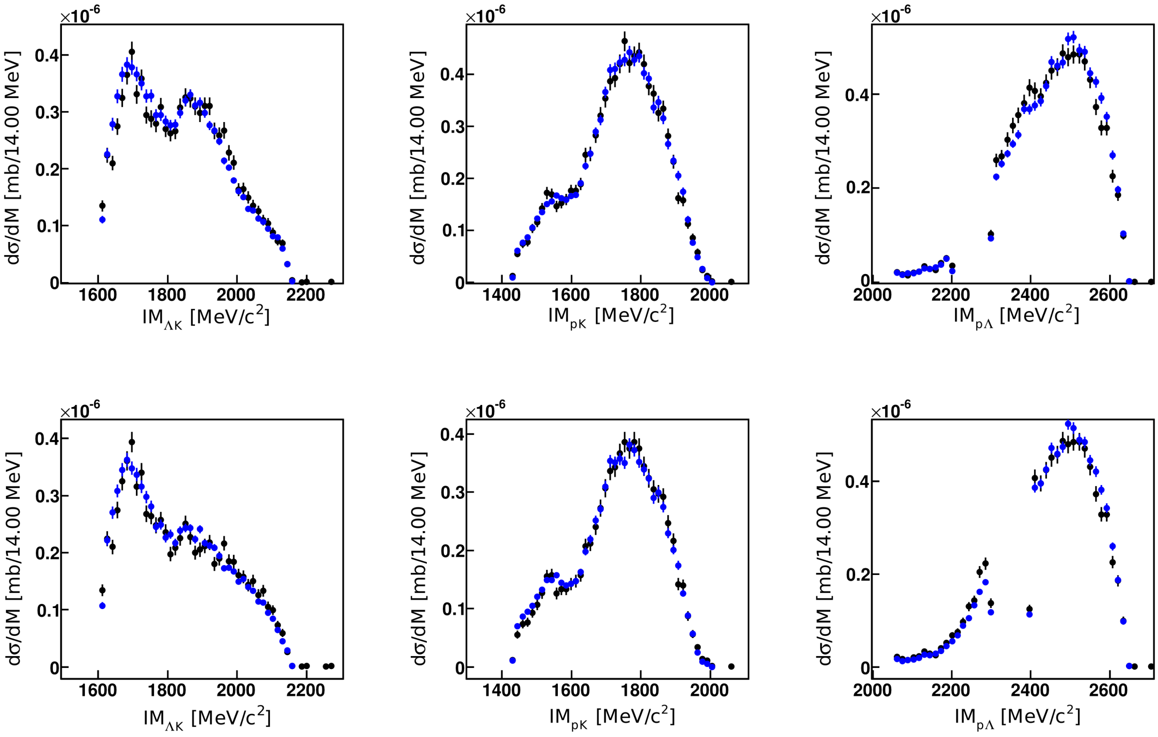

Figure 4.14: Invariant masses of two particles for the three particles for the **selected HADES data set** (black points) shown with the **best PWA solution** (blue dots), obtained by a fit to the HADES data, excluding a $M_{p\Lambda}$ mass range of 2200-2300 MeV/c^2 (upper row) and excluding a $M_{p\Lambda}$ mass range of 2300-2400 MeV/c^2 (lower row).

independent. This is an important quality check for the PWA code.

Another important check tests whether a signal in the data which was not included in the PWA, e.g the $\overline{K}NN$, could extensively bias the fit. Again, only the HADES data were fitted while the results are discussed for both data sets. The following cross check was performed: events in a certain mass range in $IM_{p\Lambda}$ were excluded from the fit; The remaining events were fitted by the PWA. This cross check was done for two mass ranges. 1) a mass range from 2200 MeV/c^2 - 2300 MeV/c^2 in $IM_{p\Lambda}$ was excluded; and 2) a mass range from 2300 MeV/c^2 - 2400 MeV/c^2 in $IM_{p\Lambda}$ was excluded from the fit. In this way one creates data samples that certainly do not contain the production of 1) a low-mass $\overline{K}NN$ and 2) a high-mass $\overline{K}NN$ and one can cross check if an exclusion of these - eventually $\overline{K}NN$ contaminated - events changes the prediction of the fit.

The results of these fits to the selected events are presented in Figure 4.14. The PWA fits also well to the reduced data sample. The two solutions, obtained from these samples, can be drawn in the complete mass range as well. This way one can determine how much the fit changes its prediction for a certain mass range when the events within this range are excluded. Figure 4.15 shows the $IM_{p\Lambda}$ for the three different solutions for the HADES and WALL data sets. Specifically the upper right panel reveals that the inclusion of mass ranges that could contain a small amount of signal seems not to bias the fit. For the WALL data set more differences between the three cases are visible. This is, however, not surprising as non of the WALL data were used for this test and the lower panels reveal, thus, the changes in the extrapolations to this phase space which are, nonetheless, small. In this respect, it is remarkable how well the fit describes the data. The fit, furthermore, seems not to be biased by events in certain mass windows, as the resulting distribution does not show a systematic difference within these mass ranges for fits that in- and exclude this range. There is one systematic deviation of the solution symbolized by the green dots in a mass range of 2220-2250 MeV/c^2 in the lower right panel of Figure 4.15. In this mass range the new solution is systematically below the original solution, shown with the blue dots. As in this solution (green dots) the mass range from 2300-2400 MeV/c^2 was excluded, and not the range of 2220-2250 MeV/c^2, the statistic that differs was actually included into the fit. For this reason this systematic difference can not be attributed to a hidden signal that changes the prediction of the PWA solution. A detailed comparison of the PWA solutions to the data in several observables is documented in Appendix D.

These cross checks strengthen the reliability of the introduced method. The successful cross check of fitting only one complete data set and extrapolating to the other data set assures us to fit both data sets simultaneously. This will further stabilize the out-coming prediction of the PWA.

4.3.3 Systematic

The application of the PWA framework to the $pK^+\Lambda$ data sample has shown that due to the large number of parameters the solution is not very sensitive to the input wave composition: the inclusion or exclusion of different N^{*+} resonances has in many cases no strong impact on the shape of the solution for the various observables. Thus, the considered data sample is not able to determine a unique set of the contributing N^{*+}. To reassure that this ambiguity does not lead to a bias of the final statement about the production of a kaonic cluster,

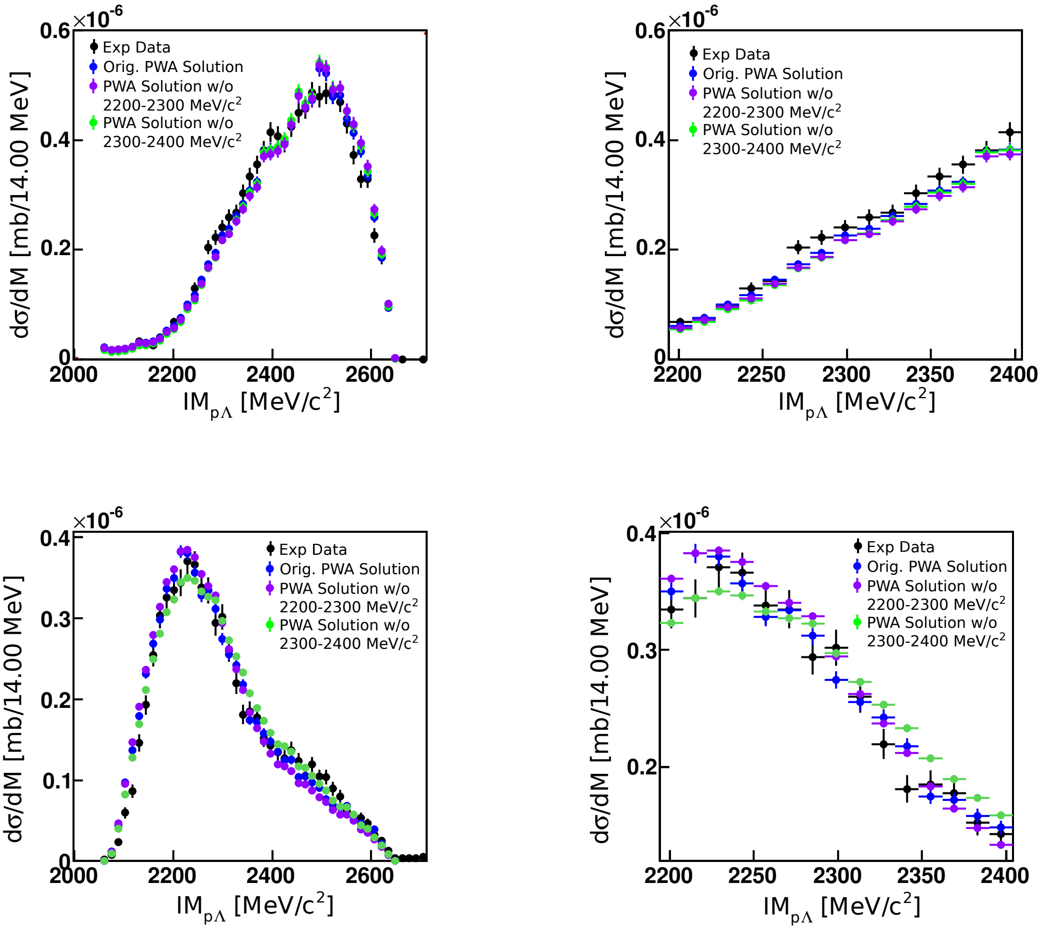

Figure 4.15: Invariant Mass of $p\Lambda$ for the **HADES data set** (upper panels) and **WALL data set** (lower panels) (both black points), presented together with the **best PWA solution** (blue dots), fitted to the HADES statistic only. Compared to these results are the two cross checks, where once events were rejected from the fit with a mass range of 2200-2300 MeV/c^2 (violet points) and once within a mass range of 2300-2400 MeV/c^2 (green points). The left panels show the full mass range and the right panels show a zoom into the excluded mass regions.

Table 4.3: Different versions of N* combinations in the PWA input.

No.	Resonance combinations
0	N(1650), N(1710), N(1720)
1	N(1650), N(1710), N(1720), N(1900)
2	N(1650), N(1710), N(1720), N(1895)
3	N(1650), N(1710), N(1720), N(1880)
4	N(1650), N(1710), N(1720), N(1875)
5	N(1650), N(1710), N(1720), N(1900), N(1880)
6	N(1650), N(1710), N(1720), N(1900), N(1895)
7	N(1650), N(1710), N(1720), N(1900), N(1875)
8	N(1650), N(1710), N(1720), N(1895), N(1880)
9	N(1650), N(1710), N(1720), N(1895), N(1875)
10	N(1650), N(1710), N(1720), N(1880), N(1875)
11	N(1875), N(1880), N(1895), N(1900)

Table 4.4: Different sets of non-resonant waves in the PWA input.

No.	Non-resonant waves
0	no non-resonant waves
1	$(pL)(^1S_0) - K$
2	previous wave + $(pL)(^3S_1) - K$
3	previous waves + $(pL)(^1P_1) - K$
4	previous waves + $(pL)(^3P_0) - K$
5	previous waves + $(pL)(^3P_1) - K$
6	previous waves + $(pL)(^3P_2) - K$
7	previous waves + $(pL)(^1D_2) - K$
8	previous waves + $(pL)(^3D_1) - K$
9	previous waves + $(pL)(^3D_2) - K$

a systematic variation of the used partial waves in the PWA input was performed. The solution itself contains resonant and non-resonant production of $pK^+\Lambda$. Therefore two types of variations have been tested. First, the number of included N*-resonances was varied. The combination of tested N*-resonances is listed in Table 4.3. Second, in each N* combination the number of non-resonant waves has been modified. The combinations of different non-resonant waves are listed in Table 4.4. Through a permutation of the input possibilities in Tables

Table 4.5: Best solutions for each N* combination in the PWA.

No. of N* combination	No. of non-res. waves	Log-likelih.
0	7	-2415.74
1	**8**	**-2708.49**
2	8	-2524.59
3	**8**	**-2712.49**
4	4	-2671.05
5	8	-2310.4
6	**9**	**-2754.37**
7	8	-2657.77
8	**8**	**-2734.97**
9	6	-2698.86
10	4	-2642.58
11	0-9	>0

Table 4.6: Naming scheme for the four best solutions.

Name	N* combination	No. of non-res. waves	Loglikelih.
1/8	N(1650), N(1710), N(1720), N(1900)	8	-2708.49
3/8	N(1650), N(1710), N(1720), N(1880)	8	-2712.49
6/9	N(1650), N(1710), N(1720), N(1900), N(1895)	9	-2754.37
8/8	N(1650), N(1710), N(1720), N(1895), N(1880)	8	-2734.97

4.3 and 4.4 a number of 120 PWA solutions have been tested. The quality of the PWA solution is determined by the loglikelihood value of the fit which is an output of the Bonn-Gatchina PWA. The comparison of the different loglikelihood values for the various permutations allows to decide which solution describes the data best. For each N* combination the solution with the best loglikelihood was determined. This value depends only on the number of non-resonant waves that have been included. In case of the resonance combination No. 11 no good value for any non-resonant combination could be achieved. Table 4.5 shows the loglikelihood value for each N* combination. The four best results are marked in bold. Table 4.6 summarizes the four best solutions and their further naming scheme. The overall best agreement with the data is obtained with a solution that contains N(1650), N(1710), N(1720), N(1900) and N(1895) as well as nine non-resonant waves of $pK^+\Lambda$. The superposition of the four best solutions in comparison to the data is illustrated by a gray band in Figures 4.16 - 4.19. The width of the band represents the scatter of the different solutions. The iterative permutation of included waves in the PWA fit procedure shows that even if the exact composition of participating partial waves to the process $p+p \rightarrow p+K^+ +\Lambda$ can not be determined unambiguously, the quality of data description is yet comparable and does not induce a large systematic uncertainty in the predicted shape of the $p\Lambda$ invariant mass distribution. This result is important as it allows a stable prediction for the $p\Lambda$ invariant mass distribution without the inclusion of a signal of a possible kaonic cluster production. The gray bands in Figures 4.16 - 4.19 are, thus, the null hypothesis (no signal) for a further statistical significance test.

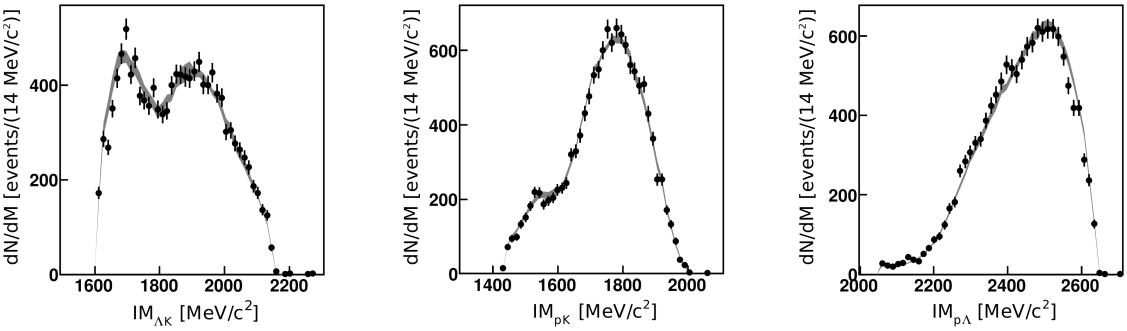

Figure 4.16: Invariant masses of two particles for the **HADES data set** (black points) shown with the **four best PWA solutions** (gray band), obtained by a fit to the HADES and WALL data.

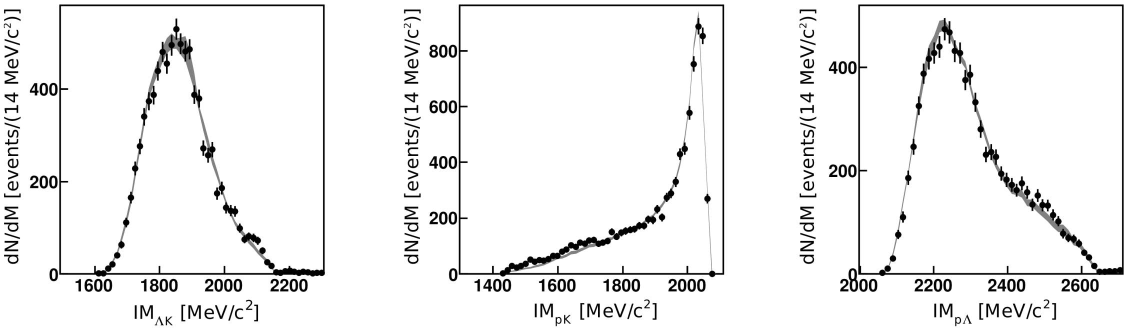

Figure 4.17: Invariant masses of two particles for the **WALL data set** (black points) shown with the **four best PWA solutions** (gray band), obtained by a fit to the HADES and WALL data.

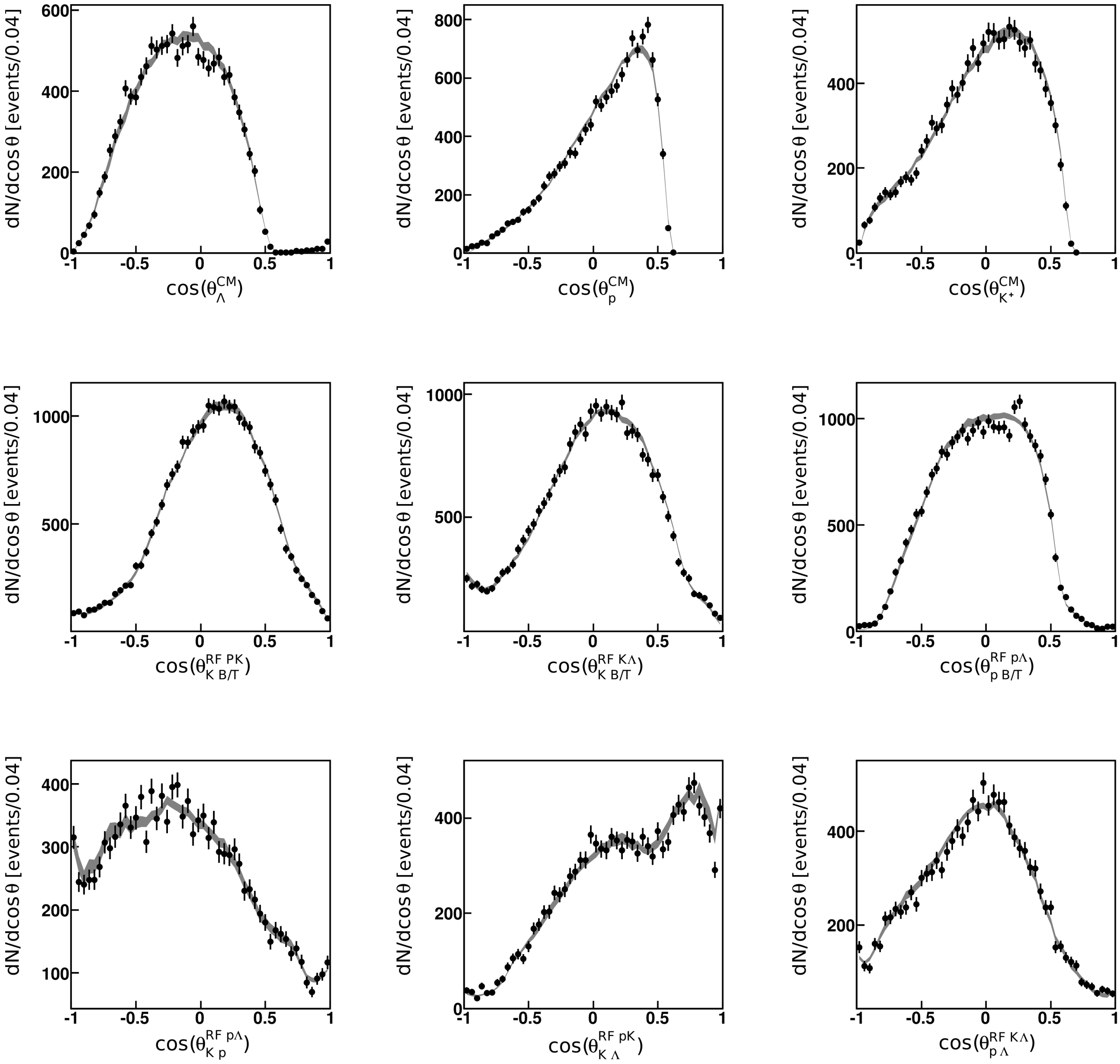

Figure 4.18: Angular correlations of the three particles for the **HADES data set** (black points) shown with the **four best PWA solutions** (gray band), obtained by a fit to the HADES and WALL data. For details about the observables see Fig. 2.6.

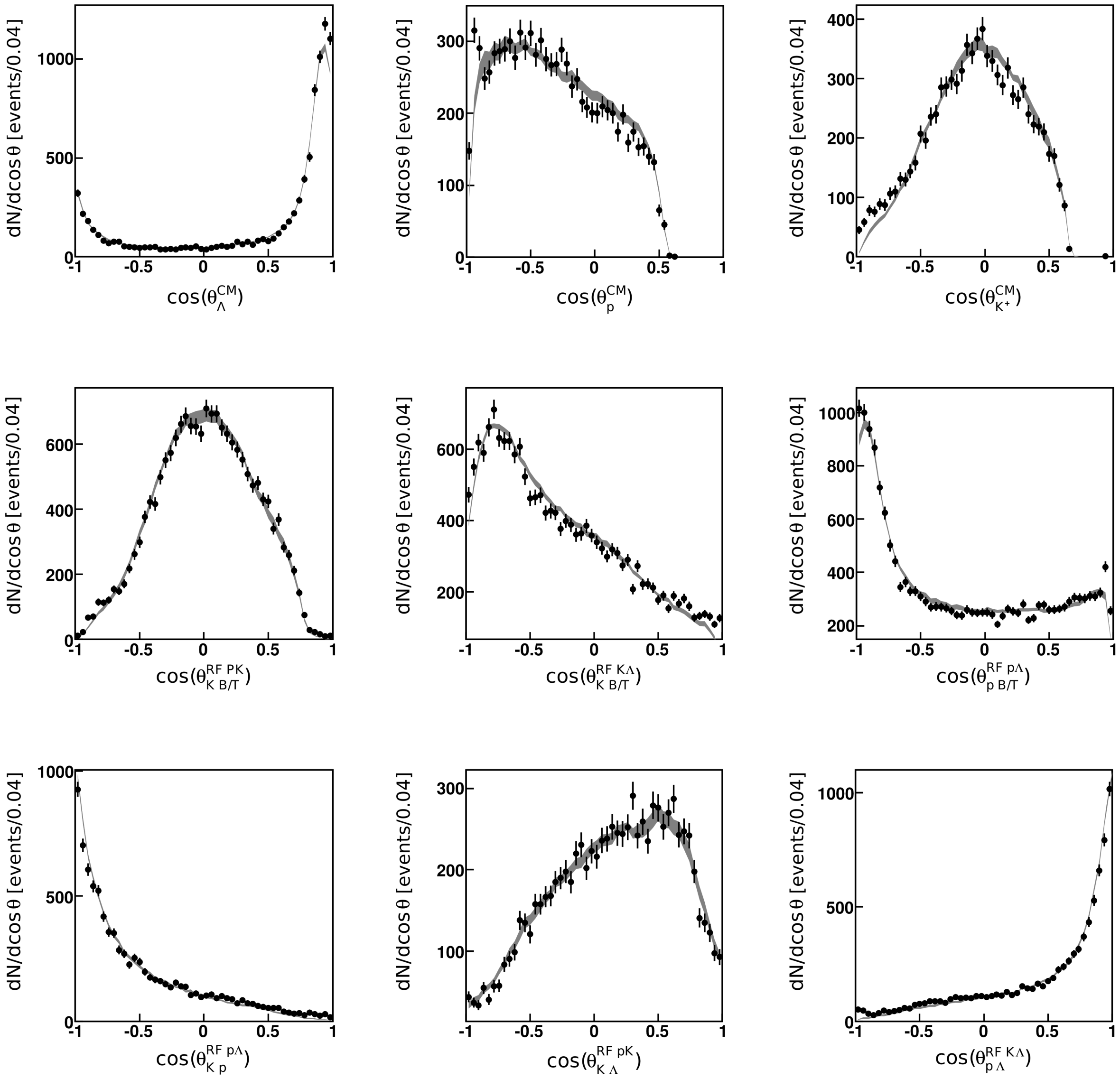

Figure 4.19: Angular correlations of the three particles for the **WALL data set** (black points) shown with the **four best PWA solutions** (gray band), obtained by a fit to the HADES and WALL data. For details about the observables see Fig. 2.6.

5 | Is There a New Signal? - A Statistical Analysis

The discovery of a new signal implies that the so far known concepts have failed to describe a measurement. Only then it is legitimate to test further hypotheses that include the existence of new particles. In order to do that, at least two hypotheses have to be tested on the data. The so called background hypothesis (established signal sources) and the signal hypothesis (new signal component and background).

This chapter discusses the test of two hypothesis compared to the data. To quantify the test results the frequentist statistics is introduced and applied.

5.1 The Frequentist Approach

The fequentist approach is based on the idea to quantify the reliability of a result based on its recurrence in case of constantly repeating an experiment. It is important to note here that the frequentist statistics will not deliver confidences in a model or parameter but the statement one obtains is about the probability to observe the measured data.

The approach quantifies the agreement between a model and data. This is done by defining a discrepancy variable (test statistic) [186].

In this analysis, the data are compared to the model in a binned representation (mass bins, angle bins etc.). Here, uncorrelated events with non-varying probability of occurrence are summarized. In such cases, the statistic inside one bin approximates a Poisson distribution [187]. This analysis uses, based on the argumentation in Ref. [186], the Pearson χ^2 statistic:

$$\chi_P^2 = \sum_{i=1}^{N_b} \frac{(m_i - \lambda_i)^2}{\lambda_i}, \tag{5.1}$$

as a discrepancy variable. Here, m_i are the number of measured events in the bin i, and λ_i are the number of expected events in the bin according to the model. N_b is the number of considered bins. In the Poisson statistic the standard deviation of the expected value is given by $\sqrt{\lambda_i}$. The denominator in Equation (5.1) is, thus, the squared error of the expected bin entry according to the model. The measured values m_i fluctuate around their expectation value λ_i. Even in case the data are compared to the correct model the discrepancy between model and data will vary with a certain probability. Due to these fluctuations χ_P^2 is also a random variable. The probability distribution of the measured χ_P^2 value, P(χ_P^2,Ndf), can be approximated by a χ^2-distribution [186], with Ndf being the number of degrees of freedom of the test. The observed χ_P^2 can take all values between 0 and ∞, where the most likely value of the probability distribution is Ndf. In most cases one would expect to measure a χ_P^2 value close to Ndf whereas large χ^2 values occur with a lower probability.

Rather than using χ^2 directly to express the trust in a model, one uses the p-value. A p-value is defined based on a discrepancy variable, as it is constructed as the integral over the probability density function (pdf) of the discrepancy variable. The integral starts from the measured discrepancy value of the examined data ($\chi_{P,d}^2$) and ends at infinity. In this approach, the p-value is calculated from a χ^2-distribution which is a good approximation for the real pdf of χ_P^2. The p-value of χ_P^2 is, thus, written as:

$$p\text{-}value = \int_{\chi_{P,d}^2}^{\infty} P(\chi^2, Ndf) d\chi^2. \tag{5.2}$$

Here, $P(\chi^2, Ndf)$ is the pdf of the χ^2-distribution and $\chi_{P,d}^2$ is the Pearson χ^2-value of the present data. As the p-value is calculated from the tail of the probability distribution, it tells, given the model is correct, how probable it would be to observe an agreement between the model and the data that is equal or worse than the observation in the present experiment. Due to its mathematical construction a p-value distribution for a correct model is expected to be flat between [0,1] [186]. Wrong models on the other hand will produce very small p-values, which have a rapidly falling distribution towards higher p-values [186]. This is the reason why p-values can be used to discriminate models. If one observes, for example, a p-value of 0.01 one would, in case the model is correct, have observed one of the 1% most unlikely experimental outcomes. In such a case one would tend to conclude that the model one used is probably not correct rather than considering a very unlikely outcome.

Unfortunately, there is a constantly reoccurring misunderstanding about the meaning of p-values. This topic is intensively discussed in the literature [188, 189, 190, 191]. Especially Ref. [191] summarizes nicely how a p-value is often misunderstood as a probability of the model or a tested parameter. This is not the case; with that method one gains no information how probable a certain scenario or parameter is. Such information can only be achieved by a Bayesian analysis. Remembering the footing of the frequentist statistic one should stick to the expression that **given the tested model one has observed one of the α% most unlikely outcomes**. Rejecting a hypothesis at a certain probable outcome does at the same time imply that in α% of the cases one would reject a hypothesis though it is actually true, only because one has had bad luck and detected a very unlikely outcome. This scenario is called a Type-I error [192]. In this sense the p-value is not a strict criteria which will falsify models on an absolute level, if a model is rejected based on the p-value it is, thus, not proven to be wrong but it is determined to be unlikely that the model would produce such an experimental outcome.

5.2 Test of the Null Hypothesis H_0

A null hypothesis is also called the background-only hypothesis and assumes that the observables can be described by well established physical signals. The search for a new signal aims to reject the null hypothesis. The null hypothesis itself is, thus, enough in order to discover a new signal. Due to the complexity of the $pK^+\Lambda$ production process there is, so far, no theoretical model that can predict the full event kinematic and with this the expected shape of the $p\Lambda$ mass distribution a priori. The only models which describe, for example, the $p\Lambda$ mass distribution are, therefore, the data based PWA solutions. These solutions contain, up to this point, no additional signal besides the production of N* resonances and non-resonant $pK^+\Lambda$ production. This is the reason why the further statistical tests are performed with the four best solutions of the PWA analysis, obtained by a fit on both experimental data sets, as null hypotheses.

The statistical test was performed on the measured data sets for HADES and WALL separately. The observable expected to be most sensitive to the production of a kaonic cluster is the invariant mass distribution of $p\Lambda$. Here, the statistic of events that contain the production of a cluster, is expected to accumulate around a certain value which would correspond to the mass of the cluster. The model is, thus, compared to the data in this observable. As discrepancy variable χ^2_P was used, as described in Section 5.1. The χ^2_P was calculated for each mass bin separately (to be sensitive to the mass of the kaonic cluster) and one, therefore, speaks of a local p_0-value.[1] To account for the systematic uncertainty

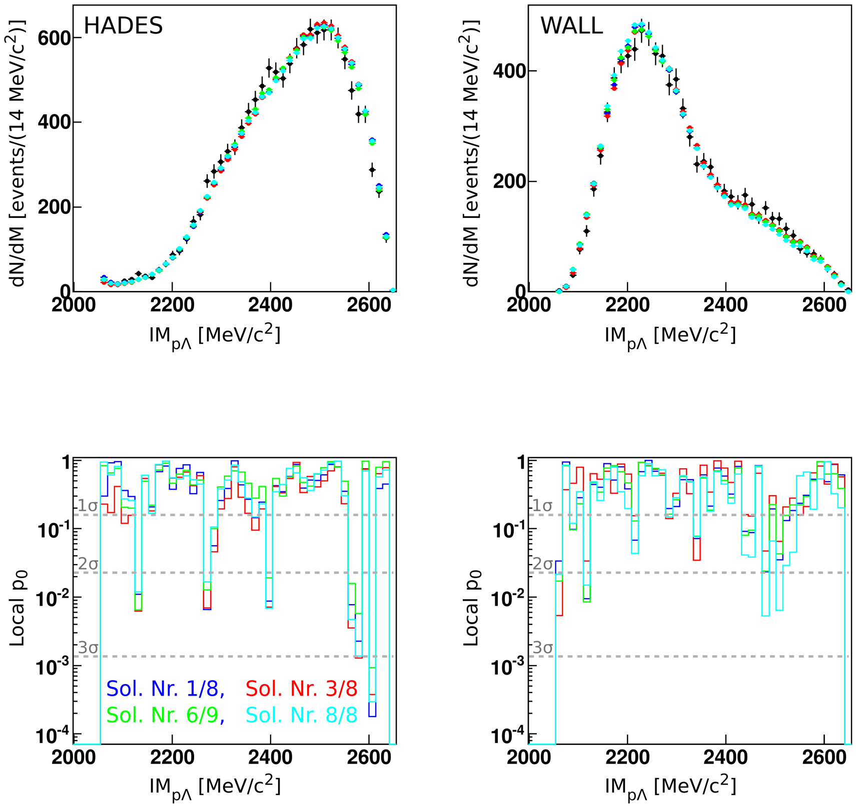

Figure 5.1: The upper figures compare the four best PWA solutions to the measured data (Based on a fit to both data sets HADES and WALL). Shown is the invariant mass of $p\Lambda$ of both data sets compared to the solutions. The lower figures contain the local p_0 distributions for the four PWA solutions compared to the measured data. The gray dashed lines mark the equivalent significances 1σ, 2σ, and 3σ, respectively.

---

[1] The index 0 indicates that it is the p-value of the null-hypothesis.

of the PWA fitting procedure the local p_0-value was determined for all four best solutions separately. Figure 5.1 summarizes the different p_0-values of these solutions for both mass distributions (see App. F for separate figures). As the four solutions predict similar values for the expected number of events in each bin the extracted p_0-values are also very similar. The uncertainty of the four extracted p-values depending on the PWA solution can be compiled in a gray systematic band. This is illustrated in Fig. 5.2. The separately calculated results can also be combined by a sum over the discrepancy in the same HADES and WALL mass bin. Then the χ^2_P from Equation (5.1) is a sum over two discrepancies. If an enhancement of the data compared to the model is present in both data sets, this sum would strengthen the observed deviation. If a deviation is present only in one data set, it is probably a fluctuation and then the combined analysis will smooth out these results. The combined p-value from both data sets is shown in Figure 5.3.

The agreement between a hypothesis and measured data, in the field of particle physics, is usually expressed in in terms of n·σ, which is called equivalent significance [192]. To obtain this equivalent significance the upper tail (p-value) of the χ^2-pdf is translated to an upper tail of the standard Gaussian pdf [192]. In this way one can translate $\chi^2_{P,d}$ to an equivalent value $gauss_d$ (in case the data would fluctuate according to a normal distribution). As $gauss_d$ expresses an upward fluctuation of a standard Gaussian random variable (instead of a Poisson random variable) it is natural to express this upward fluctuation (distance from the mean) in terms of n standard deviations (nσ). This equivalent significance is also plotted on the y-axes of Figures 5.1 and 5.2. A deviation is called significant if the probability of a data point fluctuating by chance with respect to a given model by chance is certainly low.

By pure convention a deviation is declared as indication (<3σ), observation (3σ) and discovery (5σ) respectively [193]. These standard deviations correspond to probabilities when expressed as p-values. A 3σ standard deviations for example includes 99.73% of the area under a normal distribution. As a p-value is defined as the tail of a distribution (outside nσ) this would correspond to a p-value of 0.0027. If one considers only one-sided fluctuations, as one can clearly see whether the data overestimate or underestimate the model, the probability to find a data point outside a one sided range of 3σ is 0.13%. This reads as a rather low probability and is thus classified as observation. However, only the measurement of a one sided fluctuation that occurs with a probability of 0.000029% by chance is considered to be so significant to announce a discovery of a new signal (this corresponds to a p-value of $2.9 \cdot 10^{-07}$).

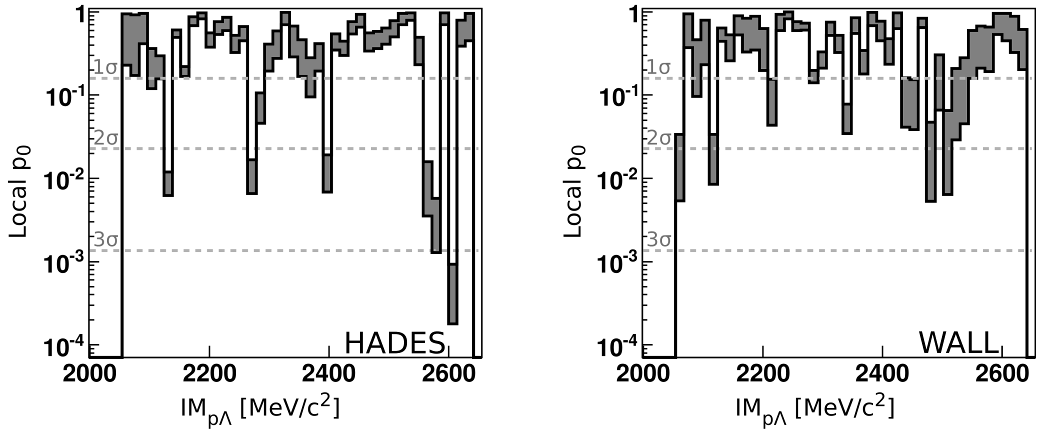

Figure 5.2: The range of p-values from the four best solutions (see Figure 5.1) is displayed here as a gray band. The gray dashed lines mark the equivalent significances 1σ, 2σ, and 3σ, respectively.

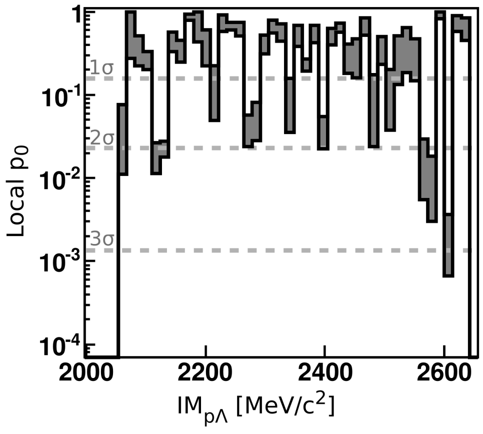

Figure 5.3: The figure shows the local p_0 distribution for a combined analysis of HADES and WALL data. The differences between the four best solutions are summarized by a gray band. The gray dashed lines mark the equivalent significances 1σ, 2σ, and 3σ, respectively.

In this test the p-values in Figure 5.2 reach only in one bin an equivalent significance of 3σ within the full range of its systematic uncertainty[2]. There is, still no observation of a signal as I) the mass of 2600MeV/c^2 is far above the mass of a bound ppK^- system below ≈2370MeV/c^2 II) The fluctuation is only visible in the HADES data set and absent in the WALL data set and III) the strongest point is that this bin shows a downward fluctuation of the data with respect to the models, see upper panel in Fig. 5.1. Thus, this can not be a sign of an additional signal. As all other local p_0-values stay far beyond 2.5σ the conclusion of this investigation is that the data are fully consistent with the null hypothesis within the systematic uncertainties. There is no need to include an additional signal into the model to describe the data. No hint of a kaonic cluster was found in both data-sets.

In tests where one calculates local p_0-values one should, in principle, take also the "look elsewhere" effect into account [194]. This effect describes the fact that also correct models can yield with a certain low probability small p-values. If one compares a model to the data in many experiments ($\widehat{=}$ many bin entries) one would increase the chance to observe in one of the experiments an improbable outcome. If one would investigate an infinite number of mass bins it will happen that at one mass bin the p-value will be so low that one could announce a discovery. This effect can be corrected. As in this data, however, no signal candidate is observed there is no need to quality check and correct the p-value for the "look elsewhere" effect.

5.3 The Research Hypothesis H_μ

The data do not support the hypothesis of a kaonic cluster being produced in the investigated process. Its existence, still, cannot be ruled out. In order to give a quantitative statement of its possible production cross section in a proton proton collision at 3.5 GeV beam kinetic energy an upper limit of the latter was determined. As we observe one particular decay channel of the kaonic cluster, see Reaction (1.12)-(1.15) of Chapter 1, we can only report about a fraction of the total production cross section.

This part of the thesis will show the test of the research hypothesis H_μ which includes a small yield of produced kaonic clusters to obtain a quantitative statement about the upper limit on its production cross section. μ here stands for a flexible production cross section that is proportional to the transition amplitude

---

[2] Visible in the HADES dataset (left panel) one of the very right mass points at 2600MeV/c^2.

of the final state in which the kaonic cluster is formed. The research hypothesis H_μ is constructed out of the null hypothesis H_0 by including an additional transition amplitude into the model. The parameters in the H_μ-hypothesis are fixed to the values of H_0. Only two parameters in H_μ are free. This is the phase and amplitude of the wave in which a kaonic cluster is produced.

The upper limit on the production strength of the kaonic cluster is obtained with the CL_s method [192, 195, 194, 196]. This method is an advancement of the standard frequentist confidence level CL. The frequentist 'confidence level' covers the true parameter with a probability of CL% $\hat{=}$ 1-α%, where α is called the size or significance level of the test and is equal to the p-value. By convention tests are usually done at a CL of 95 or 99%. The probability that the parameter is not in the stated region is then only 5% or 1%. This Type-I error rate is expressed by α and should be sufficiently small.

A parameter in a test of size α will be rejected if:

$$p_\mu \leq \alpha, \tag{5.3}$$

where p_μ is the p-value obtained in a test of a hypothesis were the tested parameter has the strength μ, e.g. the kaonic cluster production cross section.

This standard approach has a critical drawback in case of signals with a low production yield. By this conventional method one may exclude signals to which the experiment has no sensitivity [192].[3] A further critical point is the fact that one can show that the experiment with the higher expected background can set stronger constraints on a production yield as compared to a background optimized experiment [196]. The reason for this is that the CL limit will always deliver statements about the signal plus background, as it is technically not possible to separate both in most experiments. The modern approach called CL_s tries to solve these problems. Here the 'confidence level' is defined as a ratio of the H_μ and H_0 hypotheses. Is reads as follows:

$$CL_s = \frac{p_\mu}{1 - p_0}. \tag{5.4}$$

Values are rejected in a test if $CL_s \leq \alpha$. The new selection condition for p_μ translates into:

$$p_\mu \leq \alpha \cdot (1 - p_0). \tag{5.5}$$

---

[3] E.g. cases in which the background fluctuation is artificially low.

5.3.1 Implementation

The research hypothesis contains three different transitions amplitudes in which a kaonic cluster could be produced:

$$WaveA: \ 'p+p' \ \ {}^1S_0 \rightarrow \ 'ppK(2250)-K' \ \ {}^1S_0, \tag{5.6}$$

$$WaveB: \ 'p+p' \ \ {}^3P_1 \rightarrow \ 'ppK(2250)-K' \ \ {}^1P_1, \tag{5.7}$$

$$WaveC: \ 'p+p' \ \ {}^1D_2 \rightarrow \ 'ppK(2250)-K' \ \ {}^1D_2. \tag{5.8}$$

In this expression the spectroscopic notation ${}^{2S+1}L_J$ is used to characterize the initial and final state, see Equation 4.18. The produced yield of the kaonic cluster will, most likely, stem from a sum of all three waves. For technical purposes we tested three different conditions, where the whole yield stems exclusively from Wave A, Wave B, and Wave C, respectively. To take into account that our knowledge on the true N^* content in the data is limited, these three waves were implemented into each of the four best background hypotheses (H_0) to construct four different research hypotheses. This will deliver a systematic uncertainty on the extracted result. The tested combinations are summarized in Table 5.1. Since consistent information about the mass and width of the kaonic cluster are not available from theory, several mass and width combinations were tested. In this work, 16 different masses ranging from 2220 to 2370 MeV/c^2 were tested in 14 mass bins of the $p\Lambda$ mass observable. As the tested widths of the kaonic cluster are by far larger than the bin width, many bins in the model histogram will be affected by its implementation. The tested combinations are summarized in Table 5.2. The kaonic cluster is implemented in the Bonn-Gatchina PWA framework as relativistic Breit-Wigner-distribution, introduced in Equation (4.16).

Table 5.1: The combinations for each kaonic cluster value include 4 PWA solutions and three transition amplitudes. In total: 12 different hypothesis. The nomenclature of the solutions is taken from Table 4.6.

	WaveA	WaveB	WaveC
Sol No. 1/8	x	x	x
Sol No. 3/8	x	x	x
Sol No. 6/9	x	x	x
Sol No. 8/8	x	x	x

To summarize shortly: a hypothetical kaonic cluster is included in a fixed solution of the PWA. The phase of this transition is free to vary, while amplitude

Table 5.2: Tested kaonic cluster values. Each point has a combination of a certain mass and a width. In total 48 combinations were tested.

Mass [MeV/c^2]	Width [MeV/c^2]
2220	30, 50, 70
2230	30, 50, 70
2240	30, 50, 70
2250	30, 50, 70
2260	30, 50, 70
2270	30, 50, 70
2280	30, 50, 70
2290	30, 50, 70
2300	30, 50, 70
2310	30, 50, 70
2320	30, 50, 70
2330	30, 50, 70
2340	30, 50, 70
2350	30, 50, 70
2360	30, 50, 70
2370	30, 50, 70

is scaled higher and higher in each test. The outcome of the fits with varying amplitudes are compared to the data. For each solution it is tested whether the agreement with the data excesses the pre-defined CL$_s$ value. This test of increasing amplitudes is done for all four best solutions of the PWA and for all three transition amplitudes that contain a kaonic cluster. This results in twelve different upper limits which will define a range of uncertainty of the tested model, see Table 5.1. To account for the theoretical dispute on the exact properties of the kaonic cluster, means the mass and width of this state, several masses and widths were tested in combination. Table 5.2 contains all tested properties of the kaonic cluster.

5.3.2 Parameter determination

This work will deliver an upper limit for the $\overline{K}NN$ production cross section at a CL_s of 95%. To obtain this level the research hypothesis H_μ has to be compared to the data for several values of the implemented amplitude strength of the kaonic cluster production wave. To obtain the full hypothesis H_μ, however,

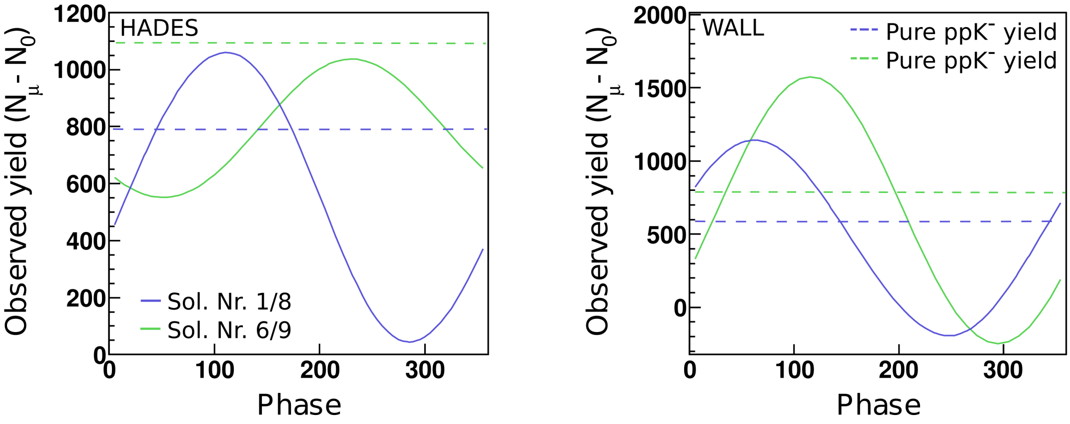

Figure 5.4: The dashed line illustrates the produced yield of kaonic clusters and the solid line illustrates the yield observed after interference. Shown are for each dataset (HADES left, WALL right) two different PWA solutions. The amplitude is fixed to 10.

the waves once more have to be fitted to the data. This has its origin in the unknown phase of the transition amplitude. Depending on this parameter the wave of the kaonic cluster may interfere constructively or destructively with all the other waves with the same J^P configuration. Due to this interference, the observed 'bump' in the $p\Lambda$ invariant mass distribution will differ. Figure 5.4 shows for a given amplitude strength the yield one observes with respect to the null hypothesis as a function of the phase of the wave. The observed yield is calculated as the difference between the null hypothesis and the research hypothesis ($N_\mu - N_0$). The input yield of the kaonic cluster, which is proportional to the amplitude strength, stays constant.

The solid, green curve in Figure 5.4 shows the observed kaonic cluster yield for the best solution No. 6/9 (Table 4.6). The kaonic cluster wave has a maximum destructive interference at a phase of 50 degree and a maximum constructive interference at 230 degree for the HADES data set. For the WALL data-set the maximum destructive interference is at about 300 degree while the maximum constructive interference is around 115 degree. The reason for this difference is based on the different geometrical acceptance of both data sets. Within the acceptances the ratio of the yield from different transition waves varies which results in specific interference patterns. In principle, the upper limit can be calculated by assuming, in a conservative case, a maximum destructive interference. In this case a maximum amplitude strength can be included with, at the same time, minimal influence on the mass spectrum. As illustrated in Figure 5.4, however, the maximum destructive interference is not clearly defined, as it differs for both data sets. The most conservative estimation (destructive interference) can, thus, not be set by hand. Because of that the phase is free to vary and is determined by a new fit to the data. For each amplitude iteration the phase that fits best to both data sets is determined. The fit will find, in an ideal case, a compromise for the minimal observed yield between the HADES and WALL data set. Still, also in case of destructive interference at a certain amplitude strength, a signal in the $p\Lambda$ mass spectrum will be visible.

After fitting the research hypothesis to the data all parameters are fixed. This procedure is repeated in a first iteration for six different amplitude strengths of equal step size. Figure 5.5 shows the development of the visible kaonic cluster yield in the research hypothesis H_μ. It is always compared to the experimental data and the null hypothesis H_0. Also displayed is the pure kaonic cluster yield before the interference. As the fit tries to create a result consistent with the data a destructive type of interference is observed. This can be recognized by the small difference between H_μ and H_0 although already an evident yield of kaonic cluster is put into the hypothesis.

To finally obtain a quantitative statement about the agreement between data and H_μ, the resulting mass distribution of the hypothesis is compared to the data for each tested amplitude strength. The p-value of the research hypothesis is calculated as follows: The resulting mass distribution of H_μ is scaled to the data in the region excluding the signal area of $M_{ppK^-} \pm \Gamma$. Then χ^2_P is calculated by a sum over all bins in the histogram, see Equation (5.1). From this χ^2_P-value the p-value of H_μ is calculated. A result of this procedure is presented in Figure 5.6, where the p_μ-value of the HADES dataset is shown as a function of the increasing amplitudes. The figure shows the test for a mass of 2370 MeV/c^2 and a width of 50 MeV/c^2. The tested solution is No. 1/8. Shown in Figure 5.6 is the p-value for all three transition waves. The p_μ-value decreases with increasing amplitude. The higher the signal strength the worse the agreement of H_μ with the measured data. The dashed orange line shows a p-value of 0.05. The p-value that satisfies the constraints of CL_s is represented by the red dashed line. This line is below 0.05 and is calculated according to Equation (5.5). The size of the test α was set to 5%. In order to determine the factor $(1 - p_0)$ the p-value of H_0 was calculated in the same region as previously for H_μ. As for each H_0 hypothesis of the four different solutions p_0 was calculated

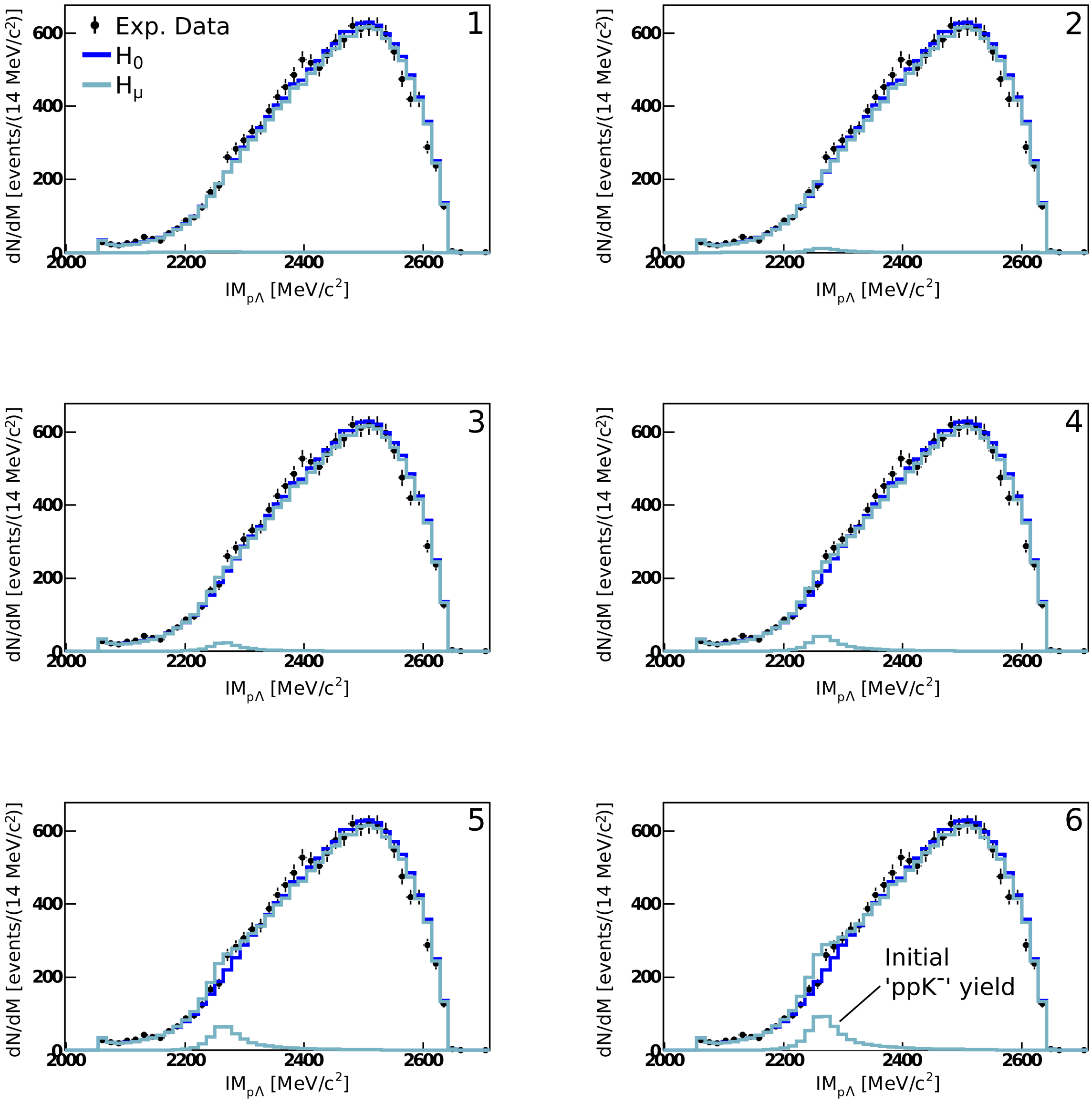

Figure 5.5: An example of the increasing amplitude strength (1-6). The pictures show the result for the HADES data set and the solution 1/8, where the kaonic cluster is produced via Wave C. The kaonic cluster was simulated with a mass M=2260 MeV/c^2 and a width of Γ=50 MeV/c^2.

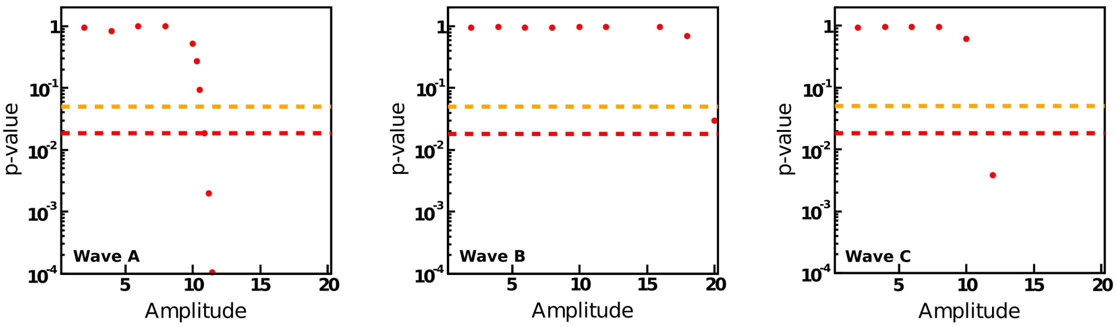

Figure 5.6: The p_μ-value of the HADES dataset as a function of the amplitude of the kaonic cluster wave. The example shows the test with M=2370 MeV/c^2, Γ=50 MeV/c^2. CL 95% (orange-dashed line), CL_s95% (red-dashed line).

separately, the extracted CL_s limit to which H_μ is compared to will differ for the four cases but will in any case be lower than 0.05.

All amplitudes that deliver a p-value lower than indicated by the red line are rejected by the fit. As the amplitude iteration steps are finite the upper limit is not determined with a fine precision but has a certain error. This finite step size is dedicated to the fact that the data have to be fitted again to extract the phase of the wave. Since this procedure is very time consuming when testing it with all the parameters the amplitudes are only increased with a finer step-size in the vicinity of the rejection amplitude.

By combining the amplitudes that fulfill the condition of CL_s one can present the result as a function of the kaonic cluster mass, as done in Figures 5.7, 5.9 and 5.11. The four different solutions are represented by the different colors. The points represent amplitudes still consistent with the CL_s criteria the error goes up to the points which were rejected by the test. The exact value at which the transition from accepted to rejected happens lies somewhere between these two limits. Only some of the amplitudes where sampled in a second iteration with smaller steps. This is the reason for the different error widths. Most important was the sampling of the solutions which gave the largest compatible amplitude as this constructs the upper limit of the kaonic cluster production strength, based on our model.

Besides extracting the amplitude at which the CL_s criteria is no longer fulfilled, the Bonn-Gatchina framework allows to translate the amplitude of a process into its percentage on the total production cross section of the final state. This

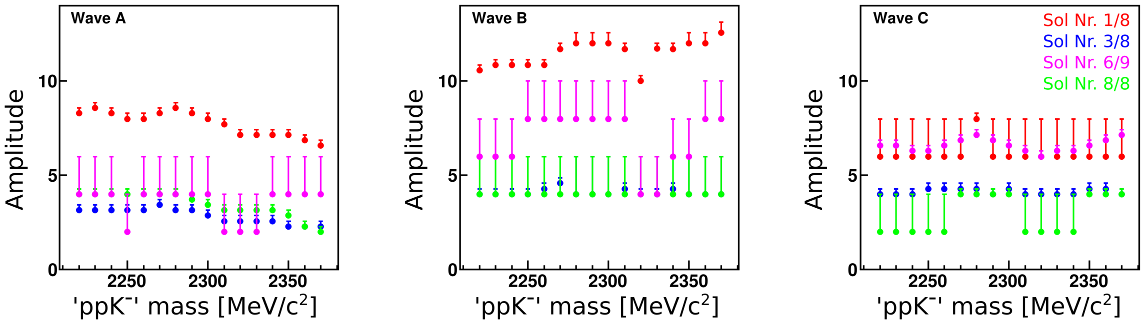

Figure 5.7: The upper accepted amplitude at a CL_s limit of 95%. The three figures show the limit for all three transition amplitudes. The different colors represent the upper limit for the four best solutions. This is obtained from the HADES data-set for a simulated width of 30 MeV/c^2.

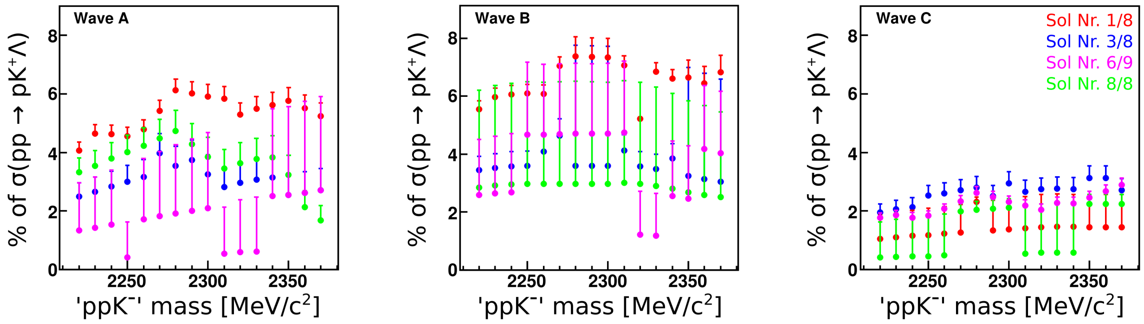

Figure 5.8: The upper limit on the production of a $\overline{K}NN$ in the measured reaction at a CL_s limit of 95%. The limit is quoted in percentage of total $pK^+\Lambda$ production cross section. The three figures show the limit for all three transition amplitudes. The different colors represent the upper limit for the four best solutions. This is obtained from the HADES data-set for a simulated width of 30 MeV.

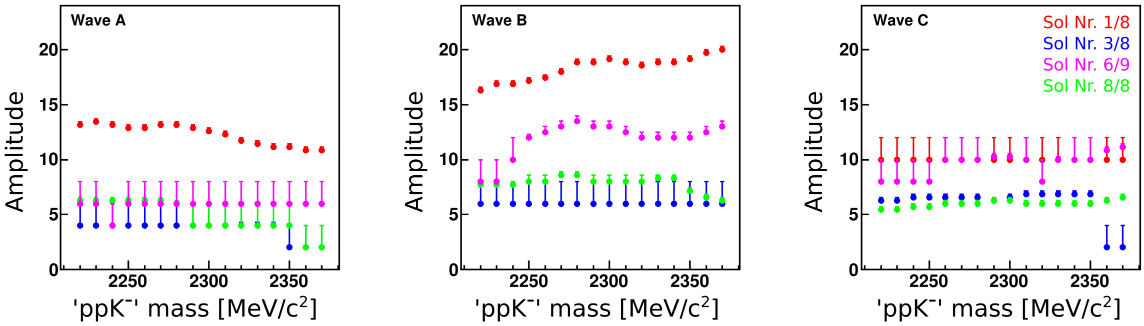

Figure 5.9: The upper accepted amplitude at a CL_s limit of 95%. The three figures show the limit for all three transition amplitudes. The different colors represent the upper limit for the four best solutions. This is obtained from the HADES data-set for a simulated width of 50 MeV/c^2.

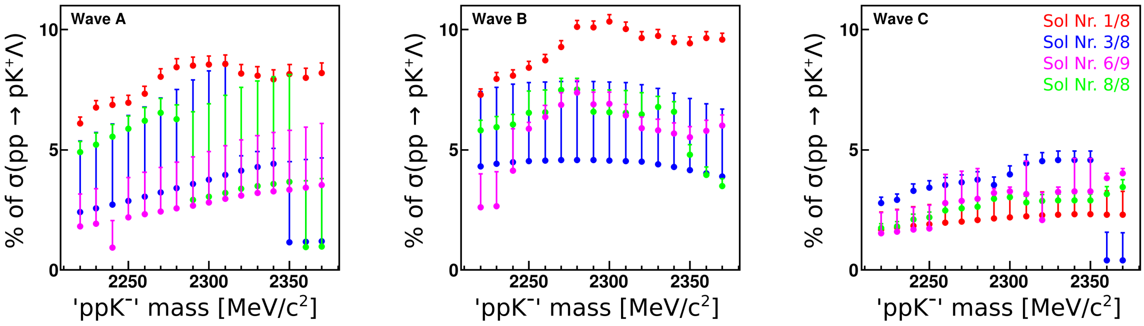

Figure 5.10: The upper limit on the production of a $\overline{K}NN$ in the measured reaction at a CL_s limit of 95%. The limit is quoted in percentage of total $pK^+\Lambda$ production cross section. The three figures show the limit for all three transition amplitudes. The different colors represent the upper limit for the four best solutions. This is obtained from the HADES data-set for a simulated width of 50 MeV.

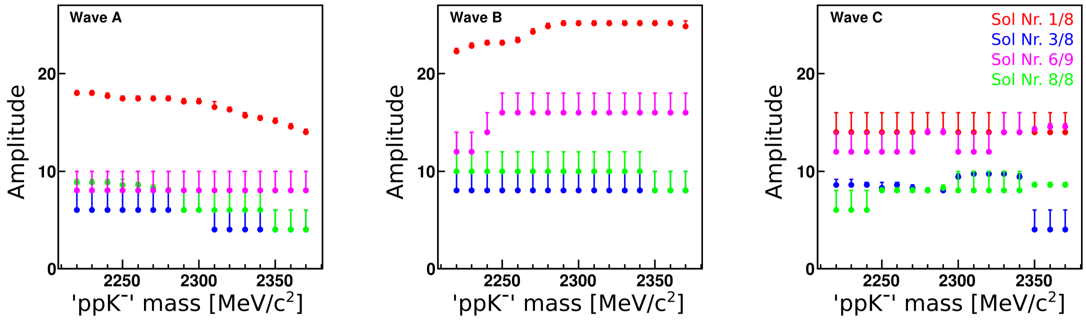

Figure 5.11: The upper accepted amplitude at a CL_s limit of 95%. The three figures show the limit for all three transition amplitudes. The different colors represent the upper limit for the four best solutions. This is obtained from the HADES data-set for a simulated width of 70 MeV/c^2.

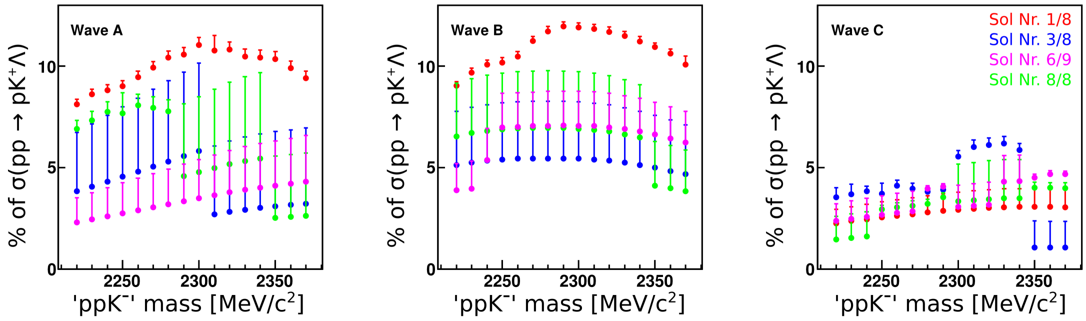

Figure 5.12: The upper limit on the production of a $\overline{K}NN$ in the measured reaction at a CL_s limit of 95%. The limit is quoted in percentage of total $pK^+\Lambda$ production cross section. The three figures show the limit for all three transition amplitudes. The different colors represent the upper limit for the four best solutions. This is obtained from the HADES data-set for a simulated width of 70 MeV.

is shown in Figures 5.8, 5.10 and 5.12. The resulting numbers might seem astonishingly high. Unlike in many analyses where the observed yield in a bump is directly related to a production yield, this can not be done with interference. When two sources interfere the final yield can not be attributed clearly to one or the other source only from observing the interference pattern. The percentages quoted in Figures 5.8, 5.10 and 5.12 are, thus, attributed to an initial yield before interference as, a final yield is not clearly defined in this approach. Only in case of absent interference one could observe directly a signal with 5% signal strength as compared to the total $pK^+\Lambda$ production cross section.

For an upper bound on the production amplitude the most conservative case at a mass point is the one that sets the limit. The differences arise from the different interference patterns in the solutions. Figure 5.4 already indicated the strong destructive interference of solution 1/8 which in this case also sets the upper limit for most of the cases. To summarize the results of Figures 5.8, 5.10 and 5.12 the highest percentage of cross section still accepted by CL_s is shown in Figure 5.13. One can see that the upper limit as a function of the kaonic cluster mass is rather structure-less. While a kaonic cluster produced via Wave A and B seems to allow a higher yield by still being consistent with the data, a production of a kaonic cluster via Wave C is stronger constrained to about half the production strength as compared to the two other cases. The larger the width of the produced state the more yield is consistent with the data.

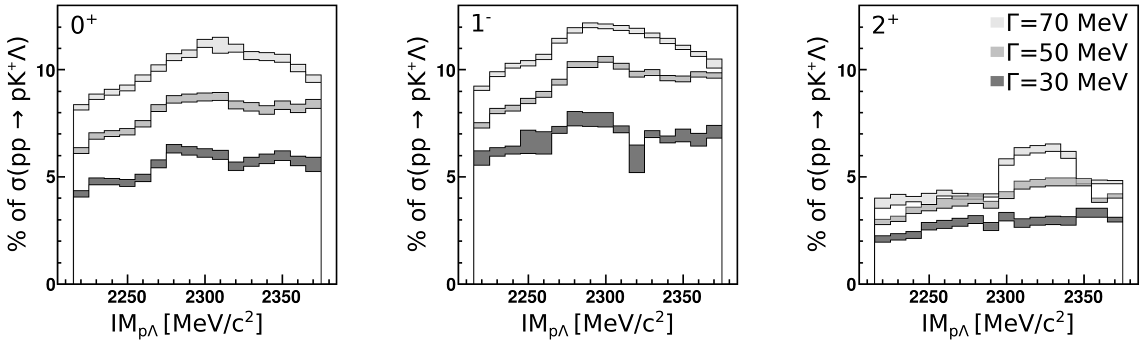

Figure 5.13: The upper limit on the production of a $\overline{K}NN$ in the measured reaction at a CL_s limit of 95%. The limit is quoted in percentage of total $pK^+\Lambda$ production cross section. The three figures show the limit for all three transition amplitudes. This is obtained from the HADES dataset for a simulated width of 30, 50, and 70 MeV.

6 | Extraction of the $pK^+\Lambda$ Production Cross Section

This chapter discusses the different PWA solutions in 4π. Contributions of single waves to the total solution are shown and explained. With help of these PWA solutions an acceptance correction of the measured data is performed. This correction allows to extrapolate the measured yield in the limited detector acceptance to the full phase space. The corrected data are then interpreted and compared to other measurements.

6.1 PWA Solution in 4π

As previously discussed, the solution of the PWA can be displayed graphically by filling events from phase space simulations with their PWA weight into a histogram. This has been shown for simulated events inside of the detector acceptance in the previous chapter. The PWA can further also assign corresponding weights to simulated events in 4π. In this way a graphical representation of the PWA solution in the full phase space is obtained. As the HADES and WALL data sets are just two sub-statistics of the same process the 4π result is the same for both of them.

Figures 6.1 and 6.2 demonstrate the observables in the full phase space according to the four best PWA solutions. To compare the four best solutions in a convenient way the histograms were normalized to the same area. The prediction for the center of mass angles and the Gottfried-Jackson angles (middle row of Figure 6.2) according to the different solutions agree well. The invariant masses and the helicity angles (lower row of Figure 6.2) show some slight disagreements. The first panel of Figure 6.1 shows the invariant mass of the $\Lambda-K^+$-pair. As this observable is very sensitive to the content of N*-resonances

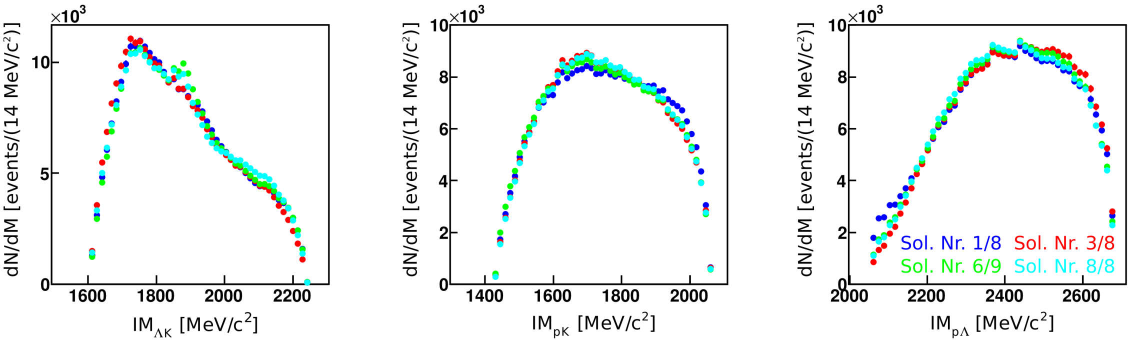

Figure 6.1: Two-particle masses for the four best solutions of the PWA (different colors). The results are normalized to the same area.

the discrepancies can be explained by their different contributions in the models. While Sol. No. 6/9 (green) and No. 8/8 (cyan) have a contribution of the N*(1895), this particle is missing in Sol. No. 1/8 (blue) and 3/8 (red). This effect reflects clearly the properties of the N*-resonance, listed in Table 4.1. The N*(1895) is the most narrow N* included in the PWA with a width of about 90 MeV/c^2 and hence its presence leads to an increased yield in the $\Lambda\, K^+$ invariant mass distribution around 1900 MeV/c^2.

Solution No. 3/8 (red) on the other hand does not contain the two high mass resonances N*(1895) and N*(1900) and has, hence, a systematic shift of its predicted $\Lambda\, K^+$ invariant mass distribution towards lower masses as compared to the other three solutions. This effect is even more clearly visible in the helicity plot in panel h) of Figure 6.2. In this reference frame solutions that contain N* resonances with low masses produce yield at small opening angles of Λ and K^+ ($\cos\theta \approx 1$), like sol. No. 3/8.

The results of the PWA can be also presented quantitatively. Table 6.1 contains the contributions of the different initial p+p waves to the total $pK^+\Lambda$ production cross section. The differences between the four best PWA solutions are obvious. The relative difference as compared to the highest value is displayed by the last column. The relative differences of the order of 50% are too large to draw conclusions about the single contributions of initial p+p amplitudes on the total production cross section. One can recognize, however, some qualitative trends. The $^3P_0$ initial state seems to have a small contribution in all solutions, while the largest contribution in all but one solution is given by the $^3F_2$ initial wave. This can be an argument to include higher partial waves of the initial state to

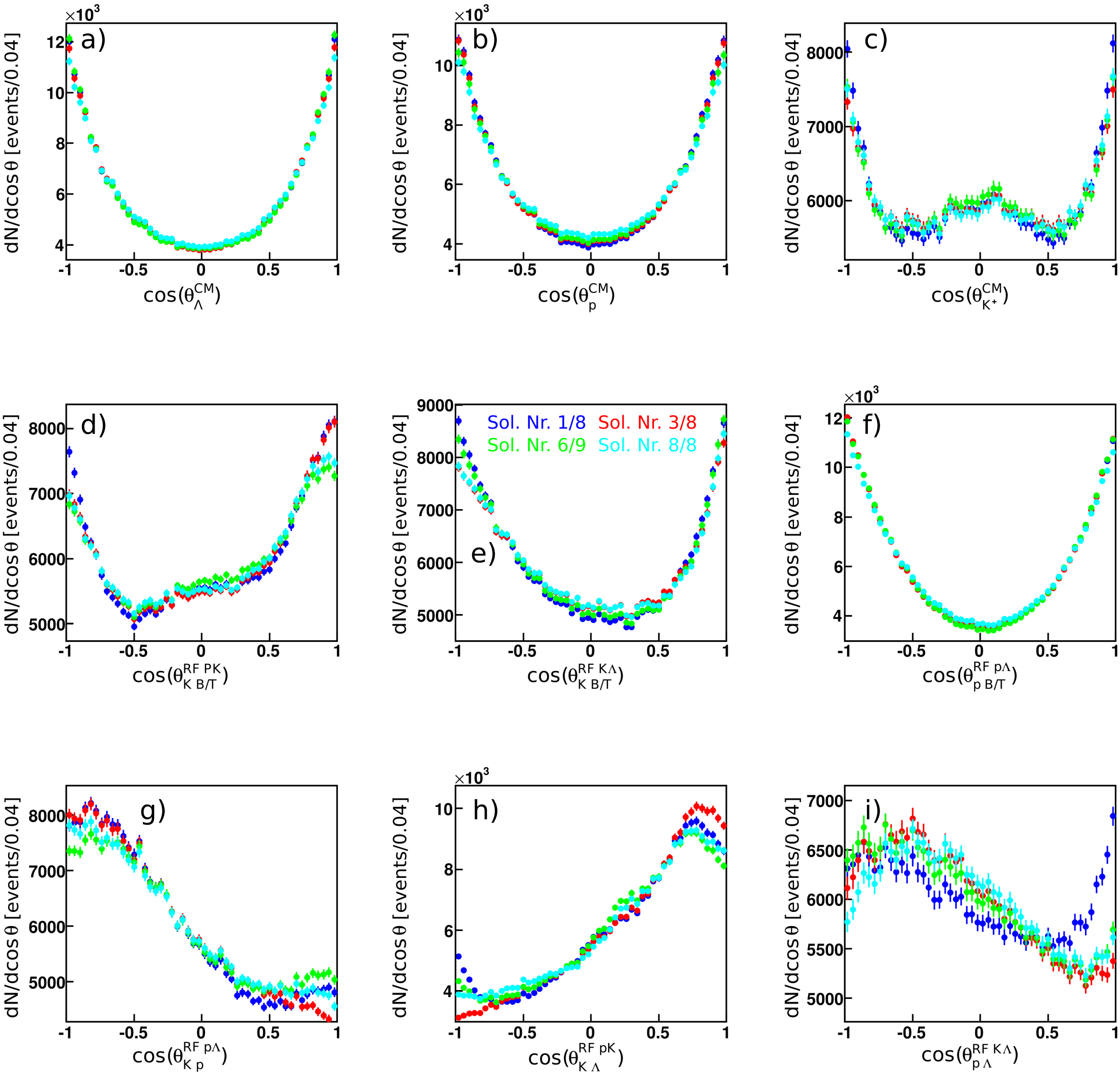

Figure 6.2: Angular correlations of the three particles for the four best PWA solutions of the PWA (different colors). The results are normalized to the same area. The upper row shows the angle of the particle in the CMS (a)-c)), the middle row show the Gottfried-Jackson distributions (d)-f)) and the lower row show the helicity angles (g)-i)). See Figure 2.6 for further explanations on the observables.

Table 6.1: Contribution of the different initial p+p waves to the total $pK^+\Lambda$ production cross section. All given in [%]. The last column shows the range R of the different solutions related to the highest value.

In. State	Sol. 1/8	Sol. 3/8	Sol. 6/9	Sol. 8/8	R/(hig. val.)
1S0	16.2	6.8	9.5	10.7	0.58
1D2	19.9	23.5	22.7	35.6	0.44
3P0	6.4	10.0	8.9	7.0	0.35
3P1	12.0	25.6	16.3	9.5	0.36
3P2	21.2	9.2	19.6	22.1	0.57
3F2	24.2	24.5	22.9	15.0	0.37

the fitting procedure by aiming to learn something about the exact partial wave contributions of the $pK^+\Lambda$ final state.

The transition waves with the different contributions of intermediate states to the $pK^+\Lambda$ final state are shown in the Tables 6.2 - 6.5. The transition waves are grouped according to their initial state, shown in the first column. All waves with the same initial state can interfere with each other. The intermediate state is shown in the second column. It expresses the N* or non resonant composition, followed by the total multiplicity (2S+1), and the angular momentum between the particles (S, P, D, and F). The contribution of each intermediate state of the transition is expressed in percent of the total $pK^+\Lambda$ production cross section. The waves marked with "-" were not included in the fitting routine of the particular solution. The range of the contributions varies largely. This means that within this approach no clear statement about the exact contribution of each wave to the final state can be drawn. To determine the exact partial wave content more data also at different beam energies and with polarization observables would probably be needed.

Table 6.2: Partial wave contributions to the 1S0 and 1D2 initial state. All in [%].

In. st.	Interm. st.	Sol. 1/8	Sol. 3/8	Sol. 6/9	Sol. 8/8	Range [%]
1S0	S_{11}(1650)p-3P	4.45	0.8	0.31	0.18	0.18-4.45
1S0	S_{11}(1895)p-3P	-	-	2.41	1.05	0.00-2.41
1S0	P_{11}(1710)p-1S	2.31	0.23	0.78	0.5	0.23-2.31
1S0	P_{11}(1880)p-1S	-	0.8	-	1.37	0.00-1.37
1S0	P_{13}(1720)p-5D	1.83	0	11.46	0.01	0.0-11.46
1S0	P_{13}(1900)p-5D	8.9	-	12.74	-	0.0-12.74
1S0	D_{13}(1875)p-3P	-	-	-	-	-
1S0	(pL)(3S1)K-3P	2.84	0.25	0.57	2	0.25-2.84
1S0	(pL)(3P0)K-1S	5.26	6.38	4.39	9.04	4.39-9.04
1S0	(pL)(3P2)K-5D	0.13	0.56	0.03	0.05	0.03-0.56
1S0	(pL)(3D1)K-3P	1.17	1	0.17	0.03	0.03-1.17
1D2	S_{11}(1650)p-3P	1.28	0.06	0.25	0.07	0.06-1.28
1D2	S_{11}(1650)p-3F	0.31	1.01	0.43	0.69	0.31-1.01
1D2	S_{11}(1895)p-3P	-	-	0.38	1.18	0.00-1.18
1D2	P_{11}(1710)p-1D	1.42	3.11	6.53	1.03	1.03-6.53
1D2	P_{11}(1710)p-3D	0.67	0.48	1.78	4.87	0.48-4.87
1D2	P_{11}(1880)p-1D	-	1.68	-	3.73	0.00-3.73
1D2	P_{11}(1880)p-3D	-	0.02	-	0.08	0.00-0.08
1D2	P_{13}(1720)p-5S	7.6	0.14	3.44	0.77	0.14-7.60
1D2	P_{13}(1720)p-3D	0.02	1.64	0.53	7.09	0.02-7.09
1D2	P_{13}(1720)p-5D	3.05	0.45	0.07	0.71	0.07-3.05
1D2	P_{13}(1900)p-5S	7.15	-	4.03	-	0.00-7.15
1D2	P_{13}(1900)p-3D	9.4	-	0.08	-	0.08-9.40
1D2	P_{13}(1900)p-5D	1.34	-	0.54	-	0.00-1.34
1D2	D_{13}(1875)p-5P	-	-	-	-	-
1D2	(pL)(1P1)K-3D	0.29	0.01	0.08	1.02	0.01-1.02
1D2	(pL)(1D2)K-5P	6.72	1.18	3.28	4.28	1.18-6.72
1D2	(pL)(1D2)K-5F	0.16	0.26	0.03	0.24	0.03-0.26
1D2	(pL)(3S1)K-3P	1.47	0.46	0.77	0.25	0.25-1.47
1D2	(pL)(3S1)K-3F	0.2	0.4	0.49	0.7	0.20-0.70
1D2	(pL)(3P0)K-1D	2.01	0.04	0.29	0.01	0.01-2.01
1D2	(pL)(3P1)K-3D	0.5	0.02	0.72	0.55	0.02-0.72
1D2	(pL)(3P2)K-5S	0.3	3.06	4.47	0.61	0.30-4.47
1D2	(pL)(3P2)K-5D	0.2	0.86	0.07	0.04	0.04-0.86
1D2	(pL)(3D1)K-3P	5	7.61	7.16	11.5	5.00-11.5
1D2	(pL)(3D1)K-3F	0.9	2.95	1.29	2.34	0.90-2.34
1D2	(pL)(3D2)K-5P	-	-	0.07	-	0.00-0.07
1D2	(pL)(3D2)K-5F	-	-	-	-	-

Table 6.3: Partial wave contributions to the 3P0 and 3P1 initial state. All in [%].

In. st.	Interm. st.	Sol. 1/8	Sol. 3/8	Sol. 6/9	Sol. 8/8	Range [%]
3P0	S_{11}(1650)p-1S	1.27	5.42	1.82	4.48	1.27-5.42
3P0	S_{11}(1895)p-1S	-	-	2.28	0.03	0.00-2.28
3P0	P_{11}(1710)p-3P	1.72	0.32	6.48	0.42	0.32-6.48
3P0	P_{11}(1880)p-3P	-	0.89	-	0.25	0.00-0.89
3P0	P_{13}(1720)p-3P	0.16	0.9	2.67	0.07	0.07-2.67
3P0	P_{13}(1900)p-3P	1.28	-	0.48	-	0.00-1.28
3P0	D_{13}(1875)p-5D	-	-	-	-	-
3P0	(pL)(1S0)K-1S	2.3	0.06	0.01	1.41	0.01-2.30
3P0	(pL)(1P1)K-3P	0.58	1.14	0.83	0.33	0.33-1.14
3P0	(pL)(3P1)K-3P	0.96	0.04	1.38	0.16	0.04-1.38
3P0	(pL)(1D2)K-5D	0.03	0.68	0	0.49	0.00-0.68
3P0	(pL)(3D2)K-5D	-	-	0.36	-	0.00-0.36
3P1	S_{11}(1650)p-3S	1.08	3.38	0.25	0.37	0.25-3.38
3P1	S_{11}(1650)p-3D	0.07	5.39	2.09	0.45	0.07-5.39
3P1	S_{11}(1895)p-3S	-	-	0.56	0.68	0.00-0.68
3P1	S_{11}(1895)p-3D	-	-	0.14	0.15	0.00-0.14
3P1	P_{11}(1710)p-1P	0.02	4.71	0.77	4.5	0.02-4.71
3P1	P_{11}(1710)p-3P	0.92	11.56	5.4	7.85	0.92-11.56
3P1	P_{11}(1880)p-1P	-	0.92	-	0.41	0.00-0.92
3P1	P_{11}(1880)p-3P	-	0.08	-	1.6	0.00-1.60
3P1	P_{13}(1720)p-3P	0.05	4.27	2.22	0.62	0.05-4.27
3P1	P_{13}(1720)p-5P	1.68	0.57	0.03	0.09	0.03-1.68
3P1	P_{13}(1720)p-5F	0	0	0	0	-
3P1	P_{13}(1900)p-3P	5.27	-	2.74	-	0.00-5.27
3P1	P_{13}(1900)p-5P	0.79	-	0.02	-	0.00-0.79
3P1	D_{13}(1875)p-3S	-	-	-	-	-
3P1	D_{13}(1875)p-3D	-	-	-	-	-
3P1	D_{13}(1875)p-5D	-	-	-	-	-
3P1	(pL)(3S1)K-3S	0.14	0.95	0.87	0.08	0.08-0.95
3P1	(pL)(3S1)K-3D	0.23	1.64	0.92	1.23	0.23-1.64
3P1	(pL)(3P0)K-1P	0.02	0.28	0.53	0	0.00-0.53
3P1	(pL)(1P1)K-3P	0.72	3.05	1.02	1.78	0.72-3.05
3P1	(pL)(3P1)K-3P	1.21	0.05	0.65	2.7	0.05-2.70
3P1	(pL)(3P2)K-5P	0.49	0.74	0.7	1.72	0.70-1.72
3P1	(pL)(3P2)K-5F	0.09	0.4	0.13	0.01	0.01-0.40
3P1	(pL)(1D2)K-5D	0.4	0.03	0.58	0.1	0.03-0.58
3P1	(pL)(3D2)K-5D	-	-	0.16	-	0.00-0.16
3P1	(pL)(3D1)K-3S	4.7	11.6	7.13	1.56	1.56-11.6
3P1	(pL)(3D1)K-3D	0.59	1.34	0.85	0.09	0.09-1.34

Table 6.4: Partial wave contributions to the 3P2 initial state. All given in [%].

In. st.	Interm. st.	Sol. 1/8	Sol. 3/8	Sol. 6/9	Sol. 8/8	Range [%]
3P2	S_{11}(1650)p-1D	2.24	1.75	1.89	5.1	1.75-5.10
3P2	S_{11}(1895)p-1D	-	-	0.08	0.45	0.00-0.45
3P2	P_{11}(1710)p-3P	0.49	0.14	3.34	7.93	0.14-7.93
3P2	P_{11}(1710)p-3F	1.69	2.21	0.34	0.04	0.04-2.21
3P2	P_{11}(1880)p-3P	-	0	-	2.11	0.00-2.11
3P2	P_{13}(1720)p-3P	4.05	1.28	7.33	0	0.00-7.33
3P2	P_{13}(1720)p-5P	8.63	0.09	1.01	0.08	0.08-8.63
3P2	P_{13}(1720)p-3F	1.05	0.33	1.2	2.94	0.33-2.94
3P2	P_{13}(1720)p-5F	5.59	0.27	0.5	0.32	0.27-5.59
3P2	P_{13}(1900)p-3P	4.74	-	6.2	-	0.00-6.20
3P2	P_{13}(1900)p-5P	2.28	-	0.07	-	0.00-2.28
3P2	D_{13}(1875)p-5S	-	-	-	-	-
3P2	D_{13}(1875)p-3D	-	-	-	-	-
3P2	D_{13}(1875)p-5D	-	-	-	-	-
3P2	(pL)(1S0)K-1D	1.99	0.06	0.09	0.03	0.03-1.99
3P2	(pL)(3S1)K-3D	0.97	0.05	0.98	0.1	0.05-0.98
3P2	(pL)(1P1)K-3P	0.92	0.22	1.32	1.77	0.22-1.77
3P2	(pL)(1P1)K-3F	0.18	0.77	0.26	0.04	0.04-0.77
3P2	(pL)(3P1)K-3P	1.55	0.16	2.22	0	0.00-2.22
3P2	(pL)(3P2)K-5P	1.02	0.04	1.46	0.27	0.04-1.46
3P2	(pL)(3P2)K-5F	0.05	0.12	0.08	0.19	0.05-0.19
3P2	(pL)(1D2)K-5S	0.73	0.04	0.64	16.24	0.04-16.24
3P2	(pL)(1D2)K-5D	0.07	0.07	0.6	0.08	0.07-0.60
3P2	(pL)(3D1)K-3D	0.56	2.4	0.81	1.99	0.56-2.40
3P2	(pL)(3D2)K-5D	-	-	0.21	-	0.00-0.21

Table 6.5: Partial wave contributions to the 3F2 initial state. All given in [%].

In. st.	Interm. st.	Sol. 1/8	Sol. 3/8	Sol. 6/9	Sol. 8/8	Range [%]
3F2	S_{11}(1650)p-1D	4.6	3.71	0.61	1.86	0.61-4.60
3F2	S_{11}(1650)p-3D	0.37	1.16	1.75	0.23	0.23-1.75
3F2	S_{11}(1895)p-1D	-	-	0.39	0.03	0.03-0.39
3F2	S_{11}(1895)p-3D	-	-	0.26	0.55	0.26-0.55
3F2	P_{11}(1710)p-3P	1.95	5.42	5.79	18.48	1.95-18.48
3F2	P_{11}(1710)p-3F	3.04	0.66	0.35	0.14	0.14-3.04
3F2	P_{11}(1880)p-3P	-	15.27	-	20.32	0.00-20.32
3F2	P_{13}(1720)p-3P	6.59	2.31	17.3	1.07	1.07-17.3
3F2	P_{13}(1720)p-5P	0.21	0.01	0.63	0.07	0.01-0.63
3F2	P_{13}(1720)p-3F	1.03	0.04	2.81	1.76	0.04-2.81
3F2	P_{13}(1720)p-5F	0.19	0.82	0.01	0.07	0.01-0.82
3F2	P_{13}(1900)p-3P	3.89	-	25.13	-	0.00-25.13
3F2	P_{13}(1900)p-5P	0.05	-	3.08	-	0.00-3.08
3F2	D_{13}(1875)p-5S	-	-	-	-	-
3F2	D_{13}(1875)p-3D	-	-	-	-	-
3F2	D_{13}(1875)p-5D	-	-	-	-	-
3F2	(pL)(1S0)K-1D	3.16	0.91	0	0.2	0.00-3.16
3F2	(pL)(3S1)K-3D	1.95	0.24	0.01	0.11	0.01-1.95
3F2	(pL)(1P1)K-3P	1.24	0.02	1.77	0.01	0.01-1.77
3F2	(pL)(1P1)K-3F	0.24	0	0.35	0.34	0.00-0.35
3F2	(pL)(3P1)K-3P	0.13	0.95	1.02	0.86	0.13-0.95
3F2	(pL)(3P2)K-5P	1.38	1.41	1.97	0.78	0.78-1.97
3F2	(pL)(3P2)K-5F	0.07	0.02	0.1	0.25	0.02-0.25
3F2	(pL)(1D2)K-5S	13.72	5.58	6.05	0.05	0.05-13.72
3F2	(pL)(1D2)K-5D	0.04	1.06	1.01	0.14	0.04-1.06
3F2	(pL)(3D1)K-3D	0.76	0.94	1.09	1.62	0.76-1.62
3F2	(pL)(3D2)K-5D	-	-	0.28	-	0.00-0.28

One can get an estimation of the different N* contributions by adding the contributions of all waves that contain a certain N* in the intermediate state. As the waves interfere with each other this does not correspond to the observed strength of the single resonances. This is expressed by the fact that the sum of the different waves exceeds 100%. Table 6.6 gives the results of this summation for all four best solutions. The intermediate state of non-resonant formation of $pK^+\Lambda$ appears to be constantly around 65% of the total $pK^+\Lambda$ production cross section. The state in which p and Λ are in a relative ($^1D_2$) or ($^3D_1$) state seems to be favored by all solutions. The interpretation of the N* contribution is more difficult. A resonance with a mass around 1900 MeV/c^2 is certainly needed by the fit. As the different resonances in this mass regime have, however, broad widths, the fit is not very sensitive to their exact contribution. The results summarized in Table 6.6 allow, thus, no clear statement about the exact resonance cocktail. The yield of N* contribution varies between 80% and 150% and is in all cases substantially larger than the non-resonant production. The ratio of res-

Table 6.6: Contribution of the different N* and non resonant intermediate states to the total $pK^+\Lambda$ production cross section. All given in[%].

Interm. State	Sol. 1/8	Sol. 3/8	Sol. 6/9	Sol. 8/8
N*(1650)	15.7	22.7	9.4	13.4
N*(1710)	14.2	28.8	31.6	45.8
N*(1720)	41.7	13.1	51.2	15.7
N*(1875)	-	-	-	-
N*(1880)	-	19.7	-	29.9
N*(1895)	-	-	6.5	4.1
N*(1900)	45.1	-	55.1	-
Sum Res	**116.7**	**84.3**	**153.8**	**108.9**
(pL)(1S0)	7.4	1.0	0.1	1.6
(pL)(3S1)	7.8	4.0	4.6	4.5
(pL)(3P0)	7.3	6.7	5.2	9.1
(pL)(3P1)	4.3	1.2	6.0	4.3
(pL)(3P2)	3.7	7.2	9.0	3.9
(pL)(1D2)	21.9	8.9	12.2	21.6
(pL)(3D1)	13.7	27.8	18.5	19.1
(pL)(1P1)	4.2	5.2	5.6	5.3
(pL)(3D2)	-	-	1.1	-
Sum non res	**70.3**	**62.0**	**62.3**	**69.4**

onance production to the total yield varies between 60% and 70%. The $pK^+\Lambda$ production is, thus, dominated by N* production.

6.1.1 4π Distribution of Single Resonances

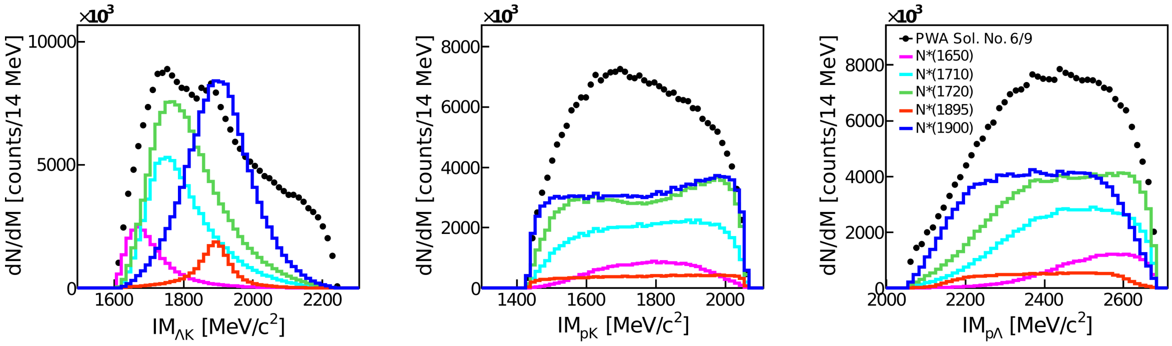

Figure 6.3: Two-particle masses for the best PWA solution (6/9) in 4π. The different histograms correspond to different single resonance contributions.

The PWA framework does also allow to visualize the 4π distributions of the single contributions in the solution. This is done in the following for the overall best solution No. 6/9. The single waves of non-resonant production of $pK^+\Lambda$ included in Sol. No. 6/9 are shown in Appendix G.1. Figures 6.3 and 6.4 present the single contributions of the different N*s to the total solution. The invariant mass of ΛK^+ in Figure 6.3 is obviously sensitive to the mass and width properties of the contributing N*-resonances, despite the fact that the broad resonances largely overlap.

The Angular Distribution in the CMS Frame

Figure 6.4 displays the different angular correlations in the production of the N* resonances. The upper rows present the CM angular distributions. As the N* resonance is produced together with a proton, the angular distribution of the latter reflects directly the production dynamics of the accompanying resonance. Therefore, the angular distribution of the proton is the most interesting observable of the CMS distributions. In case of N* production the Λ and K^+ distributions only mirror the kinematic of the leading proton.

The angular momenta between the different particles is exhibited by the angular distributions of the particles in the CMS system. In each model, that aims

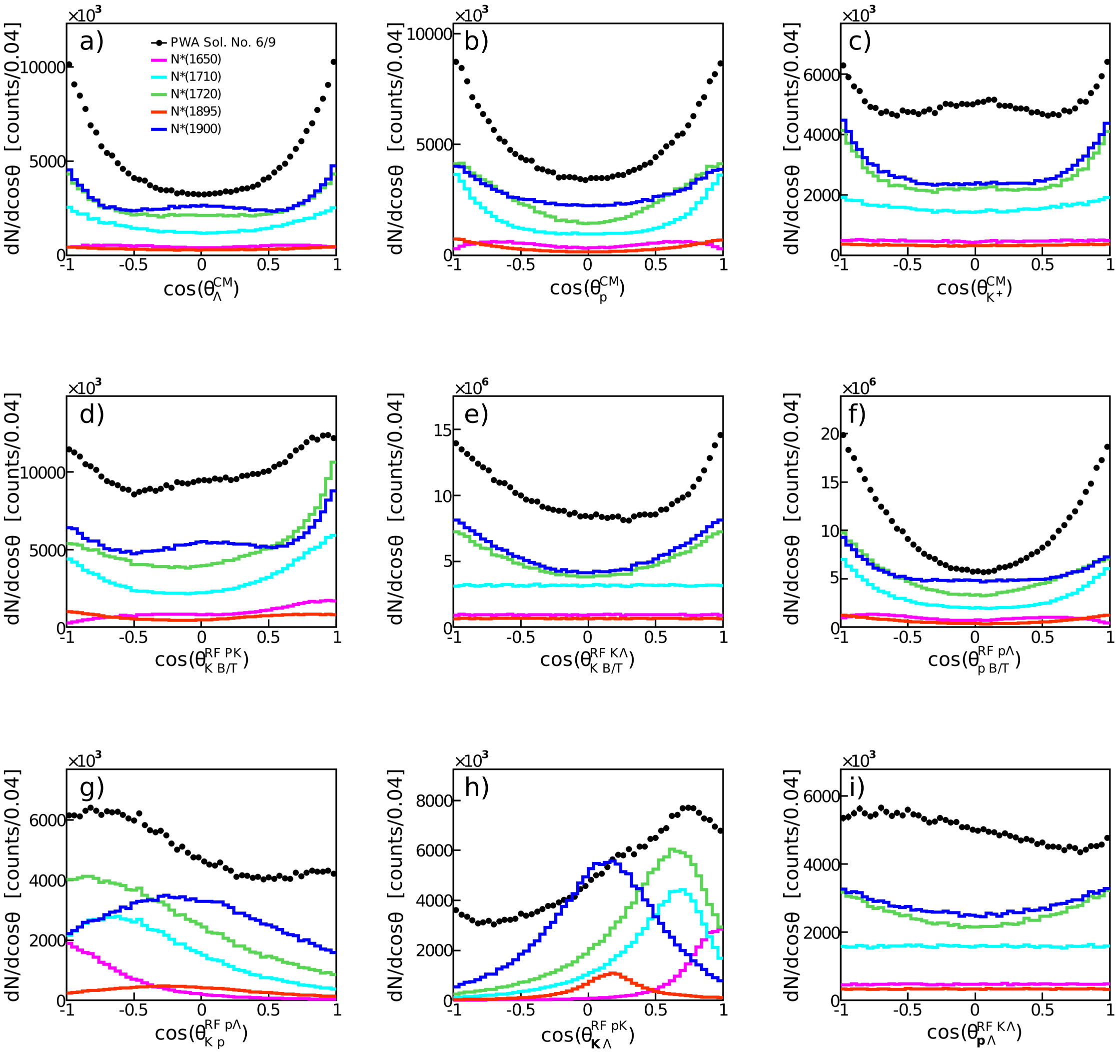

Figure 6.4: Angular distributions for the best PWA solution (6/9) in 4π. The different histograms correspond to different single resonance contributions. The upper row shows the angle of the particle in the CMS (a)-c)), the middle row show the Gottfried-Jackson distributions (d)-f)) and the lower row show the helicity angles (g)-i)). See Figure 2.6 for further explanations on the observables.

at predicting the production and decay of N* dominated final states, a proper access and incorporation of angular distributions is essential. Quantitative information about the angular distribution can be extracted from the data with help of Legendre coefficients. To do so, a sum of weighted Legendre polynomials is fit to the data. This sum of Legendre polynomials is expressed as follows:

$$\frac{dN}{dx} = A_0P_0(x)+A_1P_1(x)+A_2P_2(x)+A_3P_3(x)+A_4P_4(x)+A_5P_5(x)+A_6P_6(x), \tag{6.1}$$

with the Legendre coefficients A_x and the Legendre Polynomials:

$$P_0(x) = 1, \tag{6.2}$$

$$P_1(x) = x, \tag{6.3}$$

$$P_2(x) = \frac{1}{2}(3x^2 - 1), \tag{6.4}$$

$$P_3(x) = \frac{1}{2}(5x^3 - 3x), \tag{6.5}$$

$$P_4(x) = \frac{1}{8}(35x^4 - 30x^2 + 3), \tag{6.6}$$

$$P_5(x) = \frac{1}{8}(63x^5 - 70x^3 + 15x), \tag{6.7}$$

$$P_6(x) = \frac{1}{16}(231x^6 - 315x^4 + 105x^2 - 5). \tag{6.8}$$

As the colliding system is symmetric the angular distribution of the particles in the CMS has to be symmetric around $cos\theta = 0$. Hence, the coefficients A_1, A_3 and A_5 are fixed to zero in this fit. Further, the inclusion of a Legendre polynomial P_6 showed no large effect in the fits as the coefficients A_6 were compatible with zero. The fit to the single resonance and non-resonant contributions of the p-CMS angle is shown in Appendix G.2 and describes the PWA-model distributions in all cases perfectly. The quantitative results of the fit are summarized in Table 6.7. The Legendre coefficients were normalized to A_0 to allow for a comparison.

If the particles would be produced in S-wave only, the CMS distributions would be flat, and the coefficients $A_1 - A_6$ equal to zero. The contribution of higher orders of Legendre polynomials causes an anisotropic angular distribution and indicates higher angular momenta between the particles. As the production of single states can proceed via multiple intermediate configurations, the numbers in Table 6.7 express a sum over many transition amplitudes. Due to these multiple production ways a general trend in the coefficients is hardly visible.

Table 6.7: The Legendre coefficients of the p-angular distribution in the CMS system. The coefficients are extracted from the single distributions in Figure 6.4 and normalized to A_0=1.

Interm. State	A_0	A_1	A_2	A_3	A_4
Sum of all contr.	1	-	0.71	-	0.11
N*(1650)-p	1	-	0.13	-	-0.62
N*(1710)-p	1	-	1.06	-	0.37
N*(1720)-p	1	-	0.79	-	-0.1
N*(1875)-p	-	-	-	-	-
N*(1880)-p	-	-	-	-	-
N*(1895)-p	1	-	1.16	-	0.13
N*(1900)-p	1	-	0.43	-	0.06
(pL)(1S0)-K	1	-	0.34	-	0.01
(pL)(3S1)-K	1	-	-0.04	-	-0.06
(pL)(3P0)-K	1	-	0.09	-	0.00
(pL)(3P1)-K	1	-	-0.30	-	-0.16
(pL)(3P2)-K	1	-	0.39	-	0.01
(pL)(1D2)-K	1	-	0.46	-	-0.37
(pL)(3D1)-K	1	-	0.09	-	0.15
(pL)(1P1)-K	1	-	1.15	-	0.41
(pL)(3D2)-K	1	-	-0.08	-	0.08

The higher order coefficient A_2 shows no dependency on the resonance mass, whereas the absolute values A_4 seems to decrease approximately with increasing resonance mass. Whether this is a general feature or a coincidence due to the summation over many intermediate transitions can not be judged. The strength of A_2 and A_4 in case of non resonant production seems to vary from strong to weak without any significant feature. A_2 and A_4 can be strong or weak both for resonant and non-resonant production of the $pK^+\Lambda$ final state.

These coefficients of the single resonance contributions can be used as an input for resonance-models. The production of ΛK^+-pairs at low and intermediate beam energies proceeds - to a large extent - via N* resonances [155, 156, 157, 160, 161, 162]. The kinematic in the production of the resonances, listed in Table 6.7, can be included into transport models.

The distributions of single resonances are not accessible in an experiment, as only the interfered sum of all contributions can be measured. The first row

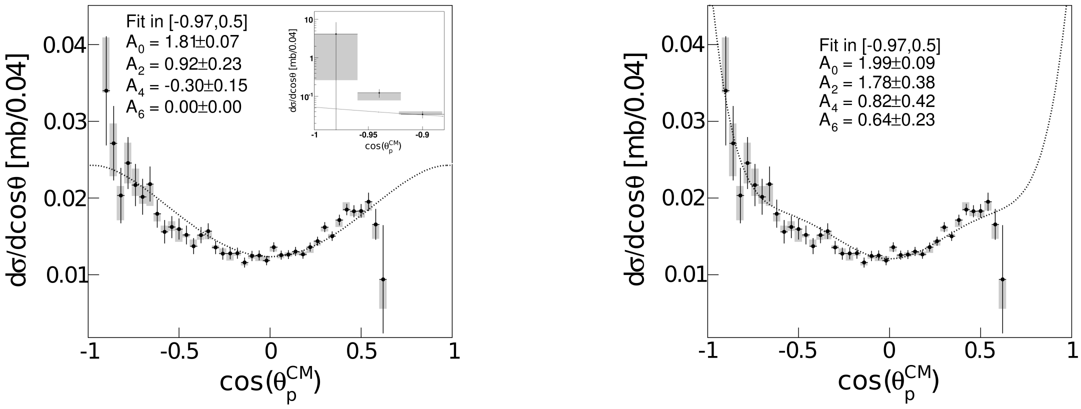

Figure 6.5: The angular distribution of the proton in the CMS system. Left figure show a fit with a sum of Legendre polynomials up to the fourth order. Right figure shows the same data fitted with Legendre polynomials up to the sixth order. The inlet shows two bins that were excluded from the fit.

of Table 6.7 shows the Legendre coefficients from a fit to an interfered sum of all contributing waves (the 4π PWA solution). This can be compared to the Legendre coefficients of the experimental data. The Legendre coefficients of the data of this work were determined by a fit of Function 6.1 to the acceptance corrected angular distribution of the proton, shown in Figure 6.5. Contrary to the coefficients of the PWA solution an inclusion of the Legendre term P_6 is necessary in order to describe the distribution.

The overall angular distribution of the proton can no longer give insight into single production processes but does still contain information. This is revealed by comparing this result to measurements of differential cross sections at other beam energies. In Ref. [172] the Legendre coefficients of proton, Λ and K^+ in $pK^+\Lambda$ production were compared to each other at different excess energies close to threshold. Figure 6.6 shows these coefficients for the proton. No clear trend was observed at low energies. Comparing the normalized Legendre coefficients at higher beam energies results in the values of Table 6.8. The low energy data are taken from tables quoted in Ref. [155]. At higher energies the distributions were scanned from the publications [197, 161, 162] and fitted with Legendre polynomials of the sixth order. The fit is shown in Appendix G.4.

Opposite to the low energy data the strength of the Legendre polynomials, expressed by the coefficients A_x increases with increasing beam energy. This

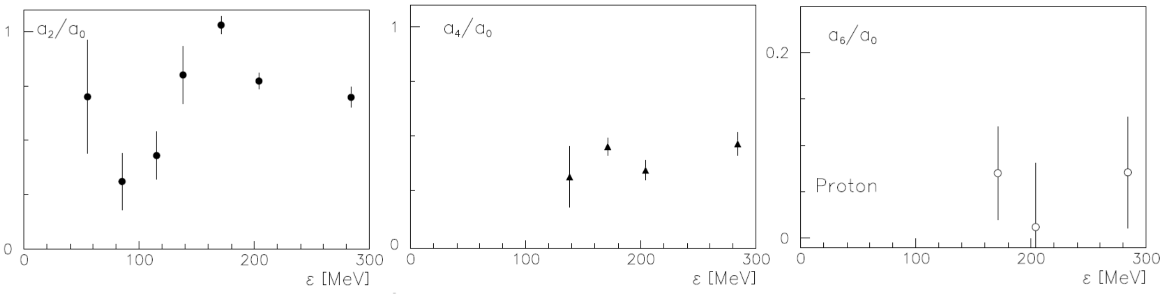

Figure 6.6: The Legendre coefficients that describe the angular distribution of the proton in the CMS system at different excess energies [172].

Table 6.8: Legendre coefficients of the proton angle in the CM-system, shown for different beam kinetic energies. Values are scaled to $A_0 = 1$. [1]This work, *scanned from the document and fitted (Appendix G.4).

Ref.	E_{kin} [GeV]	ϵ [MeV]	A_1/A_0	A_2/A_0	A_4/A_0	A_6/A_0
[155]	2.16	127.7	0.21±.10	0.99±0.18	0.42±0.14	-
[155]	2.26	161.6	-0.08±.08	0.67±0.18	0.46±0.13	-
[155]	2.4	208.4	-0.07±.28	0.84±0.53	0.56±0.43	-
[197]*	2.85	353.7	-	1.0±0.21	0.0±0.64	0.4±0.29
PWA[1]	3.5	551.9	-	0.71±0.01	0.11±0.01	0.0
Data[1]	""	""	-	0.89±0.19	0.41±0.21	0.32±0.11
[161]*	4.1	724.4	-	1.8±0.19	1.3±0.25	0.8±0.24
[162]*	5.13	1001.5	-	2.7±0.17	2.3±0.21	1.0±0.19

holds for all three coefficients A_2, A_4 and A_6. Where $A_2 > A_4 > A_6$. This trend of the strength of the Legendre polynomials which expresses the angular momentum between the particles could be caused by the fact that with increasing beam energy higher angular momenta can be excited. The higher the angular momentum (order of Legendre polynomial) the more energy is needed to excite it, which could explain the hierarchy among the coefficients.

Helicity Angles

The $p\Lambda$- and pK^+-helicity angles (panel g) and h) of Figure 6.2) show mainly the width and mass information of the N* resonances, similar to the direct mass distributions in Figure 6.3. The reason for this is that the helicity angle is a projection of the two-particle invariant masses on the $cos(\theta)$ axis. This can be expressed through the expansion of the helicity-angle in terms of invariant masses [167], here shown for the $K\Lambda$-helicity angle:

$$
\begin{aligned}
cos(\theta_{p\Lambda}^{RF\ K\Lambda}) = &\left[2M_{K\Lambda}^2(m_p^2 + m_\Lambda^2 - M_{\Lambda p}^2) + (s - M_{K\Lambda}^2 - m_p^2)(M_{K\Lambda}^2 + m_\Lambda^2 - m_K^2)\right] \\
&\cdot((s - M_{K\Lambda}^2 - m_p^2)^2 - 4M_{K\Lambda}^2 m_p^2)^{-\frac{1}{2}}((M_{K\Lambda}^2 - m_\Lambda^2 - m_K^2)^2 - 4m_\Lambda^2 m_K^2)^{-\frac{1}{2}}
\end{aligned}
\tag{6.9}
$$

For a given mass of $M_{\Lambda p}$ the $M_{K\Lambda}$ is strongly constrained from the two-body kinematics in the production. Only the width of $M_{K\Lambda}$ systems, together with the excess energy from the N* to its decay into $K\Lambda$ slightly smears out this direct connection between the two observables[1]. This way, one can see that a given mass in $M_{\Lambda p}$ determines directly the value of the opening angle between p and the Λ in the $K\Lambda$-helicity angle. Due to the smearing of the $M_{K\Lambda}$ mass information, the $K\Lambda$-helicity angle contains only minor kinematic reflections of the N* resonances. It does contain, however, another valuable information. In this frame decay properties of the N* resonances will appear. The rest-frame is constructed from the decay particles of the N* (K^+ and Λ) so that the N* is at rest in this frame. The angle, displayed in this rest frame, is the angle between proton and the Λ. The proton is produced with the N* and thus carries information about its opposite flight direction. If there is any asymmetry in the decay of the N* then this asymmetry affects the angular distribution of the decay products, in respect to the N* flight direction which is displayed by the discussed observable. One can see that all angular distributions of the N* resonances are flat (see panel i) of Figure 6.2) except the ones for N*(1720) and N*(1900). The difference between these and the other resonances is their spin. Both resonances have spin 3/2. The decay products K^+ and Λ both have only spin 1/2. As the total spin has to be conserved in the resonance decay, there has to be an orbital angular momentum between the decay particles to guarantee this conservation. This angular momentum causes an asymmetric distribution of the decay particles with respect to the mother (N*) flight direction. The total sum of all contributions in this observable does also contain interference which hinders a detailed interpretation of its sub-components in the experimental distributions.

Gottfried-Jackson Angles

The Gottfried-Jackson angles, as displayed in the panels d)-f) of Figure 6.2, contain information about angular momenta of exchange particles, like in case

---

[1] This smearing of the direct connection between the invariant masses is less pronounced in the $p\Lambda$- and pK-helicity angles which results in a good visualization of the N* resonance mass and width properties.

of pion or kaon exchange (see [168, 155, 23] for further explanations). As the exchange mechanism is not a focus of the present analysis the angles are not further discussed.

6.2 Acceptance and Efficiency Correction

The so far presented experimental results are heavily distorted by the detector acceptance and the event selection process. To obtain information about the production kinematics and involved resonances the observables should be investigated in the full phase space. Therefore, the data need to be corrected for the losses of events. The production of three particles in the final state is determined by four independent kinematic variables[2]. A model-independent acceptance correction, thus, needs to be performed in four dimensions simultaneously. This approach demands, however, a large number of simulated events to populate each four dimensional entry of an acceptance matrix with enough statistic to keep the errors low. Further, this approach does not provide any model with which one can extrapolate the cross section to acceptance hole areas. Another option is to take a model that has proven its excellent data description in a limited acceptance to extrapolate to the "blind" regions.

As the four best PWA solutions describe the data in a similar good way, see Figures 4.16–4.19 of Chapter 4 for comparison, they all can be used to build a correction function for the measured data. Due to the slight systematic variation of the PWA content, the corrections will yield different results which accounts for the systematic uncertainty on the PWA solutions. The acceptance functions are obtained in the following way: the simulated phase space events that have been assigned a PWA weight are filtered through the full simulation chain, as described in Section 2.3, and then the same analysis as for the experimental data is applied to these events. The obtained spectra for each observable are divided by their according spectra in 4π. In this way, a bin-by-bin ratio of events in the full and limited acceptance is obtained. Figures 6.7 and 6.8 show the resulting acceptance and efficiency functions. The efficiency correction is done in one dimension whereas the other three dimensions on which the efficiency depends on are integrated. The integration relies entirely upon the correct distribution of simulated events in the phase space. The acceptance and efficiency of the $pK^+\Lambda$ reconstruction is in the order of 0.5%. The loss of

---

[2] Originally the three four-vectors contain all together 12 components. Three are determined by the defined particle masses, three by momentum conservation and one by energy conservation. One observable additionally vanished due to the reaction symmetry in ϕ.

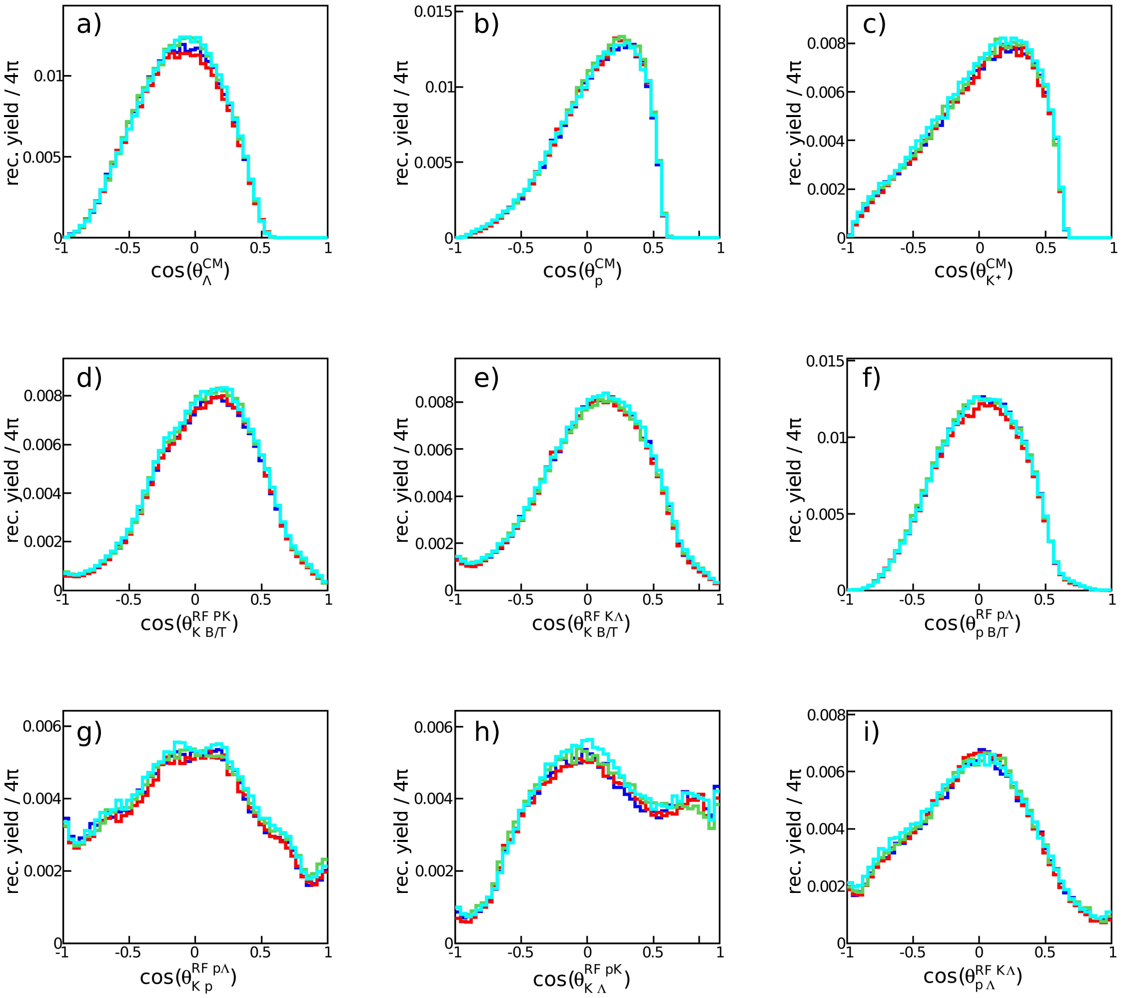

Figure 6.7: Acceptance functions of the angular correlations of the three particles for the four best PWA solutions of the PWA (different colors). Sol. No. 6/9 (green), Sol. No. 8/8 (cyan), Sol. No. 1/8 (blue) and Sol. No. 3/8 (red). a)-c) correction for CMS angles, d)-f) correction for Gottfried-Jackson angles, and g)-i) correction for the helicity angles. See Figure 2.6 for further explanations on the observables.

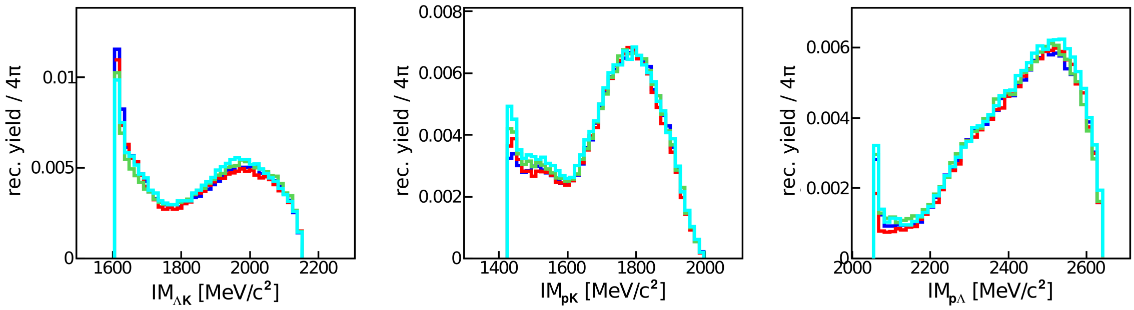

Figure 6.8: Acceptance functions of the two-particle masses for the four best PWA solutions of the PWA (different colors). Sol. No. 6/9 (green), Sol. No. 8/8 (cyan), Sol. No. 1/8 (blue) and Sol. No. 3/8 (red)

events due to the decay of the Λ into $p\pi^-$ (64%) is taken into account as the 4π distribution contains the full set of all Λs.

To obtain the experimental event distribution in 4π the experimental spectra inside the acceptance were divided by the corresponding acceptance function. This was done for each acceptance function of the four best PWA solutions. The single 4π spectra of all solutions and observables are shown in Appendix G.3. The combined results are shown in Figures 6.9 and 6.10. The bin entry corresponds to the value obtained from the correction function of Sol. No. 6/9. The displayed errors account for the statistical error of the experimental data. The gray boxes show the systematic error of the acceptance correction. This error was obtained by the maximum deviation of any of the three other correction to the one of Sol. No. 6/9. As expected, the experimental data in 4π are consisted with the predictions of the PWA solution.

The CM distributions are symmetric with respect to the CM axis. The IM$_{K^+\Lambda}$ shows the event distributions as predicted by the PWA. Single peaks due to N* resonances are not visible due to the large widths of the states. The small peak at around 1900 MeV/c^2, present in some of the solutions, seems to appear also in the experimental data but is slightly shifted to lower masses.

The K-Λ helicity angle (panel i) Figure 6.9) shows a relatively flat behavior. Within the large spread of the data points it is consistent with the PWA model that predicts a slight modulation as a function of the angle. In Ref. [167, 168] this observable was proposed to study the pΛ final state interaction. As expressed by Eq. 6.9 the helicity angle is tightly correlated with the invariant mass of two particles. An angle of $cos\theta = 1$ is related to small invariant masses

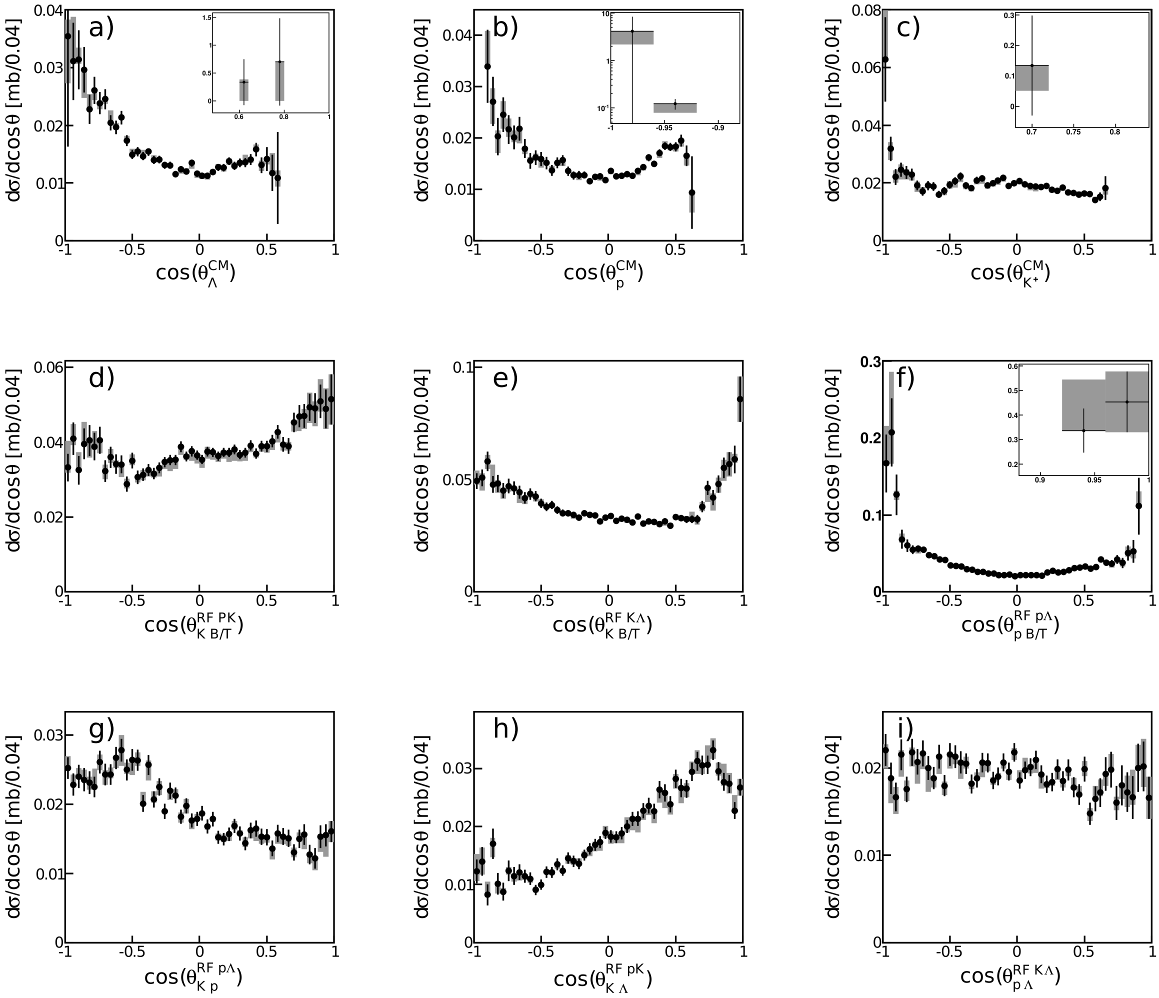

Figure 6.9: Experimental distributions of the three particle angular correlations, corrected for acceptance and efficiency. Inlets show bins that are far out as compared to the other values. See Figure 2.6 for further explanations on the observables.

of $p\Lambda$ where the final state interaction should be the strongest. In Ref. [155] an enhancement of statistic at very small $p\Lambda$ opening angles was observed for E_{kin} = 2.16, 2.26, and 2.4 GeV, respectively. This was interpreted as a trace of p-Λ final state interaction. The K-Λ helicity angle at 3.5 GeV does not show such a behavior at $cos\theta$=1. The reason for this is that at higher energies only a small portion of the phase space is influenced by final state interaction [168, 198]. Hence, these effects are less pronounced at the here investigated energy.

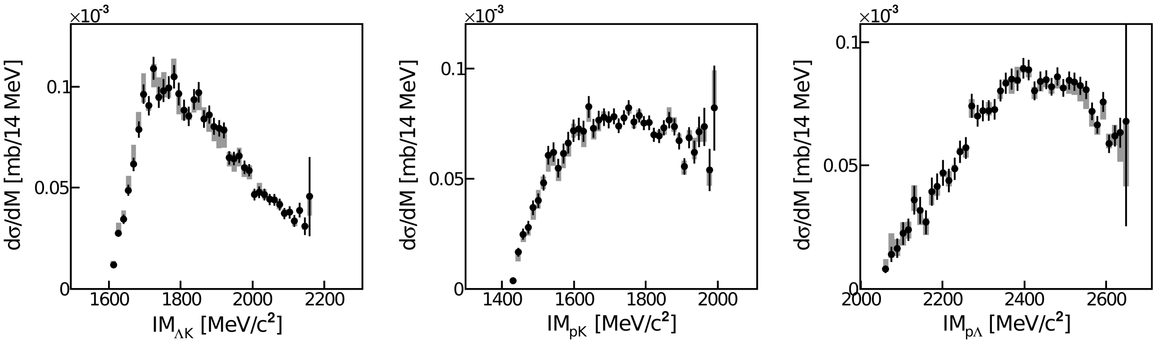

Figure 6.10: Experimental distributions for the two-particle invariant masses corrected for acceptance and efficiency.

For the investigation of the kaonic nuclear bound state $\overline{K}NN$, the invariant mass of p and Λ is the most relevant observable. The acceptance corrected spectrum of the IM$_{p\Lambda}$ of Figure 6.10 shows a smooth increase of the measured yield with increasing mass of the system. There is no broad structure at M = 2267 MeV/c^2 and Γ = 118 MeV/c^2 visible, as reported by the DISTO collaboration [125, 126]. Two bins stick out from the smooth trend of this observable. The one at 2130 MeV/c^2 can be assigned to the ΣN-cusp, a well known phenomena in the invariant mass of $p\Lambda$ [199]. This behavior is assigned to a coupled channel of $\Sigma - N \longleftrightarrow \Lambda - p$ which opens at about 2130 MeV/c^2. To investigate the bin at 2270 MeV/c^2 the four IM$_{p\Lambda}$ spectra of Appendix G.3 are shown with a zoom into the relevant mass region. Figure 6.11 presents four times the IM$_{p\Lambda}$ distribution each figure corrected for acceptance and efficiency with another model.

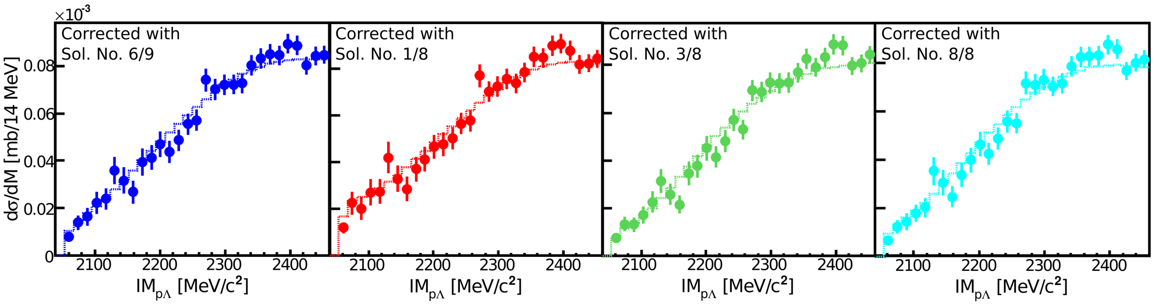

Figure 6.11: IM$_{p\Lambda}$ for the four different correction functions. Points show the experimental values and the lines the PWA-model that was used for the correction.

Only in two of the corrections the mass bin sticks out of the general trend. In all cases it is consisted with the PWA model prediction within 3σ. How significant such deviations nonetheless are is shown by a statistical analysis of this observable in Chapter 5.

Figure 6.12 shows the Dalitz-plot of $pK^+\Lambda$ events. In this representation two particle invariant masses are plotted against each other. The upper figures show the Dalitz-plot for $IM^2_{K^+\Lambda}$ vs. $IM^2_{p\Lambda}$ whereas the lower figures show $IM^2_{K^+p}$ vs. $IM^2_{p\Lambda}$. The left panels show the distributions inside of the acceptance of the HADES spectrometer. The structures that are visible here are regions of enhanced acceptance of the $pK^+\Lambda$ events. The efficiency correction is done in the same way as for the one dimensional observables. For the correction function only solution No. 6/9 was used. The efficiency corrected data are shown in the panels of Figure 6.12 marked with "Exp 4π". The Dalitz-plots show acceptance-holes for events in which two particles have a large opening angle ($\hat{=}$ high invariant masses), as in such cases the third particle escapes into the acceptance hole at low polar angles (<15°). Resonances appear as a band in the Dalitz-plot and such a band is visible at about $3\cdot10^6(\mathrm{MeV/c^2})^2$ of $IM^2_{K^+\Lambda}$ (left panel "Exp 4π" of Figure 6.12). The Λp final state interaction should appear as an enhancement in the low $p\Lambda$-invariant mass region. This is hardly visible by eye, as the statistic in this region is very scarce, but could be extracted eventually by a two dimensional fit of the Dalitz-plot similar as done in [157]. The Dalitz-plots show no band in the $IM_{p\Lambda}$ plane that could be attributed to a state that decays into proton and Lambda.

The 4π PWA distribution shows a peculiar effect at very low $p\Lambda$ invariant masses, namely a depletion of events. It is not exactly clear what is the cause of this effect. It is definitely not a repulsive $p\Lambda$ interaction, as Figure G.1 in Appendix G clearly shows the attractive component of the non-resonant wave. On could think that these are some interference effects, but as the experimental data in this region are lacking, it can not be stated whether this is a phenomenon purely in the model, or not.

6.2.1 Absolute Cross Section

The corrected distributions in 4π in Figures 6.10 and 6.9 are already scaled to an absolute cross section. This is done as described in [143]. The transformation of counts to cross section is obtained from the ratio of p+p elastic events to the p+p elastic cross section from reference measurements [143]. This ratio is

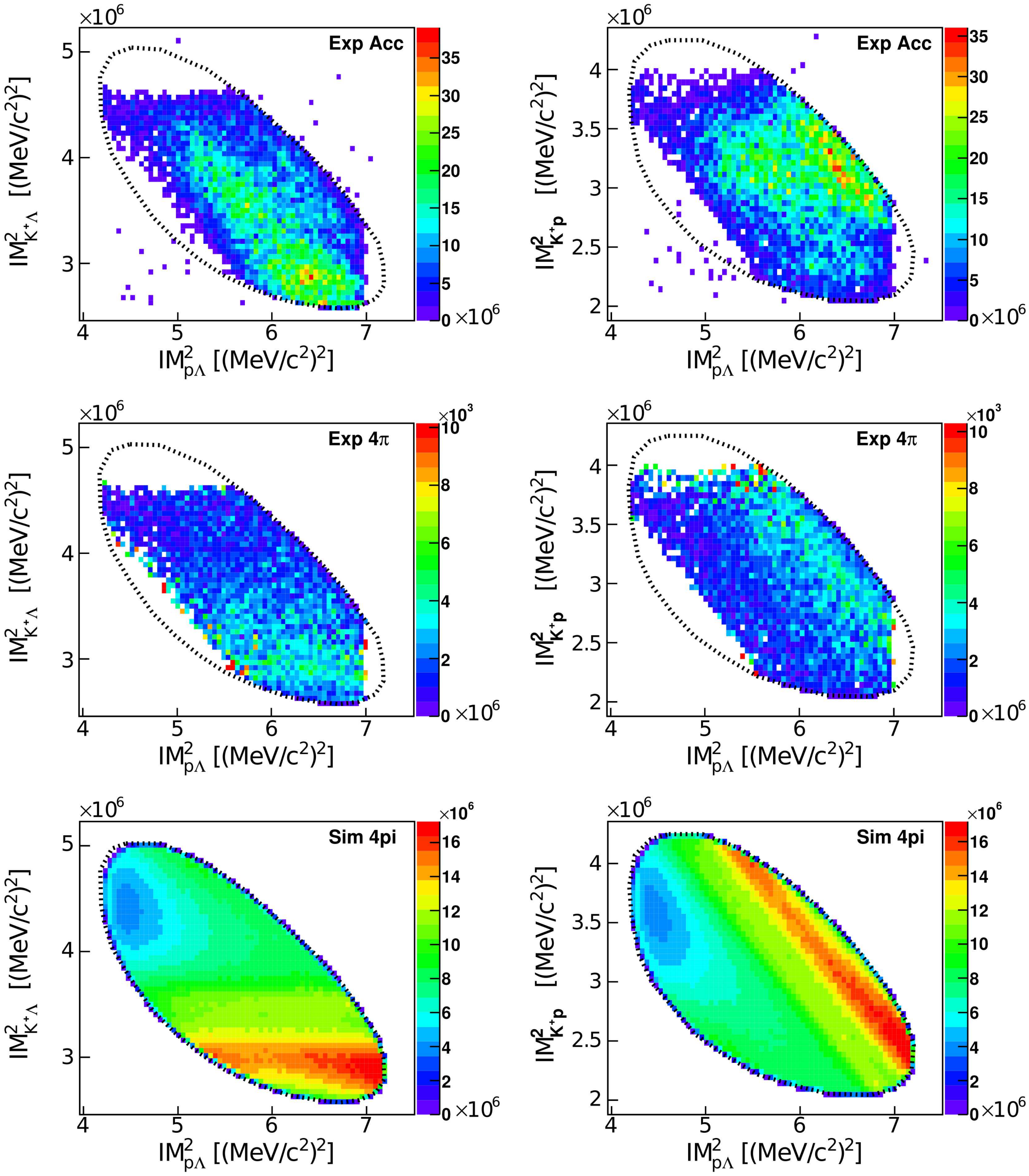

Figure 6.12: The two columns show two dalitz plots. Once for the measured data (Exp Acc), once for the data which were corrected for the losses of efficiency (Exp 4π), and once for the PWA model No. 6/9 in 4π (Sim 4π).

expressed by the Rustamov-Factor:

$$Rustamov\text{-}Factor = \frac{N^{acc}_{pp,el}}{\sigma^{acc}_{pp,el}} = \frac{N^{4\pi}_{pp,el}}{\sigma^{4\pi}_{pp,el}} = 22271,7. \qquad (6.10)$$

$N^{acc}_{pp,el}$ and $\sigma^{acc}_{pp,el}$ denote the measured yield and literature cross section of the p+p elastic reaction in a limited CM angle. This ratio also correspond to the ratio of produced elastic events in 4π and the according total elastic cross section. The "Rustamov-Factor" is given for one analyzed file. The file contains a certain amount of recorded events which is roughly constant throughout the beam-time. To obtain a cross section from a number of reconstructed events the following calculation needs to be applied:

$$\sigma^{4\pi}_{pK^+\Lambda} = N^{acc}_{pK^+\Lambda}(x) \cdot \frac{1}{AccCorr(x)} \cdot \frac{1}{R\text{-}F \cdot N_{Files}} \cdot DSF. \qquad (6.11)$$

$N^{acc}_{pK^+\Lambda}(x)$ and $AccCorr(x)$ denote the reconstructed number of events and the according correction factor as a function of the observable in which the correction is applied. $R-F$ and N_{Files} are the "Rustamov-Factor" and the number of files used for the analysis. DSF is a factor that corrects for the LVL1 trigger downscaling[3] of the experimental data of the p+p experiment and has a value of 3. The normalization of measured p+p elastic events to the literature cross section, according to Eq. (6.10) contains a systematic uncertainty of 7%.

6.2.2 The $pK^+\Lambda$ Production Cross Section

The integrated yield of the histograms in Figures 6.10 and 6.9 delivers the total production cross section of p+p→ $pK^+\Lambda$ at E_{kin}(p)=3.5 GeV. To obtain a systematic error on the total production cross section the observables in 4π where integrated for each acceptance correction function separately. Appendix G.3 shows all experimental observables corrected to a 4π acceptance for the four best PWA solutions separately. Figure 6.13 presents two examples of the 48 integrated observables. The corrected data are displayed together with the corresponding model. The model is normalized to the experimental data in the indicated range inside the brackets. To obtain the total production cross section each histogram was integrated. The experimental data are summed inside of the indicated range. Outside of this range the extrapolated model value is taken for the integration. The resulting cross section is quoted in each histogram. Table 6.9 summarizes the results of the integration of all the presented histograms of Appendix G.3. The average cross section obtained with

---

[3] only every third event, unbiased by the second level trigger, has been recorded.

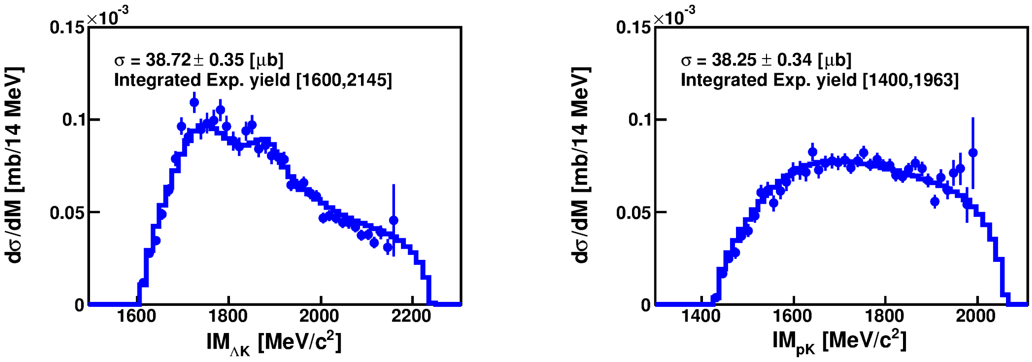

Figure 6.13: Blue data-points experimental data for $IM_{K^+\Lambda}$ and IM_{pK^+} corrected with PWA-model No. 6/9. The line shows the prediction of the PWA-model No. 6/9 overlayed to the experimental distributions.

Table 6.9: The extracted cross section of the acceptance corrected histograms. All given in [μb].

Histogram	Sol. No. 6/9	Sol. No. 1/8	Sol. No. 3/8	Sol. No. 8/8
CMS_Λ	36.88±0.36	37.79±0.37	36.41±0.35	35.95±0.35
CMS_p	38.27±0.47	39.41±0.53	36.43±0.47	36.3±0.44
CMS_{K^+}	38.8±0.32	39.57±0.33	37.68±0.3	36.7±0.3
GJ-Angle RF-pK	37.25±0.35	38.18±0.37	36.16±0.34	**35.29±0.33**
GJ-Angle RF-KΛ	38.15±0.36	39.11±0.37	37.21±0.34	36.74±0.34
GJ-Angle RF-pΛ	40.41±1.06	**41.67±1.09**	40.75±1.10	39.7±1.15
H-Angle RF-pΛ	37.63±0.37	38.47±0.38	36.97±0.36	36.14±0.35
H-Angle RF-pK	37.23±0.40	37.91±0.41	36.38±0.38	35.51±0.38
H-Angle RF-KΛ	37.75±0.42	38.36±0.44	37.22±0.42	36.24±0.40
IM(ΛK^+)	38.72±0.35	39.57±0.36	37.83±0.34	37.01±0.33
IM(pK^+)	38.25±0.34	39.27±0.35	37.52±0.33	36.59±0.32
IM(Λp)	38.07±0.38	38.83±0.40	37.35±0.36	36.41±0.36
Average	38.12±0.43	-	-	-

Sol. No. 6/9 is written in the last row of Table 6.9. The systematic error is constructed by the maximum deviations to this value, marked in bold. The uncertainty due to the normalization to p+p elastic events gives an additional error of 2.67 μb. A last error comes from the fact that the data contain a certain amount of statistic not associated to $pK^+\Lambda$ production. This amount is roughly 6% as described in Section 4.1.3. The overall total production cross section, thus, reads as:

$$\sigma_{pK^+\Lambda} = 38.12 \pm 0.43^{+3.55}_{-2.83} \pm 2.67(p{+}p\text{-}error) - 2.86(background)\ \mu\text{b}. \tag{6.12}$$

The same analysis was performed for the WALL data and is shown in Appendix H. It can, however, only be used as a qualitative cross check, as the efficiency of the Forward Wall hodoscope has never been determined. The 4π distributions of the corrected WALL data set is in a good qualitative agreement with the HADES data set. The extracted cross section is only of use if an efficiency factor of the Wall will be applied to it.

6.3 Comparison With Other Results

The extracted $pK^+\Lambda$ cross section of this work can be compared to the cross sections at other beam energies. Figure 6.14 shows in both panels the $pK^+\Lambda$ production cross sections of higher and lower beam momenta of the p+p reaction system. Figure 6.15 shows in both panels the $pK^+\Sigma^0$ production cross sections of higher and lower beam momenta of the p+p reaction system. The cross section of the $pK^+\Sigma^0$ production of this work is taken from the multifit analysis presented in Chapter 3. The left panels of Figures 6.14 and 6.15 show the model prediction of a one boson exchange model of Ferrari et al. [149, 200], which incorporates the production of $K^+\Lambda$ resonances. The different lines correspond to different cut-off parameters on the four-momentum squared of the exchange boson, and a variation of the coupling constant $G_{\Sigma^0 pK^+}$, as illustrated in Figure 6.15 [149, 200]. The models can describe the data well and are consistent with our measurement, shown by the pink star.

If no model prediction of the production process is available the measured cross sections are often fitted by a parametrisation given by [201, 202]:

$$\sigma(p_{beam}) = a \cdot \left(1 - \frac{\sqrt{p_{th}^2 + m^2} + m}{\sqrt{p_{beam}^2 + m^2} + m}\right)^b \cdot \left(\frac{\sqrt{p_{th}^2 + m^2} + m}{\sqrt{p_{beam}^2 + m^2} + m}\right)^c . \tag{6.13}$$

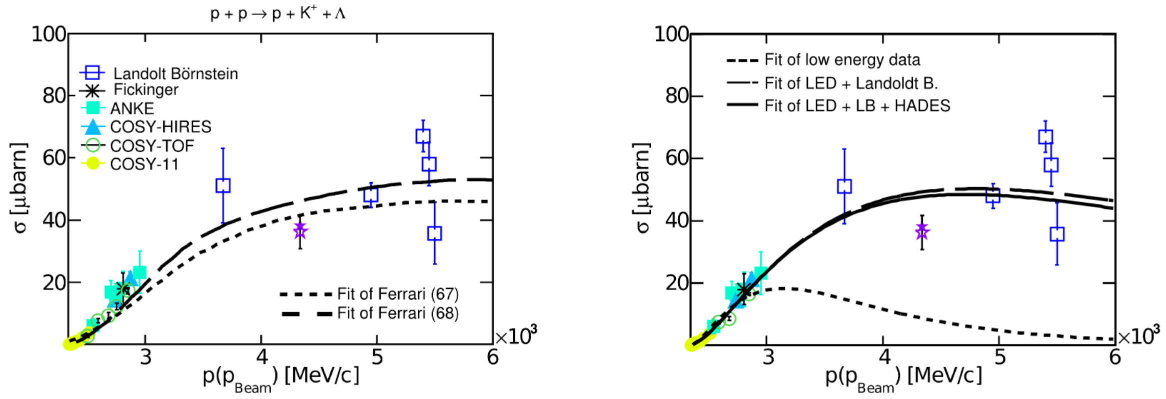

Figure 6.14: $pK^+\Lambda$ production cross section at different beam momenta. Pink star - this work. References to the data points are shown in Table G.1. Left panel shows model predictions taken from Ref. [149] (Ferrari 67) and Ref. [200] (Ferrari 68). Right panel shows a fit of a phase space function according to Eq. (6.13).

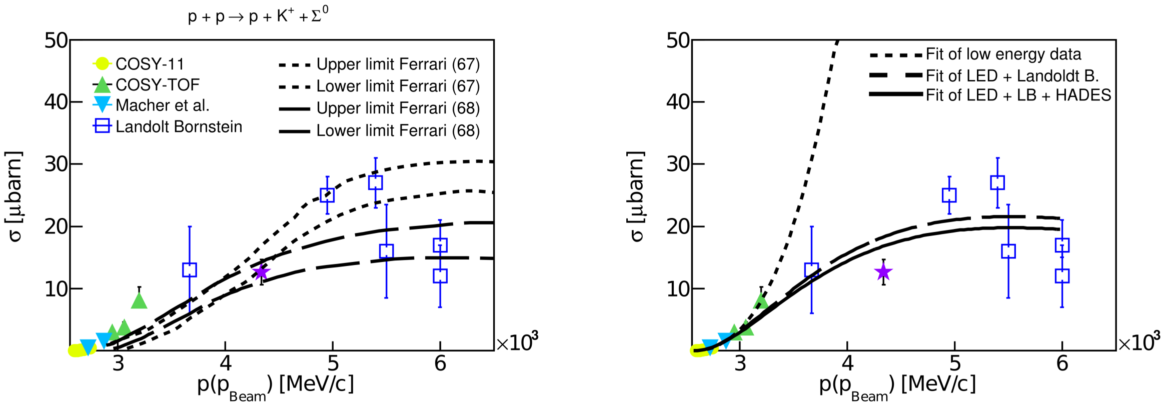

Figure 6.15: $pK^+\Sigma^0$ production cross section at different beam momenta [155]. Left panel shows model predictions taken from Ref. [149] (Ferrari 67) and Ref. [200] (Ferrari 68). Right panel shows a fit with the phase space function in Eq. (6.13).

p_{th} is the threshold momentum for the according production, p_{beam} is the beam momentum, m the mass of the proton, and a, b and c are free parameters determined by the fit. This function reproduces the energy dependence of the phase space just above the threshold reasonably well [201]. Originally the parameters a, b, and c were tuned such that they match the predictions of a boson exchange model in Ref. [202] and were not fitted to the data. The resulting model prediction of the original work is shown in Figure 6.16. It practically overestimates all but two experimental measurements. If the parameters a, b, and c are released, however, and fitted to the experimental data the three curves, shown in the right panels of Figures 6.14 and 6.15, appear. One curve is fitted only to the low-energy data of COSY and Macher et al. (LED), one also includes the high energy data from the Landoldt Börnstein Series, and the third one includes all data points such as the HADES measurement. The prediction is very sensitive to which experimental data points are included into the fit. The $pK^+\Lambda$ and $pK^+\Sigma^0$ cross-section, determined in this work, lie, like some other data at higher energies, below the phase-space parametrisation. The $pK^+\Lambda$ and $pK^+\Sigma^0$ production cross sections at a beam momentum of 4338 MeV/c (E_{Kin} = 3.5) interpolated with the different models are shown in Tables 6.10 and 6.11. The extracted cross sections of this work are consistent with these interpolated cross sections within 3σ of the experimental errors.

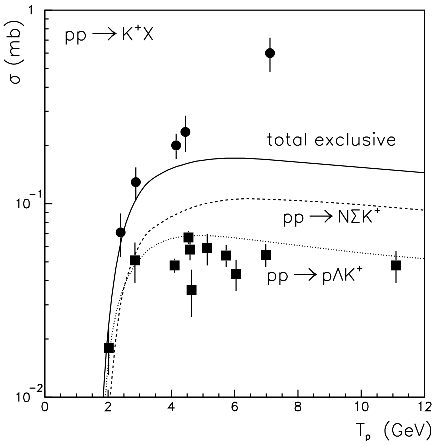

Figure 6.16: Inclusive (dots) and exclusive (squares) kaon production cross section in p+p collisions. The curves show model predictions for the three cross sections parametrized with Function (6.13) [202].

Table 6.10: Interpolated $pK^+\Lambda$ production cross section at a beam momentum of 4338 MeV/c. The cross sections of HADES are shown for the two different data analyses (multi-fit) and (PWA). They include an additional error of 7% due to the cross-section normalization to p+p elastic events.

Fit	Cross section [μb]
Ferrari (67) [149]	41.5
Ferrari (68) [200]	46.1
Low energy data	8.7
LED + Landolt Börnstein	49.24
LED + LB + HADES	47.7
HADES-values	$36.33 \pm 0.51^{+0.47}_{-0.73}$ (multifit)
	$38.12 \pm 0.43^{+3.55}_{-2.83}$-2.9 (PWA)

Table 6.11: Interpolated $pK^+\Sigma^0$ production cross section at a beam momentum of 4338 MeV/c. The cross section of HADES is shown for the data analysis from Chapter 3 (multi-fit) and includes an additional error of 7% due to the cross-section normalization to p+p elastic events.

Fit	Cross section [μb]
Ferrari (67) [149]	13.2-16.9
Ferrari (68) [200]	11.1-14.3
Low energy data	108.7
LED + Landolt Börnstein	18.3
LED + LB + HADES	16.8
HADES-value	$12.64 \pm 0.32^{+0.26}_{-0.34}$

7 | Discussion and Outlook

7.1 HADES Results in the Context

In this section, the result of this work is put in context with $pK^+\Lambda$ measurements at different beam energies and is confronted to the claims of the DISTO collaboration that the observed structure X(2265) is associated with the production of a kaonic nuclear bound state $\overline{K}NN$. Table 7.1 gives an overview of reported $p\Lambda$ mass spectra at various beam kinetic energies and the according excess energies of different production processes. The first excess energy is quoted for the $pK^+\Lambda$ production threshold, the second shows the excess energy of the hypothetical state X(2265) together with a K^+, and the third quotes the excess energy over the production threshold for the $\Lambda(1405)$-resonance.

Table 7.1: Different publications showing a $p\Lambda$ invariant mass spectrum. ^{a} Λ^* with M=1385 MeV/c^2 [23, 173].^{b} not published. The values denote E_{Kin} in [GeV] and excess energies ϵ in [MeV].

Figure	Reference	E_{Kin}	$\epsilon(pK^+\Lambda)$	ϵ(DISTO)	$\epsilon(pK^+\Lambda^*)^a$
7.2/7.3	[199]/ [157]	2.16	203.7	-9.3	-65.6
7.2	[199, 166]	2.28	246.0	33.0	-23.3
7.4/7.3	[172]/[157]	2.4	284.0	71.0	14.7
7.3	[157]	2.49	315.7	102.7	46.4
^{b}	[128]	2.5	318.2	105.1	48.8
^{b}	[125]	2.85	430.5	217.5	161.2
7.5	[203]	3.1	508.3	295.2	239.0
7.6	this work	3.5	629.3	416.3	360.0
7.7/7.8	[161]	4.1	815.0	602	545.7
7.9/7.10	[162]	5.13	1079.6	866.5	810.3
7.11	[204]	7.1	1560.4	1347.36	810.3

The results in this table should be compared to the statements of the DISTO collaboration concerning the production yield of the X(2265) structure. After the interpretation of the structure in the $p\Lambda$ spectrum as a new state (DISTO at 2.85 GeV), it was estimated that at the lower beam energy of 2.5 GeV (see Table 7.1) the defined state X(2265) could be produced with a yield of 33% of that observed at 2.85 GeV [205]. A re-analysis of the 2.5 GeV DISTO data, however, did not show any sign of the X(2265). In a report that followed, the production cross sections of the X(2265) were quoted as 16% and 0.2% of the $pK^+\Lambda$ production cross section for 2.85 GeV and 2.5 GeV, respectively [128]. An interpolation of the $pK^+\Lambda$ production cross section in Figure 7.1 delivers a production cross section of $\approx 33.7\ \mu$b and $\approx 41.0\ \mu$b for 2.5 GeV and 2.85 GeV, respectively. This translates then into the estimated cross sections for the X(2265) production of 5.4 μb and 0.008 μb. As quoted in Ref. [125], the produced yield of X is found to be as large as for the $\Lambda(1405)$ which is in agreement with the estimations for the $\Lambda(1405)$ production cross section done in the next section.

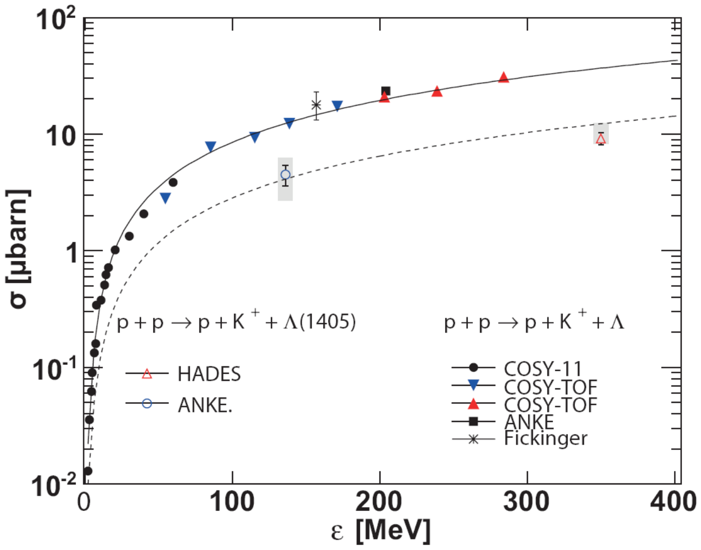

Figure 7.1: The production cross sections of the $pK^+\Lambda$ and the $pK^+\Lambda(1405)$ final state at intermediate excess energies [173].

7.1.1 DISTO Signal at Low Energies

Table 7.1 shows the excess energy for the production of a X(2265). Beginning from a beam energy of 2.4 GeV, structures of the X(2265) should be visible in the data. Given the large width of 120 MeV of this state, its production at an excess energy of -9 MeV is kinematically still allowed.

The close inspection of the $p\Lambda$ invariant mass spectra in Figures 7.2, 7.4, and 7.3 shows no sign of an enhancement of statistic at 2265 MeV/c^2 or 5.13 (MeV/c^2)^2, respectively. Together with the negative findings at a beam energy of 2.5 GeV from the DISTO collaboration itself, the interpretation of X(2265) being due to the production of a new state namely the $\overline{K}NN$ is questionable.

The absence of the structure at E_{Kin} = 2.5 GeV was interpreted as a sign for the unique production mechanism of the $\overline{K}NN$, namely via the Λ^*-doorway formation [128, 87]. In this ansatz, the production of the $\overline{K}NN$ is postulated via:

$$p + p \rightarrow K^+ + p + \Lambda(1405) \rightarrow K^+ + [p\Lambda(1405)] \rightarrow K^+ + \overline{K}NN. \tag{7.1}$$

Following this suggestion, a $\Lambda(1405)$ needs to be produced prior to the appearance of a $\overline{K}NN$, which is only possible above the Λ^* production threshold. Due to this mechanism the absence of a signal at 2.5 GeV was explained and an upper limit of 0.2% of the $pK^+\Lambda$ production cross section was reported [128].

Still, the excess values quoted in Table 7.1, on the other hand, reveal that from a beam kinetic energy of 2.4 GeV on the production of a $\Lambda(1405)$ is kinematically possible.

Figure 7.1 (Ref. [173]) shows the production cross section of the $pK^+\Lambda$ and the $pK^+\Lambda(1405)$ final state at intermediate excess energies. From this interpolation of the cross sections, a value of 4.46 μb and 1.15 μb can be estimated for the $\Lambda(1405)$ production at E_{Kin} = 2.85 and 2.5 GeV, respectively. Based on this

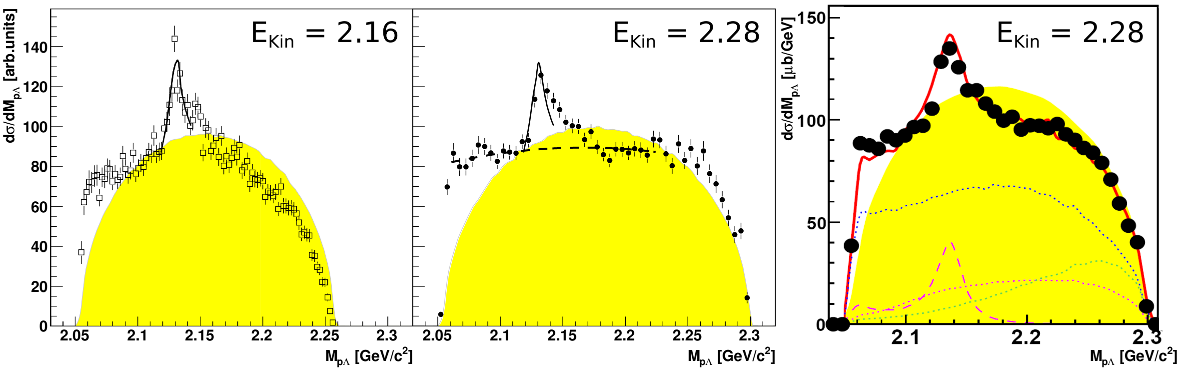

Figure 7.2: $p\Lambda$ invariant masses from p+p collisions at E_{Kin} = 2.16 and 2.28 GeV [199, 166]. The two distributions at 2.28 GeV stem from two separate analyses of the same data.

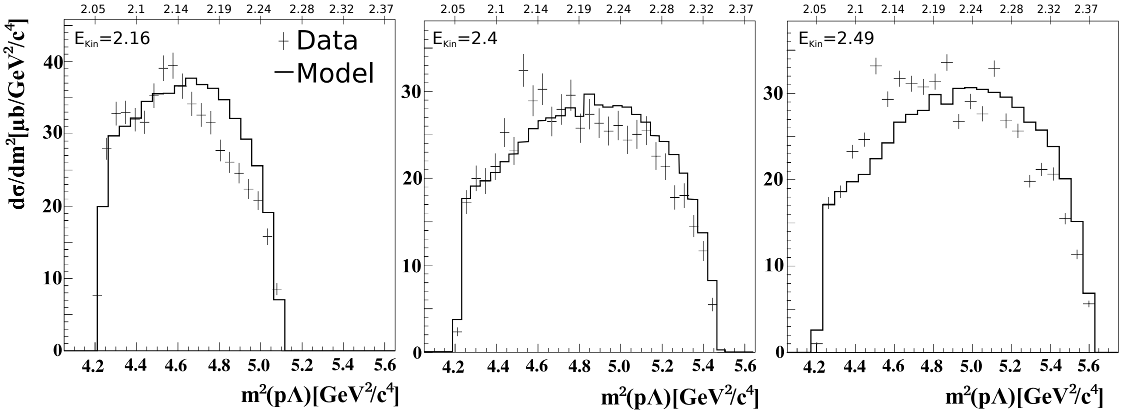

Figure 7.3: $p\Lambda$ invariant masses from p+p reactions at E_{Kin} =2.16, 2.4 and 2.45 GeV [157].

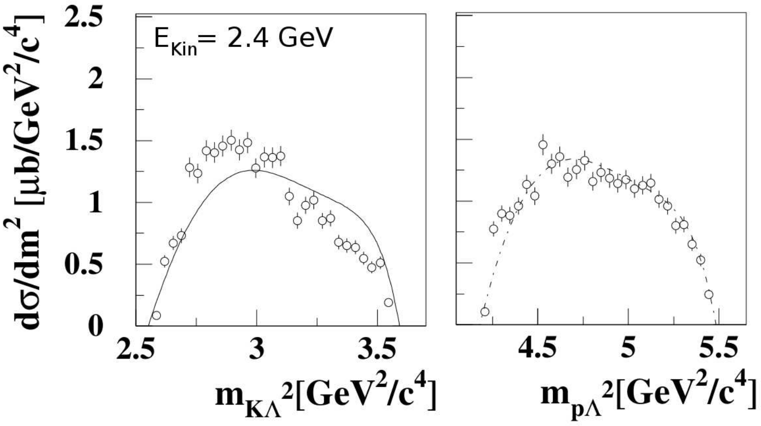

Figure 7.4: $K^+\Lambda$-, and $p\Lambda$ invariant masses from p+p collisions at E_{Kin} = 2.4 GeV [172].

comparison, a decreased yield of X(2265) rather than a complete lack is more naturally the consequence. In the $\Lambda*$-doorway picture the observed Λ(1405) particles in the final state are the remaining seeds of the $\overline{K}NN$ production. If the ratio of unaffected Λ(1405) and produced $\overline{K}NN$ via Reaction (7.1) stays constant, a produced yield of 1.38 μb for the X(2265) production would be expected. In case the sticking of the Λ(1405) and the proton to a $\overline{K}NN$ occurs only in a small amount of phase space, this ratio should be even higher at lower energies. The explanations in Ref. [128] for the missing X(2265) signals seems, thus, rather inconclusive as it is not motivated why, despite a finite yield of Λ(1405), no trace of a X(2265) signal is visible.

7.1.2 DISTO Signal at High Energies

According to the argumentation in Ref. [128, 87], the larger production rate of the Λ(1405) at higher proton beam energies should favor the production of a $\overline{K}NN$ via Reaction (7.1). This is not confirmed by several observations ranging from E_{Kin} = 3.1 to 7.1 GeV. Figures 7.5-7.11 show $p\Lambda$ invariant mass spectra in which no substantial excess compared to the model predictions is visible.

The result of this thesis adds a quantitative statement to this qualitative inspection. Figure 7.6 summarizes the mass spectra from this work. These observables show no enhancement at a $p\Lambda$ mass of 2265 MeV/c^2. This observation is accompanied by an elaborate statistical analysis which tests the possible production yield of a $\overline{K}NN$ at 3.5 GeV beam kinetic energy. The result shows that in case of interference with other production channels the contribution of a $\overline{K}NN$ to the total $pK^+\Lambda$ production cross section can be as large as ≈ 2–7% (Γ = 30 MeV), 3–10% (Γ = 50 MeV) and 3–12% (Γ = 70 MeV). With the results from Chapter 6 this translates into 0.7-2.5 μb, 1-3.5 μb, and 1-4.2 μb, respectively. This is indeed a conservative estimate as it implies destructive interference of the $\overline{K}NN$ wave with the other waves. In this way, a part of the cross section can be reserved for the production of a $\overline{K}NN$ without its appearance in the $p\Lambda$ mass spectrum.

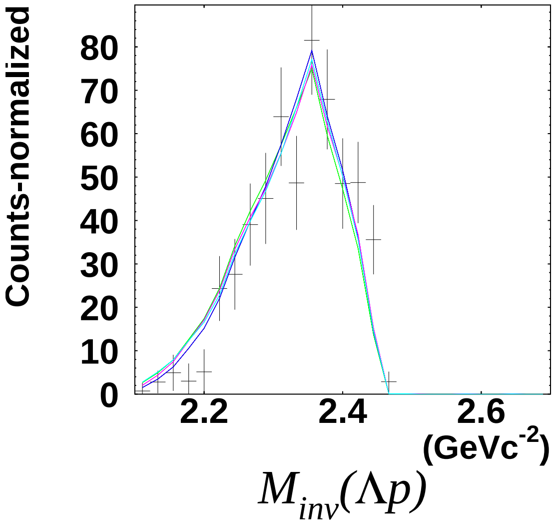

Figure 7.5: $p\Lambda$ invariant mass from p+p collisions at E_{Kin} = 3.1 [203].

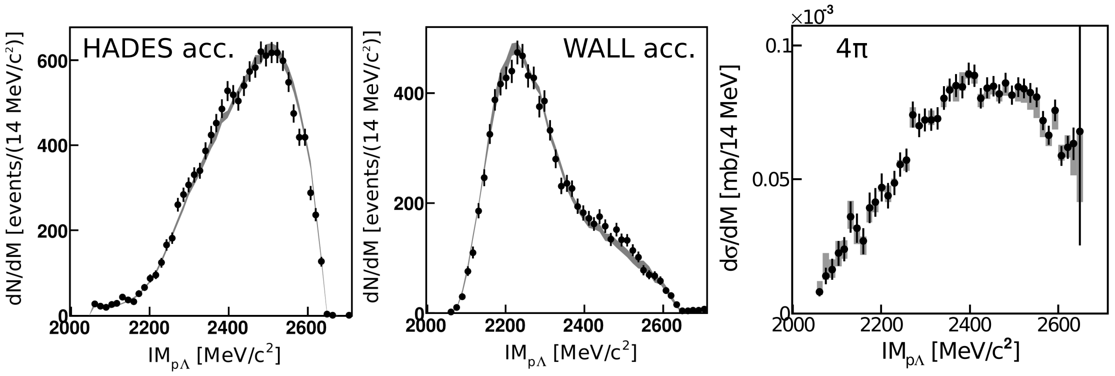

Figure 7.6: $p\Lambda$ invariant masses from p+p collisions at E_{Kin} = 3.5 GeV, shown for the two detector acceptances and 4π (this work).

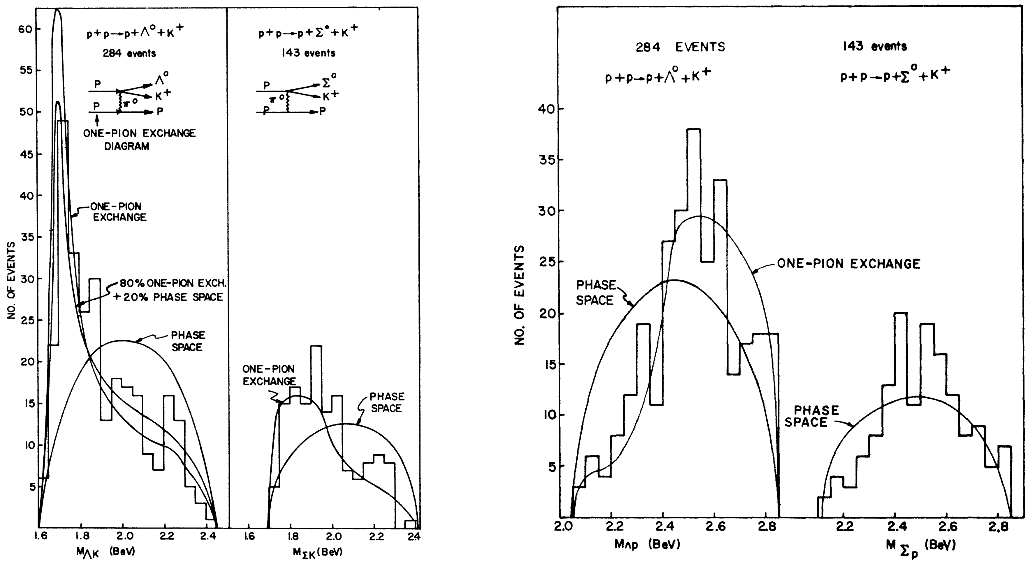

Figure 7.7: K^+Y^0-, and pY^0 invariant masses for exclusive Σ^0 and Λ from p+p collisions at E_{Kin} = 4.1 GeV [161]. The distributions show nicely the kinematic reflections of the N^*-resonance production in the $p\Lambda$ mass spectrum.

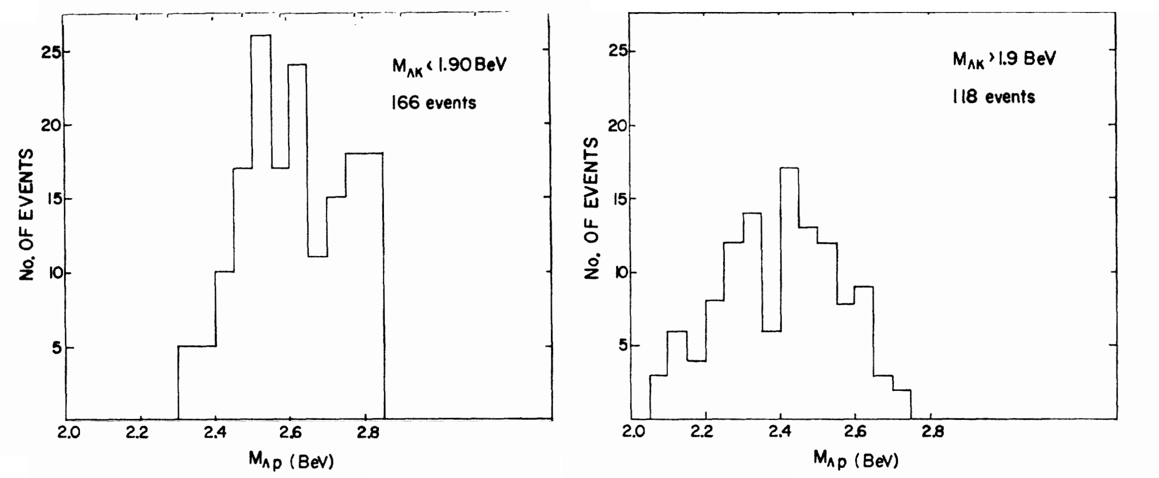

Figure 7.8: $p\Lambda$ invariant masses from p+p collisions at E_{Kin} = 4.1 GeV for low and high masses of $K^+\Lambda$ [161].

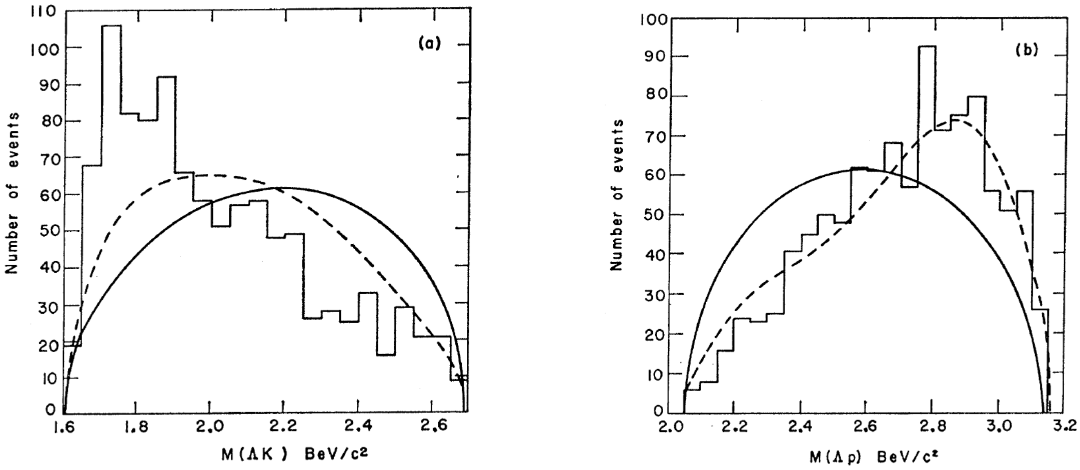

Figure 7.9: $p\Lambda$ invariant masses from p+p collisions at E_{Kin} = 5.13 GeV [162]. The figures show a comparison of the data with phase space distributions (solid line) and the inclusion of kinematic reflections (dashed line).

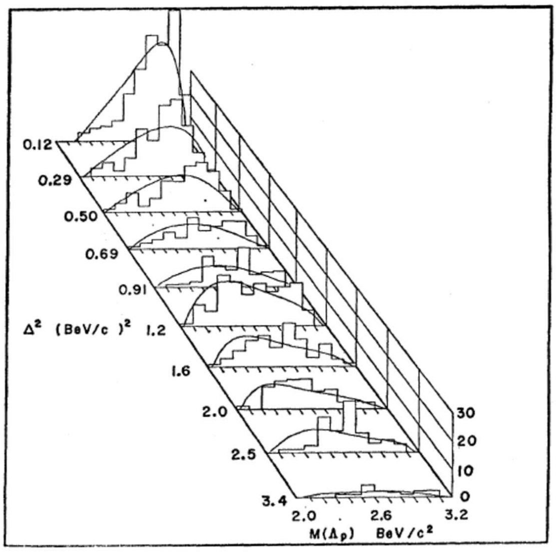

Figure 7.10: $p\Lambda$ invariant mass distributions shown as a function of the momentum transfer. The curves show phase space distributions. Produced in p+p collisions at E_{Kin} = 5.13 GeV [162].

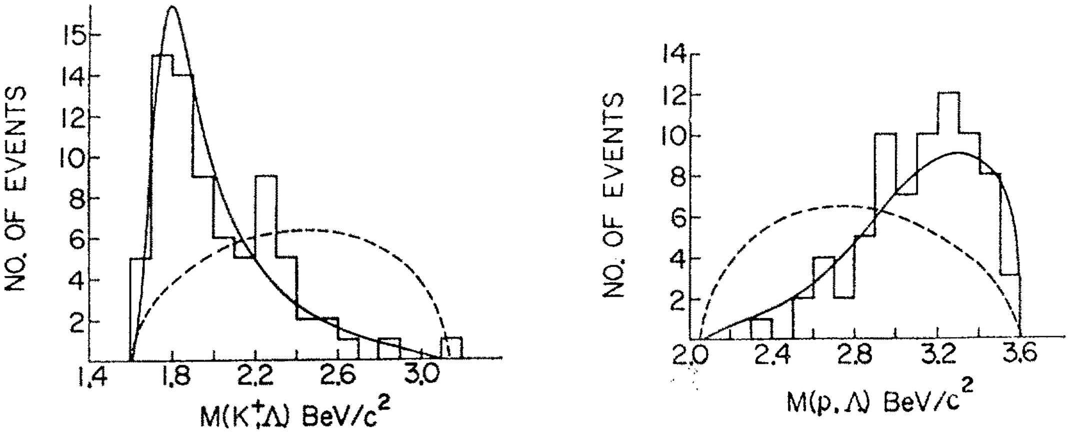

Figure 7.11: $K^+\Lambda$-, and $p\Lambda$ invariant masses from p+p collisions at E_{Kin} = 7.1 GeV [204]. The solid curve shows the predicted distribution from a one pion exchange model and the dashed curve shows the distribution for the one kaon exchange model.

A further upper limit, that also includes interferences, is reported by an analysis of data measured with the FOPI spectrometer at E_{Kin}=3.1 GeV [203], which was conducted in parallel to the here presented work. At this beam energy, an upper limit for the production cross section of the $\overline{K}NN$ of 4–55% (Γ = 20 MeV), 5–32% (Γ = 50 MeV) and 18–80% (Γ = 80 MeV), depending on the assumed mass of the hypothetical state, was deduced. The corresponding mass spectrum is visible in Figure 7.5.

The definition of a $\overline{K}NN$ contribution in this work is quite different from the one in the DISTO analysis, where the yield was associated to an observed instead of a produced yield (prior to its destructive-, or constructive interference). If the cross section in the HADES analysis would be defined by the integral of a visible signal, as done by DISTO, it would be consistent with approximately zero, as displayed in Figure 7.6.

No signal from a $\overline{K}NN$ was observed in the analysis of the HADES data, although, a certain amount of Λ(1405) is produced at E_{Kin} = 3.5 GeV, with a cross section as high as: $\sigma_{pK^+\Lambda(1405)}$=9.2±0.9$^{+3.3}_{-1.0}$±0.6 μb [23]. If the production of the $\overline{K}NN$ indeed proceeds via the sticking of a p to a Λ(1405), this observation is inconsistent with the explanations in Ref. [128] why a signal at 2.5 GeV beam energy is absent. In case of an energy independent sticking probability of the Λ(1405) and the p, the production rate of the hypothetical state X(2265) at 3.5 GeV is expected to be double as high as for the DISTO experiment at 2.85 GeV.

Non of this is observed and, thus, this work excludes the predicted "dominance of the Λ(1405)-doorway scenario" of Ref. [87] at a beam energy of 3.5 GeV. This is valid only for the $p\Lambda$ decay channel.

7.1.3 Conclusion

In view of an absent signal at lower and higher energies, the interpretation of the observed structure X(2265) in the $p\Lambda$ invariant mass spectrum (DISTO signal) as a $\overline{K}NN$ signal is called into question.

This work adds, for the first time, a quantitative statement to these observations. The analysis of 20,000 $pK^+\Lambda$ events with help of a partial wave analysis is an ideal tool to implement the production of a kaonic cluster in a consistent way. A strong statement can be made that, even though destructive interference are present in the model that allow a contribution as high as 12% (produced yield) of the $pK^+\Lambda$ production cross section, the DISTO signal strength of 16% (observed yield) at 2.85 GeV can be excluded.

The scenario of a large formation of a $\overline{K}NN$ bound state in p+p reactions, as predicted in Ref. [87], can not be confirmed by a wealth of measurements in the relevant energy regime and the quantitative results of this work. This thesis, therefore, relegates the strong claims put forward in Ref. [125] and is, thus, a crucial addition to the ongoing discussion of possible $\overline{K}NN$ signals and their interpretation.

Extending this non-observation of any signal in the $p\Lambda$ spectrum to signals from other reaction systems, one can conclude that neither a FINUDA like signal (M, Γ)= (2225±6, 67±14) MeV/c^2 [117] nor an OBELIX like signal (M, Γ)= (2212.2±4.9, < 24.4±8) MeV/c^2 [117] was observed in p+p collisions with a $pK^+\Lambda$ final state.

7.2 Outlook

7.2.1 Further Possibilities for the Partial Wave Analysis

In principle, it is possible to add the $\overline{K}NN$ directly into a PWA of measured data instead to a fixed solution with N* resonances and perform a simultaneous fit with all other waves. That was not done in this work, as the ambiguities from the N*-resonances itself are already huge. Thus, any extracted information of a $\overline{K}NN$ in such kind of fit is not solid enough to make a clear statement about possible mass width and yield values that are most consistent with the data.

One may perform such an analysis for the search of a $\overline{K}NN$, if first, the status of the existence of some N*-resonances is more solid and second, the masses and widths of them are much better established. To obtain these information, the large-scale analysis of $pK^+\Lambda$ final states at several beam energies, measured by different collaborations, is certainly the right approach [206]. This proposed program combines these data in order to perform a simultaneous partial waves analysis of the various data-sets (E_{Kin} = 1.8 – 3.5 GeV). In this way one may fix the contributions of the different N*'s with a better accuracy.

Further, one can perform a PWA of other final states of the N* decay in parallel and cross check the results for consistency. An example of such a discussion is given in Ref. [200]. If a value for the branching ratio is known, the yield from the $K^+\Lambda$ final state can be used to reconstruct the total N* production in p+p collisions which can not deviate much from the yield established from the $p\pi$ final state, for example.

These improvements may help to stabilize the prediction of the fit. Nevertheless, a critical evaluation of the proposed transition amplitude strength of a $\overline{K}NN$ contribution needs to be performed in such a kind of fitting procedure. Careful evaluation of the fitted yield as a function of the included uncertainties of other transition waves is indispensable.

7.2.2 How to find a $\overline{K}NN$?

The searches for the $\overline{K}NN$ in its $p\Lambda$ decay channel, so far, have not resulted into a breakthrough. Given the decay branching ratios in Table 1.1 of Section 1.6, a search for the $\overline{K}NN$ in other decay channels might be more promising. The most promising one would be $\overline{K}NN \rightarrow \Sigma N\pi$. As the mass spectra of such decays start at $\approx$ 2270 MeV/c^2, very deeply bound kaonic cluster can not be accessed via this final state.

Figure 7.12 presents the invariant masses of $\Sigma^+ p\pi^-$ and $\Sigma^- p\pi^+$ as a byproduct of the $\Lambda(1405)$ analysis in its charged decay channels [23]. The figure is presented inside of the HADES acceptance and shows that large opening angles (correlated with large invariant masses) are preferred by the acceptance. The statistic below 2400 MeV/c^2 is, unfortunately, too low to draw any conclusion about a $\overline{K}NN$ signal in the data. An inclusion of the Forward Wall to the analysis, as done in this work, *might* be helpful to get a better access to low opening angles between the particles. The mass observable in this case, however, should

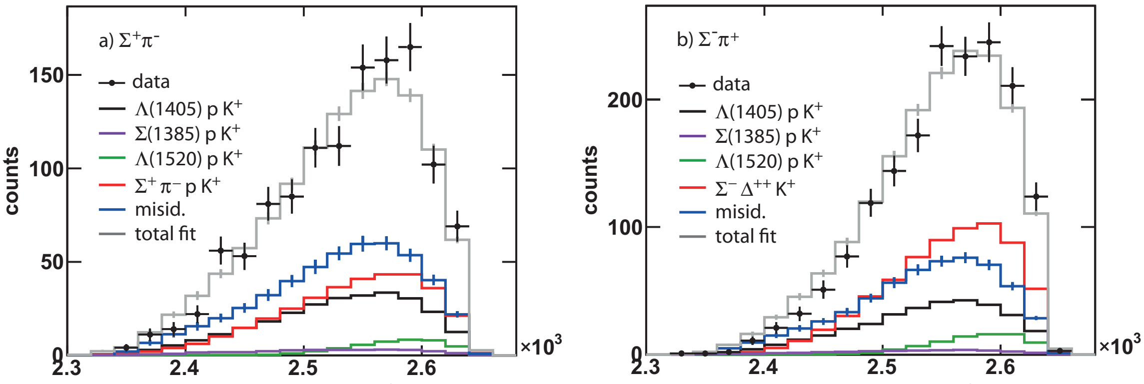

Figure 7.12: The $\Sigma N\pi$ final states from p+p collisions at 3.5 GeV [23]. The left panel shows the invariant mass of $\Sigma^+ p\pi^-$ and the right panel shows the invariant mass of $\Sigma^- p\pi^+$. A signal of the $\overline{K}NN$ is expected somewhere below 2400 MeV/c^2.

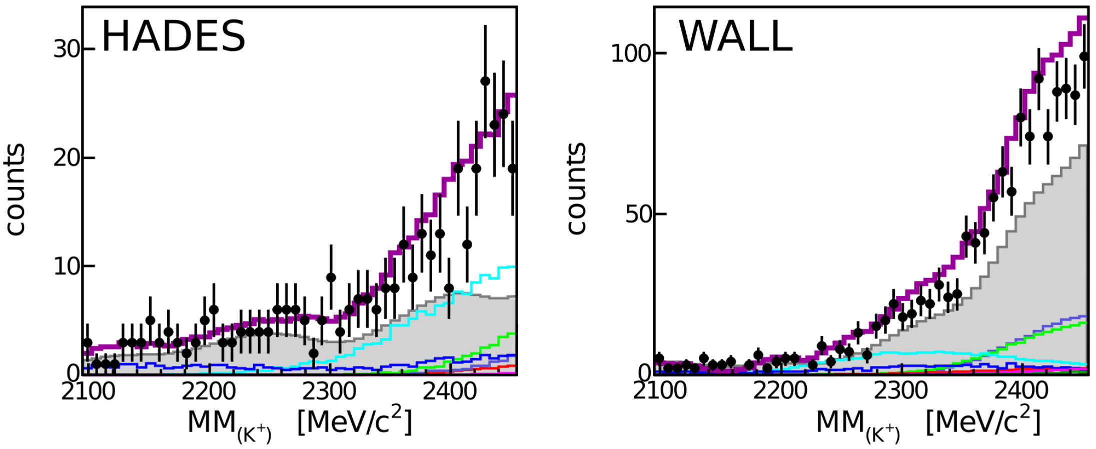

Figure 7.13: The missing mass to the K^+ from p+p collisions at 3.5 GeV. The left panel shows the statistic for the HADES acceptance and the right panel for the WALL acceptance. A signal of the $\overline{K}NN$ is expected somewhere below 2400 MeV/c^2.

be accessed via the missing mass to the kaon rather than the invariant mass of three particles, as the mass resolution of this four-vector will probably be better.

Figure 7.13 presents the missing mass to the K^+ from the analysis of the $\Lambda(1405)$ and $\Sigma(1385)^0$ decays (Chapter 3). It is a sum of missing $p\Lambda$ (blue), $p\Sigma^0$ (cyan), $p\Lambda\pi^0$ (green), $p\Sigma^0\pi^0$ (violet), and mis-identification background (gray shaded) – to name the main components. The statistic was selected to contain mainly contributions from the production of resonance and thus the mass spectrum of $MM_{K^+} \hat{=} p\Sigma^0\pi^0$ (for Λ^*) and $p\Lambda\pi^0$ (for Σ^*). This was done by a restriction of the data ($MM_{p,K^+,p,\pi^-} > 60$ MeV/c^2 (HADES), > 55 MeV/c^2 (WALL), and < 400 MeV/c^2 for both cases) which cuts away most of the $pK^+\Lambda$ and $pK^+\Sigma^0$ contribution. The sum of the components (plum-colored) can describe the measured data from both data-sets (HADES and WALL) well. No major excess is observed at the mass range below 2400 MeV/c^2. But also in this statistic the events are limited and in addition dominated by $pK^+\Sigma^0$ production, so that a detailed conclusion can not be drawn from these data. To access this decay channel in the future, experiments with a much higher statistic and a good acceptance for multi-particle final states are needed.

Appendix

A | Additional Figures to the Y^{0*}-Analysis

The mass distributions in Figures A.1 and A.2 show the MM_{pK^+} for the selected events prior to the subtraction of the mis-identification background. The figures reveal how nice the background (gray-shaded) can be modeled with the side-band data samples. The distributions after the background subtraction are shown in Figures 3.10 and 3.11 of Chapter 3.

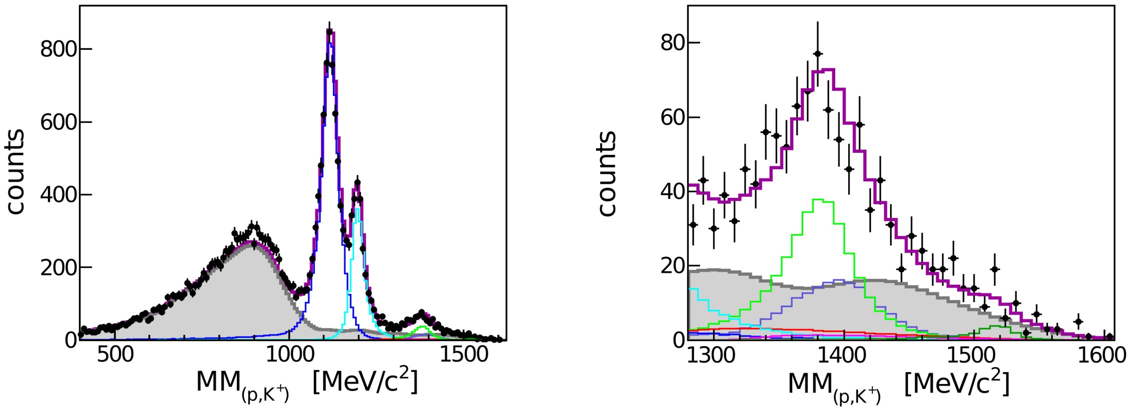

Figure A.1: Missing mass to the proton and the K^+ for the HADES data set. Left panel shows the statistic for all channels, right panel shows an enlargement of the resonance region. The color code of the different channels is explained in Table 3.2 of Chapter 3.

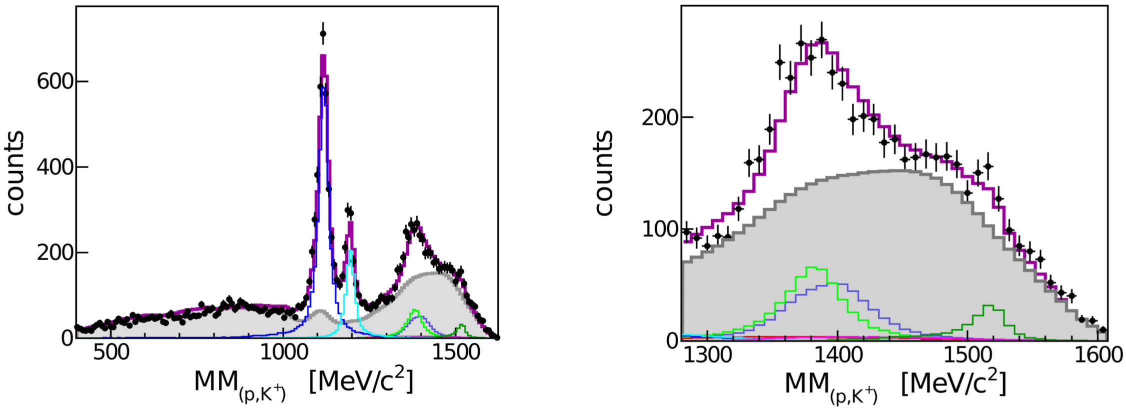

Figure A.2: Missing mass to the proton and the K^+ for the WALL data set. Left panel shows the statistic for all channels, right panel shows an enlargement of the resonance region. The color code of the different channels is explained in Table 3.2 of Chapter 3.

B | Time-of-flight Reconstruction for $pK^{+}\Lambda$ Events

As discussed in Section 2.2 of Chapter 2, a missing event-start-signal in the p+p experiment, prevents the direct measurement of the time-of-flight of the particle. This quantity can, however, be reconstructed, see Ref. [145]. The method was introduced in Section 2.2, where it was pointed out that several options for this reconstruction exist. This Appendix illustrates these methods quantitatively based on the exclusive event selection of the $pK^{+}\Lambda$ final state. Table B.1 summarizes the details of the different TOF-reconstruction methods tested in this analysis. In each method different constraints were applied to the data selection. In method No. 1, for example, both protons and the pion were used for the time-of-flight reconstruction. The kaon was only used in case it was selected by a PID cut in the dE/dx vs. momentum spectrum in both detectors: TOF and MDC. In method No. 2 the protons were only taken for the time-of-flight reconstruction in case their position in the dE/x vs. mom. spectrum did not

Table B.1: Possible methods to reconstruct the time-of-flight by combining the information of the four particles. n=not used, y=used, nK=particle was not inside the dE/dx cut for kaons. TOF and MDC indicate that the particle was only used for the reconstruction if it was identified, by the respective dE/dx cuts, as kaon.

No.	p_1	p_2	π^{-}	K^{+}
0	y	y	y	n
1	y	y	y	TOF and MDC
2	nK	nK	y	TOF and/or MDC
3	nK	nK	y	TOF and MDC
4	nK	nK	y	n

coincide with the kaon PID cut. This was done to avoid that kaons are mistaken for protons. In general, this scenario is very unlikely. Due to the data analysis the remaining statistic is, however, so strongly enhanced with kaons that this mix-up of the PID could happen. Out of all five methods only three use the kaon track for the time-of-flight reconstruction. This inclusion has to be monitored carefully, as it could introduce a bias. Thus, in these methods the kaon is only used, if at least one other track has been used for the reconstruction as well.

B.1 TOF Reconstruction for the HADES Data

Figure B.1 displays, for the events with a p-value>0.01 (see Chapter 4 for analysis details), the result of the reconstructed kaon mass distributions for each method. The data are displayed together with simulations in which the kaon candidate is a true kaon, pion or proton, respectively. The contributions were fitted to the data, such that the sum of the components describes the measured data best.

The five presented methods differ in how narrow the mass distribution is, and hence also the signal-to-background ratio (S/B) underneath the kaon peak differs among them. To calculate the signal yield, the histograms in Figure B.1, that contain the kaon contribution (red dashed), were integrated. For the background estimation, the histograms of pion and proton contribution (in blue) were integrated.

The total S/B-ratio amounts to ≈ 2.9 with minor differences between the methods. To improve this value a mass range between $0 < m_{K^+-candidate} < 710$ MeV/c^2 was chosen and the S/B ratio was computed inside this mass range separately. Additionally to those events in which the time-of-flight reconstruction worked well, there are three other cases:
Case 1: In these events, no stop signal was measured for the track of the kaon-candidate. This is the result of an efficiency of ≈ 90% in the META detector system. In this case, the kaon mass remains unknown.
Case 2: The time-of-flight could not be reconstructed by the method as not enough particles were available for the procedure. This happens in ≈0.1% of the cases and is, thus, negligible.
Case 3: The reconstructed time-of-flight of the kaon candidate has nonphysical values of v>c. The masses have, thus, negative values.

The S/B ratio in the selected mass range, as well as for the two relevant cases 1 and 3, are quoted in Table B.2. Based on the numbers in this table the methods

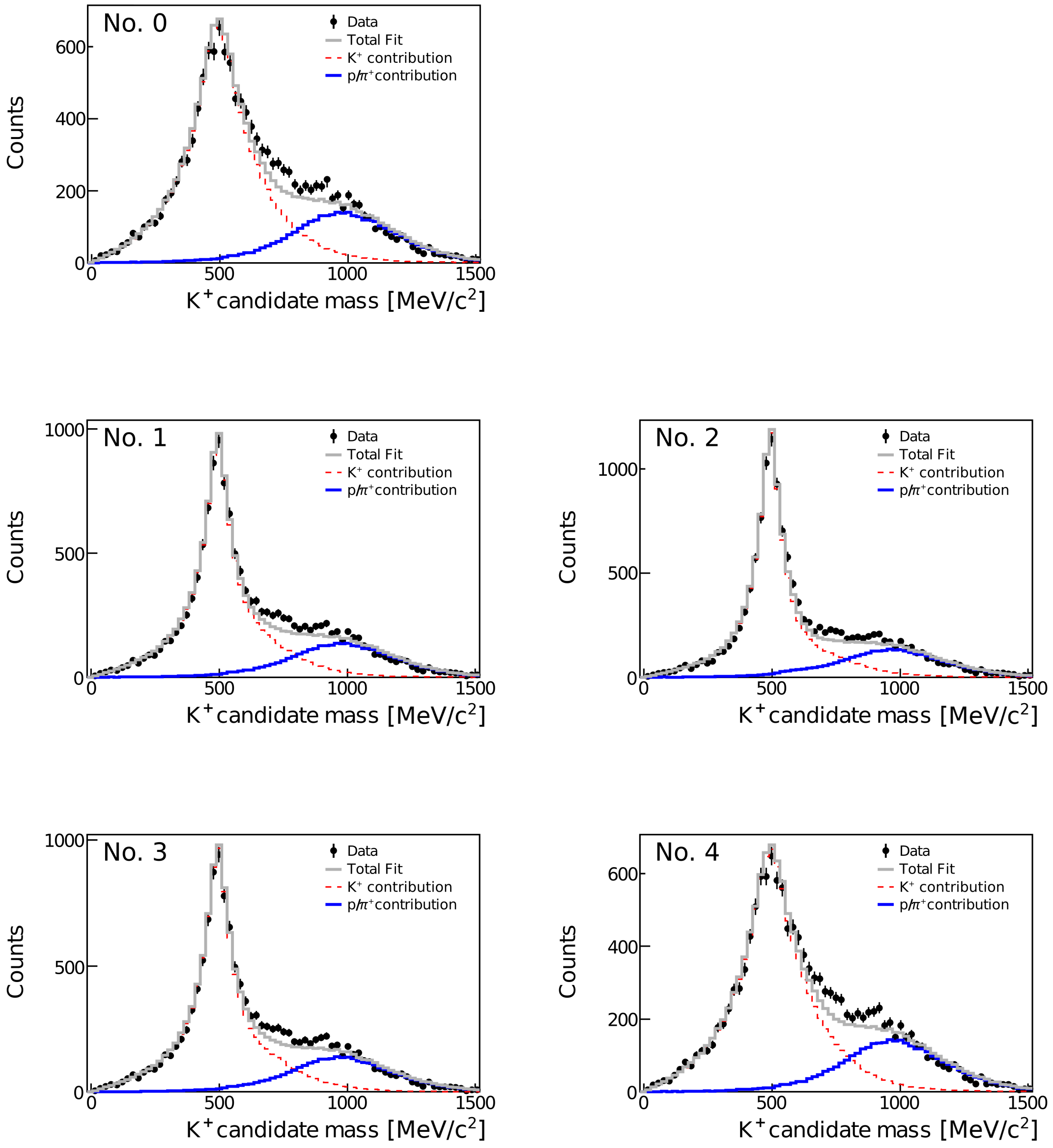

Figure B.1: The mass distributions of selected kaon candidates for five different reconstruction methods, see Table B.1. Together with the data simulations for various scenarios for the real identity of the candidate (pion, proton or indeed kaon) are shown.

Table B.2: Selected events and S/B ratio for the different reconstruction methods, all for a p-value cut of >0.01. M displays the statistic in the selected mass range (0-710 MeV/c^2), 1 and 3 show the statistic for the two cases, mentioned in the text, and Tot displays the sum of events.

No.	S/B M	S/B 1	S/B 3	S/B Tot	Data M	Data 1	Data 3	Data Tot
0	18.4	6.1	16.8	14.7	9790	2119	1536	13445
1	18.5	6.3	16.5	15	10095	2119	1412	13626
2	15.8	6.3	16.0	13.5	10537	2119	1288	13944
3	17.9	6.2	16.2	14.5	10090	2119	1425	13634
4	17.8	6	16.4	14.4	9775	2119	1554	13448

0-4 have been compared and the method No. 1 was chosen as best method for the time-of-flight reconstruction. It has the best signal to background ratio and a good yield of events. Furthermore, if one compares the selected statistic in the mass range for the three cases, described above, one may choose to take the data of Case 1 and Case 3 both into account. Their signal-to-background ratio is well and the number of 10-20% of additional events is considerably large. In case of method No. 1 the number of selected events is roughly 13600 with about 6.7% of background contamination.

To check a possible improvement of the S/B ratio two tests were performed. One test compared the resulting S/B and the selected statistic for different p-value cuts. Table B.3 shows the same information as Table B.2 for different p-value cuts in the data selection. All results are presented for a time-of-flight reconstruction with method No. 1.

A stricter p-value cut, as p-value>0.03, will increase the S/B ratio and decrease,

Table B.3: For method No. 1 and mass range 0-710 MeV/c^2: Selected events and S/B ratio for the different p-value cuts. M displays the statistic in the selected mass range (0-710 MeV/c^2), 1 and 3 show the statistic for the two cases, mentioned in the text, and Tot displays the sum of events.

p-value	S/B M	S/B 1	S/B 3	S/B Tot	Data M	Data 1	Data 3	Data Tot
>0.01	18.5	6.3	16.5	15	10095	2119	1412	13626
>0.02	20.2	6.9	17.7	16.3	9524	1970	1317	12811
>0.03	21.4	7.3	18.8	17.3	9190	1886	1263	12339
>0.04	22.2	7.6	19.5	17.9	8930	1829	1216	11975

at the same time, the number of selected events. One can compare the results for a p-value cut of >0.01 to a cut of >0.03. The background in the selected data sample decreases from 6.7% to 5.1%, but, at the same time, the loss of data is about 12%. Based on this it was decided to keep the p-value cut of >0.01 for the data selection as the best option.

The second test was done by varying the selected mass range. The results are illustrated in Table B.4. The different mass cuts change the amount of selected events and the resulting S/B ratio. To decide which option is the best, one has to choose whether a good purity or a high amount of selected events is the most important aim. In this work it was decided to go for a maximum yield rather than the smallest S/B possible. In the case of a selected mass range of 0-650 MeV/c^2 the loss of events is 8% compared to a selection of 0-710 MeV/c^2, whereas the contamination of misidentified events decreases from 7.2% to 5.5%. In this example the loss of events is too high so that this option was rejected. If one translates the percentage of contamination into counts one realizes that, if one opens the mass window from 680 MeV/c^2 to 710 MeV/c^2 one would gain 300 events but about half of them belong to the background. The best choice for the $pK^+\Lambda$ analysis is, thus, a mass cut of 0-680 MeV/c^2.

Table B.4: For Method 1 and p-value cut of >0.01: Selected statistic and S/B ratio for the different methods. M displays the statistic in the selected mass range (0-710 MeV/c^2), 1 and 3 show the statistic for the two cases, mentioned in the text, and Tot displays the sum of events.

Range [MeV/c^2]	S/B M	S/B Tot	Data M	Data Tot
0-760	14.2	12.6	10677	14212
0-730	16.5	13.9	10325	13860
0-710	16.5	13.9	10325	13860
0-680	19.4	15.3	9964	13499
0-650	26.3	17.9	9222	12757
0-620	30.2	19.0	8777	12312

In summary: for the HADES statistic method No. 1 is used to calculate the time-of-flight. The best S/B ratio is obtained with a p-value cut of >0.01. Events where selected, if the reconstructed mass is 0-680 MeV/c^2 or if case 1 or 3 of the time-of-flight reconstruction occurred in the event. The selected number of events is ≈13,500 and the resulting S/B is ≈15.3 which implies a background contamination of 6.5%.

B.2 TOF Reconstruction for the Wall Data

For the events in which one particle was detected in the Forward Wall detector, the time-of-flight reconstruction procedure stays the same as for the HADES data set. As the time information of the WALL was rejected from the procedure, there is, however, one particle less to build an average time of flight. Figure B.2 shows the results of the different time-of-flight reconstruction procedures for this data set. The resulting S/B ratio and the number of selected events are summarized in Table B.5. Given this result, the time-of-flight reconstruction method No. 2 was chosen as the best one for this data set. Compared to the HADES events the S/B ratio = 7.6 is rather low. Also the statistic is less with around 10,000 events.

Table B.5: Selected events and S/B ratio for the different reconstruction methods all for a p-value cut of >0.01. M displays the statistic in the selected mass range (0-710 MeV/c^2), 1 and 3 show the statistic for the two cases, mentioned in the text, and Tot displays the sum of events.

No.	S/B M	S/B 1	S/B 3	S/B Tot	Data M	Data 1	Data 3	Data Tot
0	6.0	6.3	5.2	5.9	5910	1384	1479	8773
1	7.6	7.7	6.3	7.3	6295	1384	1367	9046
2	7.5	8.9	7.4	7.6	7013	1384	1239	9636
3	6.9	7.6	6.2	6.8	6296	1384	1391	9071
4	5.4	6.1	5.0	5.4	5890	1384	1510	8784

Likewise to the HADES data, also in this case two checks were performed to validate a good S/B ratio and a high number of selected events. Table B.6 shows the results of the time-of-flight reconstruction with method No. 2 for

Table B.6: For Method 2 and mass range 230-700 MeV/c^2: Selected statistic and S/B ratio for the different p-value cuts. M displays the statistic in the selected mass range (0-710 MeV/c^2), 1 and 3 show the statistic for the two cases, mentioned in the text, and Tot displays the sum of events.

p-value	S/B M	S/B 1	S/B 3	S/B Tot	Data M	Data 1	Data 3	Data Tot
>0.01	7.5	8.9	7.4	7.6	7013	1384	1239	9636
>0.03	8.3	9.7	8.0	8.3	6258	1194	1095	8547
>0.06	9.7	12.6	9.0	9.8	5715	1051	987	7753

different p-value cuts. The p-value cut variation demonstrates a suppression of background contamination from 13.2% in case of a p-value >0.01 to 10.2% in case of a p-value >0.06. The amount of selected events, however, decreases from 9636 to 7753 which is a loss of ≈20% of data. This is considerably large so that a background suppression via a stricter p-value cut was not considered.

A better option is to change the selected mass range. Table B.7 shows the results for a variation of the selected mass range of the kaon candidates. If one narrows the mass cut from 230-700 MeV/c^2 to 230-640 MeV/c^2 the contamination of bad events is suppressed from 13.2% to 11.7%. This goes along with a loss of statistic of 5.9% which is equal to ≈500 events, which is a considerable improvement. Consequently, the choice was made to select a mass range of 230-640 MeV/c^2.

Table B.7: Selected statistic and S/B ratio for the different kaon mass ranges. The results were obtained with time-of-flight reconstruction method No. 2.

Range [MeV/c^2]	S/B M	S/B Tot	Data M	Data Tot
230-700	7.5	7.6	7013	9636
230-670	8.1	8.0	6730	9353
230-640	8.7	8.5	6448	9071
230-610	9.3	8.8	6113	8736

In summary: The S/B ratio for the WALL data-set is worse than for the HADES data-set. To reconstruct the start-time of the events the TOF reconstruction method No. 2 was selected. A p-value cut of >0.01 was applied to the data to improve the S/B ratio. The kaon candidates where selected, if their mass was within 230-640 MeV/c^2 or if the events belonged to Case 1 or 3 of the time-of-flight reconstruction. The selected number of events is ≈9,000 and the resulting S/B is ≈8.5 which implies a background contamination of 11.7%.

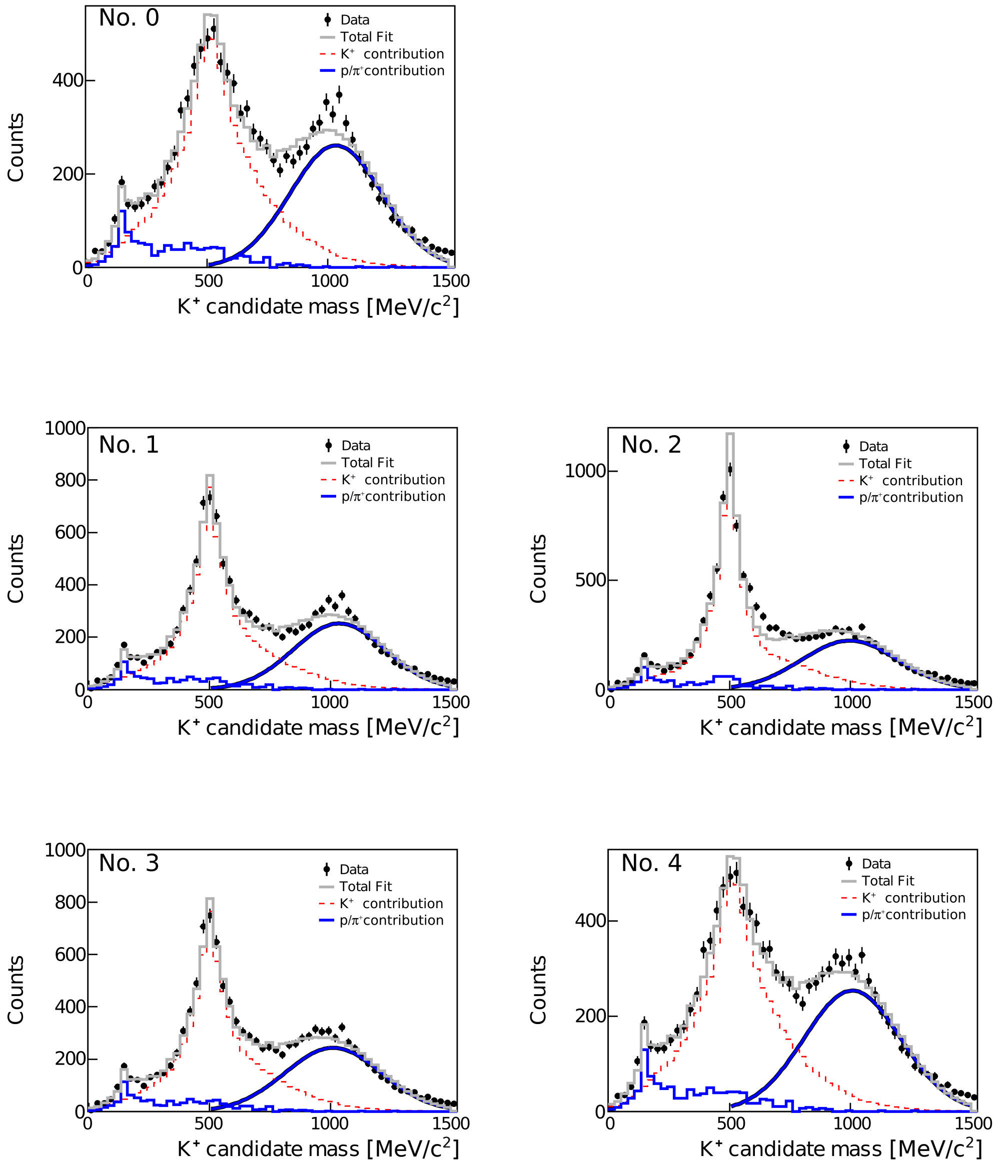

Figure B.2: The mass distributions of selected kaon candidates for five different reconstruction methods, see Table B.1. Together with the data simulations for two scenarios for the real identity of the candidate (pion or indeed kaon) are shown. The proton contribution to the data are fitted with a gauss function.

C

Selection of Transition Waves for the PWA

In the following, the spectroscopic notation [185] will be used to define initial and final states, see Equation 4.18 of Chapter 4. The states are further classified by their parity P and total spin J, in the form J^P.

C.1 Initial State of the Reaction

To characterize the initial proton proton state one needs to build all possible combinations of the quantum numbers of the two particles. The proton has the following quantum numbers: $J^P = \frac{1}{2}^+$. The spins of the two protons can be combined to a singlet or a triplet state with $S_{tot} = 0$ and $S_{tot} = 1$ respectively. Additionally, an orbital momentum L can appear between the two particles during the scattering process. The states in which the two protons react with each other are the ones listed in Tables C.1 and C.2.

As the initial system consists of two identical fermions its wave function has to

Table C.1: ${}^{2S+1}L_J$ of a combined system of two $\frac{1}{2}^+$ states. In case of a p+p system the states colored in gray are forbidden.

S_{tot} L	0	1
0	${}^1S_0$	${}^3S_1$
1	${}^1P_1$	${}^3P_0$, ${}^3P_1$, ${}^3P_2$
2	${}^1D_2$	${}^3D_1$, ${}^3D_2$, ${}^3D_3$
3	${}^1F_3$	${}^3F_2$, ${}^3F_3$, ${}^3F_4$

Table C.2: J^P of a combined system of two $\frac{1}{2}^+$ states. In case of a p+p system the states colored in gray are forbidden.

S_{tot} / L	0	1
0	0^+	1^+
1	1^-	$0^-, 1^-, 2^-$
2	2^+	1^+, 2^+, 3^+
3	3^-	$2^-, 3^-, 4^-$

be antisymmetric. For that, the following relation must be fulfilled:

$$(-1)^{S+L+1} = -1. \tag{C.1}$$

This means S+L must be an even number, which rules out the states in Tables C.1 and C.2 colored in gray.

The angular momentum which appears between the two protons is constrained by the available energy of the reaction. To describe the reaction at 3.5 GeV the angular momentum between the particles was limited to F-Waves with J<3 [183]. As a consequence of this limitation there are in total six initial combinations (without $^3F_3$, $^3F_4$) in which the two protons can react with each other.

C.2 Final State of the Reaction

In the PWA, the following compositions of a final state in $pK^+\Lambda$ were considered:

$$\rightarrow p + N^{*+} \quad \rightarrow p + K^+ + \Lambda, \tag{C.2}$$

$$\rightarrow (p\Lambda) + K^+ \quad \rightarrow p + K^+ + \Lambda, \tag{C.3}$$

$$\rightarrow ppK^- + K^+ \quad \rightarrow p + K^+ + \Lambda. \tag{C.4}$$

In the first reaction a proton with $J^P = \frac{1}{2}^+$ and an N^{*+}-resonance with various J^P are produced. In the second reaction the non-resonant production of $pK^+\Lambda$ is modeled in terms of an isobar of pΛ. This means the particles are first combined to a common state ($p\Lambda$) which could have various J^P combinations and one of these states is then combined to the kaon with J^P=0^-. In the third reaction the kaonic cluster with $J^P = 0^-$ (see Section 1.6.4 of Chapter 1) is produced together with a kaon of $J^P = 0^-$.

To determine, for example, under which condition a process according to Reaction C.4 can occur from an initial p+p state one has to determine the total spin and parity of the complete final state.

C.2.1 Final States Including N^{*+} Resonances

The N^{*+} resonances that have been used in the PWA are the following (full properties are listed in Table 4.1): $N(1650)\frac{1}{2}^{-}$, $N(1710)\frac{1}{2}^{+}$, $N(1720)\frac{3}{2}^{+}$, $N(1875)\frac{3}{2}^{-}$, $N(1880)\frac{1}{2}^{+}$, $N(1895)\frac{1}{2}^{-}$, $N(1900)\frac{3}{2}^{+}$. There are thus four different types of resonances according to their spin parity combination: $J^P = \frac{1}{2}^{-}$, $\frac{1}{2}^{+}$, $\frac{3}{2}^{-}$ and $\frac{3}{2}^{+}$. In the following tables the spin and parity of the complete final states consisting of a proton and one of these N^{*+} resonances are listed.

Table C.3: J^P of a combined system out of a $\frac{1}{2}^{-}$ and a $\frac{1}{2}^{+}$ particle.

S_{tot} L	0	1
0	0^-	1^-
1	1^+	$0^+, 1^+, 2^+$
2	2^-	$1^-, 2^-, 3^-$
3	3^+	$2^+, 3^+, 4^+$

Table C.4: J^P of a combined system of a $\frac{1}{2}^{+}$ and a $\frac{1}{2}^{+}$ particle.

S_{tot} L	0	1
0	0^+	1^+
1	1^-	$0^-, 1^-, 2^-$
2	2^+	$1^+, 2^+, 3^+$
3	3^-	$2^-, 3^-, 4^-$

Table C.5: J^P of a combined system of a $\frac{3}{2}^+$ and a $\frac{1}{2}^+$ particle.

S_{tot} L	1	3/2	2
0	1^+	$3/2^+$	2^+
1	$0^-, 1^-, 2^-$	$1/2^-$, $3/2^-$, $5/2^-$	1^-, 2^-, 3^-
2	$1^+, 2^+, 3^+$	$1/2^+$, $3/2^+$, $5/2^+$, $7/2^+$	0^+, 1^+, 2^+, 3^+, 4^+
3	$2^-, 3^-, 4^-$	$3/2^-$, $5/2^-$, $7/2^-$, $9/2^-$	1^-, 2^-, 3^-, 4^-, 5^-

Table C.6: J^P of a combined system of a $\frac{3}{2}^-$ and a $\frac{1}{2}^+$ particle.

S_{tot} L	1	3/2	2
0	$\mathbf{1}^-$	$3/2^-$	2^-
1	$0^+, 1^+, 2^+$	$1/2^+$, $3/2^+$, $5/2^+$	1^+, 2^+, 3^+
2	$\mathbf{1}^-, 2^-, 3^-$	$1/2^-$, $3/2^-$, $5/2^-$, $7/2^-$	0^-, $\mathbf{1}^-$, 2^-, 3^-, 4^-
3	$2^+, 3^+, 4^+$	$3/2^+$, $5/2^+$, $7/2^+$, $9/2^+$	1^+, 2^+, 3^+, 4^+, 5^+

Example for a Transition

A proton proton pair in the initial state J^P=1^- (spectroscopic notation $^3P_1$) could make a transition into a p+N^{*+} pair with an N^{*+} of spin parity $\frac{3}{2}^-$. This transition can happen for three combinations of L and S marked in bold in Table C.6. The spectroscopic notation of the final state reads $^3S_1$ for the case L=0 and S$_{tot}$=1, $^3D_1$ for the case L=2 and S$_{tot}$=1, and $^5D_1$ for the case L=2 and S$_{tot}$=2. In the PWA framework, the transition is written as follows into the input list of possible transition amplitudes:

$$I \rightarrow \quad 'N^* - p' \quad (2S_{tot}+1) \quad 'L'_{tot} \tag{C.5}$$

$$^3P_1 \rightarrow \; 'D13(1875) - p' \quad 3 \quad 'S', \tag{C.6}$$

$$^3P_1 \rightarrow \; 'D13(1875) - p' \quad 3 \quad 'D', \tag{C.7}$$

$$^3P_1 \rightarrow \; 'D13(1875) - p' \quad 5 \quad 'D'. \tag{C.8}$$

Here, I represents the initial state followed by the $N^* - p$ final state. The total spin of the final state is expressed by $(2S_{tot}+1)$ and L_{tot} stands for the total orbital momentum between the proton and the N*.

The states listed in the tables above are limited to F-waves. The exact order

Table C.7: N*-p final state and the maximum populated angular momentum between the particles.

Final states	$\sqrt{s_{Th}}$ [MeV]	$\sqrt{s_{Exp}}$-$\sqrt{s_{Th}}$ [MeV]	max. L populated
$N(1650)+p$	2593.27	583.1	F-wave
$N(1710)+p$	2648.27	528.1	F-wave
$N(1720)+p$	2658.27	518.1	F-wave
$N(1875)+p$	2813.27	363.1	D-wave
$N(1880)+p$	2808.27	368.1	D-wave
$N(1895)+p$	2833.27	343.1	D-wave
$N(1900)+p$	2838.27	338.1	D-wave

of orbital momentum which can be present between the proton and the N^{*+}-resonance is limited by the excess energy of their production. As an estimate for this effect one can suppose that every 150 MeV above threshold a new order of orbital momentum can be populated [183]. The CMS energy in this experiment is $\sqrt{s_{Exp}}$=3176.37 MeV. This leads to the limits in Table C.7. The complete list of possible final states in which N* resonances are produced is listed in Table C.9.

C.2.2 Final States Including Non-Resonant Production of $pK^{+}\Lambda$

To extract the properties of this three particle final state first the proton and the Lambda are combined to a common system ($p\Lambda$). The quantum numbers of this system are listed in Tables C.4 and C.8. To obtain the quantum numbers of the total final state the ($p\Lambda$) isobar is combined with the kaon. This is done as an example for the first three ($p\Lambda$) states.

Table C.8: $^{(2S+1)}L_J$ of a combined system of $\frac{1}{2}^+$ and $\frac{1}{2}^+$ (pΛ).

L \ S_{tot}	0	1
0	$^1S_0$	$^3S_1$
1	$^1P_1$	$^3P_0$, $^3P_1$, $^3P_2$
2	$^1D_2$	$^3D_1$, $^3D_2$, $^3D_3$
3	$^1F_3$	$^3F_2$, $^3F_3$, $^3F_4$

Table C.9: N*-p final states that can be produced out of a certain p+p initial state.

$^{2S+1}L_J$ (p+p)	J^P	'N*-p' (2S$_{tot}$+1)L$_{tot}$
$^1S_0$	0^+	'S11(1650)-p' 3P, 'S11(1895)-p' 3P, 'P11(1710)-p' 1S, 'P11(1880)-p' 1S, 'P13(1720)-p' 5D, 'P13(1900)-p' 5D, 'D13(1875)-p' 3P
$^3P_0$	0^-	'S11(1650)-p' 1S, 'S11(1895)-p' 1S, 'P11(1710)-p' 3P, 'P11(1880)-p' 3P, 'P13(1720)-p' 3P, 'P13(1900)-p' 3P, 'D13(1875)-p' 5D
$^3P_1$	1^-	'S11(1650)-p' 3S, 'S11(1650)-p' 3D, 'S11(1895)-p' 3S, 'S11(1895)-p' 3D, 'P11(1710)-p' 1P, 'P11(1710)-p' 3P, 'P11(1880)-p' 1P, 'P11(1880)-p' 3P, 'P13(1720)-p' 3P, 'P13(1720)-p' 5P, 'P13(1720)-p' 5F, 'P13(1900)-p' 3P, 'P13(1900)-p' 5P, 'D13(1875)-p' 3S, 'D13(1875)-p' 3D, 'D13(1875)-p' 5D
$^3P_2$, $^3F_2$	2^-	'S11(1650)-p' 1D, 'S11(1895)-p' 1D, 'P11(1710)-p' 3P, 'P11(1710)-p' 3F, 'P11(1880)-p' 3P, 'P13(1720)-p' 3P, 'P13(1720)-p' 5P, 'P13(1720)-p' 3'F', 'P13(1720)-p' 5F, 'P13(1900)-p' 3P, 'P13(1900)-p' 5P, 'D13(1875)-p' 5S, 'D13(1875)-p' 3D, 'D13(1875)-p' 5D
$^1D_2$	2^+	'S11(1650)-p' 3P, 'S11(1650)-p' 3F, 'S11(1895)-p' 3P, 'P11(1710)-p' 1D, 'P11(1710)-p' 3D, 'P11(1880)-p' 1D, 'P11(1880)-p' 3D, 'P13(1720)-p' 5S, 'P13(1720)-p' 3D, 'P13(1720)-p' 5D, 'P13(1900)-p' 5S, 'P13(1900)-p' 3D, 'P13(1900)-p' 5D, 'D13(1875)-p' 5P

Kaon Combined With a ($p\Lambda$) of Quantum Numbers $^1S_0$, (0^+)

If one wants to know if such a ($p\Lambda$) state can be produced together with a kaon from an initial p+p sate with the quantum numbers 0^+, one will see in Table C.10 that this is not possible, since such a state does not exist in this specific combination of $pK^+\Lambda$. One can, however, produce this constellation of particles from an initial state with J^P=0^- which is the $^3P_0$ wave of p+p. In the Bonn-Gatchina PWA framework a non-resonant final state is expressed as follows: the spectroscopic notation of the $p\Lambda$ state is written in brackets followed by the way how the kaon is combined to that state. The previously discussed combination would look as follows: ($^1S_0$) 1S. Outside the brackets 1 stands for (2S+1) of the combined final state and S denotes the angular momentum between the kaon and the ($p\Lambda$) state.

Table C.10: J^p of a final state in which a Kaon (0^-) was combined with a ($p\Lambda$) system of $^1S_0$, (0^+).

$J_{(p\Lambda)}$ L	0
0	0^-
1	1^+
2	2^-
3	3^+

Kaon Combined With a ($p\Lambda$) of Quantum Numbers $^3S_1$, (1^+)

Table C.11: J^p of a final state in which a Kaon (0^-) was combined with a ($p\Lambda$) system of $^3S_1$, (1^+).

$J_{(p\Lambda)}$ L	1
0	1^-
1	0^+, 1^+, 2^+
2	1^-, 2^-, 3^-
3	2^+, 3^+, 4^+

Kaon Combined With a ($p\Lambda$) of Quantum Numbers $^1P_1$, (1^-)

Table C.12: J^p of a final state in which a kaon (0^-) was combined with a ($p\Lambda$) system of $^1P_1$, (1^-).

$J_{(p\Lambda)}$ L	1
0	1^+
1	0^-, 1^-, 2^-
2	1^+, 2^+, 3^+
3	2^-, 3^-, 4^-

The total list of non-resonant waves that can be mapped to the initial p+p state is summarized in Table C.13. The non-resonant $pK^+\Lambda$ production was limited to $(p\Lambda)$ states with L<3 and J<3 [183].

Table C.13: Non-resonant waves that can be produced out of a certain p+p initial state. In the brackets: state of pL; Values outside of the brackets: state of the Kaon relative to the $(p\Lambda)$ system

$^{2S+1}L_J$ (p+p)	J^P	$^{2S+1}L_J$ $(p\Lambda)$-K
$^1S_0$	0^+	$(^3S_1)$ 3P, $(^3P_0)$ 1S, $(^3P_2)$ 5D, $(^3D_1)$ 3P, $(^3D_3)$ 7F
$^3P_0$	0^-	$(^1S_0)$ 1S, $(^1P_1)$ 3P, $(^1D_2)$ 5D, $(^3P_1)$ 3P, $(^3D_2)$ 5D
$^3P_1$	1^-	$(^1P_1)$ 3P, $(^1D_2)$ 5D, $(^3S_1)$ 3S, $(^3S_1)$ 3D, $(^3P_0)$ 1P, $(^3P_1)$ 3P, $(^3P_2)$ 5P, $(^3P_2)$ 5F, $(^3D_1)$ 3S, $(^3D_1)$ 3D, $(^3D_2)$ 5D, $(^3D_3)$ 7D
$^3P_2$, $^3F_2$	2^-	$(^1S_0)$ 1D, $(^1P_1)$ 3P, $(^1P_1)$ 3F, $(^1D_2)$ 5S, $(^1D_2)$ 5D, $(^3S_1)$ 3D, $(^3P_1)$ 3P, $(^3P_2)$ 5P, $(^3P_2)$ 5F, $(^3D_1)$ 3D, $(^3D_2)$ 5D, $(^3D_3)$ 7D
$^1D_2$	2^+	$(^1P_1)$ 3D, $(^1D_2)$ 5P, $(^1D_2)$ 5F, $(^3S_1)$ 3P, $(^3S_1)$ 3F, $(^3P_0)$ 1D, $(^3P_1)$ 3D, $(^3P_2)$ 5S, $(^3P_2)$ 5D, $(^3D_1)$ 3P, $(^3D_1)$ 3F, $(^3D_2)$ 5P, $(^3D_2)$ 5F, $(^3D_3)$ 7P, $(^3D_3)$ 7F

C.2.3 Final State Including the Production of a "ppK^-"

According to the theoretical predictions the kaonic cluster with the quantum numbers 0^- has the highest chance of existence according to its isospin configuration, see Section 1.6.4. In this case, the kaonic cluster and the kaon have both the quantum numbers J^P=0^-. The total parity of the combined system is P= (-1)·(-1)·$(-1)^L$. So P=+1 for odd angular momenta and P=-1 for even angular momenta. The total spin is S=0. These results are summarized by Table C.14. Out of these four final states only 0^+, 1^- and 2^+ can be populated as

Table C.14: J^P of a combined system of 0^- and 0^-

S_{tot} L	0
0	0^+
1	1^-
2	2^+
3	3^-

their quantum numbers coincide with the initial p+p system. The transitions are written as follows:

$$(0^+) \qquad {}^1S_0 \rightarrow \; 'ppK(2250)-K' \quad 1 \quad 'S', \tag{C.9}$$

$$(1^-) \qquad {}^3P_1 \rightarrow \; 'ppK(2250)-K' \quad 1 \quad 'P', \tag{C.10}$$

$$(2^+) \qquad {}^1D_2 \rightarrow \; 'ppK(2250)-K' \quad 1 \quad 'D'. \tag{C.11}$$

Besides this option, which is considered in the PWA of this thesis, there is the possibility that a kaonic nuclear cluster with the quantum numbers J^P=1^+ may exist, see Section 1.6.4. It would be called "dK^-". Technically it is possible to include such a state however with other quantum numbers for the waves. The latter are summarized in Table C.14. In the case of "dK^-" production, there are more possible transitions from initial to final state than in the case for the "ppK^-". All quantum numbers except: 1^+, 3^-, 3^+, and 4^+ can be mapped to an initial state. These transition waves would look like follows:

Table C.15: J^P of a combined system of 1^+ and 0^-

L \ S_{tot}	1
0	1^-
1	0^+, 1^+, 2^+
2	1^-, 2^-, 3^-
3	2^+, 3^+, 4^+

$$(0^+) \qquad {}^1S_0 \rightarrow \; 'dK^- - K' \quad 3 \quad 'P', \tag{C.12}$$

$$(1^-) \qquad {}^3P_1 \rightarrow \; 'dK^- - K' \quad 3 \quad 'S', \tag{C.13}$$

$$\qquad {}^3P_1 \rightarrow \; 'dK^- - K' \quad 3 \quad 'D', \tag{C.14}$$

$$(2^-) \qquad {}^3P_2 \rightarrow \; 'dK^- - K' \quad 3 \quad 'D', \tag{C.15}$$

$$(2^-) \qquad {}^3F_2 \rightarrow \; 'dK^- - K' \quad 3 \quad 'D', \tag{C.16}$$

$$(2^+) \qquad {}^1D_2 \rightarrow \; 'dK^- - K' \quad 3 \quad 'P', \tag{C.17}$$

$$\qquad {}^1D_2 \rightarrow \; 'dK^- - K' \quad 3 \quad 'F'. \tag{C.18}$$

D Results of the PWA fit Excluding Certain Mass Ranges in $IM_{p\Lambda}$

D.1 Test PWA Solution compared the Selected Statistic

In this appendix, a more extended look on pictures from a quality check is done which was discussed in Section 4.3.2 of Chapter 4. Figures D.1 and D.2 display the experimental distributions that result from events where the mass ranges 2200-2300 MeV/c^2 and 2300-2400 MeV/c^2 in $M_{p\Lambda}$ were rejected from the PWA fit, respectively. Together with the data the PWA solutions that were fitted to these events are shown. The two-particle invariant mass distributions in which a certain mass range of $M_{p\Lambda}$ was rejected in the data are shown in Figure 4.14 of Chapter 4.

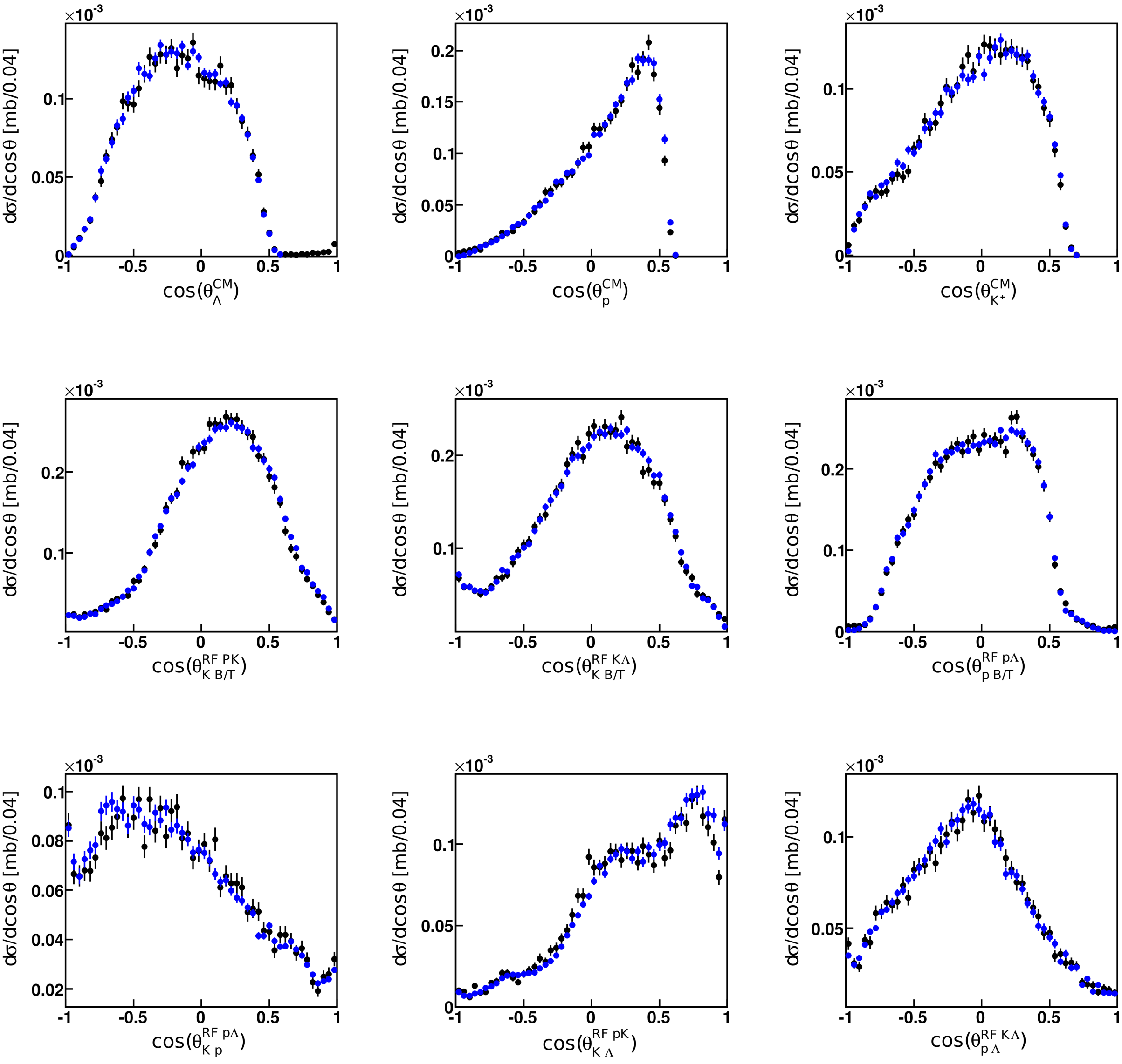

Figure D.1: Angular correlations of the three particles for the **selected HADES data set** (black points) shown with the **best PWA solution** (blue dots), obtained by a fit to the HADES data, excluding a $M_{p\Lambda}$ mass range of 2200-2300 MeV/c^2.

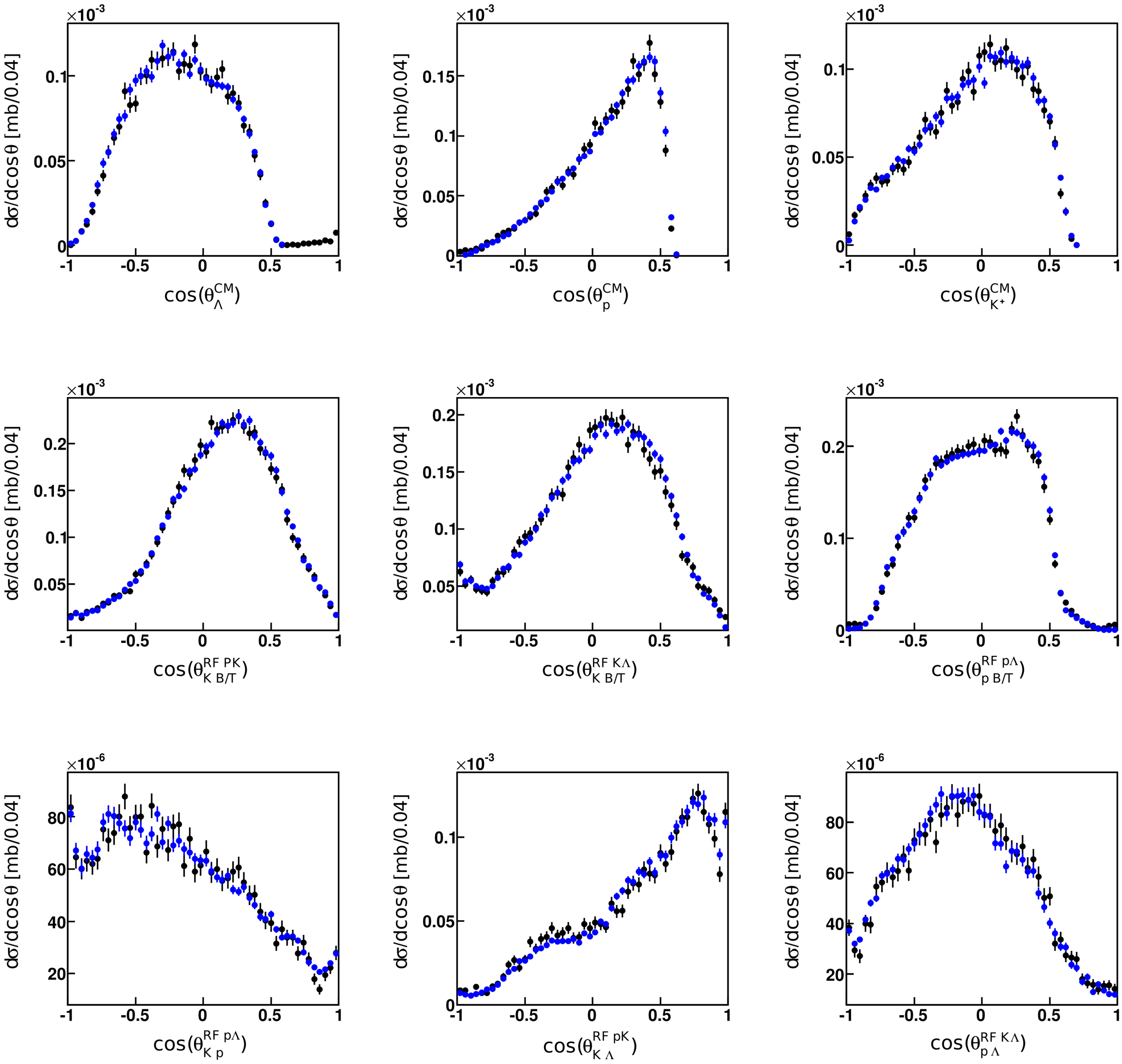

Figure D.2: Angular correlations of the the three particles for the **selected HADES data set** (black points) shown with the **best PWA solution** (blue dots), obtained by a fit to the HADES data, excluding a $M_{p\Lambda}$ mass range of 2300-2400 MeV/c^2.

D.2 Test PWA Solution compared the full Statistic

Figures D.3 and D.4 display the two particle invariant masses for the full statistic of the measured data. They are compared to the PWA test solutions in which a part of the statistic was rejected from the fit. The angular distributions for the data are shown in Figures D.5 and D.6. Also in this figures the PWA from the selected statistic is extrapolated to the full statistic and compared to the data.

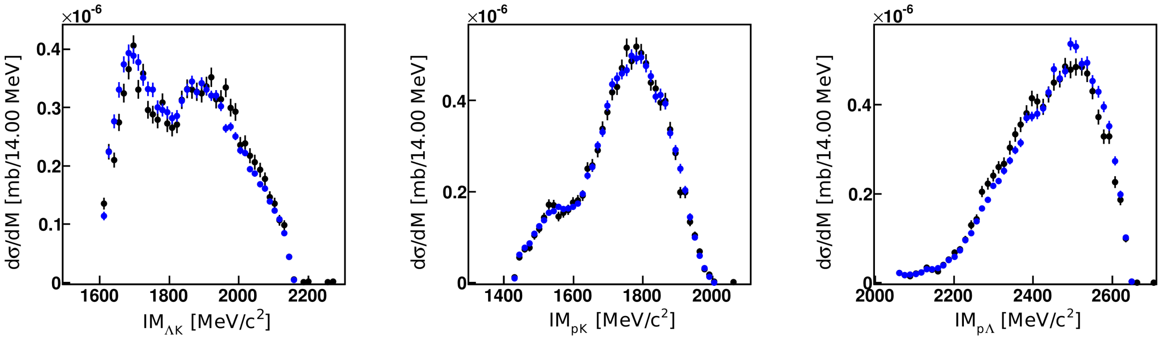

Figure D.3: Two particle invariant masses for the three particles for the **complete HADES data set** (black points) shown with the **best PWA solution** (blue dots), obtained by a fit to the HADES data, excluding a $M_{p\Lambda}$ mass range of 2200-2300 MeV/c^2.

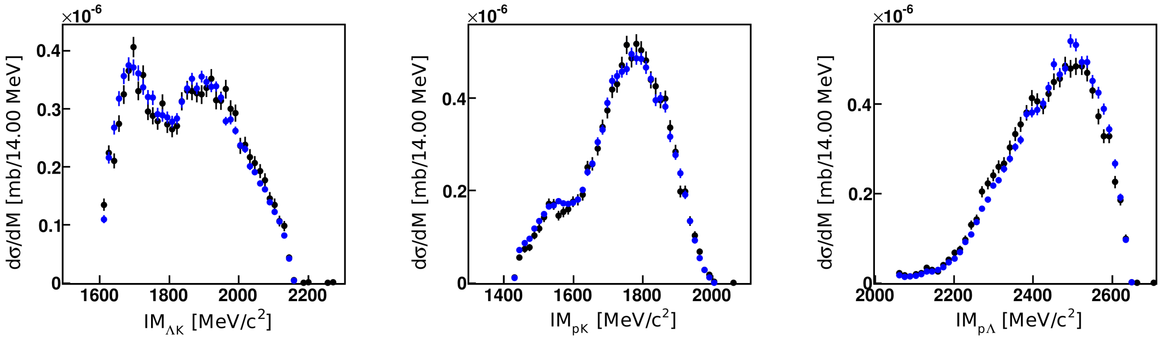

Figure D.4: Two particle invariant masses for the three particles for the **complete HADES data set** (black points) shown with the **best PWA solution** (blue dots), obtained by a fit to the HADES data, excluding a $M_{p\Lambda}$ mass range of 2300-2400 MeV/c^2.

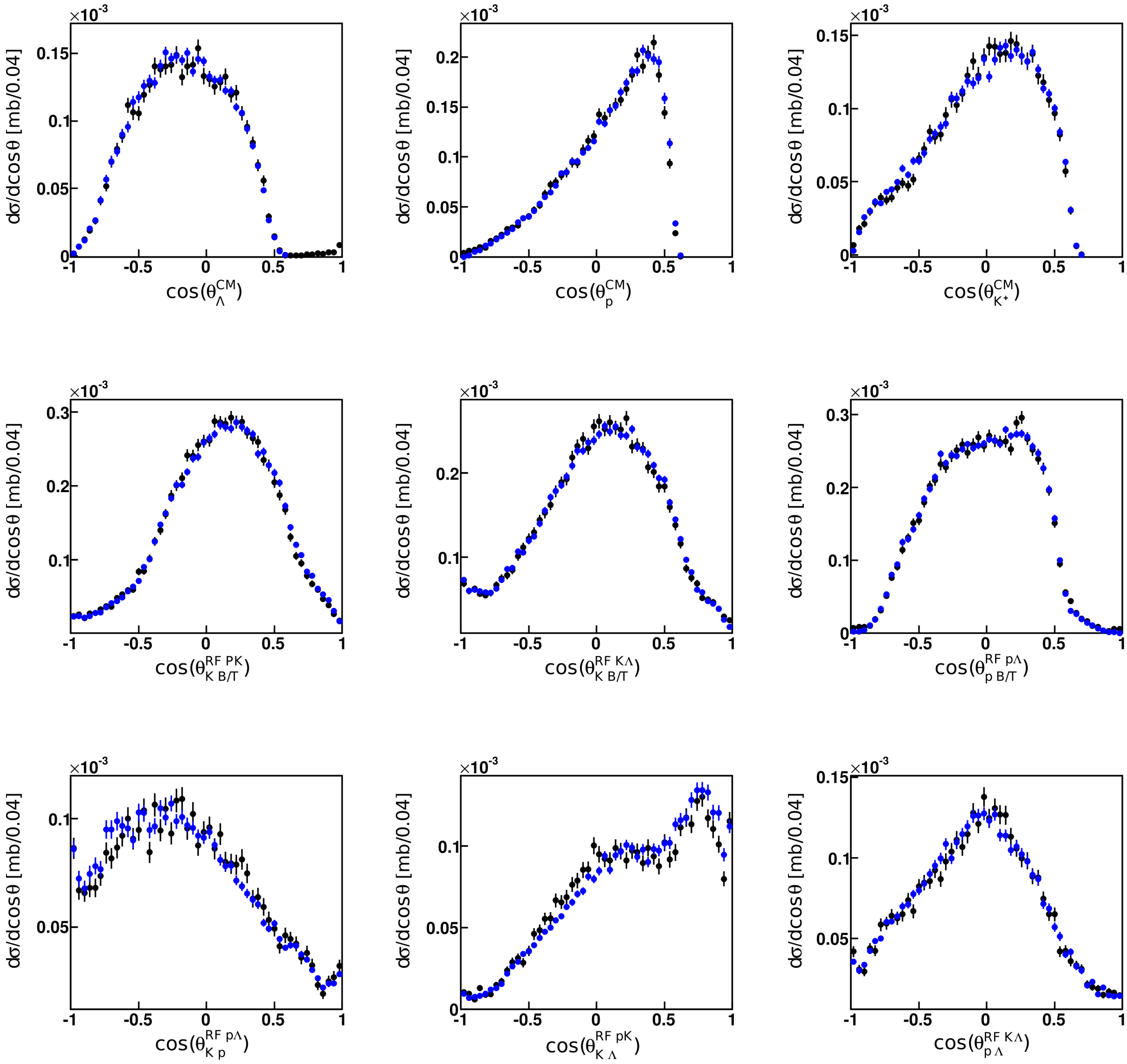

Figure D.5: Angular correlations of the three particles for the **complete HADES data set** (black points) shown with the **best PWA solution** (blue dots), obtained by a fit to the HADES data, excluding a $M_{p\Lambda}$ mass range of 2200-2300 MeV/c^2.

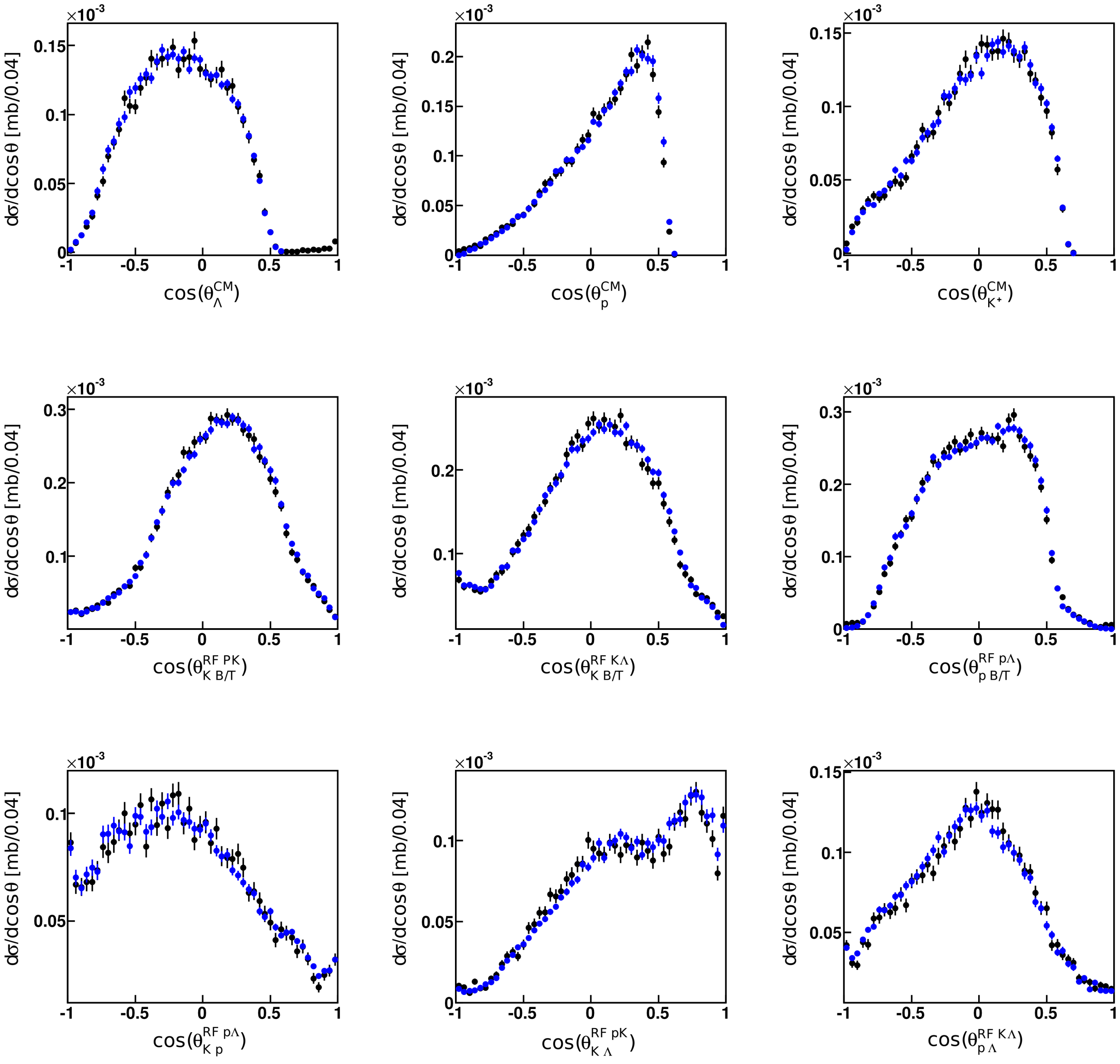

Figure D.6: Angular correlations of the the three particles for the **complete HADES data set** (black points) shown with the **best PWA solution** (blue dots), obtained by a fit to the HADES data, excluding a $M_{p\Lambda}$ mass range of 2300-2400 MeV/c^2.

The same figures for the WALL data set are shown in the following. Figure D.7 displays the invariant mass of two particles for the complete WALL statistic overlayed by PWA solutions that were obtained by a fit to a selected HADES statistic. The Figures D.8 and D.9 show the angular distributions of the complete WALL statistic together with the PWA solutions that were obtained from a fit to the mass constrained HADES data sets.

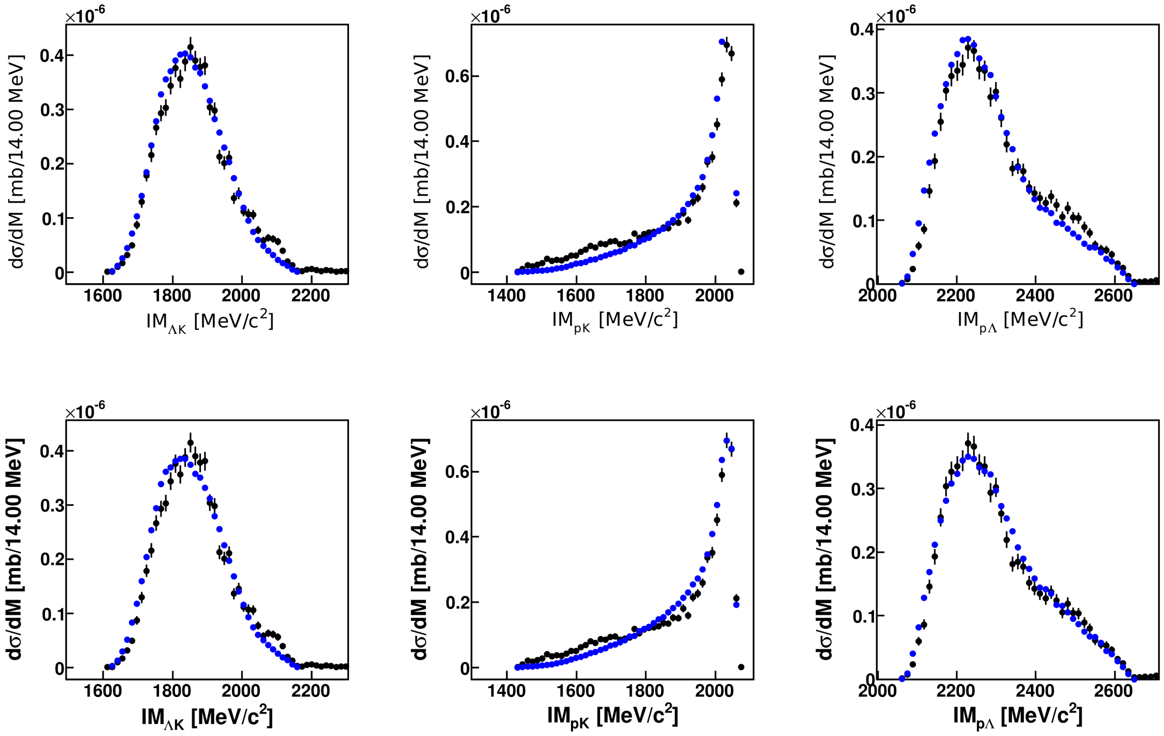

Figure D.7: Two particle invariant masses for the three particles for the **complete WALL data set** (black points) shown with the **best PWA solution** (blue dots), obtained by a fit to the HADES data, excluding a $M_{p\Lambda}$ mass range of 2200-2300 MeV/c^2 (upper figures) and 2300-2400 MeV/c^2 (lower figures).

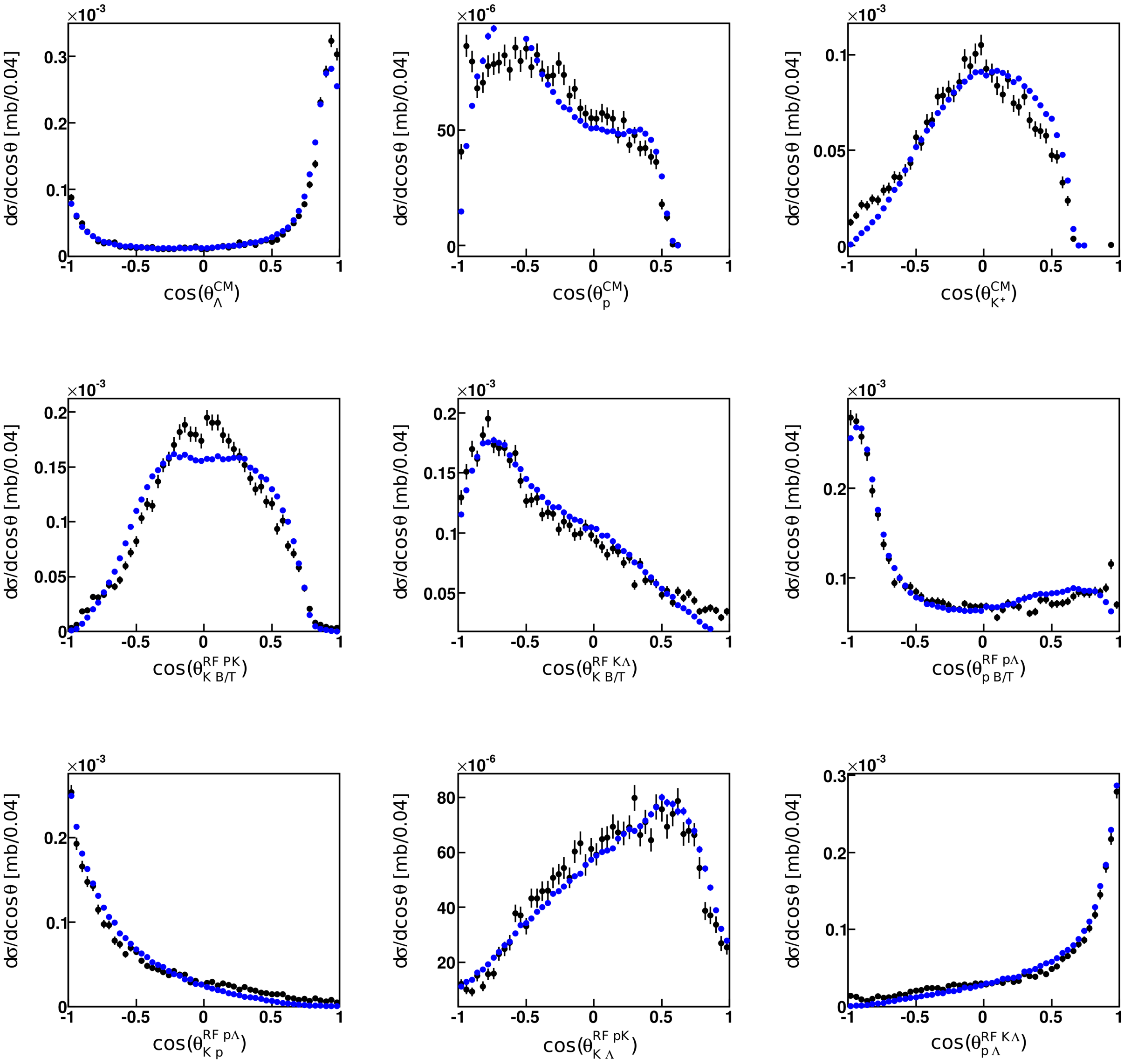

Figure D.8: Angular correlations of the the three particles for the **complete WALL data set** (black points) shown with the **best PWA solution** (blue dots), obtained by a fit to the HADES data, excluding a $M_{p\Lambda}$ mass range of 2200-2300 MeV/c^2.

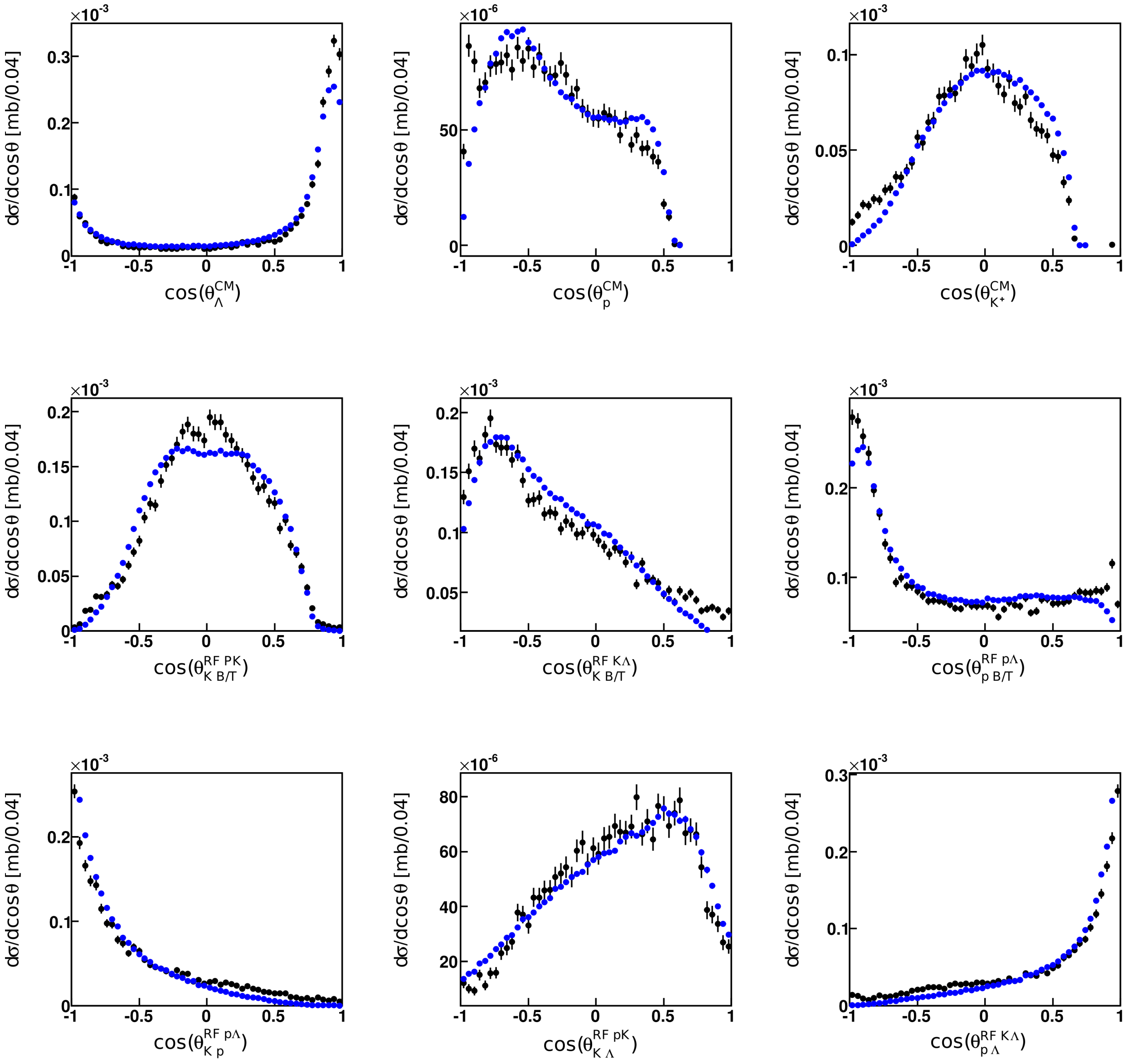

Figure D.9: Angular correlations of the the three particles for the **complete WALL data set** (black points) shown with the **best PWA solution** (blue dots), obtained by a fit to the HADES data, excluding a $M_{p\Lambda}$ mass range of 2300-2400 MeV/c^2.

E | Comparision of the Four Best PWA Results

This Appendix compares the four best PWA solutions of Chap. 4 to each other. Figure E.1 shows the mass and Figures E.3 and E.2 the angular distributions.

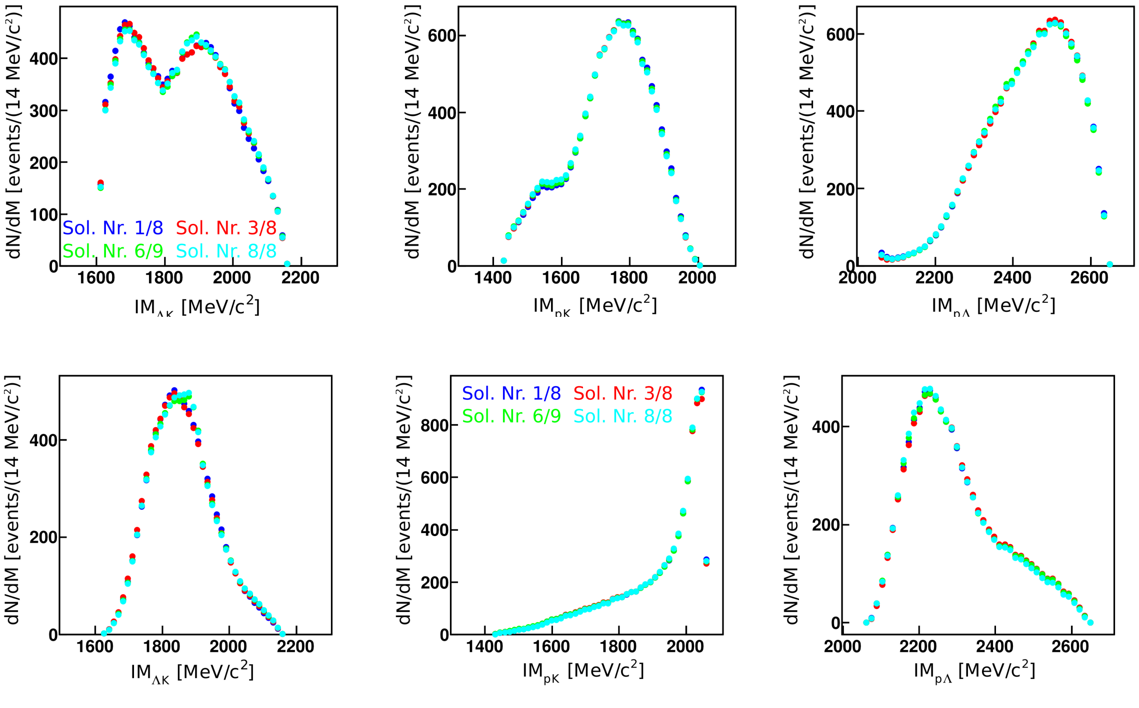

Figure E.1: Two particle masses for the four best PWA solutions inside the HADES (upper) and WALL acceptance (lower panels), normalized to the same integral.

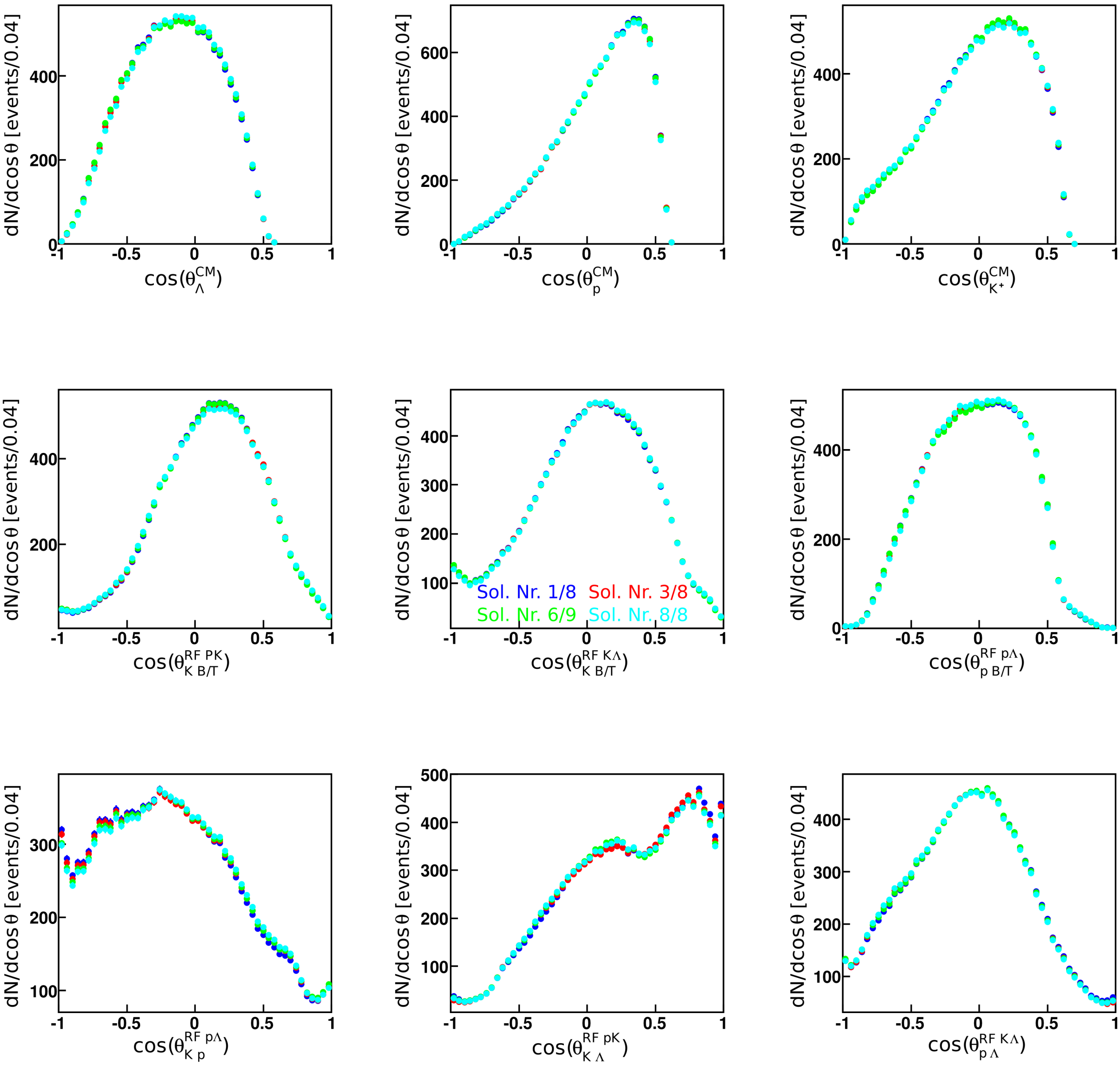

Figure E.2: Angular correlations of the three particles for the four best PWA solutions (different colors) inside of the HADES acceptance. The results are normalized to the same integral.

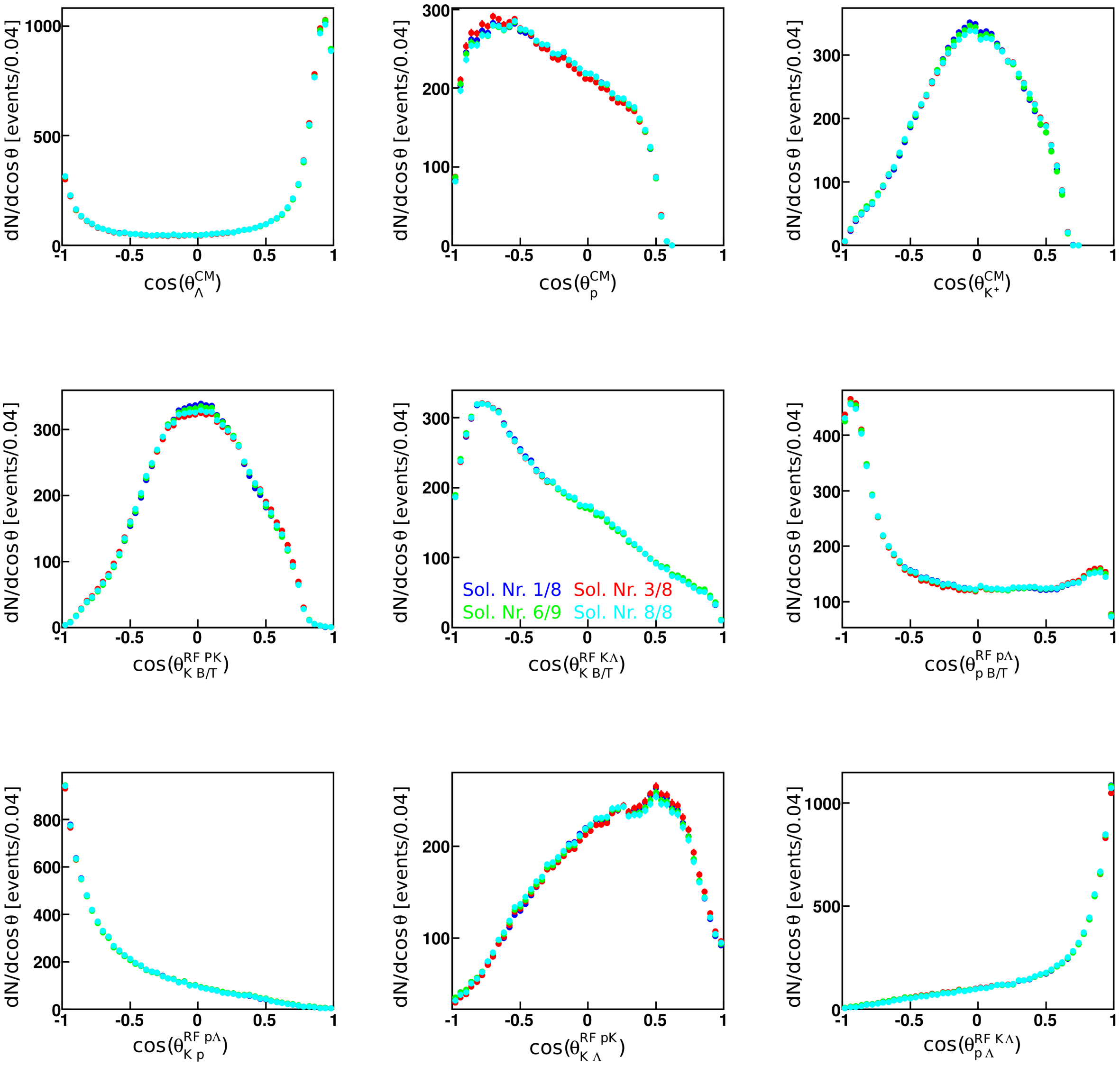

Figure E.3: Angular correlations of the three particles for the four best PWA solutions (different colors) inside of the WALL acceptance. The results are normalized to the same integral.

F | p-Values for the Four Best Solutions

This appendix shows detailed figures to the local p_0-value evaluation. While Figures F.1 and F.2 show the four best solutions compared to the measured $p\Lambda$ invariant mass distribution for the HADES and WALL data-sets, Figures F.3 - F.6 present the according local p_0-values and equivalent significance (nσ), dependent on the $p\Lambda$ invariant mass for each tested solution.

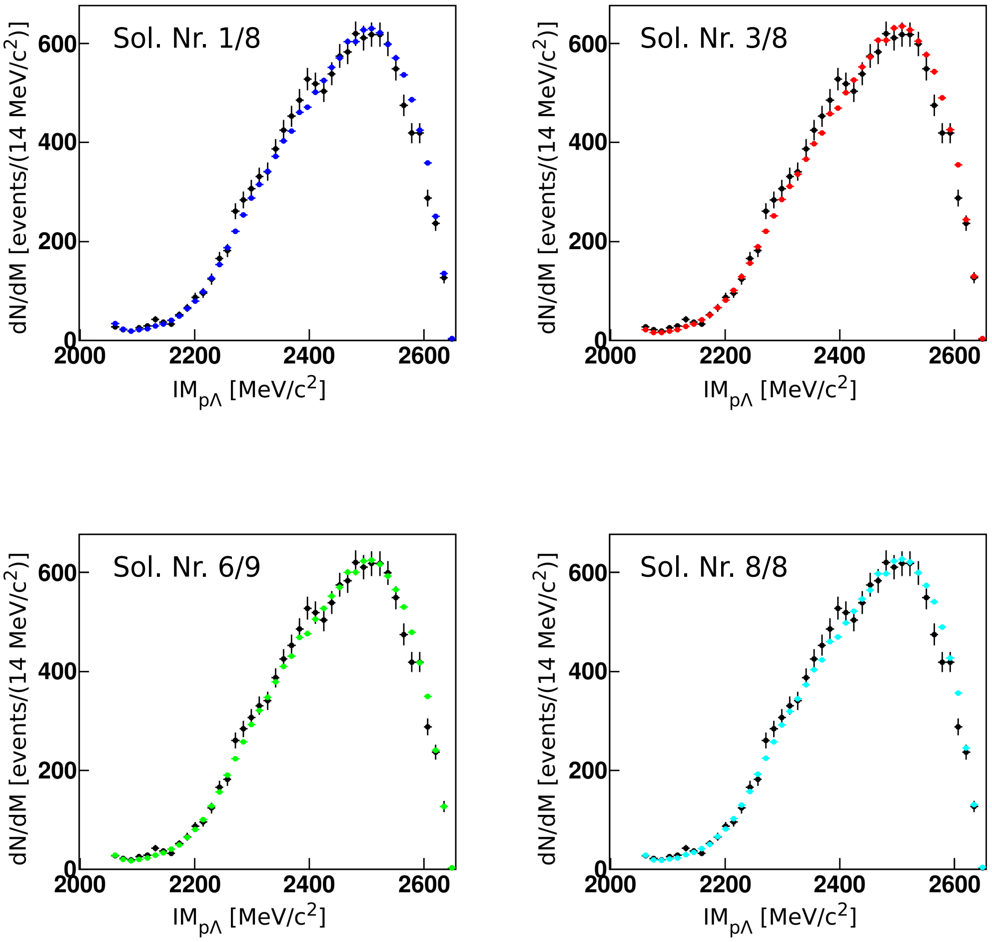

Figure F.1: The Figure compares the four best PWA solutions of a fit to both data sets HADES and WALL. Shown is the invariant mass of $p\Lambda$ of the HADES data-set compared to the solution.

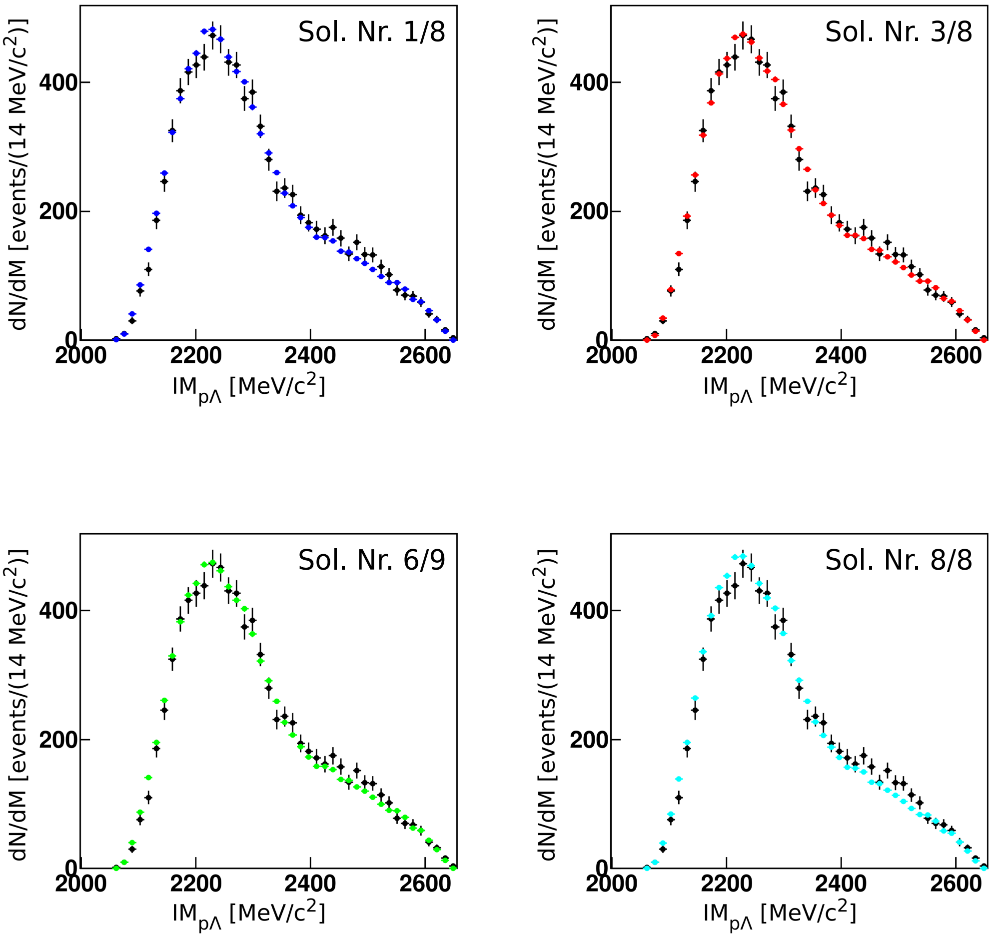

Figure F.2: The Figure compares the four best PWA solutions of a fit to both data sets HADES and WALL. Shown is the invariant mass of $p\Lambda$ of the WALL data-set compared to the solution.

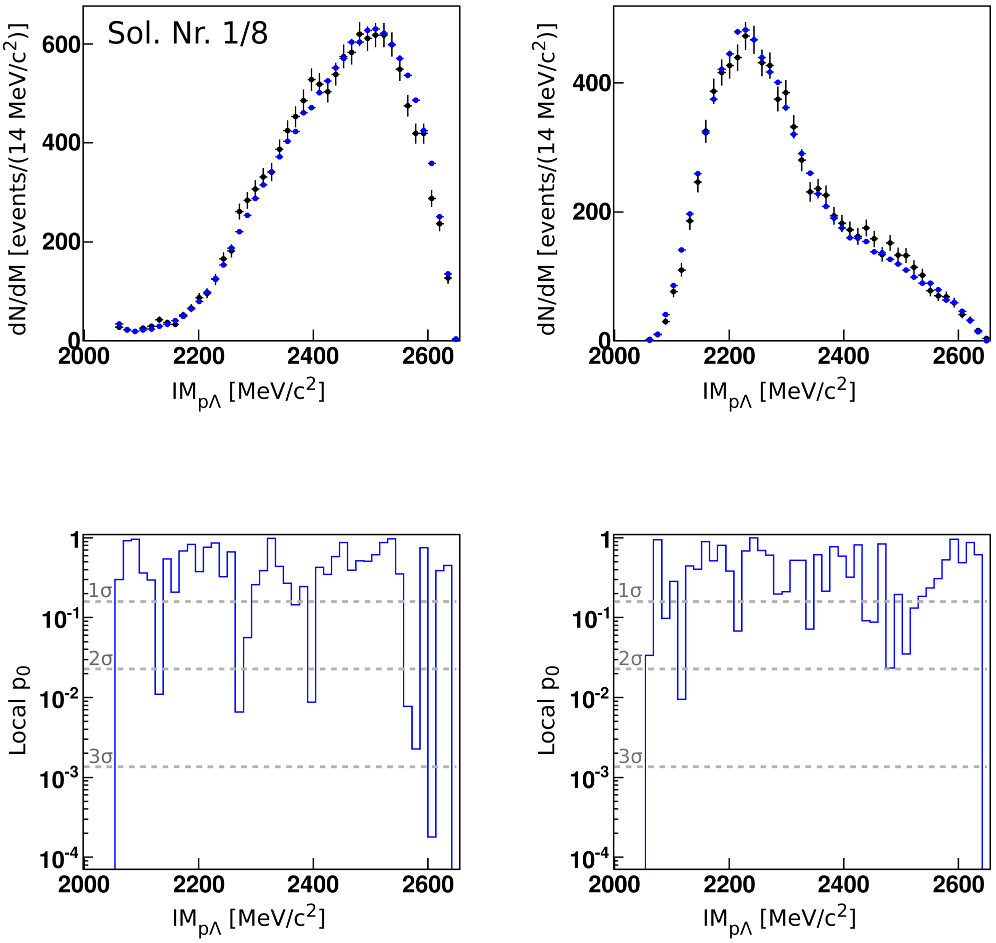

Figure F.3: The upper panels present the comparison of Sol. No. 1/8 to the analyzed events for the HADES (left) and WALL (right) data-sets. The lower panels show the calculated local p_0-value for different $p\Lambda$ invariant masses. The gray dashed lines show the equivalent significances in nσ.

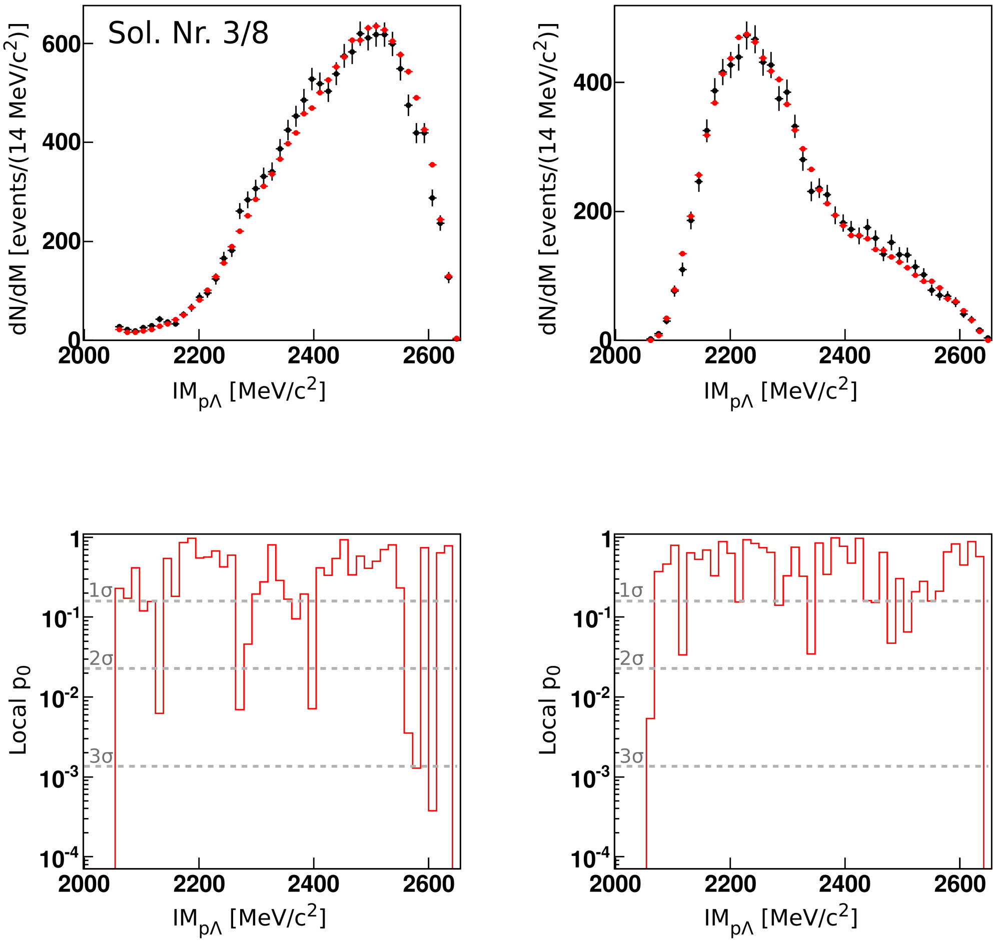

Figure F.4: The upper panels present the comparison of Sol. No. 3/8 to the analyzed events for the HADES (left) and WALL (right) data-sets. The lower panels show the calculated local p_0-value for different $p\Lambda$ invariant masses. The gray dashed lines show the equivalent significances in nσ.

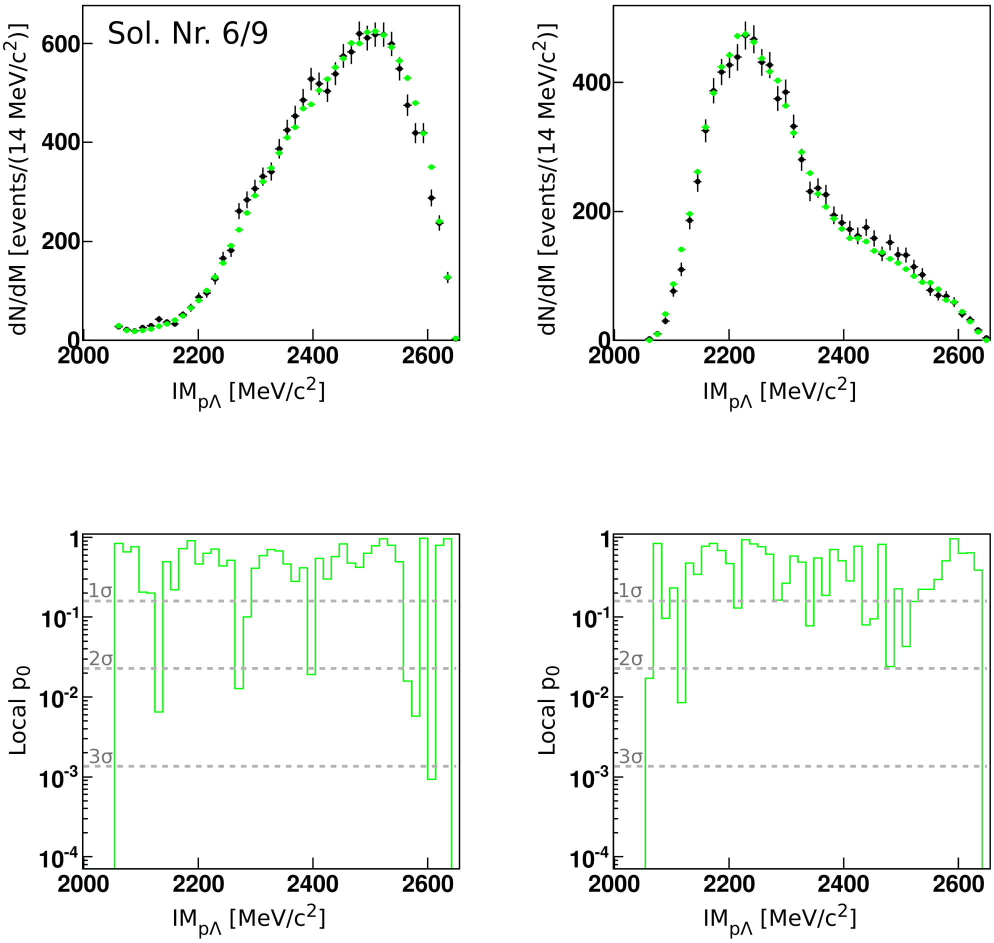

Figure F.5: The upper panels present the comparison of Sol. No. 6/9 to the analyzed events for the HADES (left) and WALL (right) data-sets. The lower panels show the calculated local p_0-value for different $p\Lambda$ invariant masses. The gray dashed lines show the equivalent significances in nσ.

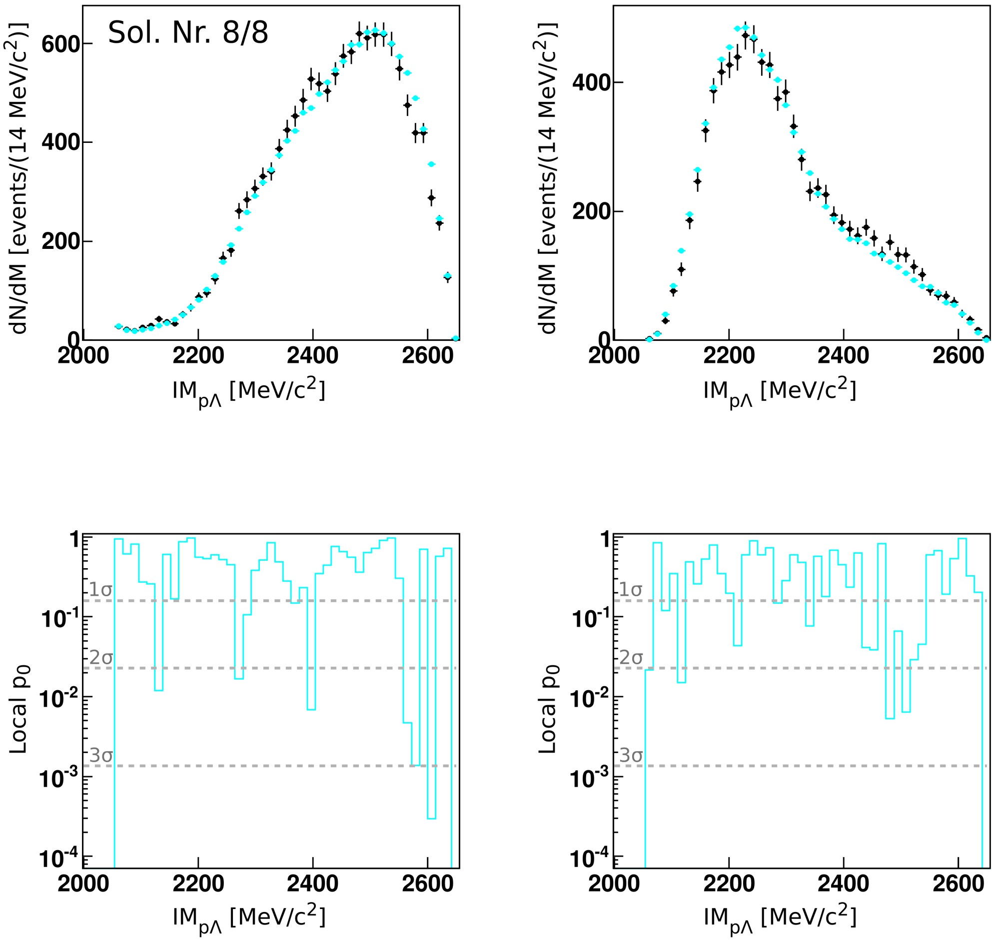

Figure F.6: The upper panels present the comparison of Sol. No. 8/8 to the analyzed events for the HADES (left) and WALL (right) data-sets. The lower panels show the calculated local p_0-value for different $p\Lambda$ invariant masses. The gray dashed lines show the equivalent significances in nσ.

G | Appendix for the 4π Distributions

G.1 4π Distributions of All Non-Resonant Waves

Figures G.1-G.3 show the invariant mass and angular distribution for single transition waves of the PWA solution for non-resonant $pK^+\Lambda$ production.

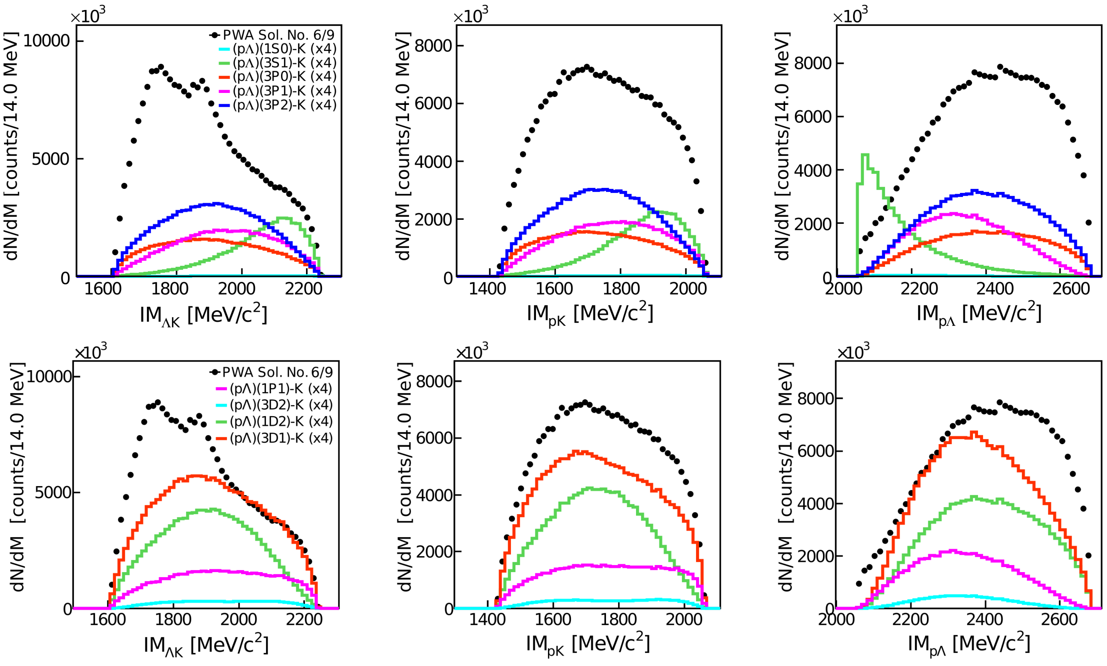

Figure G.1: Two particle invariant masses of the single non-resonant waves of $pK^+\Lambda$ production shown for Sol. No. 6/9.

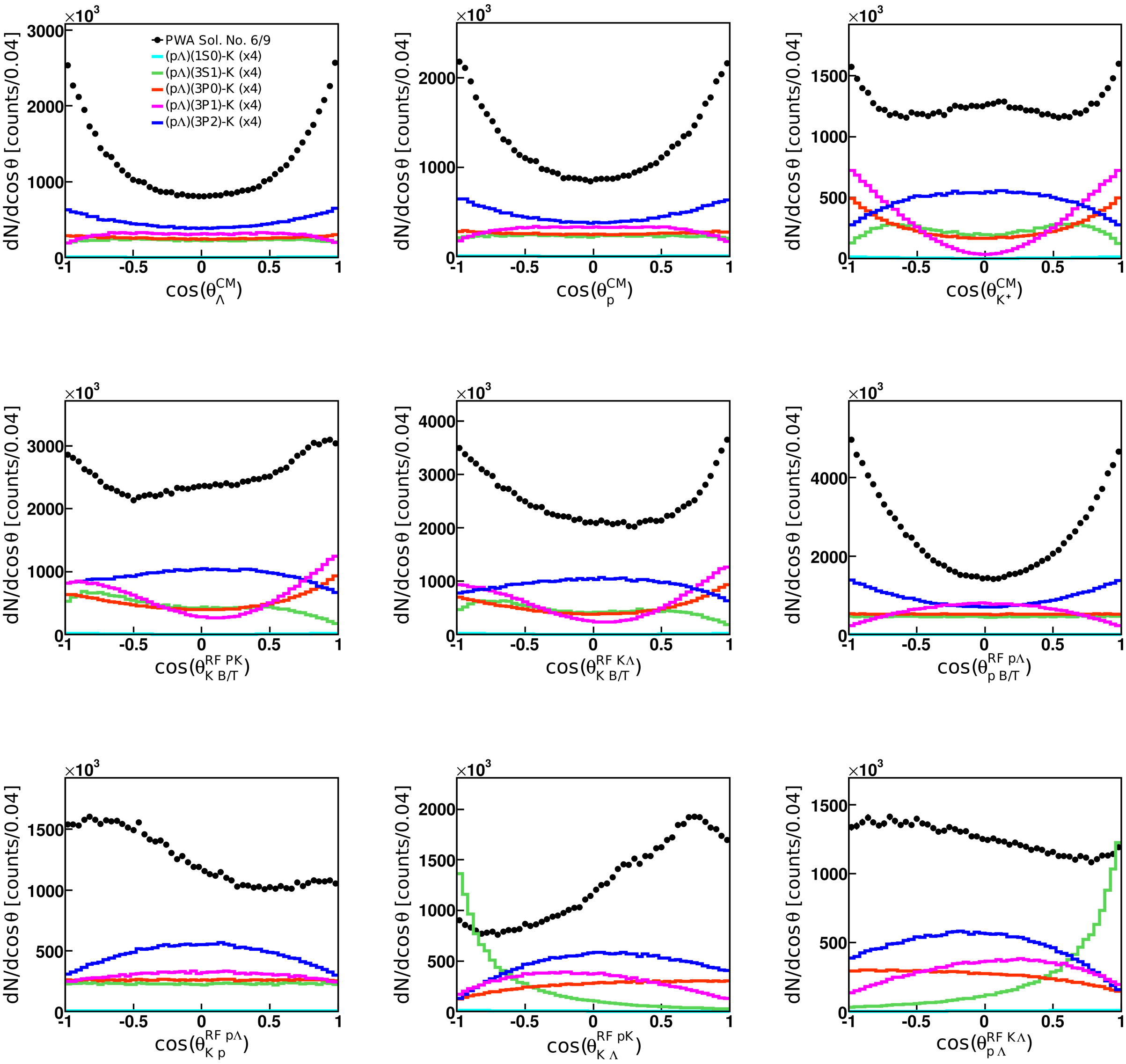

Figure G.2: Angular correlations of the three particles for the single non-resonant waves of $pK^+\Lambda$ production shown for Sol. No. 6/9.

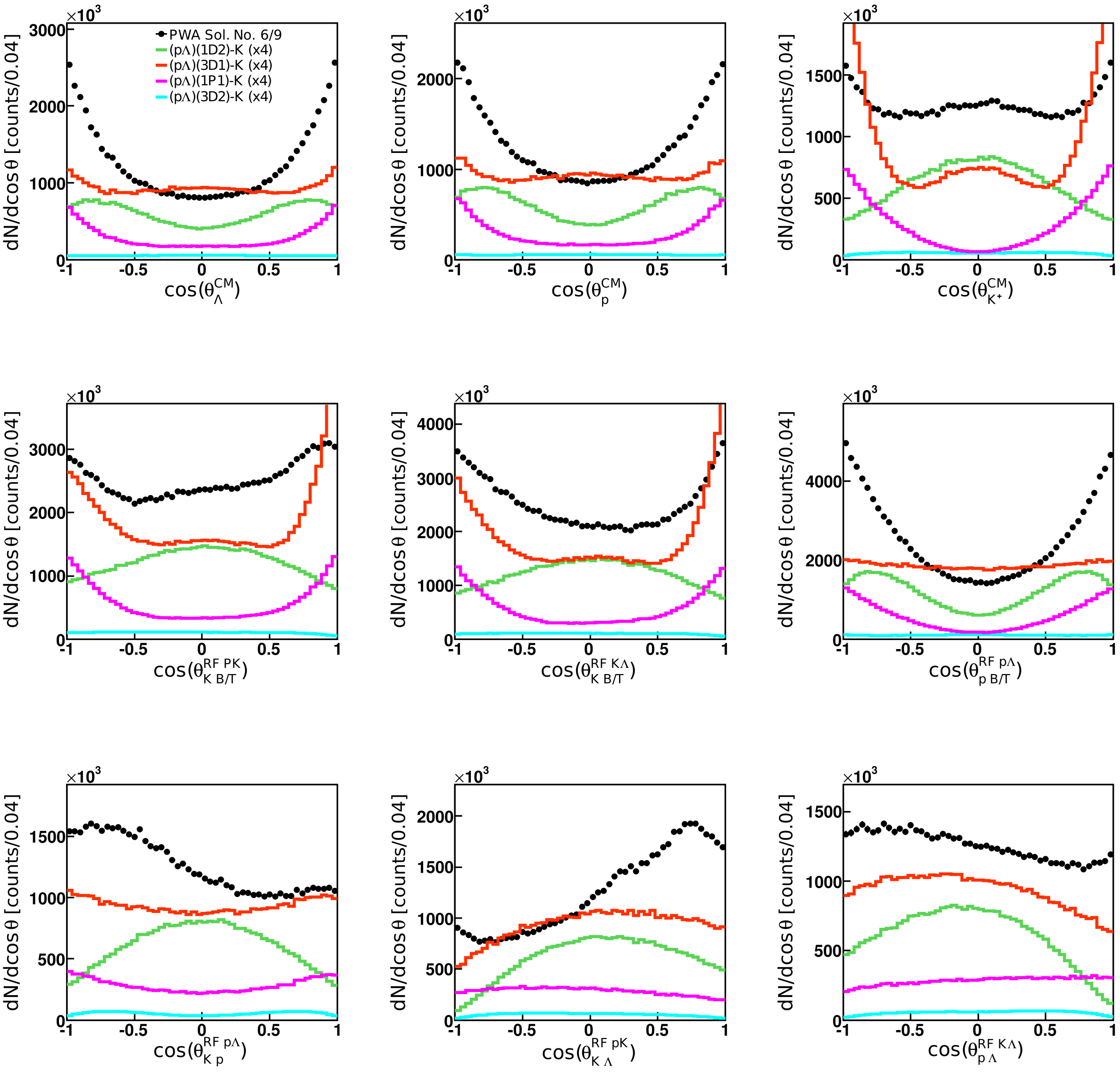

Figure G.3: Angular correlations of the three particles for the single non-resonant waves of $pK^+\Lambda$ production shown for Sol. No. 6/9.

G.2 Proton Angular Distributions in the CMS

Figure G.4 displays the angular distribution of the proton in the CMS of all waves with resonant production of $pK^+\Lambda$ of Sol. No. 6/9. Figures G.5 and G.6 show the fit of the Legendre polynomials according to Eq. (6.1) to the single PWA waves.

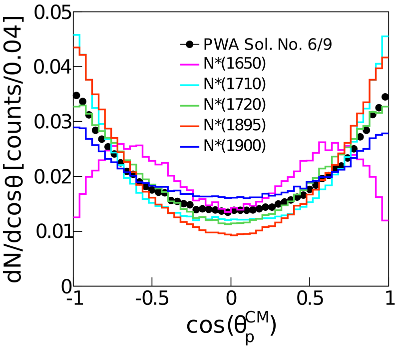

Figure G.4: The angular distributions of the proton in the CMS for the different N* resonances scaled to the same integral.

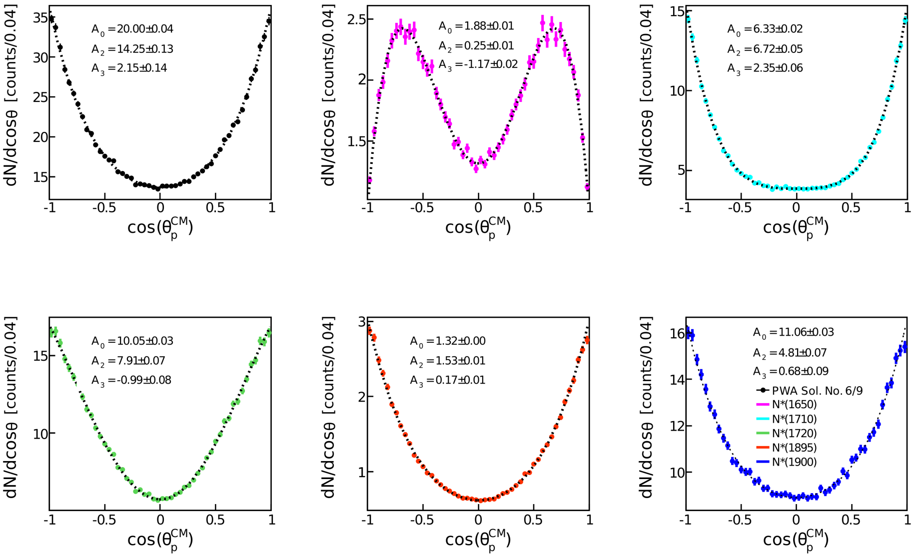

Figure G.5: The angular distributions of the proton in the CMS for the different N* resonances, fitted with Equation (6.1)

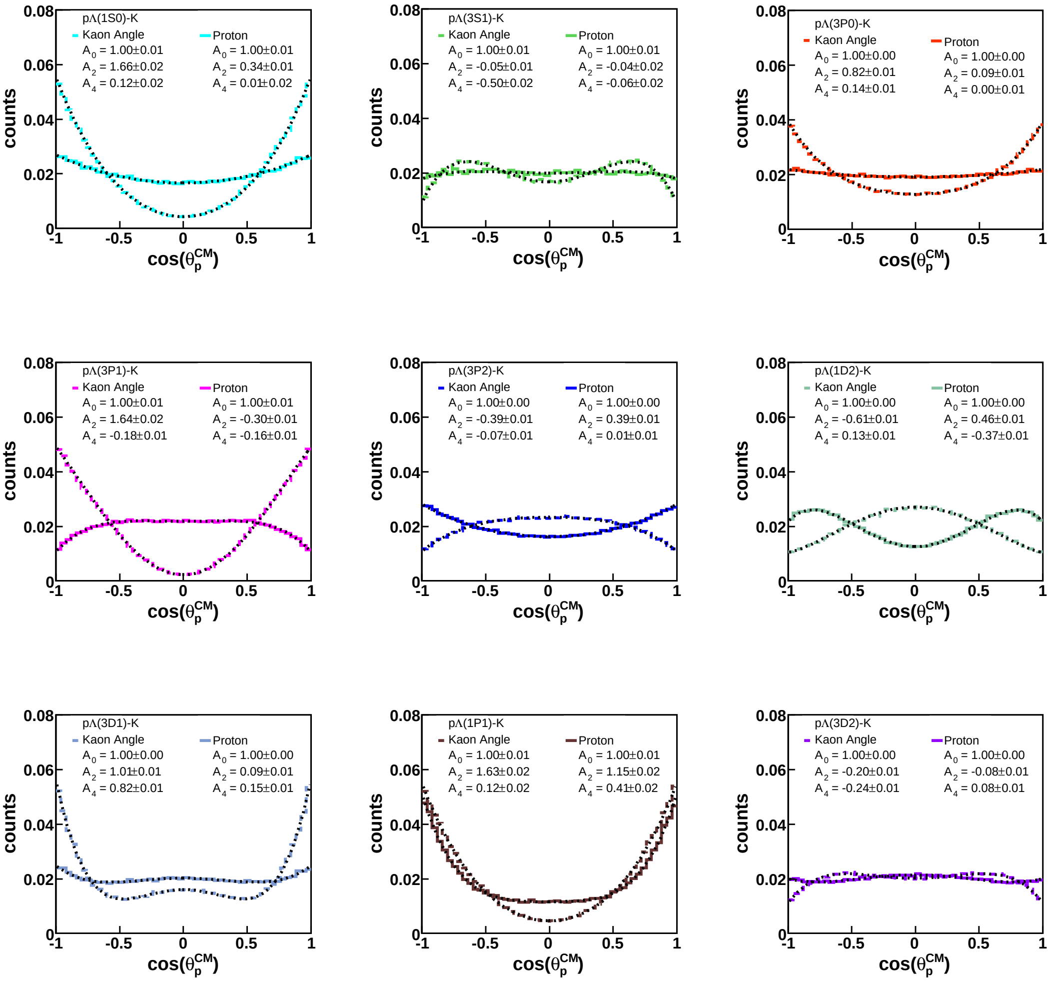

Figure G.6: The angular distributions of the proton and kaon in the CMS for the different non-resonant waves, fitted with Equation (6.1)

G.3 Systematic of the Acceptance Correction

Figures G.7-G.10 show the experimental data, corrected to 4π with help of the PWA solution. The correction of each observable is done for each of the four PWA solutions separately. The resulting spectra in 4π are compared to the PWA solution that was used for the correction. The PWA solution is scaled to the data in the indicated range in the histogram. To calculate a cross section the experimental data were summed inside of this range and the remaining yield is calculated from the integration of the model value.

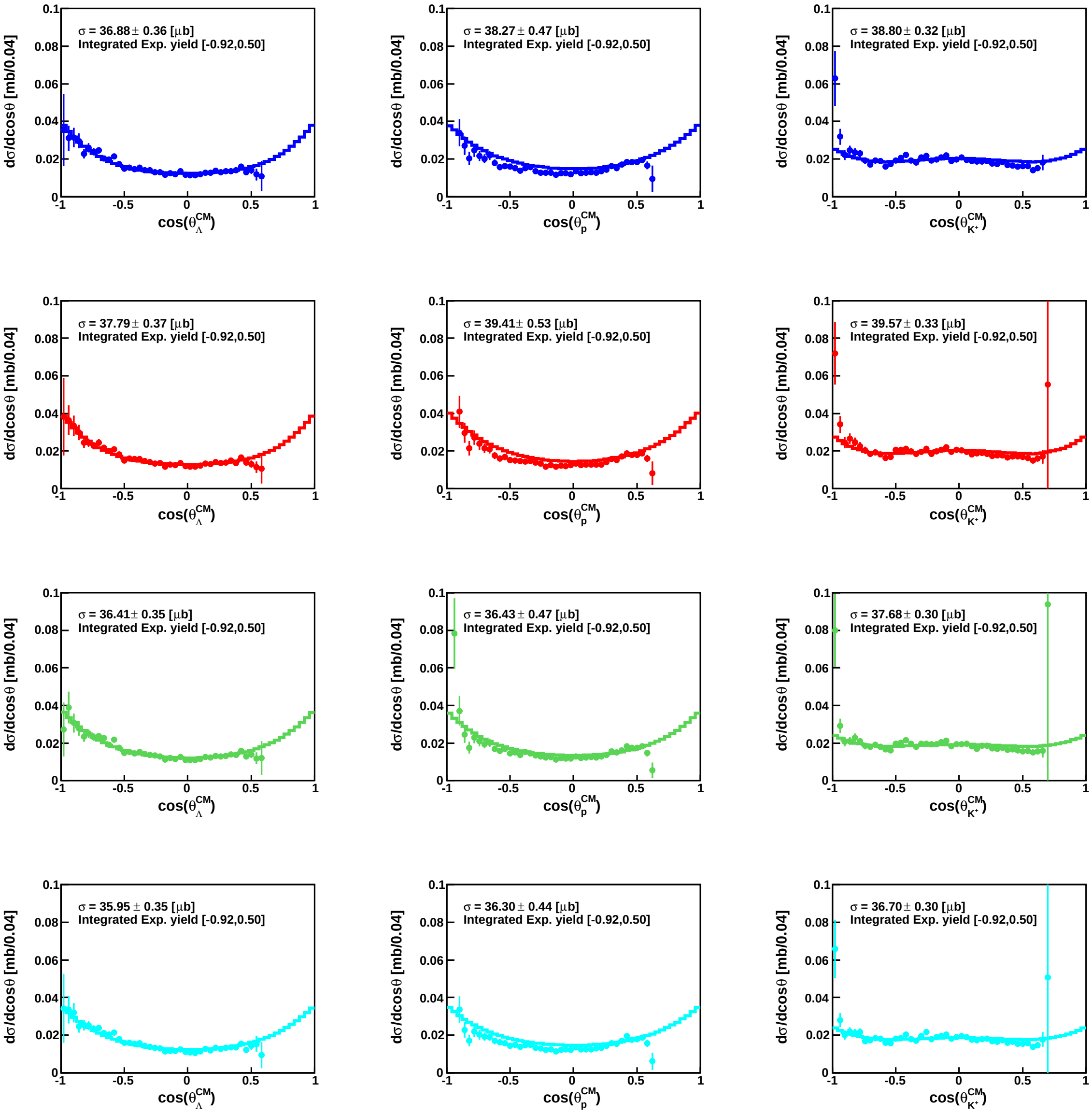

Figure G.7: CMS angles corrected with the four different models (6/9-blue, 1/8-red, 3/8-green, 8/8-cyan). Data were integrated in the indicated range. Outside the range the model value was added to obtain the total cross section.

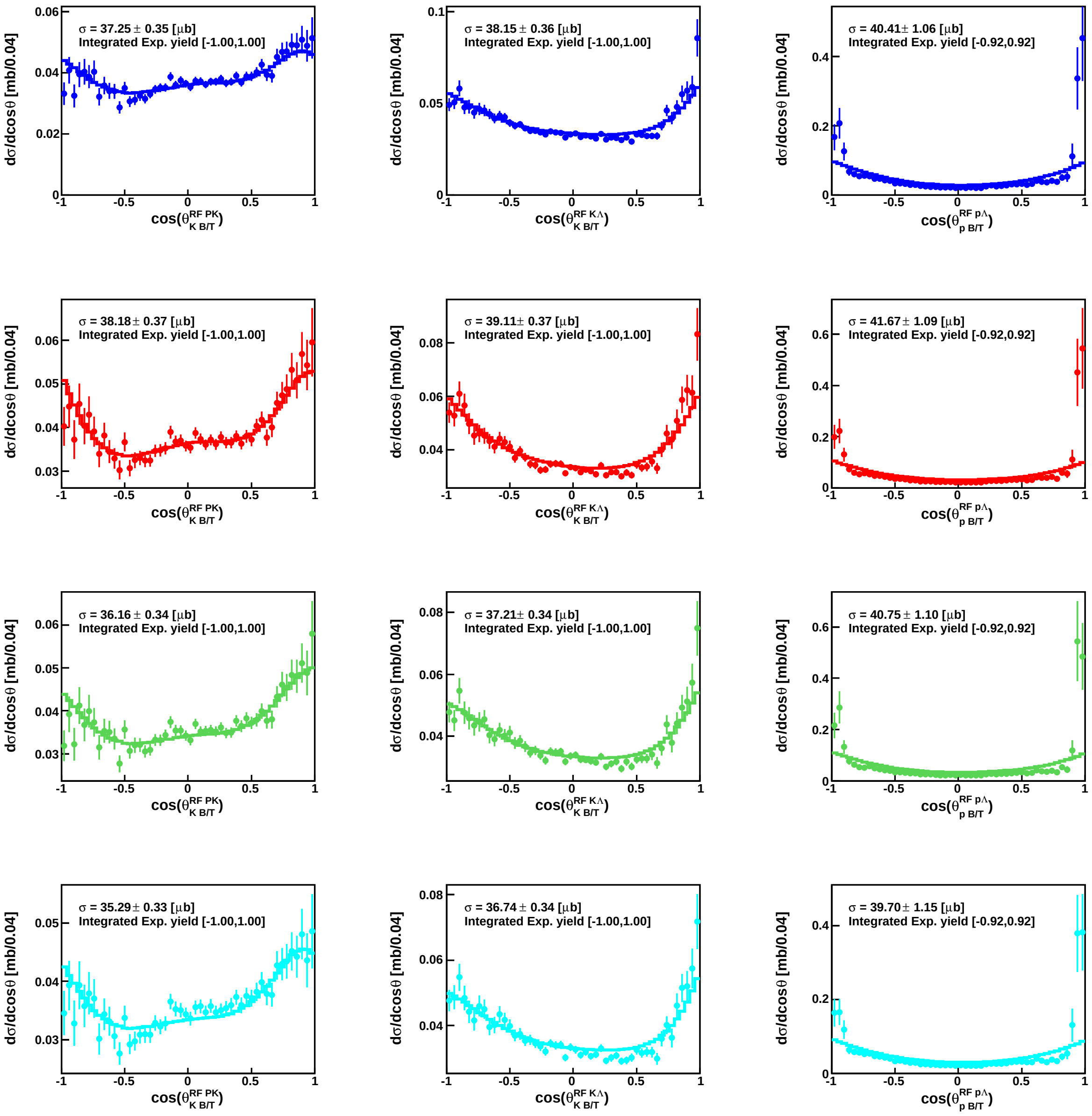

Figure G.8: Gottfried-Jackson angles corrected with the four different models (6/9-blue, 1/8-red, 3/8-green, 8/8-cyan). Data were integrated in the indicated range. Outside the range the model value was added to obtain the total cross section.

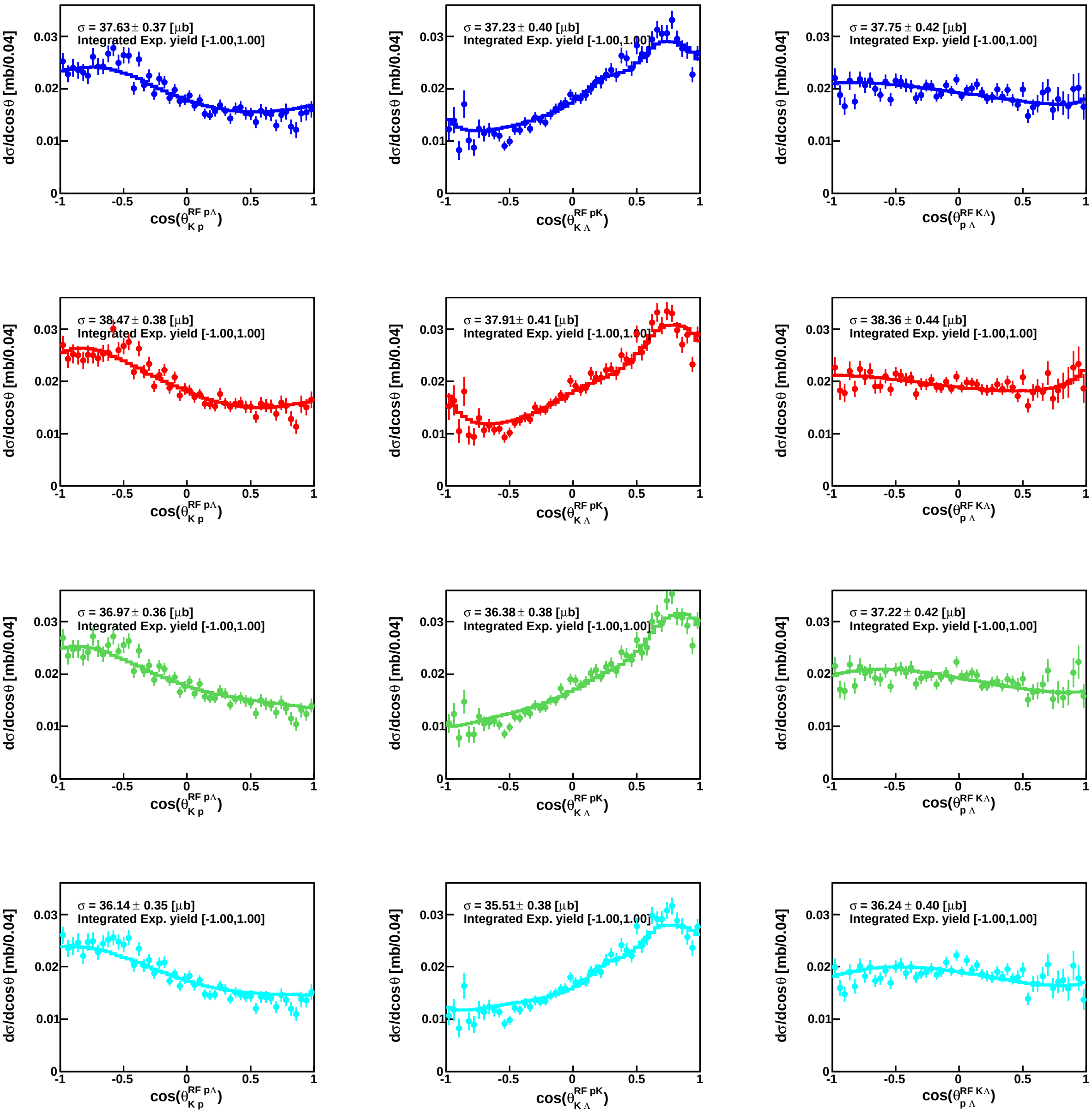

Figure G.9: Helicity angles corrected with the four different models (6/9-blue, 1/8-red, 3/8-green, 8/8-cyan). Data were integrated in the indicated range. Outside the range the model value was added to obtain the total cross section.

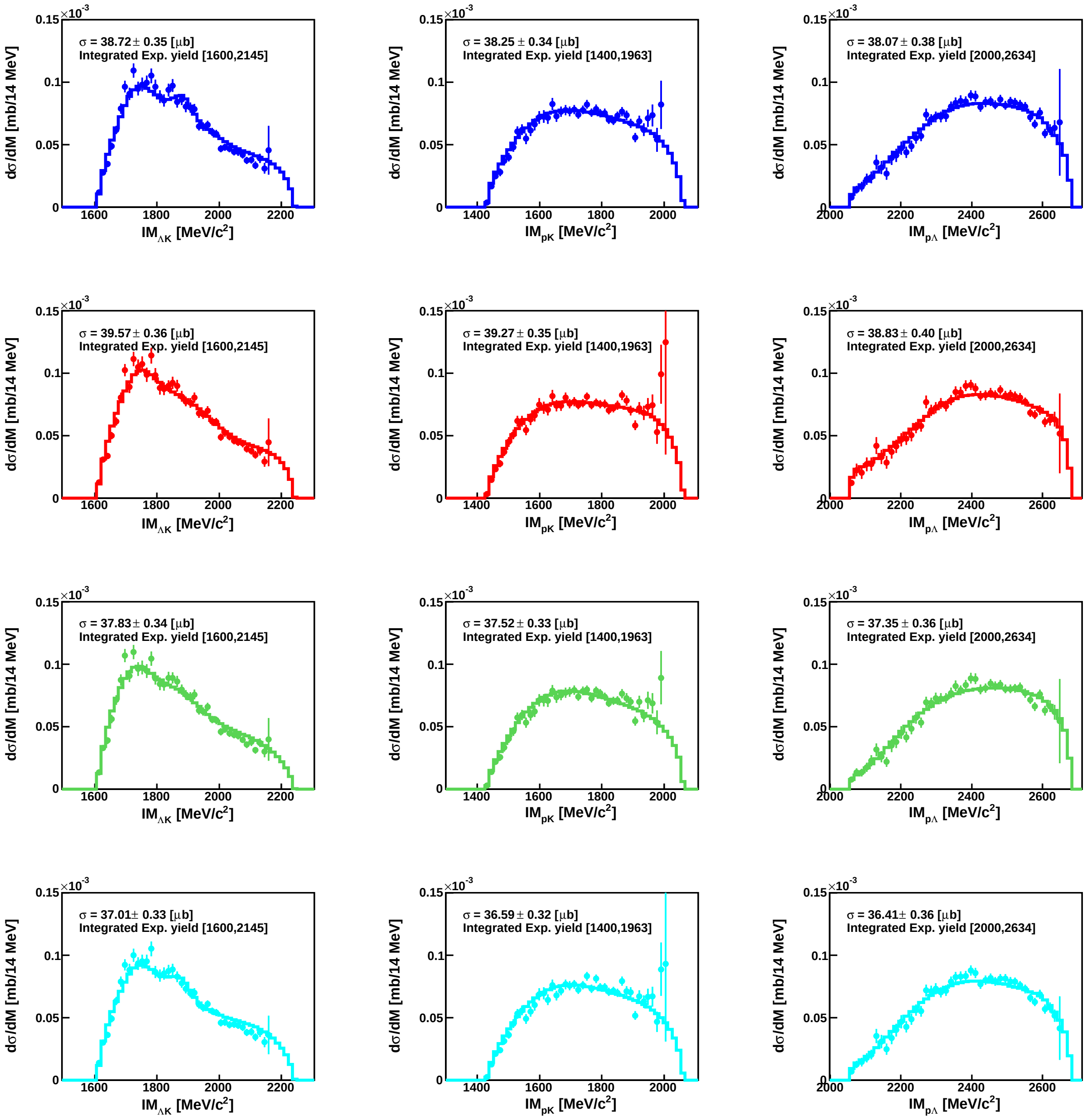

Figure G.10: Two-particle invariant masses corrected with the four different models (6/9-blue, 1/8-red, 3/8-green, 8/8-cyan). Data were integrated in the indicated range. Outside the range the model value was added to obtain the total cross section.

G.4 Angular Distribution of the Proton at Different Energies

Figure G.11 shows the measured angular distribution of the proton in the CMS frame from different experiments. The data were taken from Refs. [162, 197, 161], scanned and then fitted with a Legendre polynomial of the sixth order according to Equation (6.1). The extracted coefficients are normalized to A_0 and quoted in the figures.

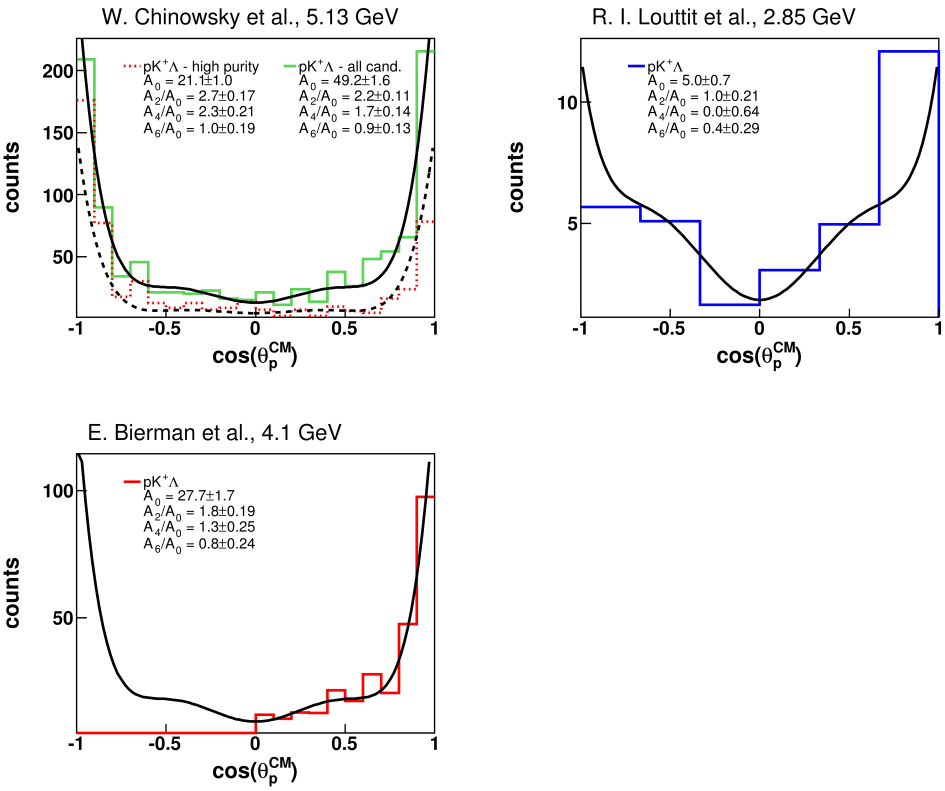

Figure G.11: Original figures can be found in W. Chinowsky et al. [162], R. Louttit et al. [197] and E. Bierman et al. [161]

G.5 $pK^+\Lambda$ Production Cross Section

Here the detailed source for the cross sections, illustrated in Figures 6.14 and 6.15 of Chapter 6, is listed. The values were all taken from the Durham HepData Project (http://hepdata.cedar.ac.uk). The according references to the single data points are summarized in Table G.1.

Table G.1: References for the different production cross sections of Figure 6.14.

Experiment	Reference
COSY-11	[207]
COSY-11	[208]
COSY-11	[209]
COSY-TOF	[156]
HiRes	[210]
ANKE	[211]
ANKE	[212]
Fickinger et al.	[213]
Landolt Börnstein	[214]

H | Acceptance correction for the WALL data set

In Chapter 6 the acceptance and efficiency correction of the HADES data set is shown. The same procedure applied for this data set can also be applied to the WALL data set. The results should, however, only be considered as a qualitative study, as the efficiency of the Forward Wall has not been determined.

Figures H.1 and H.2 show the acceptance corrected invariant mass and angular distribution of the WALL data set. The angular distribution of the Λ in the center-of-mass system shows the difference of this data set compared to the HADES data set. Here also Λ's in the very forward direction could be reconstructed. Although meaningless without the WALL efficiency factor, the histograms were also integrated and extrapolated to obtain a total yield and cross section. The values of each observable are summarized in Table H.1.

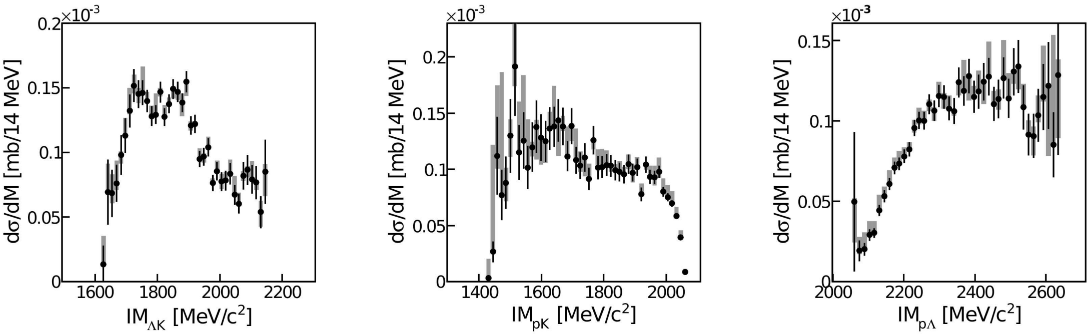

Figure H.1: Experimental distributions of the WALL data set for the two-particle invariant masses, corrected for acceptance and efficiency.

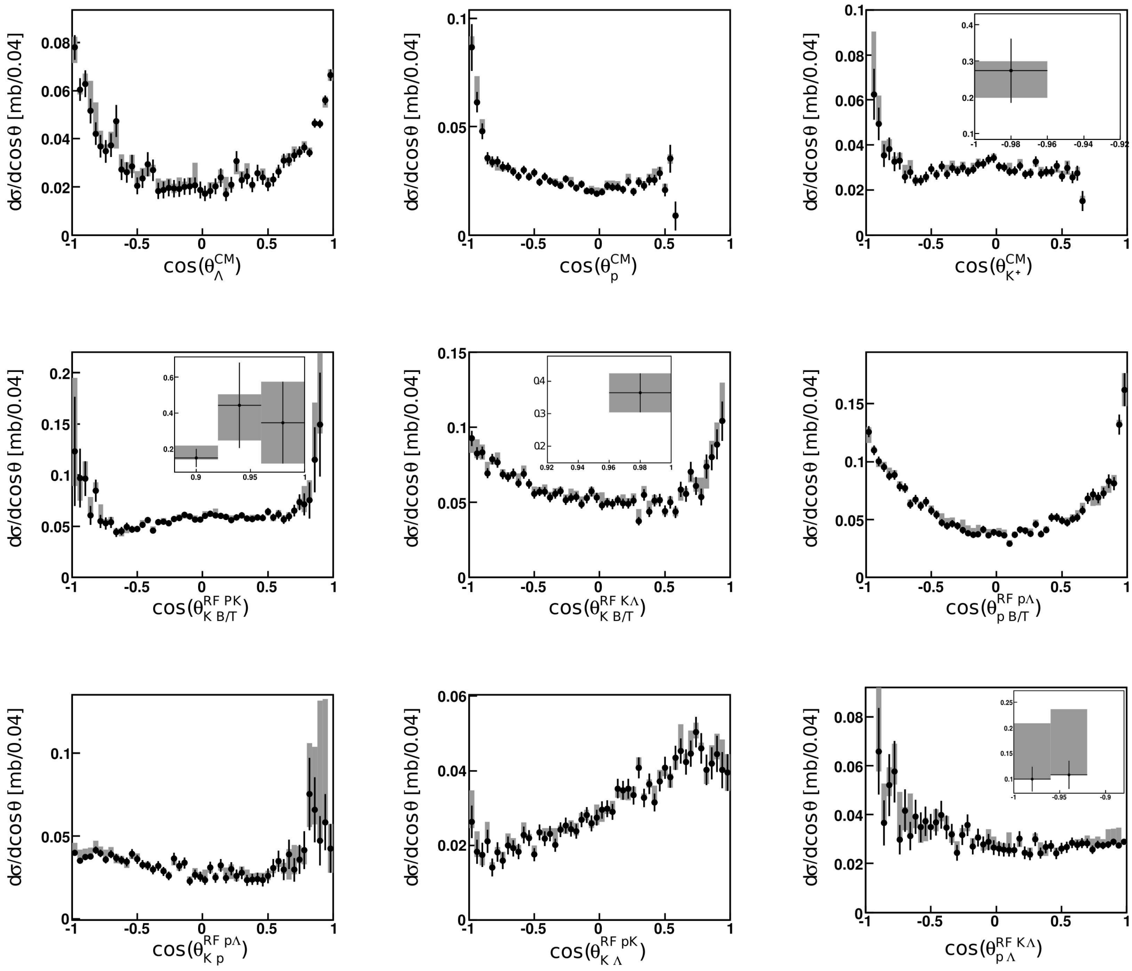

Figure H.2: Experimental distributions of the WALL data set for the three particle angular correlations, corrected for acceptance and efficiency. Inlets show bins that are far out as compared to the other values.

Table H.1: The extracted cross section of the acc. corr. WALL histograms in [μb].

Histogram	Sol. No. 6/9	Sol. No. 1/8	Sol. No. 3/8	Sol. No. 8/8
CMS_Λ	59.79±1.04	61.80±1.07	**64.34±1.14**	61.54±1.09
CMS_p	57.89±0.48	59.70±0.49	60.87±0.51	59.58±0.50
CMS_{K^+}	60.15±0.68	62.73±0.73	63.55±0.74	62.15±0.75
GJ-Angle RF-pK	60.95±1.38	61.56±1.11	62.09±1.24	64.01±2.06
GJ-Angle RF-KΛ	58.76±0.59	60.71±0.63	61.09±0.61	60.04±0.61
GJ-Angle RF-pΛ	57.63±0.51	59.39±0.53	60.33±0.53	58.76±0.52
H-Angle RF-pΛ	60.03±0.92	62.10±0.94	62.27±0.95	60.61±0.89
H-Angle RF-pK	58.72±0.80	60.31±0.84	61.14±0.83	59.92±0.82
H-Angle RF-KΛ	60.52±1.23	61.76±1.19	62.57±1.32	62.27±1.30
IM(ΛK^+)	59.20±0.87	60.56±0.88	61.29±0.96	60.11±0.93
IM(pK^+)	**56.55±0.59**	57.94±0.60	58.19±0.61	57.12±0.61
IM(Λp)	57.91±1.14	59.16±1.08	59.30±1.01	60.66±1.29
Average	59.00±0.85	-	-	-

An average cross section with the uncertainties discussed also in Section 6.2.2 reads:

$$\sigma_{pK^+\Lambda} = 59.00 \pm 0.85^{5.3}_{2.45} \pm 4.13(p{+}p\text{-}error) - 8.67(background)\ \mu\text{b}. \tag{H.1}$$

Again, this should only be taken as a starting value which needs to be corrected for the forward wall efficiency.

A qualitative comparison of the two corrected data samples is given in the Figures H.3 and H.3. Due to the different absolute scale the WALL histograms

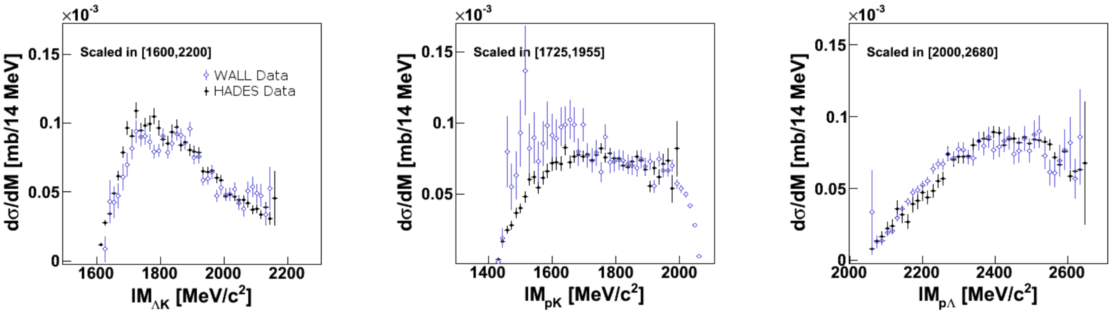

Figure H.3: Experimental distributions of the WALL and HADES data set for the two-particle invariant masses, corrected for acceptance and efficiency. The WALL histograms were scaled to the HADES histograms.

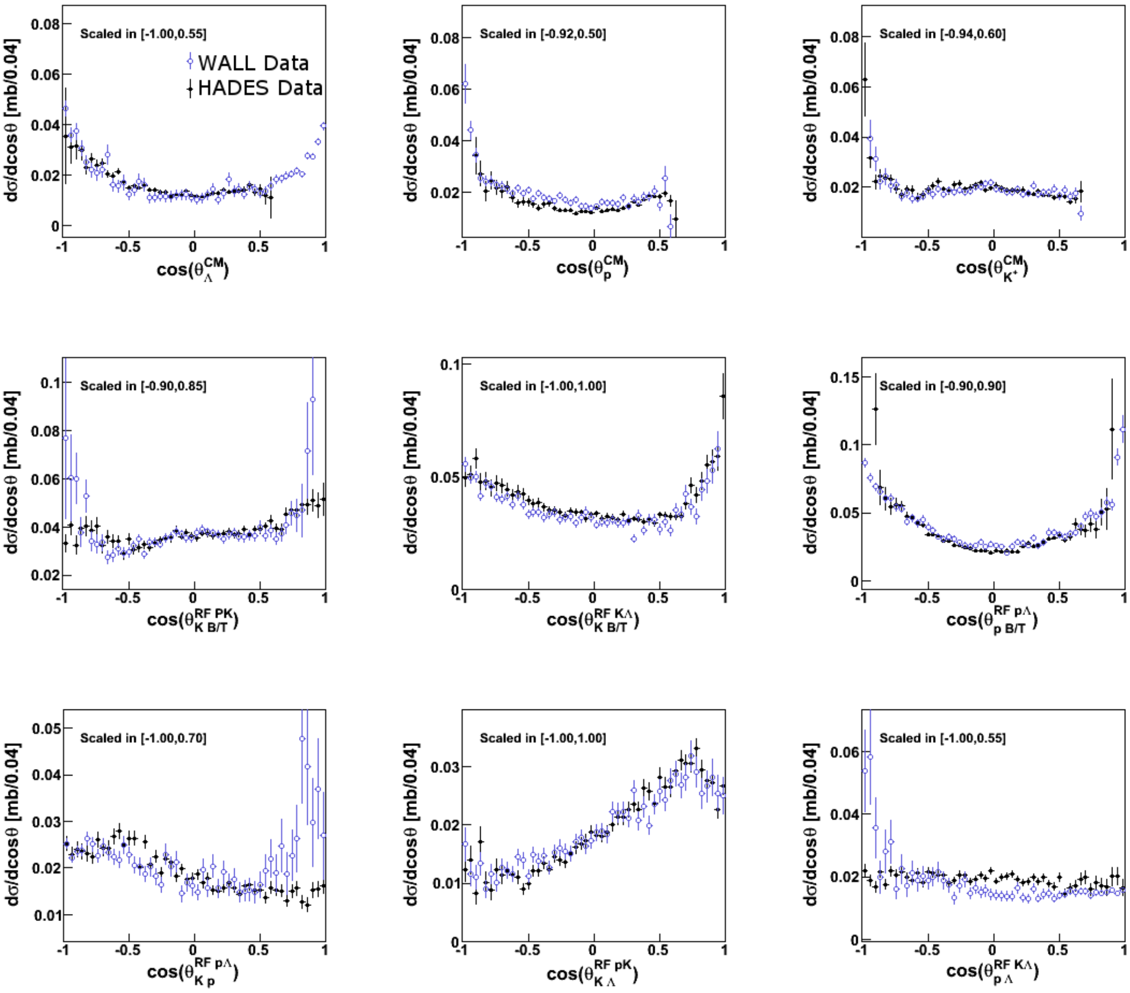

Figure H.4: Experimental distributions of the WALL and HADES data set for the three particle angular correlations, corrected for acceptance and efficiency. The WALL histograms were scaled to the HADES histograms.

were scaled down to the HADES data. The agreement is good, especially in the angular distributions. At the edges of the histograms towards angles of 0 and 180° the statistic in either one of the data sets can deviate, which is however accompanied with large statistical errors. It may be, that for these events an acceptance correction is not reasonable and that this statistic needs to be cut out. See e.g. last Gottfried-Jackson Frame in the middle row. The HADES data are strongly deviating at the borders of the histogram which seems unreasonable. The WALL statistic, in this observable, might give a better orientation of the true event distribution.

The differences between the two data sets are nicely visible in the two dimensional event distribution of the Dalitz-plot, Figure H.5. In the Dalitz-plot $IM^2_{K^+p}$ vs. $IM^2_{p\Lambda}$ the statistic is mainly concentrated on a small spot, namely large masses of IM_{K^+p}. This goes along with a large opening angle between the two particles which implies that the Λ flew into the forward direction where one of its decay products was later detected by the forward wall. The overall phase space coverage of this data sample is, thus, worse than the one of the HADES data set, see Figure 6.12 for comparison.

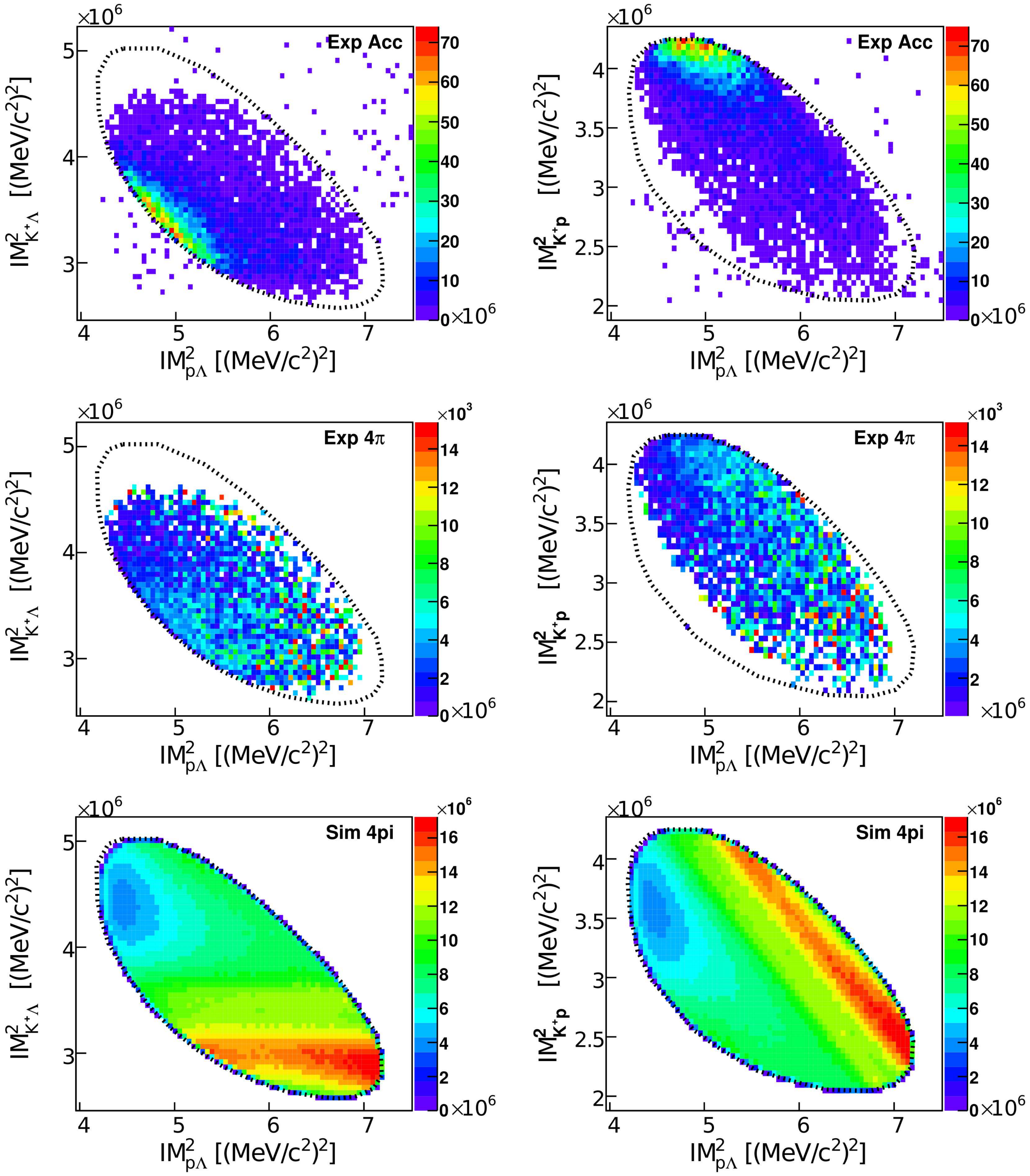

Figure H.5: The two columns show two dalitz plots. Once for the measured WALL data (Exp Acc), once for the data which were corrected for the losses of efficiency (Exp 4π), and once for the PWA model No. 6/9 in 4π (Sim 4π).

Bibliography

[1] Wikipedia, “Standard model of elementary particles.” `http://en.wikipedia.org/wiki/File:Standard_Model_of_Elementary_Particles.svg`, 27 June 2006. (Cited on page 3)

[2] M. Gell-Mann, “A Schematic Model of Baryons and Mesons,” *Phys.Lett.*, vol. 8, pp. 214–215, 1964. (Cited on page 3)

[3] G. Zweig, “An SU(3) model for strong interaction symmetry and its breaking. Version 1,” *CERN-TH-401*, 1964. (Cited on page 3)

[4] G. Aad *et al.*, “Observation of a new particle in the search for the Standard Model Higgs boson with the ATLAS detector at the LHC,” *Phys.Lett.*, vol. B716, pp. 1–29, 2012, arXiv:hep-ex/1207.7214. (Cited on page 4)

[5] S. Chatrchyan *et al.*, “Observation of a new boson at a mass of 125 GeV with the CMS experiment at the LHC,” *Phys.Lett.*, vol. B716, pp. 30–61, 2012, arxiv:hep-ex/1207.7235. (Cited on page 4)

[6] "Nobelprize.org Nobel Media AB", “The 2004 nobel prize in physics - popular information.” `http://www.nobelprize.org/nobel_prizes/physics/laureates/2004/popular.html`, 2004. (Cited on page 4)

[7] B. Borasoy, “SU(3) chiral effective field theories: A Status report,” *Nucl.Phys.*, vol. A754, pp. 191–201, 2005, arXiv:hep-ph/0402292. (Cited on page 5)

[8] J. Beringer *et al.*, “Review of Particle Physics (RPP),” *Phys.Rev.*, vol. D86, p. 010001, 2012. (Cited on pages 5, 41, 53, 69, 99, and 101)

[9] R. Machleidt and D. Entem, “Chiral effective field theory and nuclear forces,” *Phys.Rept.*, vol. 503, pp. 1–75, 2011, arXiv:nucl-th/1105.2919. (Cited on page 5)

[10] K. Tsubakihara, H. Maekawa, H. Matsumiya, and A. Ohnishi, “Lambda hypernuclei and neutron star matter in a chiral SU(3) relativistic mean field model with a logarithmic potential,” *Phys.Rev.*, vol. C81, p. 065206, 2010, arXiv:nucl-th/0909.5058. (Cited on page 5)

[11] N. Kaiser and W. Weise, “Chiral SU(3) dynamics and Lambda-hyperons in the nuclear medium,” *Phys.Rev.*, vol. C71, p. 015203, 2005, arXiv:nucl-th/0410062. (Cited on page 5)

[12] T. Inoue and E. Oset, “Eta in the nuclear medium within a chiral unitary approach,” *Nucl.Phys.*, vol. A710, pp. 354–370, 2002, arXiv:hep-ph/0205028. (Cited on page 5)

[13] H. Nagahiro, D. Jido, and S. Hirenzaki, “Eta nucleus interactions and in-medium properties of N*(1535) in chiral models,” *Phys.Rev.*, vol. C68, p. 035205, 2003, arXiv:nucl-th/0304068. (Cited on page 5)

[14] M. Nanova, “In-medium Properties of the η'-Meson from Photonuclear Reactions,” *EPJ Web Conf.*, vol. 37, p. 03007, 2012, arXiv:nucl-ex/1209.1026. (Cited on page 5)

[15] Y. Ikeda, T. Hyodo, and W. Weise, “Chiral SU(3) theory of antikaon-nucleon interactions with improved threshold constraints,” *Nucl.Phys.*, vol. A881, pp. 98–114, 2012, arXiv:nucl-th/1201.6549. (Cited on pages 5, 6, 7, 8, 9, and 10)

[16] A. Cieply and J. Smejkal, “Chirally motivated $\bar{K}N$ amplitudes for in-medium applications,” *Nucl.Phys.*, vol. A881, pp. 115–126, 2012, arXiv:nucl-th/1112.0917. (Cited on pages 5, 9, 10, and 11)

[17] M. Mai and U.-G. Meissner, “New insights into antikaon-nucleon scattering and the structure of the Λ(1405),” *Nucl.Phys.*, vol. A900, pp. 51 – 64, 2013, arXiv:nucl-th/1202.2030. (Cited on pages 5 and 9)

[18] Z.-H. Guo and J. Oller, “Meson-baryon reactions with strangeness -1 within a chiral framework,” *Phys.Rev.*, vol. C87, no. 3, p. 035202, 2013, arXiv:hep-ph/1210.3485. (Cited on pages 5, 8, 9, and 10)

[19] N. Kaiser, P. Siegel, and W. Weise, “Chiral dynamics and the low-energy kaon - nucleon interaction,” *Nucl.Phys.*, vol. A594, pp. 325–345, 1995, arXiv:nucl-th/9505043. (Cited on page 6)

[20] W. Weise, “Low-energy QCD and hadronic structure,” *Nucl.Phys.*, vol. A827, pp. 66C–76C, 2009, arXiv:nucl-th/0905.4898. (Cited on page 6)

[21] E. Oset and A. Ramos, “Nonperturbative chiral approach to s wave anti-K N interactions,” *Nucl.Phys.*, vol. A635, pp. 99–120, 1998, arXiv:nucl-th/9711022. (Cited on page 6)

[22] M. Lutz and E. Kolomeitsev, “Relativistic chiral SU(3) symmetry, large N(c) sum rules and meson baryon scattering,” *Nucl.Phys.*, vol. A700, pp. 193–308, 2002, arXiv:nucl-th/0105042. (Cited on page 6)

[23] J. Siebenson, “Strange baryonic resonance below the $\bar{K}N$ threshold - Results from p+p reactions at the HADES experiment,” Doctoral dissertation thesis, Technische Universität München, 2013. (Cited on pages 7, 42, 49, 54, 57, 59, 60, 65, 67, 69, 76, 81, 82, 149, 163, 171, and 173)

[24] L. Roca and E. Oset, “On the isospin 0 and 1 resonances from $\pi\Sigma$ photoproduction data,” 2013, arXiv:nucl-th/1307.5752. (Cited on page 7)

[25] D. Tovee, D. Davis, J. Simonovic, G. Bohm, J. Klabuhn, *et al.*, “Some properties of the charged sigma hyperons,” *Nucl.Phys.*, vol. B33, pp. 493–504, 1971. (Cited on page 9)

[26] R. Nowak, J. Armstrong, D. Davis, D. Miller, D. Tovee, *et al.*, “Charged Sigma Hyperon Production by K- Meson Interactions at Rest,” *Nucl.Phys.*, vol. B139, pp. 61–71, 1978. (Cited on page 9)

[27] M. Iwasaki, R. Hayano, T. Ito, S. Nakamura, T. Terada, *et al.*, “Observation of Kaonic Hydrogen K_α X Rays,” *Phys.Rev.Lett.*, vol. 78, pp. 3067–3069, 1997. (Cited on page 9)

[28] G. Beer *et al.*, “Measurement of the kaonic hydrogen X-ray spectrum,” *Phys.Rev.Lett.*, vol. 94, p. 212302, 2005. (Cited on page 9)

[29] M. Bazzi, G. Beer, L. Bombelli, A. Bragadireanu, M. Cargnelli, *et al.*, “A New Measurement of Kaonic Hydrogen X rays,” *Phys.Lett.*, vol. B704, pp. 113–117, 2011, arXiv:nucl-ex/1105.3090. (Cited on page 9)

[30] A. Cieply, E. Friedman, A. Gal, and J. Mares, “Study of chirally motivated low-energy K- optical potentials,” *Nucl.Phys.*, vol. A696, pp. 173–193, 2001, arXiv:nucl-th/0104087. (Cited on pages 11 and 14)

[31] A. Baca, C. Garcia-Recio, and J. Nieves, “Deeply bound levels in kaonic atoms,” *Nucl.Phys.*, vol. A673, pp. 335–353, 2000, arxiv:nucl-th/0001060. (Cited on pages 11 and 13)

[32] A. Ramos and E. Oset, “The Properties of anti-K in the nuclear medium,”

Nucl.Phys., vol. A671, pp. 481–502, 2000, arXiv:nucl-th/9906016. (Cited on page 11)

[33] M. Lutz, “Nuclear kaon dynamics,” *Phys.Lett.*, vol. B426, pp. 12–20, 1998, nucl-th/9709073. (Cited on page 11)

[34] J. Schaffner-Bielich, V. Koch, and M. Effenberger, “Medium modified cross-sections, temperature and finite momentum effects for anti-kaon production in heavy ion collisions,” *Nucl.Phys.*, vol. A669, pp. 153–172, 2000, arXiv:nucl-th/9907095. (Cited on page 11)

[35] E. Friedman, A. Gal, and C. Batty, “Density dependence in kaonic atoms,” *Phys.Lett.*, vol. B308, pp. 6–10, 1993. (Cited on page 11)

[36] E. Friedman, A. Gal, and C. Batty, “Density dependent K- nuclear optical potentials from kaonic atoms,” *Nucl.Phys.*, vol. A579, pp. 518–538, 1994. (Cited on page 11)

[37] E. Friedman, A. Gal, and J. Mares, “K- Nucleus relativistic mean field potential consistent with kaonic atoms,” *Phys.Rev.*, vol. C60, p. 024314, 1999, arXiv:nucl-th/9804072. (Cited on page 11)

[38] T. Waas, N. Kaiser, and W. Weise, “Effective kaon masses in dense nuclear and neutron matter,” *Physics Letters B*, vol. 379, no. 1-4, pp. 34 – 38, 1996. (Cited on page 11)

[39] E. Friedman and A. Gal, “Nuclear medium effects from hadronic atoms,” 2011, arXiv:nucl-th/1108.2156. (Cited on pages 11 and 34)

[40] A. Cieply, E. Friedman, A. Gal, D. Gazda, and J. Mares, “Chirally motivated K^- nuclear potentials,” *Phys.Lett.*, vol. B702, pp. 402–407, 2011, arXiv:nucl-th/1102.4515. (Cited on page 11)

[41] A. Pais and R. Serber, “Interaction between $\bar{K}$-particles and nucleons,” *Phys. Rev.*, vol. 99, pp. 1551–1555, Sep 1955. (Cited on page 11)

[42] W. B. Cheston, “Interaction of $\bar{K}$-particles with nuclear matter,” *Phys. Rev.*, vol. 102, pp. 517–521, Apr 1956. (Cited on page 11)

[43] C. Franzinetti and G. Morpurgo, “Binding of the new particles to nucleons - hyperfragments,” *Il Nuovo Cimento*, vol. 6, no. 2, pp. 780–802, 1957. (Cited on page 11)

[44] R. H. Dalitz, “K mesons and hyperons their strong and weak interactions,” *Reports on Progress in Physics*, vol. 20, no. 1, p. 163, 1957. (Cited on page 11)

[45] Y. Nogami, “Possible existence of $\bar{K}NN$ bound states,” *Physics Letters*, vol. 7, no. 4, pp. 288 – 289, 1963. (Cited on pages 12 and 20)

[46] R. Dalitz and S. Tuan, “The energy dependence of low energy K^- -proton processes,” *Annals Phys.*, vol. 8, pp. 100–118, 1959. (Cited on page 12)

[47] R. Dalitz and S. Tuan, “A possible resonant state in pion-hyperon scattering,” *Phys.Rev.Lett.*, vol. 2, pp. 425–428, 1959. (Cited on page 12)

[48] R. Dalitz and S. Tuan, “The phenomenological description of -K -nucleon reaction processes,” *Annals Phys.*, vol. 10, pp. 307–351, 1960. (Cited on page 12)

[49] A. E. Kudryavtsev, V. Mur, and V. Popov, “Possible bound state of a K^- meson with a ^{4}He nucleus,” *JETP Lett.*, vol. 37, pp. 489–492, 1983. (Cited on page 12)

[50] A. E. Kudryavtsev, V. Mur, and V. Popov, “Possible existence of K^- light nucleus bound states,” *Phys.Lett.*, vol. B143, pp. 41–44, 1984. (Cited on page 12)

[51] V. Popov, A. E. Kudryavtsev, V. Lisin, and V. Mur, “Shallow nuclear levels and radiative tansitions in hadronic atoms,” *Sov.Phys.JETP*, vol. 61, pp. 420–426, 1985. (Cited on page 12)

[52] C. Batty, “Light Kaonic and Anti-protonic Atoms,” *Nucl.Phys.*, vol. A508, pp. 89–98, 1990. (Cited on page 12)

[53] L. Staronski and S. Wycech, “The puzzle of Kα bound state,” *Czech.J.Phys.*, vol. B36, pp. 903–906, 1986. (Cited on pages 12, 13, and 20)

[54] S. Okada, G. Beer, H. Bhang, M. Cargnelli, J. Chiba, *et al.*, “Precision measurement of the 3d → 2p x-ray energy in kaonic He-4,” *Phys.Lett.*, vol. B653, pp. 387–391, 2007, arXiv:nucl-ex/0707.0448. (Cited on page 12)

[55] M. Bazzi *et al.*, “Kaonic helium-4 X-ray measurement in SIDDHARTA,” *Phys.Lett.*, vol. B681, pp. 310–314, 2009. (Cited on page 12)

[56] R. Seki, “K^- Nucleus Optical Potential in K^--Mesonic Atoms,” *Phys.Rev.*, vol. C5, pp. 1196–1205, 1972. (Cited on page 13)

[57] E. Friedman and A. Gal, “K^- and $\bar{p}$ deeply bound atomic states,” *Nucl.Phys.*, vol. A658, pp. 345–361, 1999, arxiv:nucl-th/9907052. (Cited on page 13)

[58] C. Batty, E. Friedman, A. Gal, and G. Kalbermann, “Finite-range effects in hadronic atoms: (II). Kaonic and antiprotonic atoms,” *Nuclear Physics A*, vol. 535, no. 3-4, pp. 548 – 572, 1991. (Cited on page 13)

[59] M. Krell, “Repulsive effects due to the absorption in exotic atoms,” *Phys.Rev.Lett.*, vol. 26, pp. 584–587, 1971. (Cited on page 13)

[60] J. H. Koch, M. M. Sternheim, and J. F. Walker, “Eigenstates of Optical Potentials for Exotic Atoms,” *Phys.Rev.Lett.*, vol. 26, pp. 1465–1468, 1971. (Cited on page 13)

[61] A. Gal, E. Friedman, and C. Batty, “On the interplay between Coulomb and nuclear states in exotic atoms,” *Nucl.Phys.*, vol. A606, pp. 283–291, 1996. (Cited on page 13)

[62] J. H. Koch, M. M. Sternheim, and J. F. Walker, “Complex Eigenvalues of a Coupled-Channels Model,” *Phys.Rev.*, vol. C5, pp. 381–383, 1972. (Cited on page 13)

[63] E. Friedman and A. Gal, “Narrow deeply bound K^- atomic states,” *Phys.Lett.*, vol. B459, pp. 43–48, 1999, arxiv:nucl-th/9902036. (Cited on page 13)

[64] S. Hirenzaki, Y. Okumura, H. Toki, E. Oset, and A. Ramos, “Chiral unitary model for the kaonic atom,” *Phys.Rev.*, vol. C61, p. 055205, 2000. (Cited on page 13)

[65] J. Fink, P.J., J. Schnick, and R. Landau, “A microscopic calculation of K^- atomic and Λ^* hypernuclear carbon,” *Phys.Rev.*, vol. C42, pp. 232–240, 1990. (Cited on pages 13 and 17)

[66] S. Wycech, “On Possibilities of Narrow Nuclear States of K^-,” *Nucl.Phys.*, vol. A450, pp. 399C–402C, 1986. (Cited on pages 13 and 20)

[67] T. Kishimoto, “Kaonic nuclei excited by the (K-, N) reaction,” *Phys.Rev.Lett.*, vol. 83, pp. 4701–4704, 1999, arxiv:nucl-th/9910014. (Cited on pages 14 and 25)

[68] Y. Akaishi and T. Yamazaki, “Nuclear anti-K bound states to be formed by He-4(stopped K-, n),” *Nucl.Phys.*, vol. A684, pp. 409–413, 2001. (Cited on pages 14 and 23)

[69] Y. Akaishi and T. Yamazaki, “Nuclear anti-K bound states in light nuclei,” *Phys.Rev.*, vol. C65, p. 044005, 2002. (Cited on pages 14, 16, 18, 23, and 34)

[70] A. Gal, "Phenomenology of K- atoms and other strange hadronic atoms," *Nucl.Phys.*, vol. A691, pp. 268–277, 2001, arxiv:nucl-th/0101010. (Cited on page 14)

[71] M. Iwasaki, K. Itahashi, A. Miyajima, H. Outa, Y. Akaishi, *et al.*, "^{4}He(stopped K^-,n) spectroscopy for deeply bound kaonic nuclear states," *Nucl.Instrum.Meth.*, vol. A473, pp. 286–301, 2001. (Cited on page 14)

[72] A. Gal, "Overview of anti-K-Nuclear Quasi-Bound States," *Nucl.Phys.*, vol. A790, pp. 143–150, 2007, arXiv:nucl-th/0610090. (Cited on page 15)

[73] T. Hyodo and D. Jido, "The nature of the resonance in chiral dynamics," *Progress in Particle and Nuclear Physics*, vol. 67, no. 1, pp. 55 – 98, 2012. (Cited on page 15)

[74] N. Barnea, A. Gal, and E. Liverts, "Realistic calculations of $\bar{K}NN$, $\bar{K}NNN$, and $\bar{K}\bar{K}NN$ quasibound states," *Phys.Lett.*, vol. B712, pp. 132–137, 2012, arXiv:nucl-th/1203.5234. (Cited on pages 15, 16, 17, 18, 19, and 20)

[75] E. Oset, D. Jido, T. Sekihara, A. Martinez Torres, K. Khemchandani, *et al.*, "A new perspective on the Faddeev equations and the $\bar{K}NN$ system from chiral dynamics and unitarity in coupled channels," *Nucl.Phys.*, vol. A881, pp. 127–140, 2012, arXiv:hep-ph/1203.4798. (Cited on pages 15, 16, and 20)

[76] N. Shevchenko, A. Gal, J. Mares, and J. Revai, "$\overline{K}NN$ quasi-bound state and the $\overline{K}N$ interaction: Coupled-channel Faddeev calculations of the $\overline{K}NN$-$\pi\Sigma N$ system," *Phys.Rev.*, vol. C76, p. 044004, 2007, arXiv:nucl-th/0706.4393. (Cited on pages 15, 16, 17, 18, and 34)

[77] M. Bayar and E. Oset, "$\bar{K}NN$ Absorption within the Framework of the Fixed Center Approximation to Faddeev equations," 2012, arXiv:hep-ph/1207.1661. (Cited on pages 16 and 18)

[78] N. Shevchenko, A. Gal, and J. Mares, "Faddeev calculation of a K^-pp quasi-bound state," *Phys.Rev.Lett.*, vol. 98, p. 082301, 2007, arXiv:nucl-th/0610022. (Cited on pages 16, 18, and 34)

[79] Y. Ikeda and T. Sato, "Strange dibaryon resonance in the $\bar{K}$NN - πYN

system," *Phys.Rev.*, vol. C76, p. 035203, 2007, arXiv:nucl-th/0704.1978. (Cited on pages 16, 18, and 34)

[80] Y. Ikeda and T. Sato, "On the resonance energy of the $\bar{K}$NN - πYN system," *Phys.Rev.*, vol. C79, p. 035201, 2009, arXiv:nucl-th/0809.1285. (Cited on pages 16 and 18)

[81] Y. Ikeda, H. Kamano, and T. Sato, "Energy dependence of $\bar{K}N$ interactions and resonance pole of strange dibaryons," *Prog.Theor.Phys.*, vol. 124, pp. 533–539, 2010, arXiv:nucl-th/1004.4877. (Cited on pages 16 and 18)

[82] M. Bayar and E. Oset, "Improved Fixed Center Approximation of the Faddeev equations for the $\bar{K}NN$ system with S=0," *Nucl.Phys.*, vol. A883, pp. 57–68, 2012, arXiv:nucl-th/1203.5313. (Cited on pages 16, 17, and 18)

[83] J. Revai and N. Shevchenko, "Faddeev calculations of the $\bar{K}NN$ system with chirally-motivated $\bar{K}N$ interaction. II. The $K^{-}pp$ quasi-bound state," 2014, arXiv:nucl-th/1403.0757. (Cited on pages 16, 17, and 18)

[84] A. Gal, "Recent studies of kaonic atoms and nuclear clusters," *Nuclear Physics A*, vol. 914, no. 0, pp. 270 – 279, 2013. {XI} International Conference on Hypernuclear and Strange Particle Physics (HYP2012). (Cited on pages 16 and 18)

[85] A. Dote, T. Hyodo, and W. Weise, "Variational calculation of the ppK^{-}system based on chiral SU(3) dynamics," *Phys.Rev.*, vol. C79, p. 014003, 2009, arXiv:nucl-th/0806.4917. (Cited on pages 16, 17, 18, 21, and 34)

[86] A. Dote, T. Hyodo, and W. Weise, "K^{-}pp system with chiral SU(3) effective interaction," *Nucl.Phys.*, vol. A804, pp. 197–206, 2008, arXiv:nucl-th/0802.0238. (Cited on pages 16, 17, 18, and 34)

[87] T. Yamazaki and Y. Akaishi, "The Basic $\bar{K}$ nuclear cluster $K^{-}pp$ and its enhanced formation in the $p+p \to K^{+}+X$ reaction," *Phys.Rev.*, vol. C76, p. 045201, 2007, arXiv:nucl-th/0709.0630. (Cited on pages 16, 17, 20, 165, 167, 171, and 172)

[88] A. Arai, M. Oka, and S. Yasui, "Λ^{*} - Hypernuclei in Phenomenological Nuclear Forces," *Prog.Theor.Phys.*, vol. 119, pp. 103–115, 2008, arXiv:nucl-th/0705.3936. (Cited on pages 16, 17, and 34)

[89] S. Wycech and A. M. Green, "Variational calculations for $\overline{K}$–few-nucleon systems," *Phys. Rev. C*, vol. 79, p. 014001, 2009. (Cited on pages 16, 18, 19, 20, and 34)

[90] T. Yamazaki and Y. Akaishi, "(K^-,π^-) production of nuclear $\bar{K}$ bound states in proton-rich systems via Λ^* doorways," *Phys.Lett.*, vol. B535, pp. 70–76, 2002. (Cited on pages 16, 18, and 34)

[91] M. Faber, A. Ivanov, P. Kienle, J. Marton, and M. Pitschmann, "Molecule model for kaonic nuclear cluster $\bar{K}NN$," *Int.J.Mod.Phys.*, vol. E20, pp. 1477–1490, 2011, arXiv:nucl-th/0912.2084. (Cited on pages 16 and 18)

[92] T. Uchino, T. Hyodo, and M. Oka, "The Λ^*N interaction and two-body bound state based on chiral dynamics," *Nucl.Phys.*, vol. A868-869, pp. 53–81, 2011, arXiv:nucl-th/1106.0095. (Cited on page 17)

[93] A. Gal, "Meson Assisted Strange Dibaryons," Nov 2010. Comments: Submitted to a Festschrift honoring Gerry Brown's 85th birthday. (Cited on pages 18 and 48)

[94] S. Wycech, "Private communication," 2013. (Cited on page 18)

[95] N. Shevchenko and J. Revai, "Faddeev calculations of the $\bar{K}NN$ system with chirally-motivated $\bar{K}N$ interaction. I. Low-energy K^-d scattering and antikaonic deuterium," 2014, arXiv:nucl-th/1402.3935. (Cited on page 20)

[96] T. Sekihara, D. Jido, and Y. Kanada-En'yo, "Lambda(1405)-induced non-mesonic decay in kaonic nuclei," *Phys.Rev.*, vol. C79, p. 062201, 2009, arXiv:nucl-th/0904.2822. (Cited on pages 21 and 22)

[97] J. Mares, E. Friedman, and A. Gal, "Widths of $\bar{K}$ - nuclear deeply bound states in a dynamical model," *Phys.Lett.*, vol. B606, pp. 295–302, 2005, arXiv:nucl-th/0407063. (Cited on page 22)

[98] Y. Akaishi, K. S. Myint, and T. Yamazaki, "Kaonic nuclear systems $\overline{K}N$ and $\overline{K}NN$ as decaying states," *Proc.Jpn.Acad.*, vol. B84, p. 264, 2008. (Cited on page 22)

[99] D. Gazda and J. Mares, "Calculations of K^- nuclear quasi-bound states based on chiral meson-baryon amplitudes," *Nucl.Phys.*, vol. A881, pp. 159–168, 2012, arXiv:nucl-th/1206.0223. (Cited on page 23)

[100] S. Wycech, "On nuclear states of $\bar{K}$ mesons," *J. Phys.: Conf. Ser.*, vol. 374, p. 012005, 2012. (Cited on page 23)

[101] T. Suzuki, H. Bhang, G. Franklin, K. Gomikawa, R. Hayano, *et al.*, "Discovery of a strange tribaryon $S^0(3115)$ in ^{4}He(stopped $K-$, p) reaction," *Phys.Lett.*, vol. B597, pp. 263–269, 2004. (Cited on page 23)

[102] M. Iwasaki, T. Suzuki, H. Bhang, G. Franklin, K. Gomikawa, *et al.*, "Evidence for a strongly bound kaonic system K^-ppn in the ^{4}He(stopped K^-,n) reaction," 2003, arXiv:nucl-ex/0310018. (Cited on page 23)

[103] T. Suzuki, H. Bhang, G. Franklin, K. Gomikawa, R. Hayano, *et al.*, "A Search for deeply bound kaonic nuclear states," *Nucl.Phys.*, vol. A754, pp. 375–382, 2005, arXiv:nucl-ex/0501013. (Cited on pages 23 and 24)

[104] H. Yim, H. Bhang, J. Chiba, S. Choi, Y. Fukuda, *et al.*, "Search for strange tribaryons in the ^{4}He(K^-_{stop}, n$\pi^\pm$) reaction," *Phys.Lett.*, vol. B688, pp. 43–49, 2010. (Cited on pages 23 and 24)

[105] M. Sato, H. Bhang, J. Chiba, S. Choi, Y. Fukuda, *et al.*, "Search for strange tribaryon states in the inclusive ^{4}He($K^-_{stopped}$, p) reaction," *Phys.Lett.*, vol. B659, pp. 107–112, 2008, arXiv:nucl-ex/0708.2968. (Cited on pages 23 and 24)

[106] T. Kishimoto and T. Hayakawa and S. Ajimura and S. Minami and A. Sakaguchi and Y. Shimizu and R.E. Chrien and M. May and P. Pile and A. Rusek and R. Sutter and H. Noumi and H. Tamura and M. Ukai and Y. Miura and K. Tanida, "Kaonic nuclei probed by the in-flight reaction," *Nuclear Physics A*, vol. 754, no. 0, pp. 383 – 390, 2005. Proceedings of the Eighth International Conference on Hypernuclear and Strange Particle Physics. (Cited on page 25)

[107] T. Kishimoto, T. Hayakawa, S. Ajimura, F. Khanam, T. Itabashi, *et al.*, "Kaon-nucleus interaction studied through the in-flight (K$^-$,N) reaction," *Prog.Theor.Phys.*, vol. 118, pp. 181–186, 2007. (Cited on pages 25 and 34)

[108] T. Kishimoto, T. Hayakawa, S. Ajimura, F. Khanam, T. Itabashi, *et al.*, "Kaon-nucleus interaction studied through the in-flight (K$^-$,N) reactions," *Nucl.Phys.*, vol. A827, pp. 321C–323C, 2009. (Cited on page 25)

[109] G. Bendiscioli, A. Fontana, L. Lavezzi, A. Panzarasa, A. Rotondi,

et al., “Search for signals of bound K^- nuclear states in antiproton ^{4}He annihilations at rest,” *Nucl.Phys.*, vol. A789, pp. 222–242, 2007. (Cited on pages 26 and 27)

[110] G. Bendiscioli, T. Bressani, L. Lavezzi, and P. Salvini, “A new analysis improving the evidence of a narrow peak in the invariant-mass distribution of the Λp system observed in the $\bar{p}$ annihilation at rest on ^{4}He,” *Eur.Phys.J.*, vol. A40, pp. 11–22, 2009. (Cited on pages 26 and 27)

[111] S. Piano, “Recent results on absorption at rest by few nucleons and the bound kaonic nuclear state puzzle,” *Nuclear Physics A*, vol. 835, no. 1-4, pp. 35 – 42, 2010. Proceedings of the 10th International Conference on Hypernuclear and Strange Particle Physics. (Cited on page 27)

[112] A. Filippi and S. Piano, “Studies of K^-absorption on light nuclei and the search for bound nuclear kaonic states,” *Journal of Physics: Conference Series*, vol. 312, no. SECTION 2, 2011. cited By (since 1996)1. (Cited on page 27)

[113] T. Nagae, “Experimental searches for antikaonic clusters,” *Nuclear Physics A*, vol. 881, no. 0, pp. 141 – 149, 2012. Progress in Strangeness Nuclear Physics. (Cited on page 27)

[114] T. Buran, O. Eivindson, O. Skjeggestad, H. Tøfte, and I. Vegge, “Study of the $\Lambda - p$ effective mass spectrum and the Λ lifetime,” *Physics Letters*, vol. 20, no. 3, pp. 318 – 320, 1966. (Cited on page 27)

[115] D. P. Goyal and A. V. Sodhi, “Observation of Λp mass enhancement in the reaction $K^- d \to \Lambda p \pi^+ \pi^- \pi^-$,” *Phys. Rev. D*, vol. 18, pp. 948–953, Aug 1978. (Cited on page 27)

[116] F. Sakuma, C. Curceanu, M. Iwasaki, P. Kienle, H. Ohnishi, M. Tokuda, K. Tsukada, E. Widmann, T. Yamazaki, and J. Zmeskal, “Double antikaonic nuclear clusters in antiproton-3He annihilation at J-PARC,” *Hyperfine Interactions*, vol. 213, no. 1-3, pp. 51–61, 2012. (Cited on page 27)

[117] M. Agnello *et al.*, “Evidence for a kaon-bound state K^-pp produced in K^- absorption reactions at rest,” *Phys.Rev.Lett.*, vol. 94, p. 212303, 2005. (Cited on pages 28 and 172)

[118] V. Magas, E. Oset, A. Ramos, and H. Toki, “A Critical view on the deeply bound K^-pp system,” *Phys.Rev.*, vol. C74, p. 025206, 2006, arXiv:nucl-th/0601013. (Cited on page 28)

[119] J. Mares, E. Friedman, and A. Gal, “Anti-K nuclear bound states in a

dynamical model," *Nucl.Phys.*, vol. A770, pp. 84–105, 2006, arXiv:nucl-th/0601009. (Cited on page 28)

[120] G. Pandejee, N. Upadhyay, and B. Jain, "Study of K^- absorption at rest in nuclei followed by $p\Lambda$ emission," *Phys.Rev.*, vol. C82, p. 034608, 2010, arXiv:nucl-th/1003.1615. (Cited on page 28)

[121] M. Agnello *et al.*, "Correlated Λd pairs from the $K^-_{(stop)}A \rightarrow \Lambda dA'$ reaction," *Phys.Lett.*, vol. B654, pp. 80–86, 2007, arXiv:nucl-ex/0708.3614. (Cited on page 29)

[122] M. Agnello *et al.*, "The A($K^-_{(stop)}$, $\Lambda d)A'$ reaction, a tool to observe [$\overline{K}NNN$] clusters," *Eur.Phys.J.*, vol. A33, pp. 283–286, 2007. (Cited on page 29)

[123] V. Magas, E. Oset, and A. Ramos, "Critical review of [K^-ppn] bound states," *Phys.Rev.*, vol. C77, p. 065210, 2008, arXiv:nucl-th/0801.4504. (Cited on page 29)

[124] T. Suzuki *et al.*, "Λd correlation from ^4He(stopped-K^-, d) reaction," *Phys.Rev.*, vol. C76, p. 068202, 2007, arXiv:nucl-ex/0709.0996. (Cited on page 29)

[125] T. Yamazaki, M. Maggiora, P. Kienle, K. Suzuki, A. Amoroso, *et al.*, "Indication of a deeply bound compact K^-pp state formed in the pp→ $p\Lambda K^+$ reaction at 2.85 GeV," *Phys.Rev.Lett.*, vol. 104, p. 132502, 2010, arXiv:nucl-ex/1002.3526. (Cited on pages 29, 30, 31, 32, 153, 163, 164, and 172)

[126] M. Maggiora *et al.*, "DISTO data on K^-pp," *Nucl.Phys.*, vol. A835, pp. 43–50, 2010, arXiv:hep-ex/0912.5116. (Cited on pages 29, 30, 31, and 153)

[127] W. Hogan, P. Piroue, and A. Smith, "K^+-Meson Production in p-p Collisions at 2.5-3.0 GeV," *Phys.Rev.*, vol. 166, pp. 1472–1481, 1968. (Cited on pages 30 and 45)

[128] P. Kienle, M. Maggiora, K. Suzuki, T. Yamazaki, M. Alexeev, *et al.*, "Formation of the $S = -1$ resonance X(2265) in the reaction pp→ XK^+ at 2.50 and 2.85 GeV," *Eur.Phys.J.*, vol. A48, p. 183, 2012, arXiv:nucl-ex/1102.0482. (Cited on pages 32, 163, 164, 165, 166, 167, and 171)

[129] A. Tokiyasu *et al.*, "Search for K^-pp bound state via $\gamma d \rightarrow K^+\pi^-X$ reaction at $E_\gamma = 1.5 - 2.4$ GeV," *Phys.Lett.*, vol. B728, pp. 616–621, 2014, arXiv:nucl-ex/1306.5320. (Cited on page 33)

[130] O. Vazquez, C. Curceanu, K. Piscicchia, A. Scordo, and I. Tucaković, "Studies on the $\Lambda(1405)$ and the antikaon-nucleon interactions with the KLOE Drift Chamber," *PoS*, vol. Hadron2013, p. 183, 2014. (Cited on page 34)

[131] I. Tucaković, "Λ-p/d/t correlations with the KLOE Drift Chamber by the AMADEUS collaboration," *PoS*, vol. Bormio2014, 2014. (Cited on page 34)

[132] S. Marcello, F. De Mori, and A. Filippi, "Search of Kaonic Nuclear States at the SuperB factory," *Few Body Syst.*, vol. 54, pp. 1201–1203, 2013, arXiv:nucl-ex/1210.2939. (Cited on page 34)

[133] A. Filippi, "Study of hadronic Υ(nS) decays in (multi-)baryons," *PoS*, vol. Bormio2013, p. 031, 2013. (Cited on page 34)

[134] A. O. Tokiyasu, "Search for the $\overline{K}NN$ bound state at LEPS/SPring-8," *PoS*, vol. Hadron2013, p. 180, 2013. (Cited on page 34)

[135] S. Enomoto, "Search for deeply-bound $\bar{K}$-nuclear states via the 3He(inflight-K-,n) reaction at J-PARC," *PoS*, vol. Hadron2013, p. 182, 2013. (Cited on page 34)

[136] Y. Ichikawa *et al.*, "Study of kaonic nuclei by the d(π^+, K^+) reaction at J-PARC," *PoS*, vol. Hadron2013, p. 181, 2013. (Cited on page 34)

[137] T. Koike and T. Harada, "Deeply-bound K^-pp state in the ^3He(in-flight K^-, n) spectrum and its moving pole near the $\pi\Sigma N$ threshold," *Phys.Rev.*, vol. C80, p. 055208, 2009, arXiv:nucl-th/0906.3659. (Cited on pages 34 and 35)

[138] A. Ivanov, P. Kienle, J. Marton, and E. Widmann, "Phenomenological model of the kaonic nuclear cluster K^-pp in the ground state," 2005, arXiv:nucl-th/0512037. (Cited on page 34)

[139] T. Nishikawa and Y. Kondo, "K^-pp bound states from Skyrmions," *Phys.Rev.*, vol. C77, p. 055202, 2008, arXiv:hep-ph/0710.0948. (Cited on page 34)

[140] J. Yamagata, S. Hirenzaki, H. Nagahiro, and D. Jido, "Structure and formation of kaonic atoms and kaonic nuclei," *Mod.Phys.Lett.*, vol. A23, pp. 2528–2531, 2008. (Cited on page 34)

[141] A. Schmah, "Produktion von Seltsamkeit in Ar+KCl Reaktionen bei 1.756 AGeV mit HADES," Doctoral dissertation thesis, Technische Universität Darmstadt, 2008. (Cited on pages 37 and 57)

[142] G. Agakishiev *et al.*, "The High-Acceptance Dielectron Spectrometer HADES," *Eur.Phys.J.*, vol. A41, pp. 243–277, 2009, arXiv:nucl-ex/0902.3478. (Cited on pages 37, 38, and 83)

[143] G. Agakishiev *et al.*, "Inclusive dielectron spectra in p+p collisions at 3.5 gev kinetic beam energy," *The European Physical Journal A*, vol. 48, no. 5, pp. 1–11, 2012. (Cited on pages 38 and 154)

[144] H. Bethe, "Theory of the passage of fast corpuscular rays through matter," *Annalen Phys.*, vol. 5, pp. 325–400, 1930. (Cited on page 41)

[145] E. Epple, "The Λ(1405)-Resonance measured via its decay into $\Sigma^0\pi^0$ in proton-proton collisions with the HADES Spectrometer," Diploma thesis, Technische Universität München, 2009. (Cited on pages 42, 57, 62, 84, and 179)

[146] I. Frohlich, L. Cazon, T. Galatyuk, V. Hejny, R. Holzmann, *et al.*, "Pluto: A Monte Carlo Simulation Tool for Hadronic Physics," *PoS*, vol. ACAT2007, p. 076, 2007, arXiv:nucl-ex/0708.2382. (Cited on page 43)

[147] I. Frohlich, T. Galatyuk, R. Holzmann, J. Markert, B. Ramstein, *et al.*, "Design of the Pluto Event Generator," *J.Phys.Conf.Ser.*, vol. 219, p. 032039, 2010, arXiv:nucl-ex/0905.2568. (Cited on page 43)

[148] R. Brun, F. Carminati, and S. Giani, "GEANT Detector Description and Simulation Tool," *CERN-W5013, CERN-W-5013*, 1994. (Cited on page 44)

[149] E. Ferrari and S. Serio, "Three-body associated production in proton-proton collisions and the one-boson-exchange model," *Phys. Rev.*, vol. 167, pp. 1298–1308, Mar 1968. (Cited on pages 45, 158, 159, and 161)

[150] R. Louttit, T. Morris, D. Rahm, R. Rau, A. Thorndike, *et al.*, "Production of Strange Particles in p-p Collisions at 2.85 Bev," *Phys.Rev.*, vol. 123, pp. 1465–1471, 1961. (Cited on page 45)

[151] A. Melissinos, N. Reay, J. Reed, T. Yamanouchi, E. Sacharidis, *et al.*, "Observation of the Low-Energy Λ-p Interaction," *Phys.Rev.Lett.*, vol. 14, pp. 604–607, 1965. (Cited on page 45)

[152] J. Reed, A. Melissinos, N. Reay, T. Yamanouchi, E. Sacharidis, *et al.*, "Production of K^+ Mesons in 2.85- and 2.40-BeV p-p Collisions," *Phys.Rev.*, vol. 168, pp. 1495–1508, 1968. (Cited on page 45)

[153] F. Balestra *et al.*, "Spin transfer in exclusive Λ production from $\vec{p}p$ collisions at 3.67-GeV/c," *Phys.Rev.Lett.*, vol. 83, pp. 1534–1537, 1999, nucl-ex/9906011. (Cited on page 45)

[154] M. Maggiora, "New results from DISTO for spin observables in exclusive hyperon production," *Nucl.Phys.*, vol. A691, pp. 329–335, 2001. (Cited on page 45)

[155] M. Abdel-Bary *et al.*, "Production of Λ and Σ^0 hyperons in proton-proton collisions," *Eur.Phys.J.*, vol. A46, pp. 27–44, 2010, 1008.4287. (Cited on pages 45, 49, 64, 96, 145, 146, 147, 149, 152, and 159)

[156] S. Abdel-Samad *et al.*, "Hyperon production in the channel $pp \rightarrow K^+\Lambda p$ near the reaction threshold," *Phys.Lett.*, vol. B632, pp. 27–34, 2006. (Cited on pages 45, 47, 96, 145, and 230)

[157] S. Abd El-Samad *et al.*, "Influence of N*-resonances on hyperon production in the channel pp→ $K^+\Lambda p$ at 2.95, 3.20 and 3.30 GeV/c beam momentum," *Phys.Lett.*, vol. B688, pp. 142–149, 2010, arXiv:nucl-ex/1003.0603. (Cited on pages 45, 46, 47, 96, 145, 154, 163, and 166)

[158] S. Barsov *et al.*, "Beam Request: The separation of spin-singlet and triplet Λp amplitudes and final state interactions through the measurement of the spin correlation in the $p + p \rightarrow K^+\Lambda p$ reaction at ANKE." `http://collaborations.fz-juelich.de/ikp/anke/proposal/prop_Lambda2014_v2.pdf`, 13 January 2014. (Cited on page 45)

[159] P. Piroue, "Possible existence of a B=2, S=-1 resonance," *Physics Letters*, vol. 11, no. 2, pp. 164 – 167, 1964. (Cited on pages 45 and 48)

[160] W. Cleland, A. Delfosse, P.-A. Dorsaz, J.-L. Gloor, M. Kienzle-Focacci, G. Mancarella, A. Martin, M. Martin, B. Morel, P. Muhlemann, C. Nef, T. Pal, J. Rutschmann, and H. Zeidler, "The reaction p+p → $(\Lambda^0 K^+)p$ at 50 and 30 GeV/c: Partial-wave analysis, Deck model and double Regge exchange," *Nuclear Physics B*, vol. 239, no. 1, pp. 27 – 51, 1984. (Cited on pages 45, 96, and 145)

[161] E. Bierman, A. Colleraine, and U. Nauenberg, "Search for Dibaryon Resonant States," *Phys.Rev.*, vol. 147, pp. 922–931, 1966. (Cited on pages 45, 96, 145, 146, 147, 163, 168, 169, and 229)

[162] W. Chinowsky, R. Kinsey, S. Klein, M. Mandelkern, J. Schultz, *et al.*, "Production of K mesons in three-body states in proton-proton interactions at

6 BeV/c," *Phys.Rev.*, vol. 165, pp. 1466–1478, 1968. (Cited on pages 45, 96, 145, 146, 147, 163, 169, 170, and 229)

[163] V. Kubarovsky *et al.*, "Search for Θ^{++} pentaquarks in the exclusive reaction $\gamma p \rightarrow K^+K^-p$," *Phys.Rev.Lett.*, vol. 97, p. 102001, 2006, hep-ex/0605001. (Cited on page 47)

[164] A. Solaguren-Beascoa Negre, "Strange Multibaryon Systems: Predictions and Experiments," Master thesis, Technische Universität München, 2012. (Cited on page 47)

[165] A. Budzanowski, A. Chatterjee, H. Clement, E. Dorochkevitch, P. Hawranek, *et al.*, "High resolution study of the Lambda p final state interaction in the reaction $p + p \rightarrow K^+ + (\Lambda p)$," *Phys.Lett.*, vol. B687, pp. 31–35, 2010, 1003.0290. (Cited on page 47)

[166] M. Röder *et al.*, "Final-State Interactions in the Process $\vec{p}p \rightarrow pK^+\Lambda$," *Eur.Phys.J.*, vol. A49, p. 157, 2013, arXiv:nucl-ex/1305.0451. (Cited on pages 47, 48, 163, and 165)

[167] A. Sibirtsev, J. Haidenbauer, H.-W. Hammer, and U.-G. Meissner, "Phenomenology of the Λ/Σ^0 production ratio in pp collisions," *Eur.Phys.J.*, vol. A29, pp. 363–367, 2006, arXiv:hep-ph/0608098. (Cited on pages 48, 148, and 151)

[168] A. Sibirtsev, J. Haidenbauer, H.-W. Hammer, and S. Krewald, "Resonances and final state interactions in the reaction pp→ $p + K^+\Lambda$," *Eur.Phys.J.*, vol. A27, pp. 269–285, 2006, arXiv:nucl-th/0512059. (Cited on pages 48, 149, 151, and 152)

[169] A. Budzanowski *et al.*, "Upper limits for a narrow resonance in the reaction $p+p \rightarrow K^+ + (\Lambda p)$," *Phys.Rev.*, vol. D84, p. 032002, 2011, 1105.2281. (Cited on page 48)

[170] R. Siebert and R. Frascaria, "Search for strange (S = -1) dibaryons by means of the reaction $pp \rightarrow K^+X$," *Nucl.Phys.*, vol. A479, pp. 389C–397C, 1988. (Cited on page 48)

[171] R. Siebert, J. Didelez, R. Frascaria, T. Reposeur, E. Warde, *et al.*, "High resolution study of hyperon nucleon interactions by associated strangeness production in p p collisions," *Nucl.Phys.*, vol. A567, pp. 819–843, 1994. (Cited on page 48)

[172] W. Schröder, "Untersuchung der assoziierten Strangeness-Production in den Reaktionen p+p→ $K^+\Lambda p$ und p+p→ $K^+\Sigma^0 p$," Doctoral disser-

tation thesis, Friedrich-Alexander-Universität Erlangen-Nürnberg, 2003. (Cited on pages 49, 146, 147, 163, and 166)

[173] G. Agakishiev *et al.*, “Baryonic resonances close to the $\bar{K}N$ threshold: the case of $\Lambda(1405)$ in pp collisions,” *Phys.Rev.*, vol. C87, p. 025201, 2013, arXiv:nucl-ex/1208.0205. (Cited on pages 54, 65, 69, 76, 82, 163, 164, and 165)

[174] G. Agakishiev *et al.*, “Associate K^0 production in p+p collisions at 3.5 GeV: The role of $\Delta(1232)^{++}$,” 2014, arXiv:nucl-ex/1403.6662. (Cited on page 63)

[175] S. Klein, W. Chinowsky, R. Kinsey, M. Mandelkern, J. Schultz, *et al.*, “Four-body strange-particle production in pp collisions at 6 Bev/c,” *Phys.Rev.*, vol. D1, pp. 3019–3030, 1970. (Cited on page 73)

[176] I. Zychor, M. Büscher, M. Hartmann, A. Kacharava, I. Keshelashvili, *et al.*, “Shape of the $\Lambda(1405)$ hyperon measured through its $\Sigma^0\pi^0$ Decay,” *Phys.Lett.*, vol. B660, pp. 167–171, 2008, arXiv:nucl-ex/0705.1039. (Cited on pages 73 and 75)

[177] G. Agakishiev *et al.*, “Baryonic resonances close to the $\bar{K}$ N threshold: The Case of $\Sigma(1385)^+$ in pp collisions,” *Phys.Rev.*, vol. C85, p. 035203, 2012, arXiv:nucl-ex/1109.6806. (Cited on pages 76, 77, and 82)

[178] J. Siebenson, “Exclusive analysis of the $\Lambda(1405)$ resonance in the charged $\Sigma\pi$ decay channels in proton proton reactions with HADES,” Diploma thesis, Technische Universität München, 2010. (Cited on page 87)

[179] D. Pleiner, “Hunting the ppK^-: A kinematic refit for the exclusive analysis of the reaction $p+p \rightarrow pK^+\Lambda$,” Diploma thesis, Technische Universität München, 2012. (Cited on page 87)

[180] K. Ermakov, V. Medvedev, V. Nikonov, O. Rogachevsky, A. Sarantsev, *et al.*, “The study of the proton-proton collisions at the beam momentum 1628 MeV/c,” *Eur.Phys.J.*, vol. A47, p. 159, 2011, arXiv:hep-ex/1109.1111. (Cited on page 97)

[181] A. Anisovich, V. Anisovich, E. Klempt, V. Nikonov, and A. Sarantsev, “Baryon-baryon and baryon-antibaryon interaction amplitudes in the spin-momentum operator expansion method,” *Eur.Phys.J.*, vol. A34, pp. 129–152, 2007. (Cited on page 97)

[182] A. Anisovich and A. Sarantsev, “Partial decay widths of baryons in

the spin-momentum operator expansion method," *Eur.Phys.J.*, vol. A30, pp. 427–441, 2006, arXiv:hep-ph/0605135. (Cited on pages 97 and 98)

[183] A. Sarantsev, "private communication." 2013. (Cited on pages 97, 188, 191, and 194)

[184] A. Anisovich, E. Klempt, A. Sarantsev, and U. Thoma, "Partial wave decomposition of pion and photoproduction amplitudes," *Eur.Phys.J.*, vol. A24, pp. 111–128, 2005. (Cited on page 98)

[185] S. Farrington, "Spectroscopic notation." `http://www2.warwick.ac.uk/fac/sci/physics/current/teach/module_home/px429/ssweek45.pdf`, 2013. (Cited on pages 99 and 187)

[186] F. Beaujean, A. Caldwell, D. Kollar, and K. Kroninger, "p-values for model evaluation," *Phys.Rev.*, vol. D83, p. 012004, 2011. (Cited on pages 115 and 116)

[187] A. Bhattacharyya, "The poisson distribution." `http://web.mit.edu/abhatt/8.13/poisson.pdf`, 2003. (Cited on page 115)

[188] M. J. Schervish, "P values: What they are and what they are not," *The American Statistician*, vol. 50, no. 3, pp. 203–206, 1996. (Cited on page 117)

[189] N. Espinoza, "Higgs boson "discovery" and how to not interpret p-values." `http://randomastronomy.wordpress.com/2012/07/04/higgs-boson-discovery-and-how-to-not-interpret-p-values/`, July 2012. (Cited on page 117)

[190] G. D'Agostini, "Confidence limits: What is the problem? Is there the solution?," 2000, arXiv:hep-ex/0002055. (Cited on page 117)

[191] G. D'Agostini, "Probably a discovery: Bad mathematics means rough scientific communication," 2011, arXiv:physics.data-an/1112.3620. (Cited on page 117)

[192] J. Beringer *et al.*, "Review of Particle Physics (RPP)," *Phys.Rev.*, vol. D86, p. pp. 394, 2012. (Cited on pages 117, 119, and 122)

[193] K. Staley, "On the five sigma standard in particle physics." `http://errorstatistics.com/2013/04/04/guest-post-kent-staley-on-the-five-sigma-standard-in-particle-physics/`, April 2013. (Cited on page 119)

[194] A. L. Read, "Modified frequentist analysis of search results (The CL(s) method)," *CERN-OPEN-2000-205*, 2000. (Cited on pages 121 and 122)

[195] T. Junk, "Confidence level computation for combining searches with small statistics," *Nucl.Instrum.Meth.*, vol. A434, pp. 435–443, 1999, arXiv:hep-ex/9902006. (Cited on page 122)

[196] A. L. Read, "Presentation of search results: The CL(s) technique," *J.Phys.*, vol. G28, pp. 2693–2704, 2002. (Cited on page 122)

[197] R. Louttit, T. Morris, D. Rahm, R. Rau, A. Thorndike, *et al.*, "Production of Strange Particles in p-p Collisions at 2.85 Bev," *Phys.Rev.*, vol. 123, pp. 1465–1471, 1961. (Cited on pages 146, 147, and 229)

[198] A. Sibirtsev, C. Elster, J. Haidenbauer, and J. Speth, "Incoherent photoproduction of eta mesons from the deuteron near threshold," *Phys.Rev.*, vol. C64, p. 024006, 2001, arXiv:nucl-th/0104011. (Cited on page 152)

[199] S. Abd El-Samad, E. Borodina, K.-T. Brinkmann, H. Clement, E. Doroshkevich, R. Dzhygadlo, K. Ehrhardt, A. Erhardt, W. Eyrich, H. Freiesleben, W. Gast, A. Gillitzer, D. Grzonka, C. Hanhart, F. Hauenstein, P. Klaja, K. Kilian, M. Krapp, J. Ritman, E. Roderburg, M. Röder, M. Schulte-Wissermann, W. Schroeder, T. Sefzick, G. Wagner, P. Wintz, and P. Wüstner, "On the ΣN cusp in the pp→ $pK^+\Lambda$ reaction," *The European Physical Journal A*, vol. 49, no. 3, pp. 1–8, 2013. (Cited on pages 153, 163, and 165)

[200] E. Ferrari, "Further comments on the description of three-body associated production in proton proton collisions through the one-boson-exchange model," *Phys.Rev.*, vol. 175, pp. 2003–2009, 1968. (Cited on pages 158, 159, 161, and 172)

[201] K. Tsushima, A. Sibirtsev, A. W. Thomas, and G. Li, "Resonance model study of kaon production in baryon baryon reactions for heavy ion collisions," *Phys.Rev.*, vol. C59, pp. 369–387, 1999, arXiv:nucl-th/9801063. (Cited on pages 158 and 160)

[202] A. Sibirtsev and W. Cassing, "Strangeness production in proton proton collisions," 1998, arXiv:nucl-th/9802019. (Cited on pages 158 and 160)

[203] R. Münzer, "Search for the kaonic bound state ppK^-. Exclusive analysis of the p+p→ $p + K^+ + \Lambda$ reaction at the FOPI experiment at GSI," Doctoral dissertation thesis, Technische Universität München, 2014. (Cited on pages 163, 167, and 171)

[204] M. Firebaugh, G. Ascoli, E. Goldwasser, R. Sard, and J. Wray, "Strange-particle production in 8-BeV/c proton-proton interactions," *Phys.Rev.*, vol. 172, pp. 1354–1369, 1968. (Cited on pages 163 and 170)

[205] K. Suzuki, P. Kienle, M. Maggiora, and T. Yamazaki, "Population of the X(2265) resonance in the $p + p \to X + K^+$ reaction at T_p = 2.5 GeV," *Hyperfine Interact.*, vol. 210, pp. 71–75, 2012. (Cited on page 164)

[206] E. Epple, L. Fabbietti, R. Münzer, and J. Siebenson, "Partialwellen analyse von ereignissen in proton-proton reaktionen für energien zwischen 1.9 und 3.5 gev." DFG: Proposal FA 898/2-1, 2014. (Cited on page 172)

[207] J. Balewski, A. Budzanowski, H. Dombrowski, W. Eyrich, C. Goodman, *et al.*, "Total cross-section of the reaction $pp \to pK^+\Lambda$ close to threshold," *Phys.Lett.*, vol. B420, pp. 211–216, 1998, arXiv:nucl-ex/9803003. (Cited on page 230)

[208] S. Sewerin, G. Schepers, J. Balewski, A. Budzanowski, W. Eyrich, *et al.*, "Comparison of Λ and Σ^0 threshold production in proton proton collisions," *Phys.Rev.Lett.*, vol. 83, pp. 682–685, 1999, arXiv:nucl-ex/9811004. (Cited on page 230)

[209] P. Kowina, M. Wolke, H. Adam, A. Budzanowski, R. Czyzykiewicz, *et al.*, "Energy dependence of the Λ/Σ^0 production cross-section ratio in p p interactions," *Eur.Phys.J.*, vol. A22, pp. 293–299, 2004, arXiv:nucl-ex/0402008. (Cited on page 230)

[210] A. Budzanowski *et al.*, "Cross section of the $pp \to K^+\Sigma^+n$ reaction close to threshold," *Phys.Lett.*, vol. B692, pp. 10–14, 2010, arXiv:hep-ex/1007.1542. (Cited on page 230)

[211] Y. Valdau, S. Barsov, M. Büscher, D. Chiladze, S. Dymov, *et al.*, "The energy dependence of the $pp \to K^+n\Sigma^+$ reaction close to threshold," *Phys.Rev.*, vol. C81, p. 045208, 2010, arXiv:hep-ex/1002.3459. (Cited on page 230)

[212] Y. Valdau, V. Koptev, S. Barsov, M. Büscher, S. Dymov, *et al.*, "The $pp \to K^+n\Sigma^+$ reaction near threshold," *Phys.Lett.*, vol. B652, pp. 245–249, 2007, arXiv:nucl-ex/0703044. (Cited on page 230)

[213] W. J. Fickinger, E. Pickup, D. K. Robinson, and E. O. Salant, "p-p Interactions at 2 Bev. I. Single-Pion Production," *Phys. Rev.*, vol. 125, pp. 2082–2090, Mar 1962. (Cited on page 230)

[214] A. Baldini, V. Flaminio, W. G. Moorhead, and D. R. O. Morrison, “Total cross-sections for reactions of high energy particles,” in *Landolt-Börnstein, New Series*, vol. 12 Subvolume a and b, p. 417(a) and 468(b), Heidelberg: Springer-Verlag, 1985. (Cited on page 230)

👍 Acknowledgments 👍

Ich möchte mich zuallererst bei Prof. Dr. Laura Fabbietti bedanken, dass sie mir die Möglichkeit gegeben hat in ihrer Gruppe meine Wissenschaftliche Arbeit anzufertigen. Ihr Fokus gilt stehts der Formulierung von klaren wissenschaftlichen Statements die auch über unsere Gruppe hinaus einen Beitrag für andere Wissenschaftler liefern, was mich sicherlich geprägt hat. Das unermüdliche fordern von Präzision bei Vorträgen und Texten ist mir mittlerweile in Fleisch und Blut übergegangen und ich danke ihr daher auch für die vielen Korrekturen die sie immer wieder gegenüber meiner Arbeit angebracht hat.

Meinem Lieblingsbüronachbarn Johannes, dem ich immernoch hinterher trauere 🌧, möchte ich für die vielen Jahre der Diskussion und Inspiration danken. Unser $\Lambda(1405)$ Tandem war einmalig, wenn auch leider etwas assymetrisch was den Wissenschaftlichen output angeht.

Im April 2008, als ich zur KClus Gruppe kam warteten dort meine allerersten Kollegen Robert und Martin die mir daher immer besonders verbunden waren. Danke für die schöne Zeit euch beiden.

KClus wurde größer und kleiner und die, die geblieben sind, haben alle auf ihre Weise zur Erheiterung meiner Laune beigetragen wie Chii, Rafal, Oliver, Piotr, Dimitar, Joanna und Verena. Danke euch allen für den quatsch und ganz besonders für die vielen Kuchen hmmmmm.

Bianca möchte ich danken, dass sie mir geholfen hat die unglaublich vielen $\overline{K}NN$ Zustände durchzusimulieren. Das war eine große Hilfe.

Unter denen die gegangen sind möchte ich besonders Alexander Schmah danken der uns Studenten der ersten Generation alle das 1x1 von Tiffini und root beigebracht hat, was man am taktischsten bei einer Datenanalyse macht, und wann man sich mal kräftig über jemanden aufregen darf.

Für das lesen und korrigieren von Teilen meiner Arbeit möchte ich Oliver, Robert, Chii, Johannes, Kirill und Laura danken, das hat dem ganzen sicherlich den letzten Schliff gegeben.

Zuletzt möchte ich mich bei meiner kleinen und grossen Familie bedanken: Kirill und Greta, und meinen Eltern Hanna und Karl sowie Annika und Achim. Danke, dass ihr versucht mein Leben so angenehm wie möglich zu machen ohne etwas zu beschönigen. Ohne euch wäre ich jetzt nicht da wo-, und wie ich heute bin.